Doctoral Dissertation
博士論文

The measurement of the highest-energy cosmic ray energy spectrum with the extended surface detector array of the Telescope Array experiment
(TA 実験拡張地表検出器アレイによる最高エネルギー宇宙線エネルギースペクトルの測定)

A Dissertation Submitted for the Degree of Doctor of Philosophy
December 2023
令和５年１２月博士（理学）申請

Department of Physics, Graduate School of Science,
The University of Tokyo
東京大学大学院理学系研究科物理学専攻

Kozo Fujisue
藤末　紘三

Abstract

The origins of the ultra-high-energy cosmic rays (UHECRs) have not been unveiled since the first observation in the 1960s. Recently, an indication of intermediate-scale anisotropy of UHECRs with energies greater than 5.7×10^{19} eV, called the TA hotspot, was reported by the Telescope Array (TA) experiment. However, the anisotropy has not been confirmed statistically. In addition to the anisotropy, a difference in the energy spectrum observed by the TA experiment and the Pierre Auger Observatory (PAO) is recognized. The difference is possibly due to astrophysical origins since the fields of view of the experiments are quite different; the TA experiment observes mainly the northern sky, while the PAO observes mainly the southern sky. However, the experimental systematic biases might produce the difference. Understanding the difference between the experiments is significant for discussing UHECR in the whole sky.

The expansion of the TA experiment — the TA×4 experiment — started its observation in 2019 with an additional 257 surface detectors (SDs) with 2.08 km detector spacing and two new fluorescence detector (FD) stations. The expanded detectors have an observation area of approximately 1000 km^2. The TA×4 SD array is the largest detector array in the Northern Hemisphere. The primary mission of the TA×4 experiment is increasing the number of UHECR events, especially for $E > 5.7 \times 10^{19}$ eV, and confirming the existence of the TA hotspot. In addition, the increasing statistics will contribute to more precise measurements of the highest-energy cosmic ray energy spectrum and the energy spectrum anisotropy. The hybrid observation by the SD and FD also contributes to understanding the mass composition of the highest-energy cosmic rays.

In this work, we establish analysis methods for the expansion surface detector array, the TA×4 SD array, reproduce the time-dependent running status of the TA×4 SD array by the established Monte Carlo (MC) simulation, and measure the highest-energy cosmic ray energy spectrum above 10^{19} eV with the TA×4 SD array for the first time. The running status of the TA×4 SD array varied over time due to initial malfunctions, repairs, and improvement of the trigger system. We achieved the stable operation of the TA×4 SD array through remote operation and maintenance. The running status is well reproduced by the MC simulation regardless of the running status.

We calibrate the energy measured by the TA×4 SD array with a newly developed method. In the method, energy is calibrated by comparing the number of events observed by the TA×4 SD array with that expected by the MC simulation, assuming the previously measured energy spectrum by the TA SD array. The energy scale, which is a factor to calibrate the energy to the FD energy, of the TA×4 SD array is determined to be 1.36 ± 0.05.

The energy spectrum measured with the TA×4 SD array prefers a broken power law model over a single power law model, although neither models is ruled out; the p-values of the chi-square test for both models are 0.140 and 0.0811, respectively. The best fit of the broken power law model is consistent with the previous TA SD measurement. This consistency indicates that the energy is correctly determined.

We calculate the UHECR energy spectrum by combining the TA SD data and the TA×4 SD data. The exposure of the TA×4 SD array in three years of observation is approximately 30% of the exposure of the TA SD array in 14 years of observation. The combined energy spectrum prefers a power-law model with three breaks over a model with two breaks; the p-values of the chi-square test for both models are 0.246 and 0.0329, respectively. This test indicates that a spectral feature corresponding

to the so called "instep" feature observed in the southern sky by the PAO is also measured in the northern sky. The significance of the cutoff structure is calculated to be 8.2σ with the combined data of the TA SD array and the TA×4 SD array. These are the most statistically precise measurements of the UHECR energy spectrum in the northern sky.

We also compare the energy spectrum of the common declination band, where both the TA experiment and the PAO observe, considering declination-dependent exposures, which have not been considered in the previous analysis. The energy spectrum of the common declination band should agree between both experiments if there is no systematic bias between them. The energy spectra of the common declination band is found to differ between the experiments with a statistical significance of 3.5σ without considering the declination-dependent exposures, but the discrepancy reduces to 2.2σ with the model considering them. The significance of 2.2σ is not small, and it does not fully explain the difference in the energy spectra observed in the full fields of view of the TA experiment and PAO.

At last, we discuss future results expected to be observed by the TA×4 SD array, including the TA SD array. The TA×4 experiment will be able to confirm the TA hotspot with a significance of 5.7σ by 2030, assuming that the event rate from the TA hotspot region is constant with the average over the first 15 years of observation.

Acknowledgements

I am grateful to my doctoral supervisor Takashi Sako for continuously guiding my research and supporting me devoting much of his time. I am also grateful to my master's program supervisor Hiroyuki Sagawa for continuously supporting me even after not being my supervisor. I would like to thank them not only for guiding my research but also supporting my research activities a lot including writing this thesis and making presentations. I am grateful to Eiji Kido for teaching me since I started my research as a master student. My study is based on his pioneering studies. I have learnt a lot from him while continuing my research: the design and data acquisition of TA×4 surface detectors, analysis methods, on-site maintenance, and physics. I would like to thank Dmitri Ivanov, Jihyun Kim, and Gordon Thomson for insightful discussion and collaborative research. Through discussion and research with them, my study has become more sophisticated. Jihyun Kim gave me advice not only on my study but also as a researcher. I am grateful to Keitaro Fujita for advising me a lot about analysis and techniques, sharing his knowledge and data set, and encouraging me. I used the MC data sets and the observational data sets of the TA SD he prepared in the Chapter 7 and 8. I would like to thank to Hyomin Jeong for pioneering work on the TA×4 SD analysis and sharing them with me. I would also like to thank Matthew Potts for sharing me TA×4 hybrid analysis results. I am grateful to Shoichi Ogio for giving me a lot of advice about my research and supporting my research activities. I would like to express my appreciation to Kazumasa Kawata, Toshiyuki Nonaka, and Masahiro Takeda for teaching and advising me a lot through my master and doctoral program. I would like to show my gratitude to Anatoli Fedynitch, Toshihiro Fujii, Charlie Jui, John N. Matthews, Takeshi Okuda, Naoto Sakaki, Yuichiro Tameda, Takayuki Tomida, Yoshiki Tsunesada, and Shigeharu Udo for advising and supporting my research. Charlie Jui, Jihyun Kim, John N. Matthews and Gordon Thomson kindly hosted me when I visited University of Utah. John N. Matthews reviewed English of this thesis. Of course, any mistakes and ambiguities are my responsibility. I am grateful to Ryo Higuchi, Sei Kato, Hitoshi Oshima, Shunsuke Sakurai, and Heungsu Shin. They gave me advice about studies and research life as a young researcher, and they also encouraged me a lot. I would like to thank students in ICRR, Kaoru Takahashi, Chisato Koyama, Yoshichika Yokoe, Teruyoshi Kawashima, and Atsushi Mizuno. They encouraged and supported me a lot. I would also like to express grateful to students in other institutes including those who have already graduated. I have been encouraged by them.

I would like to express my gratitude to Adrian Baum, Robert Cady, Gary McDonough, and Patrick Wright for continuous maintenance of the TA×4 SDs. Their fast and precise work kept the stable observation of the TA×4 SD array, especially in the COVID-19 pandemic. I would like to thank technical stuffs in ICRR Nao Okazaki, Koichi Sekino, Hideaki Shimodaira for their work on the maintenance and supporting me. I am also grateful to secretaries Takako Idomura, Atsuko Kitsugi, and Ryoko Shiraga for supporting me about procedures related to business travel and payroll.

I am grateful to referees of this PhD thesis Takanori Yoshikoshi, Katsuaki Asano, Masaya Ishino, Hidetoshi Kubo, and Masashi Yokoyama. This thesis were polished up with their advice and suggestions. I appreciate support from WINGS-QSTEP, the University Fellowship program for Science and Technology Innovations. I would like to thank once again all those who have been involved in my research activities.

Finally, I would like to express my gratitude to my family for supporting my life.

The Telescope Array experiment is supported by the Japan Society for the Promotion of Science(JSPS) through Grants-in-Aid for Priority Area 431, for Specially Promoted Research JP21000002, for Scientific Research (S) JP19104006, for Specially Promoted Research JP15H05693, for Scientific Research (S) JP19H05607, for Scientific Research (S) JP15H05741, for Science Research (A) JP18H03705, for Young Scientists (A) JPH26707011, and for Fostering Joint International Research (B) JP19KK0074, by the joint research program of the Institute for Cosmic Ray Research (ICRR), The University of Tokyo; by the Pioneering Program of RIKEN for the Evolution of Matter in the Universe (r-EMU); by the U.S. National Science Foundation awards PHY-1806797, PHY-2012934, PHY-2112904, PHY-2209583, and PHY-2209584 as well as AGS-1613260, AGS-1844306, and AGS-2112709; by the National Research Foundation of Korea (2017K1A4A3015188, 2020R1A2C1008230, & 2020R1A2C2102800); by the Ministry of Science and Higher Education of the Russian Federation under the contract 075-15-2020-778, IISN project No. 4.4501.18, by the Belgian Science Policy under IUAP VII/37 (ULB), by National Science Centre in Poland grant 2020/37/B/ST9/01821. This work was partially supported by the grants of The joint research program of the Institute for Space-Earth Environmental Research, Nagoya University and Inter-University Research Program of the Institute for Cosmic Ray Research of University of Tokyo. The foundations of Dr. Ezekiel R. and Edna Wattis Dumke, Willard L. Eccles, and George S. and Dolores Doré Eccles all helped with generous donations. The State of Utah supported the project through its Economic Development Board, and the University of Utah through the Office of the Vice President for Research. The experimental site became available through the cooperation of the Utah School and Institutional Trust Lands Administration (SITLA), U.S. Bureau of Land Management (BLM), and the U.S. Air Force. We appreciate the assistance of the State of Utah and Fillmore offices of the BLM in crafting the Plan of Development for the site. We thank Patrick A. Shea who assisted the collaboration with much valuable advice and provided support for the collaboration's efforts. The people and the officials of Millard County, Utah have been a source of steadfast and warm support for our work which we greatly appreciate. We are indebted to the Millard County Road Department for their efforts to maintain and clear the roads which get us to our sites. We gratefully acknowledge the contribution from the technical staffs of our home institutions. An allocation of computing resources from the Center for High Performance Computing at the University of Utah as well as the Academia Sinica Grid Computing Center (ASGC) is gratefully acknowledged.

Contents

Chapter 1

Introduction

Cosmic rays, charged particles originating from the universe, were first discovered by V. Hess in 1912 [1]. Since their discovery, cosmic rays have been observed with energies ranging from 10^8 eV to beyond 10^{20} eV. Figure 1.1 shows the cosmic ray energy spectrum measured by several experiments. The figure shows that the cosmic ray energy spectrum approximately follows a power law E^{α} in a wide energy range where the index α is approximately -3 but dependent on energy. Cosmic rays with energies less than $\sim 10^{14}$ eV are directly observed in space, whereas cosmic rays with energies greater than $\sim 10^{14}$ eV are observed indirectly at ground level by means of the air showers of secondary particles resulting from the interaction of primary cosmic rays with atmospheric nuclei. The details of the air shower are described in Sec. 2.1.

Cosmic rays with energies greater than 10^{18} eV, observed indirectly via air showers, are called ultra-high-energy cosmic rays (UHECRs). The origins of UHECRs remain elusive despite their first observation in the 1960s [3]. The difficulties in identifying the origins of UHECRs stem from some factors. One of the significant factors is that UHECRs are charged particles and, therefore, do not travel straight under the influence of cosmic magnetic fields. According to the recent galactic magnetic field model [4], the deflection of the UHECR by the galactic magnetic field is expected to be $15 \sim 40 \times \frac{10EeV}{E/Z}$ degrees, where E and Z are energy and charge per elementary charge of the UHECR, respectively. Another major factor is the low arrival frequency of UHECRs: less than one particle with energy greater than 10^{20} eV arrives per one square kilometer per century. Therefore, a giant observation area of several hundred square kilometers is necessary to observe the UHECR and make statistical arguments.

This chapter provides an overview of the basic concepts of UHECRs, including their scientific interests, current observational results, and current topics to be studied. At the end of this chapter, we describe the motivation and goals for this study.

1.1 Ultra-high-energy cosmic rays and scientific interests

The comprehension of UHECRs is a focal point in astrophysics, driven by their status as the most energetic particles in the universe. This section introduces scientific interests in UHECRs from astrophysics and particle physics.

1.1.1 Interests in astrophysics

UHECRs are expected to originate from the most extreme phenomena in the universe. Theoretically, some potential candidates could be origins of UHECRs from small-scale objects such as gamma-ray bursts to large-scale objects such as galaxy clusters [5]. Figure 1.2, referred to as the Hillas plot, shows the constraints on the

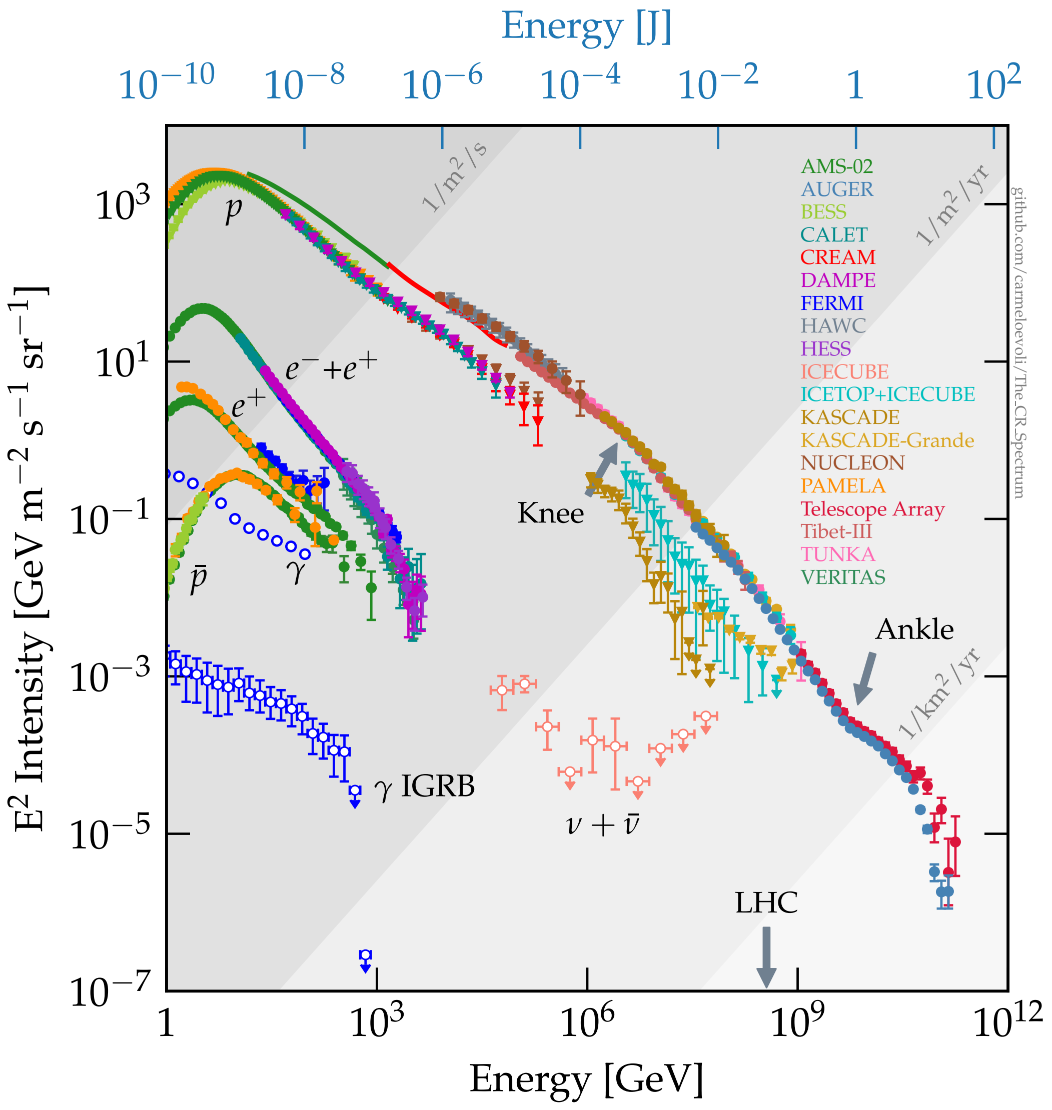

FIGURE 1.1: The cosmic ray energy spectrum measured by several experiments, taken from [2]. The flux is multiplied by E^2.

UHECR sources in terms of size and magnetic field strength required for UHECR confinement [6]. As seen in the figure, many astronomical objects of a wide range of sizes satisfy this constraint and there is no candidate which is able to confine cosmic rays with energies much greater than 10^{20} eV. In addition to the confinement limit, the UHECR sources have to exist in the local universe within several hundred Mpc since UHECRs lose their energy by interacting with background photons as shown in Fig. 1.3. Although many candidates for the UHECR source have been discussed, none of them have been confirmed experimentally as UHECR sources. Revealing the sources of UHECRs is crucial to understanding the acceleration mechanism in extreme environments.

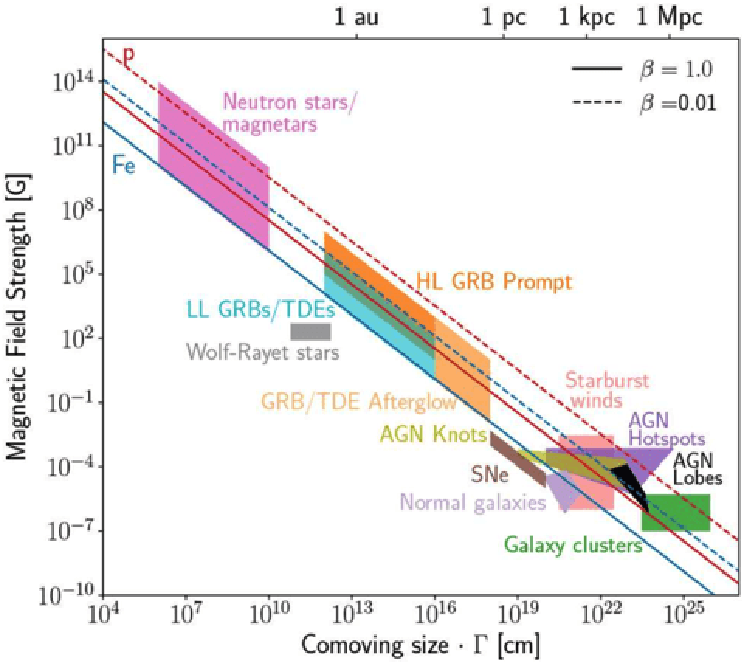

FIGURE 1.2: The Hillas plot, taken from [5]. The sources lie to the right of the diagonal lines can confine 10^{20} eV proton (red) and iron (blue) nuclei.

In addition to understanding the extreme phenomena in the universe, UHECRs offer means to explore cosmic magnetic fields [8] [9].

1.1.2 Interests in particle physics

UHECRs are not only connected to astrophysics but also particle physics. The maximum center of mass energy $\sqrt{s}$ of proton-proton collision is $\sim$ 14 TeV by Large Hadron Collider (LHC). This energy corresponds to a collision between a proton cosmic ray with energy of $\sim 10^{17}$ eV and an atmospheric nucleon. This means UHECR measurements could be experiments to verify particle interaction at extremely high energies beyond those produced by humans. The connection between UHECR and particle physics will be described later in Sec. 2.5.

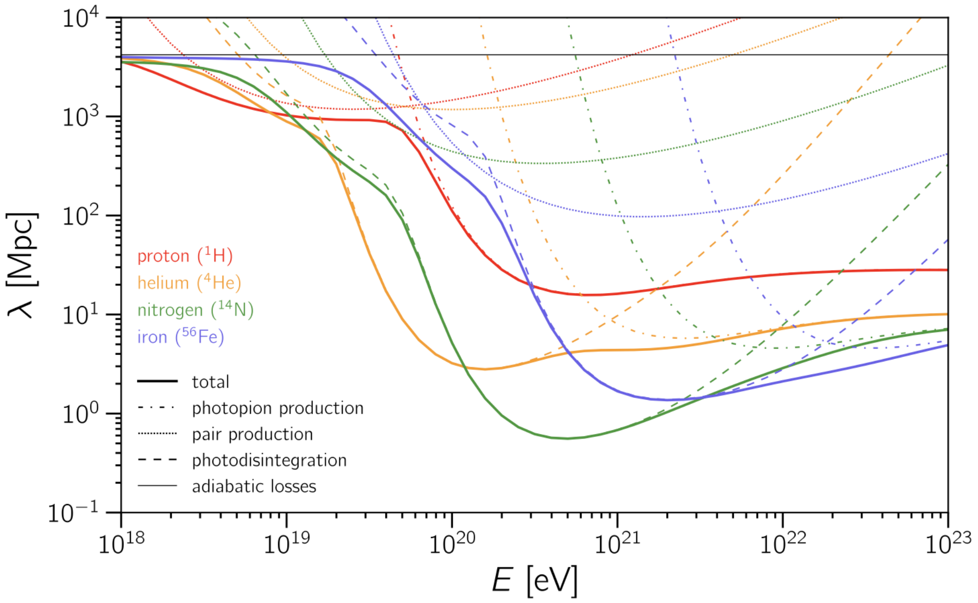

FIGURE 1.3: The energy loss length λ of UHECRs as a function of energy, taken from [7]. The different colors indicate different masses of UHECRs.

1.2 Recent observational results of UHECRs: the UHECR energy spectrum and the TA hotspot

This section introduces the recent observational results on the UHECR energy spectrum and the TA hotspot. Other recent observational results will be introduced in Sec. 2.4. We especially focus on the observational results from two UHECR observatories: the Telescope Array (TA) experiment [10] and the Pierre Auger Observatory (PAO) [11]. The TA experiment is located in the Northern Hemisphere (39.1° N, 112.9° W), while the PAO is located in the Southern Hemisphere (35.2° S, 69.2° W). The whole sky is covered by combining the two experiments. The descriptions of the two observatories will be given in Sec. 2.3.

1.2.1 Energy spectrum

The cosmic ray energy spectrum follows approximately a power law with an index of -3. Shock acceleration [12] can explain the power-law structure. Some features have been observed in the UHECR energy spectrum as shown in Fig. 1.4: the hardening around 5×10^{18} eV, and the suppression around 5×10^{19} eV (referred to as *ankle* and *cutoff*, respectively). Recently, the PAO observed a new softening feature at 1.3×10^{19} eV (referred to as *instep*) [13]. These features could reflect the acceleration mechanism, the mass composition, the propagation, and the distribution of the sources of cosmic rays. The interpretation of structures in the energy spectrum will be introduced in Sec. 2.4.3.

Cutoff of the cosmic rays energy spectrum

Greisen [15], and Zatsepin and Kuzmin [16] predicted a strong suppression in the cosmic rays energy spectrum at $10^{19.8}$ eV due to the interaction between proton and

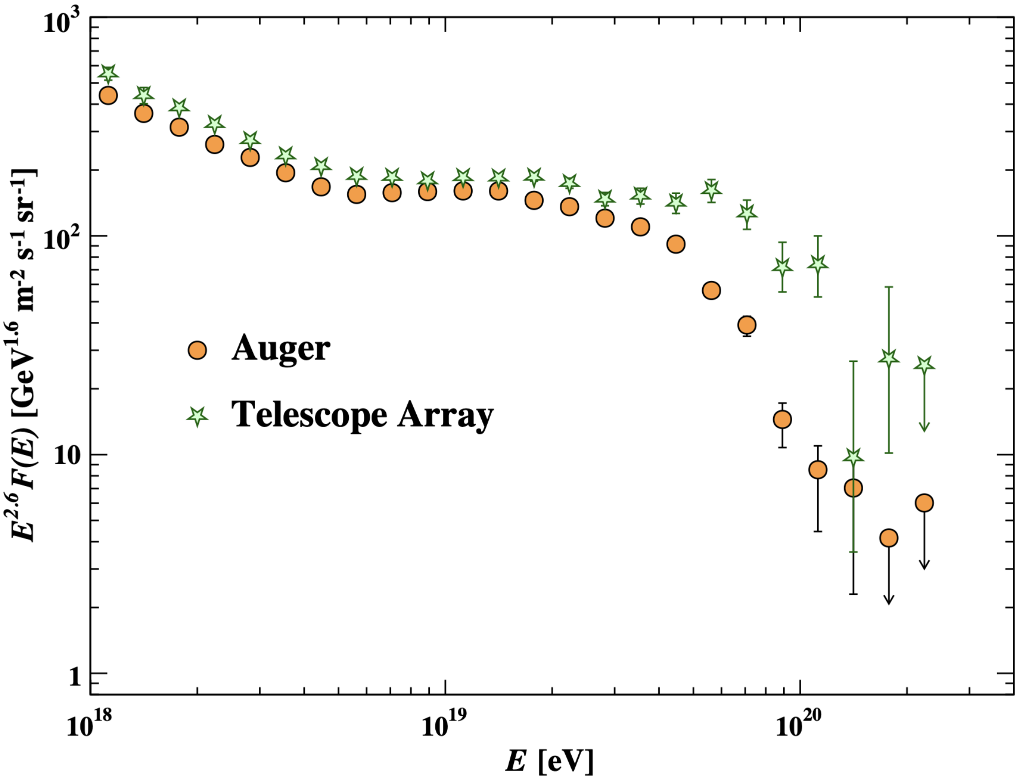

FIGURE 1.4: The energy spectrum of UHECRs measured by the Telescope Array experiment and the Pierre Auger Observatory [14].

cosmic microwave background (CMB) in 1966. This suppression is referred to as the GZK cutoff.

The Akeno Giant Air Shower Array (AGASA) experiment measured 11 events with energies above 10^{20} eV, which suggested the absence of the GZK cutoff [17]. On the other hand, the High-Resolution Fly's Eye (HiRes) experiment measured the energy spectrum with the cutoff structure with a significance above 5σ [18]. The energy spectrum observed by both experiments is shown in Fig. 1.5. The discrepancy between the two experiments was one of the biggest problems in astroparticle research in the 2000s. One of the difficulties in solving the problem was the different observational techniques used in the experiments: surface detectors for the AGASA and fluorescence detectors for the HiRes experiment. This problem motivated the next generation of UHECR observatories: the PAO and the TA experiment, which adopted sets of surface and fluorescence detectors.

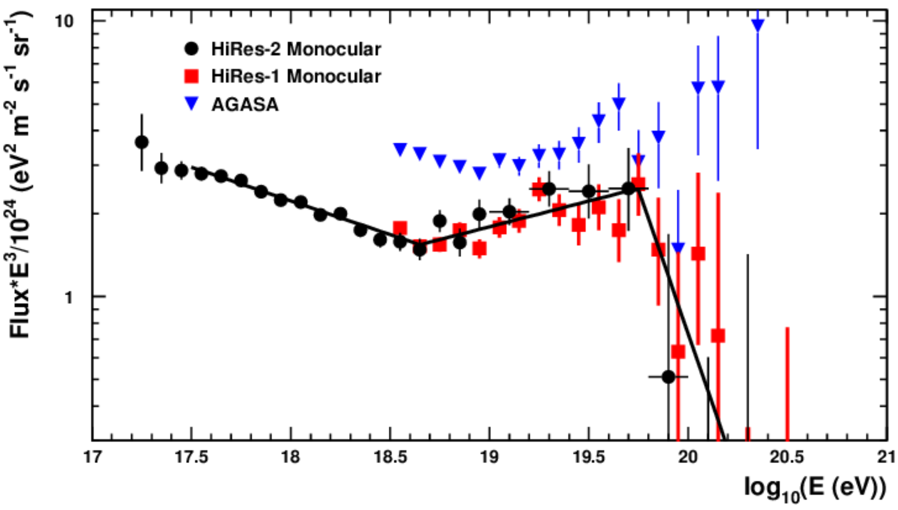

FIGURE 1.5: The energy spectrum measured by the Hires experiment [18] (black circles and red squares) and the AGASA experiment [17] (blue triangles), taken from [18].

Both the PAO and the TA experiment reported the cutoff feature in the cosmic ray energy spectrum (Fig. 1.4). The cutoff feature can be explained not only by the GZK cutoff but also by the photodisintegration of nuclei (as shown by a blue dashed line in Fig. 1.3). In addition to the energy loss during the propagation, the acceleration limits in sources of UHECRs are possibly reflected in the cutoff. According to the combined fit of the energy spectrum and the mass composition reported by the PAO, the cutoff structure might be explained by the interplay between the photodisintegration of nuclei during the propagation and the acceleration limit [19]. On the other hand, the combined fit reported by the TA experiment indicates that the cutoff might be explained by the GZK-effect [20]. These combined fit results are explained in Sec. 2.4.3. Observing more UHECR events in the highest-energy region is necessary to understand the nature of the cutoff.

Differences in the energy spectrum between the Telescope Array experiment and the Pierre Auger observatory

Differences between the energy spectra measured by the TA experiment and the PAO have been recognized. As seen in Fig. 1.4, there are two types of difference. One is the difference in energy scale. This difference is approximately 9% in energy scale independent of energy, which is within the systematic uncertainties of the TA experiment (21%) and the PAO (14%) [21]. The Auger-TA joint working group reported that the differences up to $10^{19.5}$ eV can be reduced from 9% to 1–3% by using the same fluorescence yield model, missing energy model in the fluorescence detectors (FDs), and method of calibrating the energy of surface detectors with that of FDs [22] (Fig. 1.6). The other is the difference of the spectral shape for energy greater than $10^{19.5}$ eV. The latter difference above $10^{19.5}$ eV has not been understood.

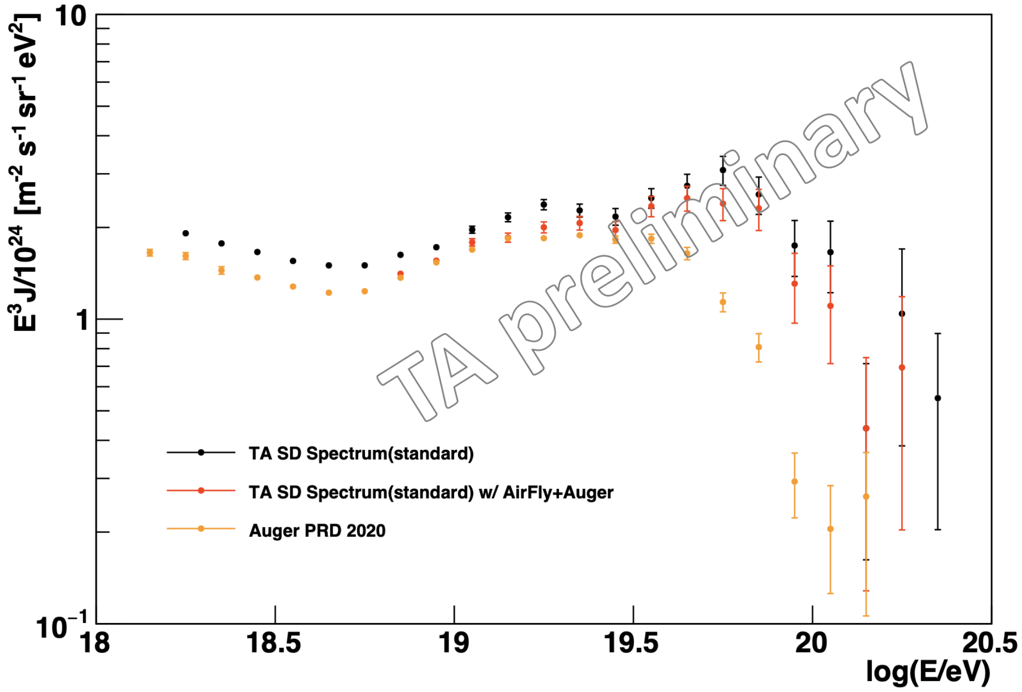

FIGURE 1.6: The energy spectra measured by the TA experiment (black points and red open circles) and the PAO (orange points) [22]. The black points indicate the energy spectrum measured by the TA experiment using their conventional way, while the red open circles indicate that using the same fluorescence yield model and the missing energy model in the fluorescence detectors (FDs) and the same method of calibrating the energy of surface detectors with that of FDs as PAO.

Since the TA experiment observes mainly the northern sky, and the PAO observes mainly the southern sky, the difference of the spectral shape above $10^{19.5}$ eV possibly reflects the UHECR source distribution. In fact, the TA experiment reported a declination dependence in the energy spectrum in the northern sky [23]. In contrast, the PAO reported no such dependence in the southern sky [13]. Figure 1.7 shows the energy spectra observed in different declination bands.

An accurate comparison of the two experiments' systematic uncertainties is necessary to test the models that explain the differences by astrophysical origins. For

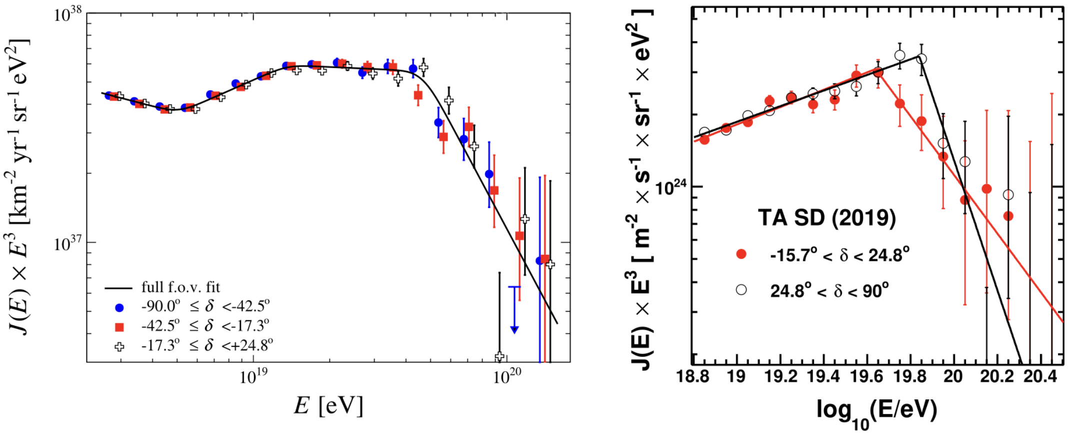

FIGURE 1.7: The energy spectra observed in different declination bands observed by the PAO (left) [13] and the TA experiment (right) [23].

example, the difference of the spectral shape above $10^{19.5}$ eV could be explained if there is a local UHECR source in the Northern Hemisphere [24]. Understanding the systematic uncertainties in the two experiments is important not only for understanding the spectral difference but also for studying UHECR an a whole-sky basis. One strategy to evaluate their systematic uncertainties is a comparison of the energy spectra in the common declination band where both the TA experiment and the PAO observe. They must agree since both experiments observe the same sky region. Figure 1.8 shows the energy spectra of the common declination band [25]. As seen in the figure, the difference persists in the common declination band, although the difference reduces compared with the energy spectra of their full fields of view. This difference is discussed later in Chap. 8.

1.2.2 TA hotspot

The TA experiment reported an indication of intermediate-scale anisotropy of UHECRs with energies greater than 5.7×10^{19} eV (*TA hotspot*) with five years of the observation (Fig. 1.9) [26]. The direction of the TA hotspot is 19° off the supergalactic plane in the vicinity of the Ursa Major cluster. By 20°-radius circle oversampling, 19 of the 72 events above 5.7×10^{19} eV were found to the direction where the maximum pre-trial significance was obtained. This corresponds to a 5.1σ excess, and the post-trial probability is 3.4σ. With the recent data set of the TA experiment with 15 years of observation, the post-trial probability is 2.8σ (Fig. 1.10) [27]. The TA hotspot is a clue to understand the UHECR source.

A lot of studies tried to reveal the source of the TA hotspot [28] [29] [30] [31] [32]. For example, a single source model considering energy-dependent magnetic deflections is discussed in [28]. In the model, UHECRs are bent according to their energy; the higher the UHECR energy, the less it is bent by the magnetic field. The source position, the strength of the coherent deflection, the direction of the coherent deflection, and the strength of the random deflection are free parameters in the model. Figure. 1.11 shows the best fit of the model with the 5 years of the TA SD data. The best-fit source position is near the starburst galaxy M82. Because of the limited statistics, source candidates can not narrowed to one; there are eight source

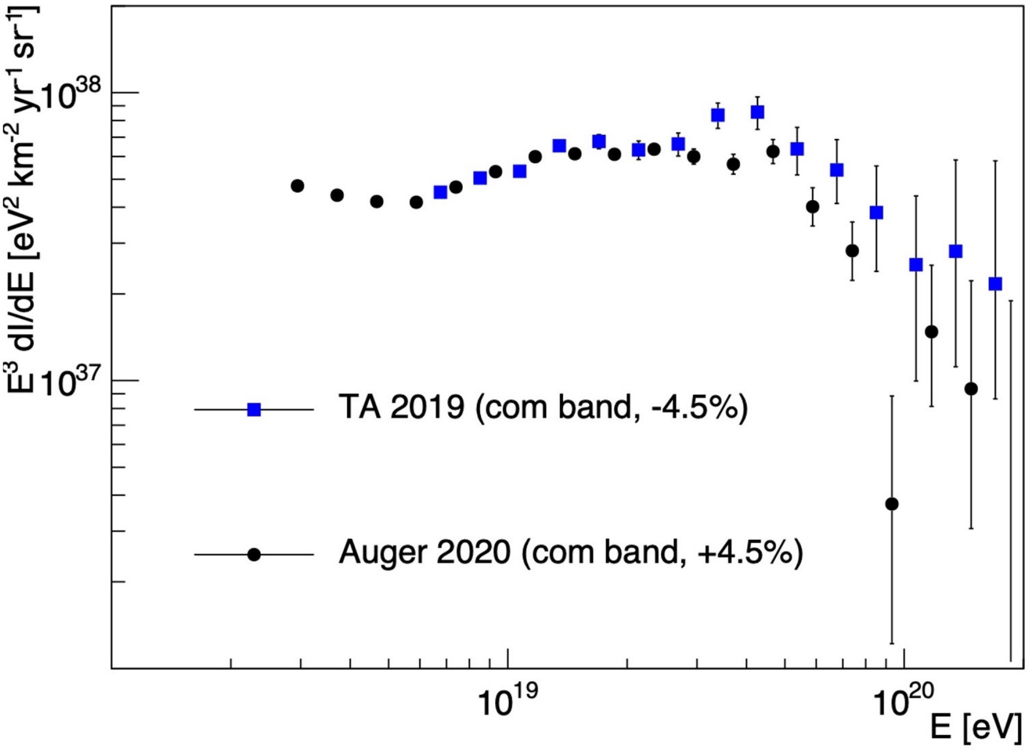

FIGURE 1.8: The energy spectra in the common declination band observed by the TA experiment (blue squares) and the PAO (black points). The energies are scaled by -4.5% and $+4.5\%$ for the TA experiment and the PAO, respectively [25].

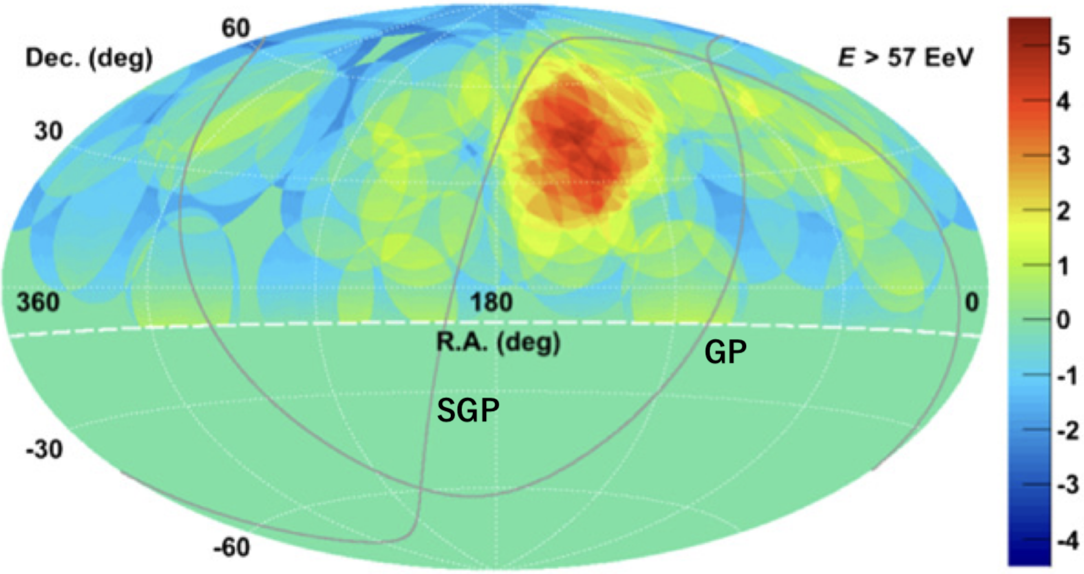

FIGURE 1.9: Aitoff projection of the UHECR map above 5.7×10^{19} eV in equatorial coordinates observed by the TA experiment [26] with five years of observation. The color indicates the local significance of the excess within a circle with a 20° radius. The solid lines show the Galactic plane (GP) and the supergalactic plane (SGP).

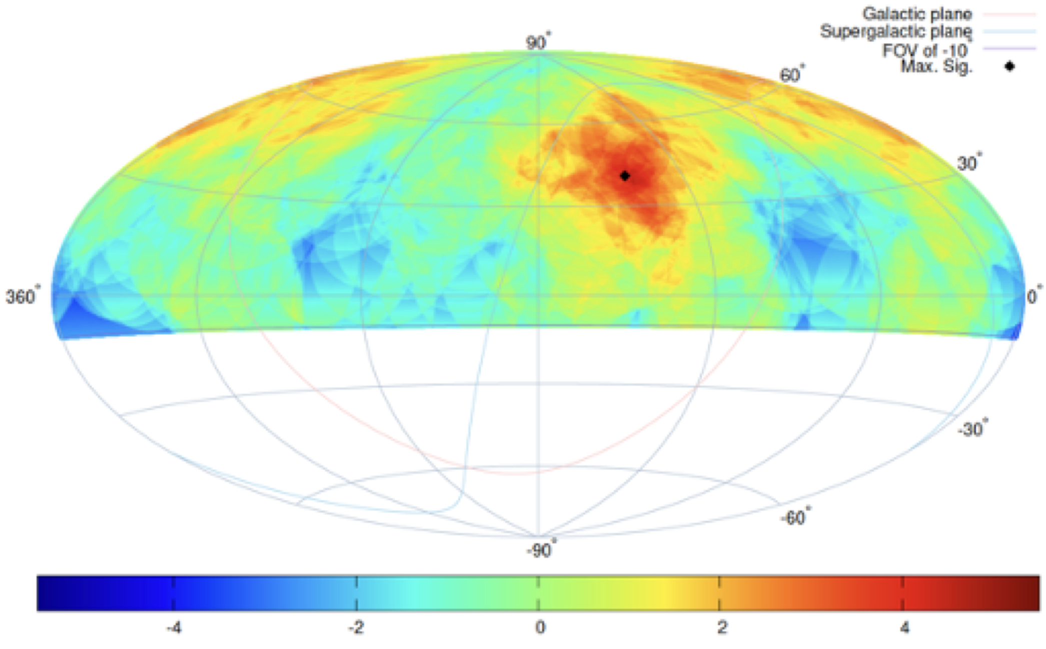

FIGURE 1.10: Aitoff projection of the UHECR map above 5.7 × 10^{19} eV in equatorial coordinates observed by the TA experiment with 15 years of observation [27]. The color indicates the local significance of the excess within a circle with a 25° radius.

candidates in the 1σ contour in Fig. 1.11. More statistics are required to verify and understand the TA hotspot. Future prospects of the observation of the TA hotspot is discussed in Chap. 9.

1.3 The motivation and goals for this study

The origins of UHECR are still veiled. The TA×4 experiment was constructed to increase the event rate of the UHECR, especially for energies greater than 5.7 × 10^{19} eV to confirm the TA hotspot statistically. The extended surface detector array at the first stage started observation in 2019 with an additional observational area of approximately 1000 km^2. This extension is approximately half of the final goal of the extension. In this work, the extended surface detector array at the first stage is referred to as the TA×4 SD array. The TA×4 SD array combining the original surface detector array, referred to as the TA SD array, is the largest air shower observatory in the Northern Hemisphere. The main mission of the TA×4 experiment is verifying the TA hotspot with more statistics. Understanding the difference between the energy spectra of the TA and the PAO becomes an important mission as the difference of spectral shape above $10^{19.5}$ eV has been recognized. In addition to those particular problems, more precise measurements of the energy spectrum, arrival directions, and the mass composition of the highest-energy cosmic rays in the northern sky will be achieved by the TA×4 experiment, including the originally constructed detectors. Details of the TA×4 experiment are given in Chap. 3.4 and Chap. 4.

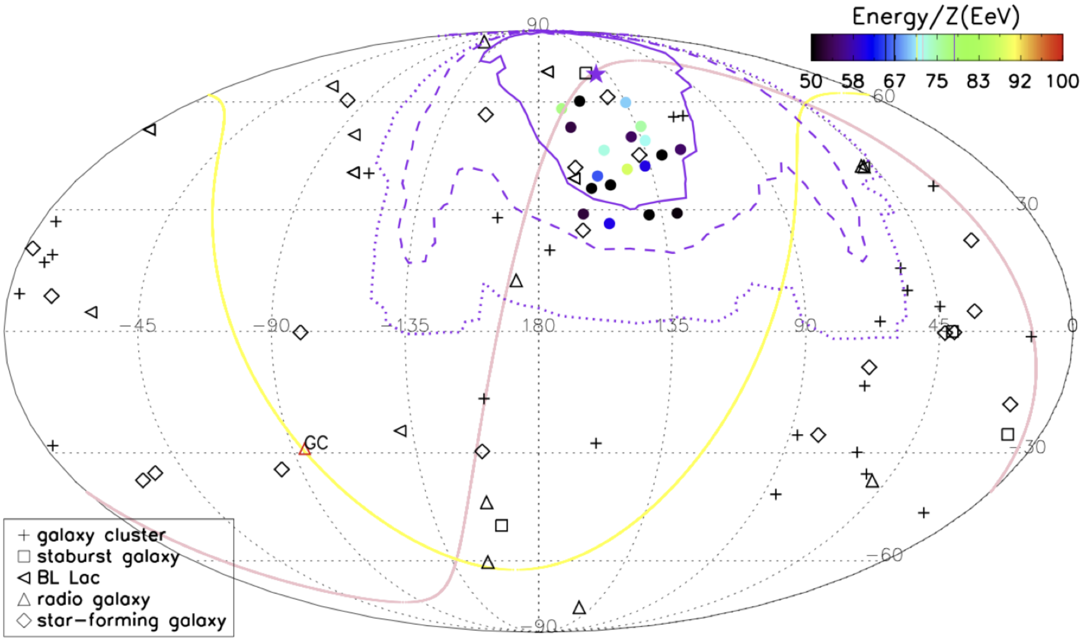

FIGURE 1.11: The best-fit coordinate of the TA hotspot source (represented by the purple star) in the single source model considering energy-dependent magnetic deflections [28]. The filled circles represent the 19 events in the TA hotspot region that the TA experiment observed with the 5 years of the observation. The color of the filled circles indicates their energy. The purple lines represent contours of 1σ, 2σ, and 3σ.

1.3.1 The contribution of this study to the UHECR research: the first observation of the highest-energy cosmic ray energy spectrum by the TA×4 SD array

In this work, we describe the running status of the TA×4 SD array (the extended SD array with the area of 1000 km^2), the analysis method established for the TA×4 SD array, and its first observational result: the highest-energy cosmic ray energy spectrum.

The TA×4 SD array has a larger detector spacing (2.08 km) compared with the TA SD array (1.2 km). Therefore, the performances are different between them. In addition, the first four years of the operation of the TA×4 were specific; the trigger system changed, and the occupancy rate of the SDs varied depending on the time since travel to the observational site had been restricted due to COVID-19 in the period.

To understand and analyze the observational data of the TA×4 SD array, it is necessary to establish a Monte Carlo (MC) simulation which reflects the status of the SD, including its time variability. I adjusted the MC simulation technique and the reconstruction method developed for the TA SD array to the TA×4 SD array by performing step-by-step verification of the data process. With the established MC simulation, I calibrated the energy estimated by the TA×4 SD array. In the case of the TA SD, the energy was calibrated using hybrid events simultaneously observed by the SD array and fluorescence detector (FD). In the case of the TA×4 SD array, however, the number of hybrid events is not sufficient to calibrate the SD energy due to the observational period and higher energy threshold. I proposed a new calibration method in which the energy spectrum measured by the TA SD is assumed. I also determined event selection criteria considering the performance of the TA×4 SD array.

I calculated the highest-energy cosmic ray energy spectrum above 10^{19} eV using the first three years of the TA×4 SD data with the established energy scale and the event selection criteria. I introduced a new method that is less dependent on the input energy spectrum than the method adopted in the TA SD array to verify and measure the cutoff independently from the previous measurement with the TA SD array. Then, I obtained the UHECR energy spectrum using the combined data of the TA×4 SD and the TA SD. The instep feature, reported by the PAO, is tested with the combined data. The significance of the cutoff is calculated as well. It is the measurement of the UHECR energy spectrum with the largest statistics in the Northern Hemisphere.

The comparison of the energy spectra in the common declination band of the TA and PAO, which is to be performed with the TA×4 SD array in the future, was discussed using the TA SD data with a model which considers declination-dependent exposures of the experiments. The declination-dependent exposures have not been considered in previous analyses, although they have to be considered.

At last, I calculated future projections expected to be observed by the TA×4 SD array: the UHECR energy spectrum, spectral anisotropy, and the TA hotspot. They are topics to be studied with the TA×4 SD array in the next decade.

The contents of this work are described in the following structure. In Chap. 2, we introduce the basic description of the phenomena and the measurement techniques of air showers. In Chap. 3, we introduce the TA experiment and the TA×4 experiment. In Chap. 4, we describe the design of the TA×4 SD and its running status for the first four years in detail. In Chap. 5, we describe the Monte Carlo simulation technique used in the TA×4 SD analyses. In Chap. 6, we describe the reconstruction method and the performance of the TA×4 SD array. In Chap. 7, the main chapter of this paper, we show the energy calibration method of the TA×4 SD array, comparison between the MC simulation and the observation, the highest-energy cosmic ray energy spectrum with the TA×4 SD data, and the UHECR energy spectrum combining the TA SD data and the TA×4 SD data. In Chap. 8, in which the TA×4 SD data is not used, we discuss the energy spectra of the TA and PAO in the common declination band considering the declination-dependent exposure. In Chap. 9, we discuss projections of the future observational results expected to be observed by the TA×4 SD array with increasing statistics. The final chapter, Chap. 10 is the conclusion of this work.

Chapter 2

The Air shower measurement

In this chapter, we introduce the basic description of the air shower phenomena and two techniques to observe the air showers: measurement of the lateral distributions by surface detectors (SDs) and measurement of the longitudinal profiles by fluorescence detectors (FDs).

We also introduce the current UHECR observatories, the Telescope Array (TA) experiment, and the Pierre Auger Observatory (PAO). Both experiments employ SD and FD.

A review of the recent observational results in the UHECR research (Sec. 2.4) that have not been mentioned in Sec. 1.2 are described along with the connection between UHECR and particle physics.

2.1 Air shower

When a UHECR enters the atmosphere of the earth, it interacts with a nucleus in the high atmosphere and produces multiple secondary particles. These secondary particles also produce another multiple particles by interacting with atmospheric nuclei. Consequently, many particles arrive at the ground. This phenomenon is called an air shower. The lateral distribution of particles in an air shower with 10^{20} eV at 1400 m, the altitude of the TA experiment, reaches $\sim$10 km. By measuring air showers, we estimate the energy, the arrival direction, and the particle type of the primary particles.

2.1.1 Physics of air showers

Pions are the most frequently generated secondary particles when an ultra-high-energy nucleus interacts with an atmospheric nucleus. Since neutral pions have a short mean lifetime ($(8.43 \pm 0.13) \times 10^{-17}$ sec [14]), most secondary neutral pions decay into two photons ($\pi^0 \rightarrow \gamma + \gamma$). The produced photons generate electromagnetic air showers by repetition of $e^{\pm}$ production by photon and photon production by $e^{\pm}$. Charged pions, on the other hand, have a relatively long mean lifetime (2.60×10^{-8} sec [14]). Therefore, many of the secondary charged pions interact before decaying and produce another cascade consisting of hadrons. The decayed charged pions produce muons and neutrinos ($\pi^{\pm} \rightarrow \mu^{\pm} + \nu_\mu / \bar{\nu_\mu}$). The cascades, consisting of hadrons, muons, and neutrinos, are often referred to as a hadronic shower. The secondary muons decay into electrons (positrons) and neutrinos ($\mu^{\pm} \rightarrow e^{\pm} + \bar{\nu_\mu} / \nu_\mu + \nu_e / \bar{\nu_e}$), but most of them arrive at ground level before decaying.

Figure 2.1 shows a schematic view of an air shower, and Fig. 2.2 shows the average lateral distribution and the average longitudinal profile of proton-induced vertical air showers with the energy of 10^{19} eV.

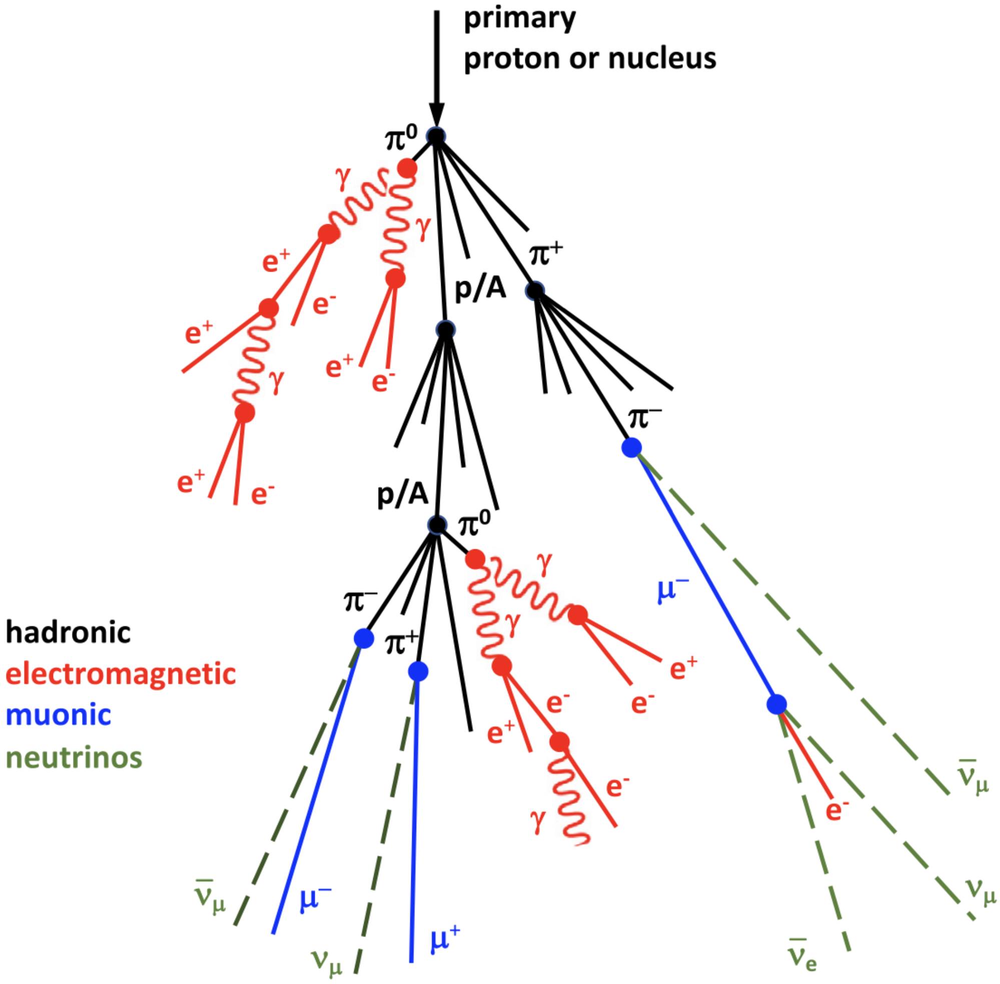

FIGURE 2.1: A schematic view of an air shower induced by a UHECR, taken from [7].

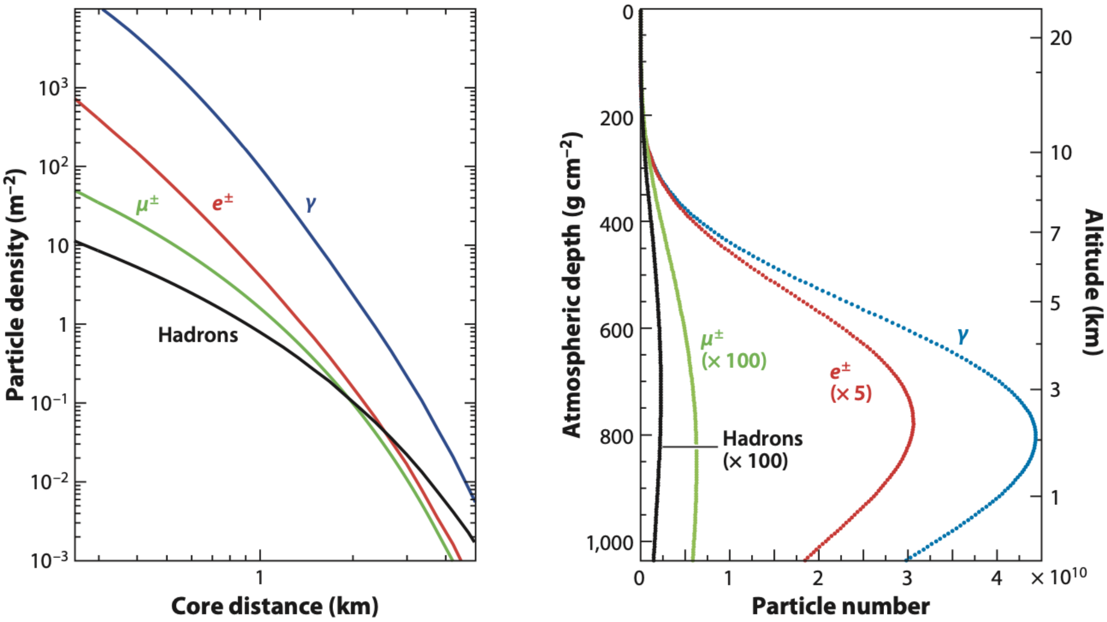

FIGURE 2.2: The average lateral (left) and longitudinal profiles of vertically incident proton air showers with energy of 10^{19} eV, taken from [33]. The lateral distribution is at the ground level of the Pierre Auger Observatory (870 g/cm^2).

Electromagnetic showers

The development of electromagnetic showers is described by $e^{\pm}$ pair production by photons, bremsstrahlung by $e^{\pm}$, and ionization loss of $e^{\pm}$. The critical energy where energy losses due to ionization and bremsstrahlung are equivalent is $E_c \sim 84$ MeV at one atmospheric pressure [34]. Below the critical energy, the energy losses due to ionization are more effective than those due to bremsstrahlung, so photon production is suppressed, and the number of photon and $e^{\pm}$ starts to decrease.

The characteristics of the longitudinal development of an electromagnetic shower can be described by the Heitler model [35] although the model is a very simple approximation. This model describes the development of an electromagnetic shower with the following four simplifications: (1) the secondary $e^{\pm}$ produced by photon via pair production has half of the energy of the parent photon, (2) the photon produced by $e^{\pm}$ via bremsstrahlung has half of the energy of the parent $e^{\pm}$, (3) the interaction ($e^{\pm}$ pair production and bremsstrahlung) happens after transporting a certain depth λ^{em}, and (4) the particle production stops at the critical energy E_c, below which ionization loss of $e^{\pm}$ is more effective than bremsstrahlung of $e^{\pm}$. Following this toy model, the number of electromagnetic particle N^{em} at the depth X at which n times interactions have happened is $N^{\mathrm{em}}(X) = 2^n = 2^{X/\lambda^{\mathrm{em}}}$. Denoting E_0 as the energy of the primary photon (or $e^{\pm}$) with $n = 0$, the energy E of each particle in the electromagnetic shower at the depth X is $E(X) = E_0/2^n = E_0/2^{X/\lambda^{\mathrm{em}}}$. N^{em} reaches maximum just before the electromagnetic shower start attenuating i.e. $E = E_{\mathrm{c}}$. Using these equations, the maximum number of particles in the electromagnetic shower $N^{\mathrm{em}}_{\mathrm{max}}$ follows $N^{\mathrm{em}}_{\mathrm{max}} = E_0/Ec$, and the depth $X^{\mathrm{em}}_{\mathrm{max}}$ at which $N^{\mathrm{em}}(X^{\mathrm{em}}_{\mathrm{max}}) = N^{\mathrm{em}}_{\mathrm{max}}$ follows:

$$X^{\mathrm{em}}_{\mathrm{max}}(E_0) = \lambda^{\mathrm{em}} \frac{\ln(E_0/E_{\mathrm{c}})}{\ln 2}. \tag{2.1}$$

This equation implies that the depth at which the number of electromagnetic particles is at maximum is proportional to the logarithm of energy of the primary photon ($e^{\pm}$) in a unit of the critical energy $E_{\rm c}$.

Hadronic showers

In contrast to electromagnetic showers, hadronic showers do not have analytic descriptions that can describe their characteristics well because hadronic interactions happening in air showers can not be described by perturbative QCD. However, the fundamental relationships between hadronic showers and electromagnetic showers can be described by the Heitler-Matthews model [36]. This model consists of following three simplifications: (1) a hadron with energy E produces $n_{\rm tot}$ secondary particles with energy $E/n_{\rm tot}$, (2) two-thirds of the secondary particles are $\pi^{\pm}$, which produce further hadron showers, and remaining one-third are π^0, which decay into photons and generate electromagnetic showers, and (3) $\pi^{\pm}$ interacts after transporting a certain depth $\lambda^{\rm inel}$ as far as the energies of $\pi^{\pm}$ are greater than specific energy $E^{\pi^{\pm}}_{\rm decay}$. Denoting $E^{\rm had}_0$ as the energy of the primary hadronic particle and n as the number of interactions at depth X, i.e., $n = X/\lambda^{\rm inel}$, the total energies in the hadronic shower, which includes muon components and neutrino components generated by the decay of hadrons, $E_{\rm had}$ and the electromagnetic shower $E_{\rm em}$ follow:

$$E_{\rm had}(X) = \left(\frac{2}{3}\right)^{n} E^{\rm had}_0 = \left(\frac{2}{3}\right)^{X/\lambda^{inel}} E^{\rm had}_0 \tag{2.2}$$

$$E_{\rm em}(X) = \left[1 - \left(\frac{2}{3}\right)^{n}\right] E^{\rm had}_0 = \left[1 - \left(\frac{2}{3}\right)^{X/\lambda^{\rm inel}}\right] E^{\rm had}_0, \tag{2.3}$$

respectively. By substituting $n = 5$ to the Eq. 2.3, we obtain $E_{\rm em}/(E_{\rm had} + E_{\rm em})|_{n=5} = 0.88$, i.e., 88% of the energy is carried by the electromagnetic components after five times hadronic interactions.

Characteristics of proton-induced air showers

Since the number of hadronic interactions before the air-shower attenuation for energies $E > 10^{15}$ eV is on average $n > 5$ [37], most of the energy of a UHECR-induced air shower is carried by electromagnetic component. Therefore, the maximum depth of a proton-induced air shower can be considered as the maximum depth of the electromagnetic sub-shower of the air shower. It means that the maximum depth of the air shower generated by the proton primary is approximately given by the maximum depth of the electromagnetic shower with initial energy $E^p_0/n_{\rm tot}$:

$$X^p_{\rm max}(E^p_0) = \lambda^{\rm em} \frac{\ln\left(E^p_0/(n_{\rm tot}E_{\rm c})\right)}{\ln 2}. \tag{2.4}$$

Denoting $n_{\rm decay}$ as the number of hadronic interactions at which hadrons in an air shower reach the critical energy $E^{\pi^{\pm}}_{\rm decay}$, $E^p_0/n^{n_{\rm decay}}_{\rm tot} = E^{\pi^{\pm}}_{\rm decay}$ holds. The number of muons in the air shower after $n_{\rm decay}$ times hadronic interactions is equal to the number of charged pions: $N_\mu = N_{\pi^{\pm}} = (\frac{2}{3}n_{\rm tot})^{n_{\rm decay}}$, therefore the maximum number of muons in proton-induced air shower with energy E_0^p is given by

$$N_{\mu,\,\mathrm{max}}^p(E_0^p) = \left(\frac{E_0^p}{E_{\mathrm{decay}}^{\pi^\pm}}\right)^\beta,\ \beta = \frac{\ln \frac{2}{3} n_{\mathrm{tot}}}{\ln n_{\mathrm{tot}}}. \tag{2.5}$$

As the above equation shows, $\beta \neq 1$ and the muon number are not proportional to energy. The parameter β is predicted to be in the range of 0.88 to 0.92 [38], which corresponds to n_{tot} of 30 to 200.

The maximum number of electromagnetic particles (photon and $e^\pm$) in the proton-induced air shower is $N_{\mathrm{em,\,max}}^p(E_0^p) = E_{\mathrm{em}}(X_{\mathrm{max}}^{\mathrm{em}})/E_{\mathrm{c}} = (E_0^p - E_{\mathrm{had}}(X_{\mathrm{max}}^{\mathrm{em}}))/E_{\mathrm{c}}$. The energy carried by hadronic components is smaller than that by electromagnetic components with $n > 5$ at the depth $X = X_{\mathrm{max}}^{\mathrm{em}}$, therefore $N_{\mathrm{em,\,max}}^p(E_0^p)$ is approximated as

$$N_{\mathrm{em,\,max}}^p(E_0^p) \sim \frac{E_0^p}{E_{\mathrm{c}}}. \tag{2.6}$$

Characteristics of nucleus-induced air showers: superposition model of air showers

When an ultra-high-energy nucleus with the mass number A and energy E_A interacts with an atmospheric nucleus, the generated air shower can be approximated by a superposition of air showers generated by protons with energy $E_p = E_A/A$ because the binding energy of nucleons is $\sim$ 5 MeV, which is much smaller than the interaction energy. According to this superposition model, we can obtain the maximum depth $X_{\mathrm{max}}^A(E_0)$, the maximum number of muons $N_{\mu,\,\mathrm{max}}^A(E_0)$, and the maximum number of electromagnetic particles $N_{\mathrm{em,\,max}}^A(E_0)$ of nucleus-induced air showers using the proton-induced air showers formulas (Eq. 2.4, Eq. 2.5, and Eq. 2.6):

$$X_{\mathrm{max}}^A(E_0) = X_{\mathrm{max}}^p(E_0/A) = X_{\mathrm{max}}^p(E_0) - \frac{\lambda^{\mathrm{em}}}{\ln 2} \ln A, \tag{2.7}$$

$$N_{\mu,\,\mathrm{max}}^A(E_0) = A \times \left(\frac{E_0/A}{E_{\mathrm{decay}}^{\pi^\pm}}\right)^\beta = A^{1-\beta} \times N_{\mu,\,\mathrm{max}}^p(E_0), \tag{2.8}$$

$$N_{\mathrm{em,\,max}}^A(E_0) = A \times N_{\mathrm{em,\,max}}^A(E_0/A) \sim N_{\mathrm{em,\,max}}^p(E_0), \tag{2.9}$$

where E_0 is the energy of the primary nucleus. The important implication of the equations is that we can estimate the mass of the primary particle by observing X_{max} or N_μ along with its energy E_0. The left panel of Fig. 2.3 shows the relationships among X_{max}, the energy, and the mass of primary particles. The right panel of Fig. 2.3 shows the relationships among $N_{e^\pm}$, N_μ, the energy, and mass of primary particles.

2.2 Techniques of air shower observation

In this section, two types of technique to observe air showers produced by UHECRs are introduced. One is a surface detector (SD) array, which measures lateral distributions of air shower particles on the ground, and the other one is a fluorescence detector (FD), which measures the longitudinal development of air showers. Figure 2.4 shows a schematic view of the observation by the SD array and the FD.

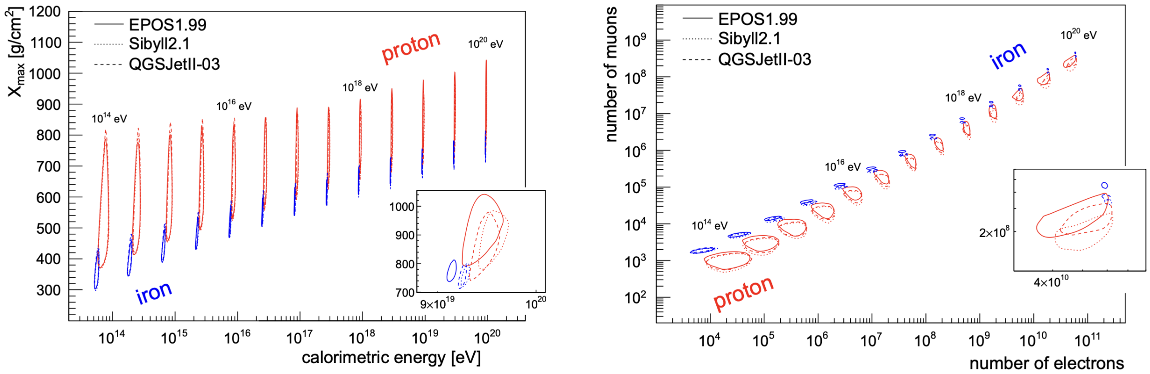

FIGURE 2.3: (Left) The simulated relation between the $X_{\max}$ and energy of the air showers for proton (red) and iron (blue) primaries. (Right) The simulated relation between the $(N_{e^\pm}, N_\mu)$ and energy of the air showers for proton and iron primaries, which induce vertically. The ground level is 800 g/cm^2. In both figures, the contours indicate regions that include 90% of the simulated showers in the corresponding energy bins. Both figures are taken from [34].

Surface detector array

Surface detector (SD) arrays are composed of a lot of particle detectors, such as scintillator detectors, water Cherenkov detectors, and so on (see Fig. 2.5 as a schematic view). When an air shower is induced to an SD array, a cluster of the surface detectors record signals within a particular time duration ($\sim$ 10 μ s in the case of the TA experiment). The arrival direction of the primary cosmic ray is estimated by the hit timings of the detectors (see Fig. 2.4). The energy of the primary cosmic ray is estimated by the lateral distribution of the air shower particles. Signal size at a certain distance from an axis of an air shower is often used as an estimator of energies of air showers [39]. The distances between the SDs are determined according to the primary energy which experimentalists want to observe. Larger detector spacing raises the energy threshold of the observation of cosmic rays but allows for a larger observation area with the same number of detectors. SD arrays can observe cosmic rays with ~100% duty cycle.

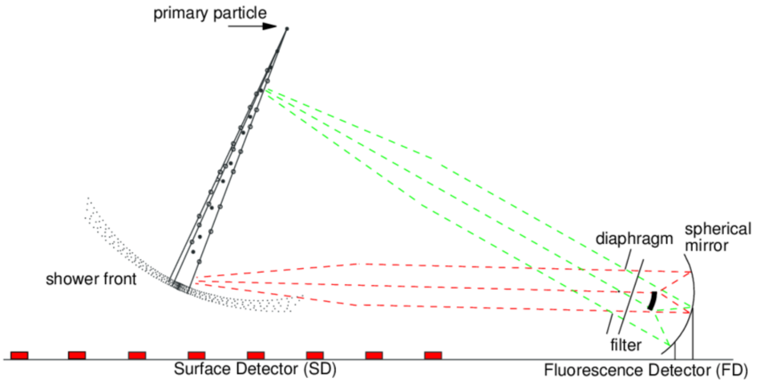

FIGURE 2.4: A schematic view of the observation by the surface detector (SD) array and the fluorescence detector (FD), taken from [40].

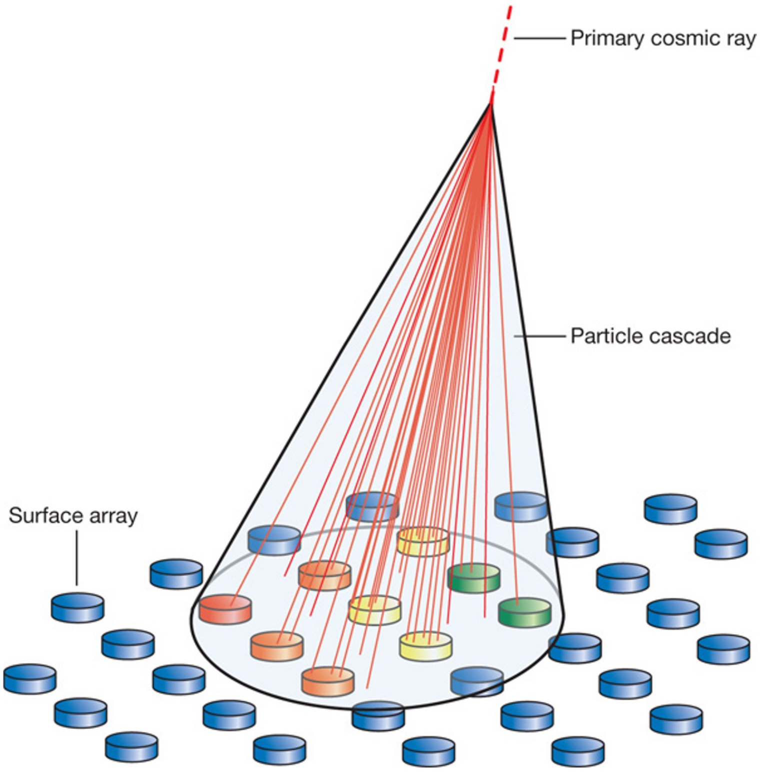

FIGURE 2.5: A schematic view of the surface detector array, taken from [41].

Fluorescence detector

When air shower particles pass the atmosphere, the atmospheric molecules are excited, emit fluorescence light, and return to their ground states. Fluorescence detectors (FDs) observe longitudinal developments of air showers by detecting the fluorescence light. The arrival direction of the primary cosmic ray is estimated by the geometrical structure of the shower profile. The energy of the primary cosmic ray is estimated by the number of detected fluorescence photons. This is a calorimetric measurement because the number of fluorescence photons follows the energy deposit of the air shower by ionization in the atmosphere. FDs are also able to measure X_{max}, which is the depth at which the number of air shower particles is at maximum. X_{max} is related to primary masses of UHECRs [34] as described in Sec. 2.1, so that FDs can measure mass composition of UHECRs. The observation by FDs is limited to clear, moonless nights. Therefore, the duty cycle of FD observation is approximately 10%.

Hybrid detection of air showers

SD arrays have $\sim$100% duty cycle but cannot measure the energy of primary cosmic rays calorimetrically and X_{max} directly. On the other hand, FDs are able to measure energy calorimetrically and X_{max} directly, but have a duty cycle of about 10%. Complementary observation can be performed by employing both SD arrays and FDs. In particular, by observing air showers simultaneously by an SD array and FDs, the energy estimation of the SD array can be calibrated to the calorimetric energy estimation of the FDs.

2.3 Recent observatories of UHECRs

Currently, two major experiments observe UHECRs: the Telescope Array (TA) experiment and the Pierre Auger Observatory (PAO). The experiments include surface detectors (SDs) and fluorescence detectors (FDs).

The Telescope Array experiment

The Telescope Array (TA) experiment [10], located in Millard County, Utah State, U.S. (39.1° N, 112.9° W), is the largest cosmic ray observatory in the Northern Hemisphere. The mean altitude of the observatory is $\sim$1400 m. The TA experiment consists of 507 plastic scintillators in a square grid pattern with 1.2 km spacing and three FD stations that look over the SD array. The SD array covers approximately 700 km^2. The TA experiment started observation in May 2008. The details of the TA experiment are described in Chap. 3.

The Pierre Auger Observatory

The Pierre Auger Observatory (PAO) [11], located in the Province of Mendoza, Argentina (35.2° S, 69.2° W), is the largest cosmic ray observatory. The mean altitude of the observatory is $\sim$1400 m. The PAO consists of an array of water Cherenkov detectors (WCDs) and four FD stations that look over the SD arrays. The SD array covers an area of approximately 3,000 km^2. In addition to the baseline array, 1660 WCDs in a triangular grid pattern with 1.5 km spacing, there is a dense small array with a spacing of 750 m together with High Elevation Auger Telescopes (HEAT) fluorescence detectors to observe cosmic rays down to 10^{17} eV. Figure 2.6 shows the configuration of the PAO. The coverage of the SD arrays is approximately 3000 km^2.

An upgrade of the PAO, AugerPrime [42], is ongoing. It is the upgrade of detectors by adding the following to the WCD:

- a surface scintillator detector (SSD) unit consisting of two scintillators, each of which covers an area of 1.9 m^2,
- a radio detector (RD) unit, consisting of a 1.2 m diameter short aperiodic loaded loop antenna,
- an additional PMT in the WCD to extend the dynamic range, and
- a new electronics (Upgraded Unified Boards, UUB) to accommodate new detectors and enhance the performance: faster sampling rate (120 MHz) than the previous one (40 MHz), larger dynamic range, and powerful FPGA.

The upgraded surface detector is shown in Fig. 2.7. In addition to the upgrade of the SD, underground muon detectors (UMDs) are buried at a depth of 2.3 m to measure muon components of air showers directly. One of the main aims of the AugerPrime is the estimation of the mass of UHECR on an event-by-event basis by separately measuring electromagnetic and muonic components by WCDs and SSDs. The RD measures radio emission from air showers and is especially useful for inclined air showers, whose electromagnetic components are largely absorbed in the atmosphere.

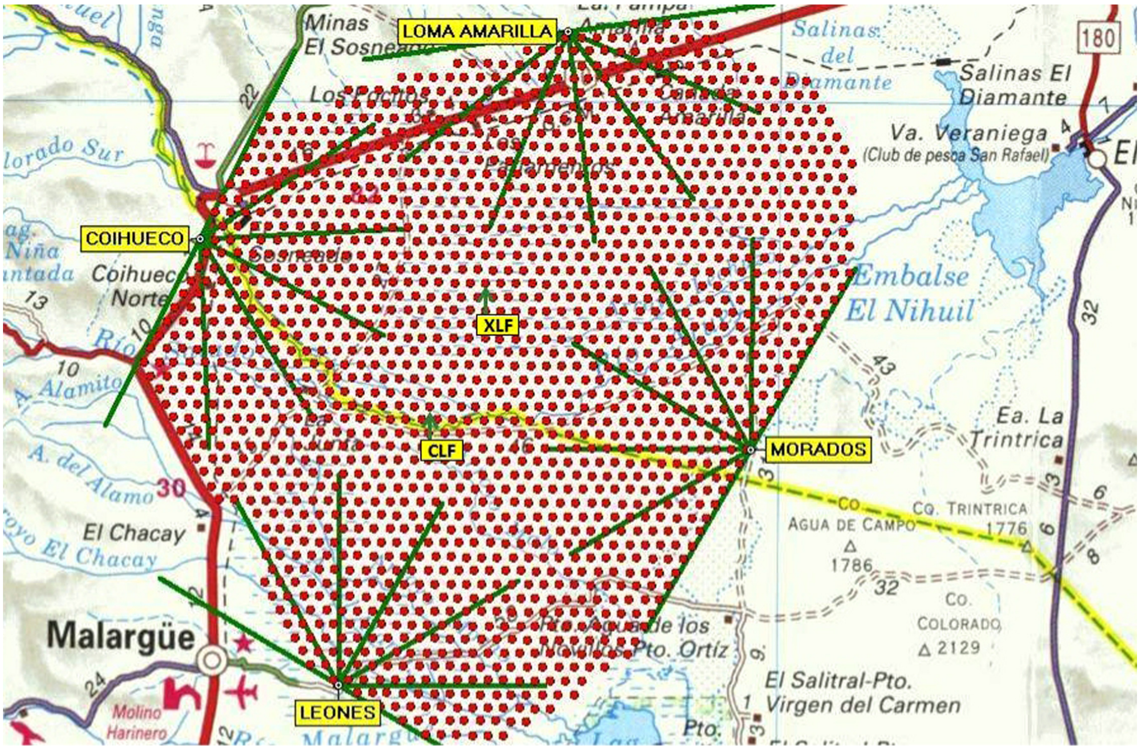

FIGURE 2.6: The configuration of the Pierre Auger Observatory, taken from [11]. The red points indicate surface detectors. Four fluorescence detector enclosures (COIHUECO, LEONES, MORADOS, and LOMA AMARILLA) and two laser facilities (CLF and XLF) are also shown.

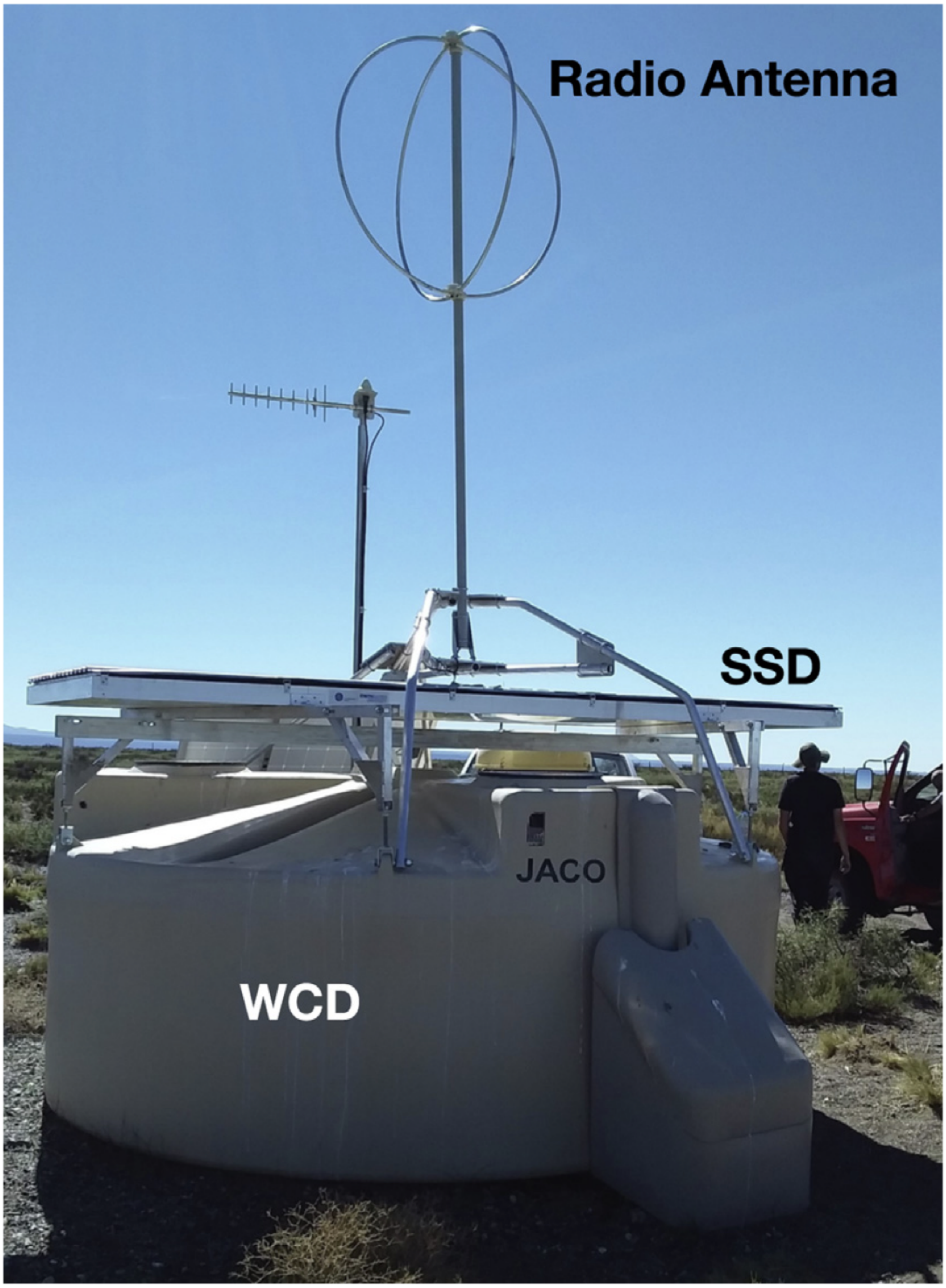

FIGURE 2.7: An upgraded detector of the AugerPrime, taken from [42]. It consists of a water-Cherenkov detector (WCD), a scintillator surface detector (SSD), and a radio antenna.

2.4 Recent observational results of UHECRs

In this section, we will introduce the recent observational results of UHECRs which have not been mentioned in Sec. 1.2.

2.4.1 Anisotropy

Large-scale anisotropy

The PAO reported dipole anisotropy of UHECRs with energies greater than 8×10^{18} eV in 2017 [43]. The global significance of the anisotropy is more than 5.2σ. The direction of the dipole is $(l, b) = (233^\circ, -13^\circ)$ in the Galactic coordinates, and the amplitude is $\sim 7\%$. This measurement that the direction of the dipole is off the Galactic center indicates that UHECRs with energies greater than 8×10^{18} eV are of extragalactic origin. The direction and the amplitude of the dipole anisotropy can be reproduced by assuming that extragalactic UHECR source density is proportional to the matter density and considering the Galactic and extragalactic magnetic fields [44]. The dipole measured by the TA experiment is consistent with both an isotropic distribution and the PAO measurement [45].

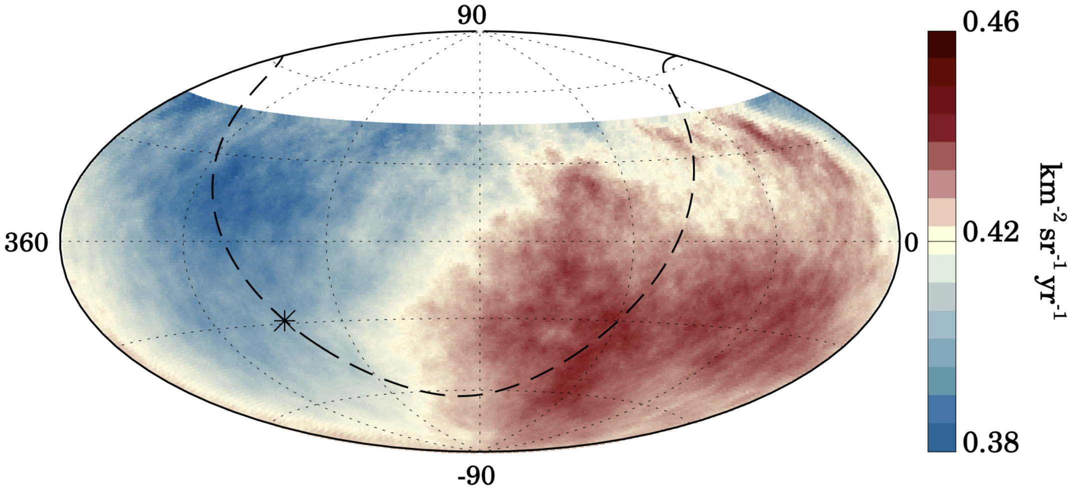

FIGURE 2.8: Flux of UHECR above 8×10^{18} eV in equatorial coordinates observed by the PAO [43]. The Galactic center is marked with an asterisk, and a dashed line indicates the Galactic plane.

Intermediate-scale anisotropy

In addition to the TA hotspot, mentioned in Sec. 1.2.2, the TA experiment reported another indication of intermediate-scale anisotropy of UHECRs with energies greater than $10^{19.4}$ eV in the direction of Perseus-Pieces supercluster (PPSC) (Fig. 2.9) [46]. The chance probability to observe the excess close to the PPSC is 3.5σ. The significance is not very large, and we need more statistics to verify and understand the PPSC excess as well as the TA hotspot.

The PAO reported the intermediate-scale anisotropy above $\sim 4 \times 10^{19}$ eV in the direction of CenA [47].

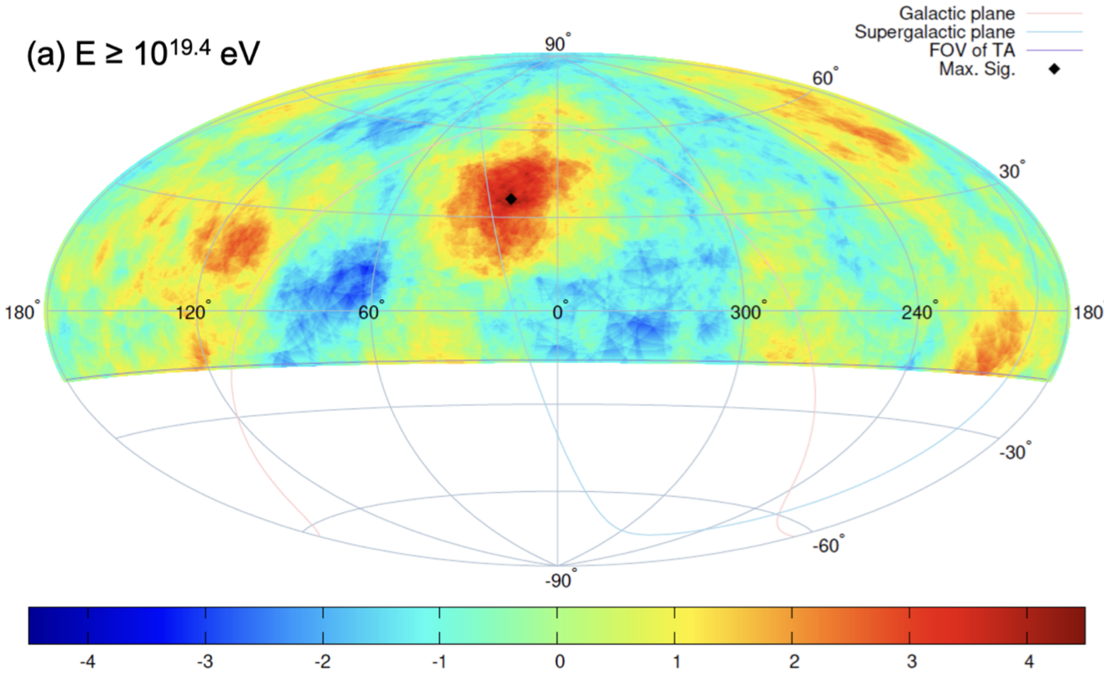

FIGURE 2.9: Map of UHECRs above $10^{19.4}$ eV in equatorial coordinates observed by the TA experiment [46]. The color indicates the local significance of the excess within a circle with a 20° radius. The solid lines show the Galactic plane (red) and the supergalactic plane (blue).

Correlation with nearby galaxies

The PAO has studied the correlation between the arrival directions of UHECRs and nearby galaxies [47]. The most significant correlation was obtained with the starburst galaxies taken from [48] with the significance of 4.2σ. The Auger-TA working group also reported the correlation with the starburst galaxies in the entire sky with the global significance of 4.7σ [49]. Approximately 10% of the total flux can be explained with starburst galaxies, and the remaining $\sim$ 90% is explained to be isotropic in the study. Figure 2.10 shows the observed full-sky flux above $\sim 4 \times 10^{19}$ eV and the prediction with the starburst galaxy model. The analysis on the whole sky basis is very important in terms of being able to consider all sources as well as the large statistics.

The significance of the correlation with nearby starburst galaxies is growing as statistics increase [49]. With more statistics, we would be able to observe the correlation with a significance of more than 5σ.

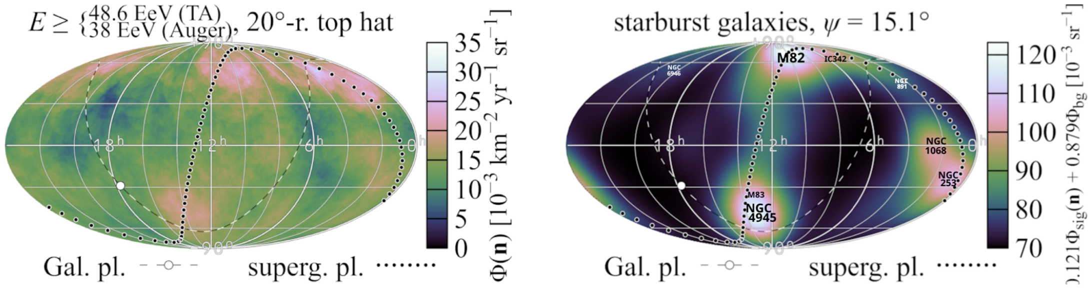

FIGURE 2.10: (Left) The observed full-sky UHECR flux above 3.8×10^{19} eV on the PAO energy scale (4.9×10^{19} eV on the TA energy scale). (Right) The starburst galaxy model predictions [49]. The energy threshold is the same as the left figure.

2.4.2 Mass composition

The mass composition of UHECRs is essential to study not only the acceleration mechanism at UHECR sources but also the propagation and magnetic deflection of UHECRs. Figure 2.11 shows the mean value of $X_{\max}$ measured by the TA experiment [50] and the PAO [51]. The TA experiment reported subdominant light primary composition of UHECRs [50]. The PAO reported that the composition of UHECRs is light below $10^{18.2}$ eV and is becoming heavier as energy increases [51]. The Auger-TA joint working group reported, however, that their mass composition estimations are compatible with statistical and systematic uncertainties [52] (Fig. 2.12).

In addition to the direct $X_{\max}$ measurement by FD, machine learning techniques with SD data are recently used to estimate the mass composition of UHECR [53] [54]. The measurement by SD has statistical strengths and is complementary to the measurement by FD.

2.4.3 Combined fit of energy spectrum and mass composition

Combined fits of the energy spectrum and mass composition enable us to estimate the acceleration mechanism and the environment of the UHECR sources. As the

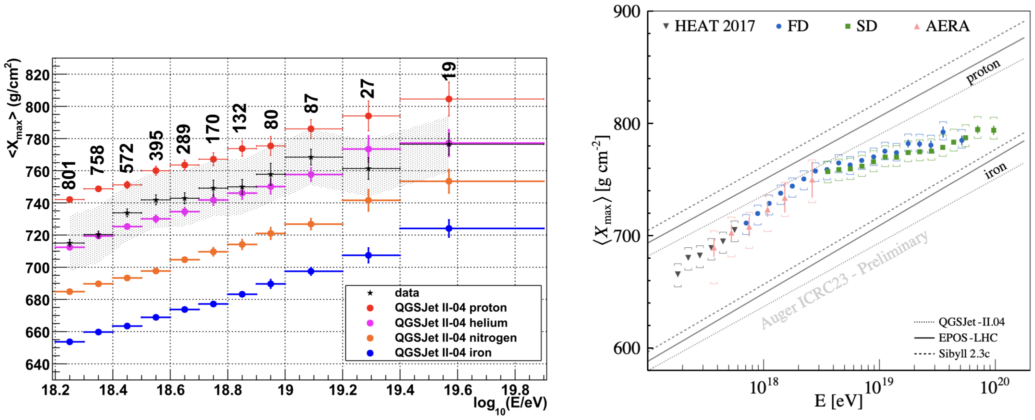

FIGURE 2.11: (Left) The mean values of X_{max} measured by the TA hybrid observation [50].
(Right) The mean values X_{max} measured by PAO [51].

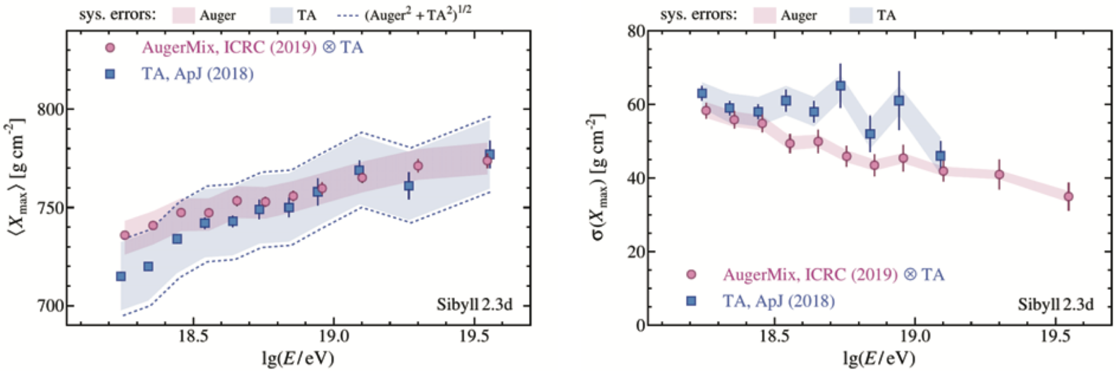

FIGURE 2.12: (Left) The mean value of X_{max}. (Right) The second moment of X_{max} reported in [52]. In both figures, the blue squares indicate the measurement of the TA experiment and the pink circles are simulated results of the TA experiment observation assuming mixed mass composition model measured by the PAO using SIBYLL 2.3d [55] as a hadronic interaction model.

model of the energy spectrum at the UHECR source in the combined fits, a power-law function with a rigidity-dependent cutoff is often used. The rigidity-dependent cutoff is based on the assumption that UHECRs are accelerated by electromagnetic process, and they escape from the source at a maximum rigidity that the UHECR source can confine. As a result, heavier nuclei can be accelerated to greater energies due to their greater electric charge. This mechanism is often referred to as Peters cycle [56]. The propagation effects (including the interaction with the background photons and adiabatic energy loss) the air shower development with a hadronic interaction model, and the detector effects are simulated. The simulated data sets are compared with the observations to fit free parameters which describe the characteristics of the UHECR source.

The PAO performed the combined fit of the energy spectrum and the mass composition for energies greater than $10^{17.77}$ eV [19]. Figure 2.13 shows the best-fit result of the model in which the Galactic component and two types of extra-galactic component are considered. In the study, ankle could be explained by two types of extragalactic source regardless of the Galactic contribution. The fair fraction below the ankle might be produced by the interactions of nuclei in the source environment, suggested in [57] [58]. They also reported that the instep feature might be explained by the interplay of light-to-intermediate nuclei following the Peters cycle. The cutoff structure would be the interplay of the photodisintegration of heavy nuclei during the propagation and the acceleration limit (the maximum rigidity accelerated at the sources is $\sim 10^{18.2}$ V) [19].

The TA experiment performed the similar combined fit above the ankle (for the energy greater than $10^{18.68}$ eV) [20]. Figure 2.14 shows the best-fit result of the model. In the study, the best-fit fractions of the mass of the UHECR at the source are 99.2% and 0.8% for He and Fe, respectively, and 0.0% for H, N, and Si. The predominant protons at the top of the atmosphere are produced by spallation of He during propagation in the model. The maximum rigidity of the accelerator is $10^{20.26}$ V, and the cutoff can be explained by the GZK-cutoff of the photodisintegration of He and the GZK-effect of proton. This result is different from the result of the PAO [19].

2.5 The connection between UHECR and particle physics

As mentioned in Sec. 1.1.2, UHECR observation could be an experiment to test particle interactions in extremely high energy beyond those produced by terrestrial accelerators. In this subsection, we describe examples of the connection between UHECR and particle physics.

2.5.1 Muon puzzle

The muon component in the air shower is used to estimate the particle type of the primary cosmic ray (see Sec. 2.1.1). Various experiments have measured it, and some measurements reported that the measured number of muons exceeds the number of muons in the simulation even considering pure iron component (Fig. 2.15). In addition to this discrepancy, there is a discrepancy between the mass composition estimated by the muon component and that estimated by the optical measurements, such as X_{max} measurement by FD. These discrepancies are often called the muon puzzle. The puzzle allows testing QCD in extreme conditions.

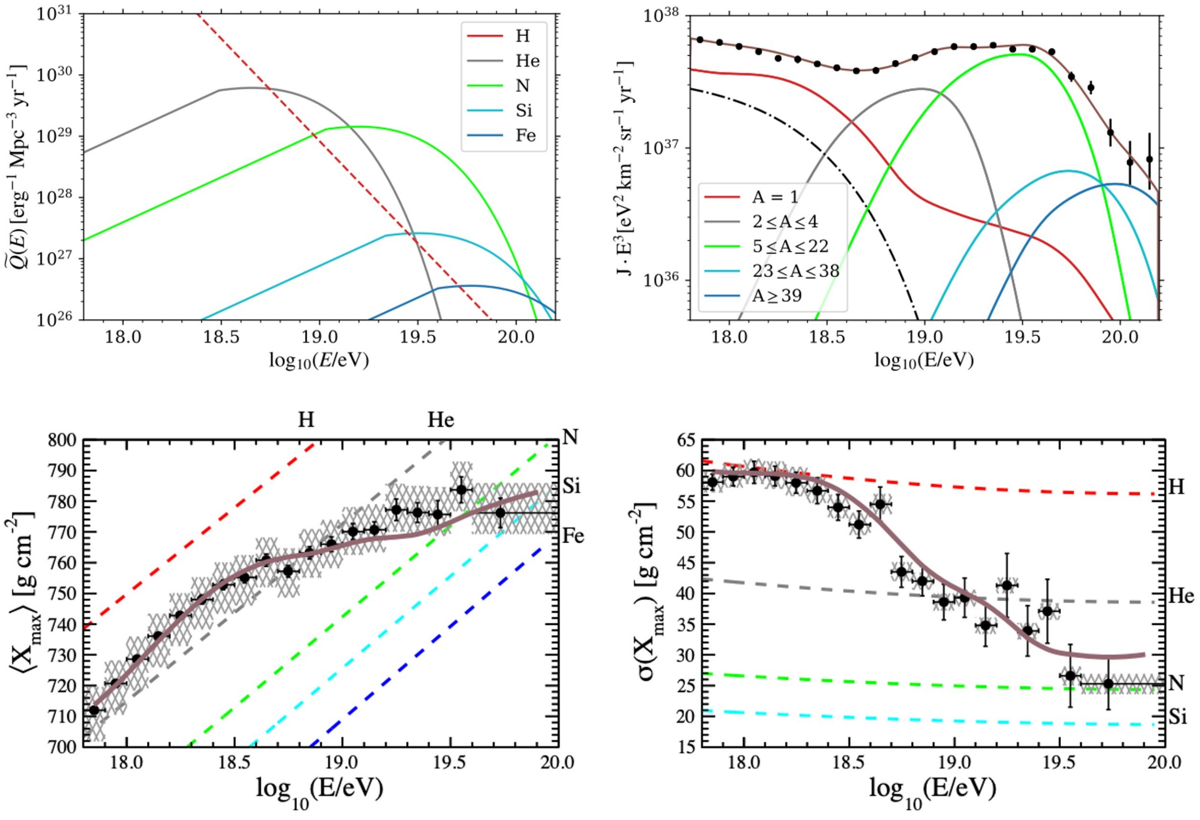

FIGURE 2.13: The best-fit result of the combined fit with the UHECR energy spectrum and X_{max} observed by the PAO with the data up to August 2018 and December 2017, respectively [19]. In the model, Galactic component and two types of extra-galactic component (low energy and high energy components) are considered. The free parameters of the Galactic component at Earth are the normalization factor of the flux and the maximum rigidity of the acceleration (R_{max}). The mass composition is fixed to be pure nitrogen, and the index of the power-low is fixed to be γ =-3.2. The low energy extragalactic component is pure proton. The maximum rigidity, integral flux, and the index of the power-law are free parameters. The high energy extragalactic component is the mixture of the H, He, N, Si, and Fe nuclei. The normalization factor of the flux of each nuclei is a free parameter. The maximum rigidity and the index of the power-law are free parameters as well. The extragalactic components are uniformly distributed. EPOS-LHC is used as a hadronic interaction model in this model. The upper left panel shows the best-fit generation rate of UHECR for each particle species. The dashed red line shows the low energy extragalactic component ($R_{\mathrm{max}} > 10^{19.3}$ V, $\gamma = -3.34 \pm 0.07$), and solid lines show the high energy extragalactic components ($R_{\mathrm{max}} = 10^{18.19\pm0.02}$ V, $\gamma = 1.47 \pm 0.13$, the ratio(%) of H, He, N, Si, and Fe are 0.0 ± 0.0, 23.6 ± 1.6, 72.1 ± 3.3, 1.3 ± 1.3, and 3.1 ± 1.3, respectively). The upper right panel shows the energy spectrum at the top of the atmosphere. The dot-dashed line indicates the Galactic component ($R_{\mathrm{max}} = 10^{17.48\pm0.02}$ V), and the solid lines indicate the extragalactic components grouped according to mass. The lower panels show the best-fit of the average of X_{max} (left) and the standard deviation of the X_{max} (right). The dashed lines are predictions for pure components according to EPOS-LHC.

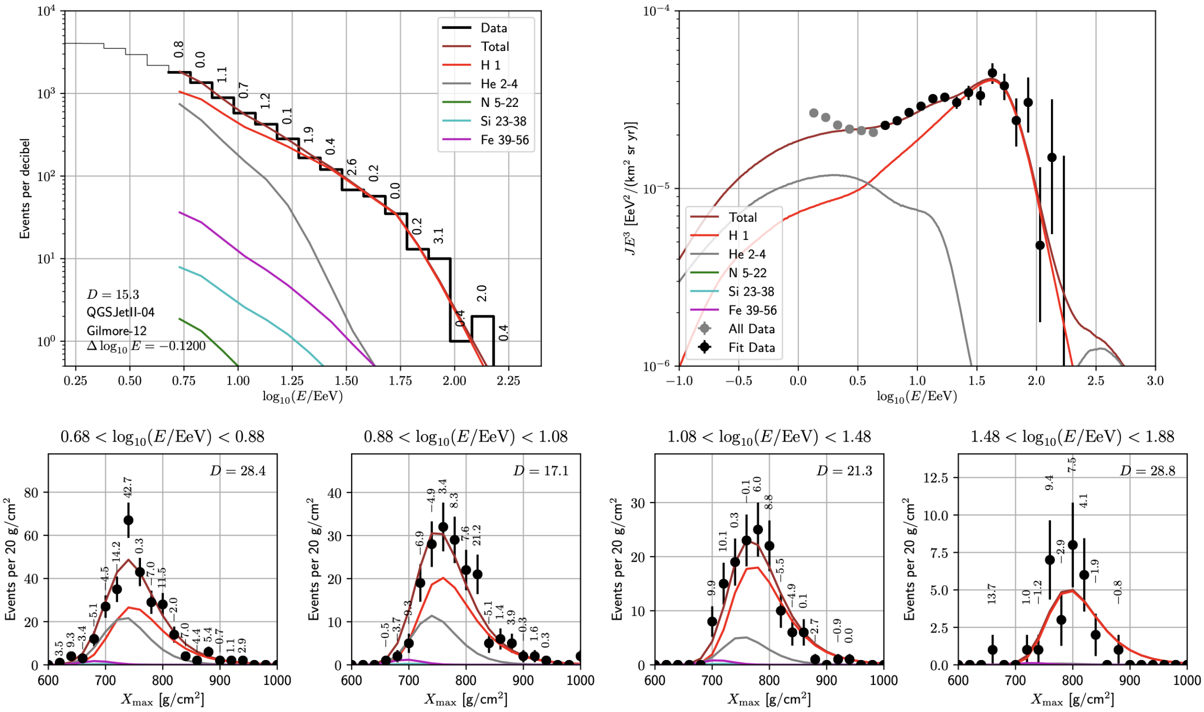

FIGURE 2.14: The best-fit result of the combined fit with the UHECR energy spectrum and $X_{\max}$ observed by the TA with nine years of the observation [20]. In the model, identical extragalactic source whose energy spectrum is a power-law with a maximum rigidity $R_{\max}$ is assumed. The sources are uniformly distributed. QGSJET II-04 is used as a hadronic interaction model in the air shower development. The upper left panel shows the energy distribution of the observation (black histogram) and the best-fit prediction (solid lines). The upper right panel shows the energy spectrum at the top of the atmosphere of the observation (circles) and the best fit (solid lines). The lower panels show the $X_{\max}$ distribution of the observation (black circles) and the best fit (solid lines) for four energy bins. The best-fit parameters of the maximum rigidity and the index of the power law are $R_{\max} = 10^{20.26}$V and $\gamma = -2.06$, respectively.

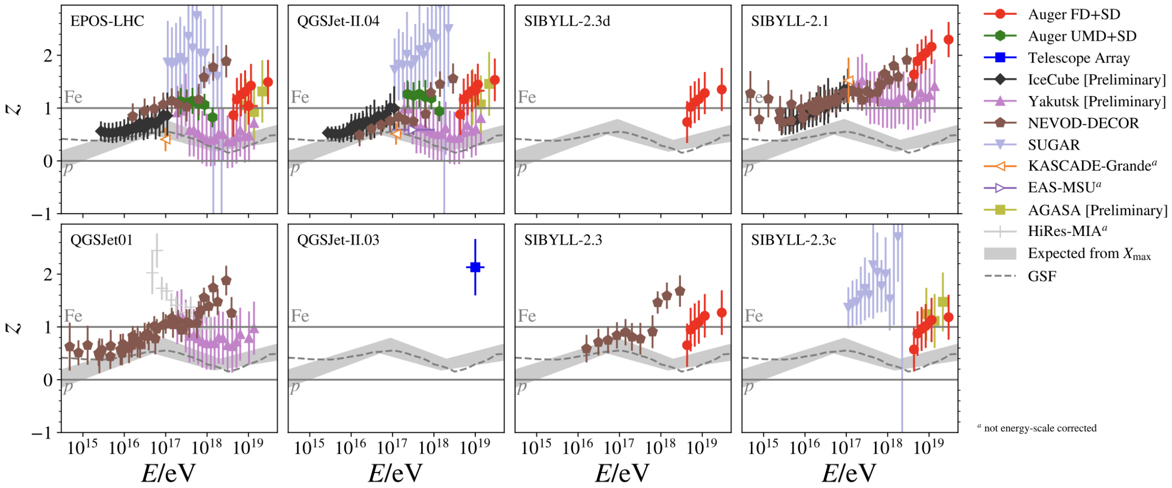

FIGURE 2.15: Compilation of muon density measurements, taken from [59]. The z-scale, the y-axis of the figure, is defined as follows:

$$z = \frac{\ln < N_{\mu}^{\text{det}} > - \ln < N_{\mu,\,\text{p}}^{\text{det}} >}{\ln < N_{\mu,\,\text{Fe}}^{\text{det}} > - \ln < N_{\mu,\,\text{p}}^{\text{det}} >}. \tag{2.11}$$

As the above equation shows, $z = 1$ means that the measured muon density agrees with the simulated iron shower, and z=0 agrees with the simulated proton shower. The gray band is the estimation from optical measurements.

2.5.2 Proton-air cross section

The measurement of the longitudinal profile of the air shower can be used to determine the cross section between UHECRs and the atmospheric nuclei. In particular, the proton-air cross section is measured by selecting proton-like events, measuring the attenuation length of proton-induced air showers, and converting it to the cross section. Figure 2.16 shows proton-air cross section measured by various cosmic ray observatories and predictions from some hadronic interaction models (QGSJET01 [60], QGSJEY II-04 [61], SIBYLL2.3[62], EPOS-LHC [63]). The measured proton-air cross section is compatible with the hadronic interaction models. Complementary use of UHECR measurements, which cover energies beyond accelerator experiments, with accelerator experiments would provide a deeper understanding of hadronic interactions.

2.5.3 Physics beyond the standard model

Furthermore, UHECRs serve as potential physics probes beyond the standard model. For example, Lorentz-invariance violation (LIV) is possible in some theories beyond the standard model. If LIV happens in extremely high energies, ultra-high-energy protons beyond the GZK horizon can arrive on earth compared to those without LIV. Recent UHECR observation constrains the LIV coefficients [65].

Another example is superheavy dark matter (SHDM). If SHDMs with energies above $\sim 10^9$ GeV exist, they may decay, produce neutrinos, photons, and nucleons, and be detected by UHECR observatories [66].

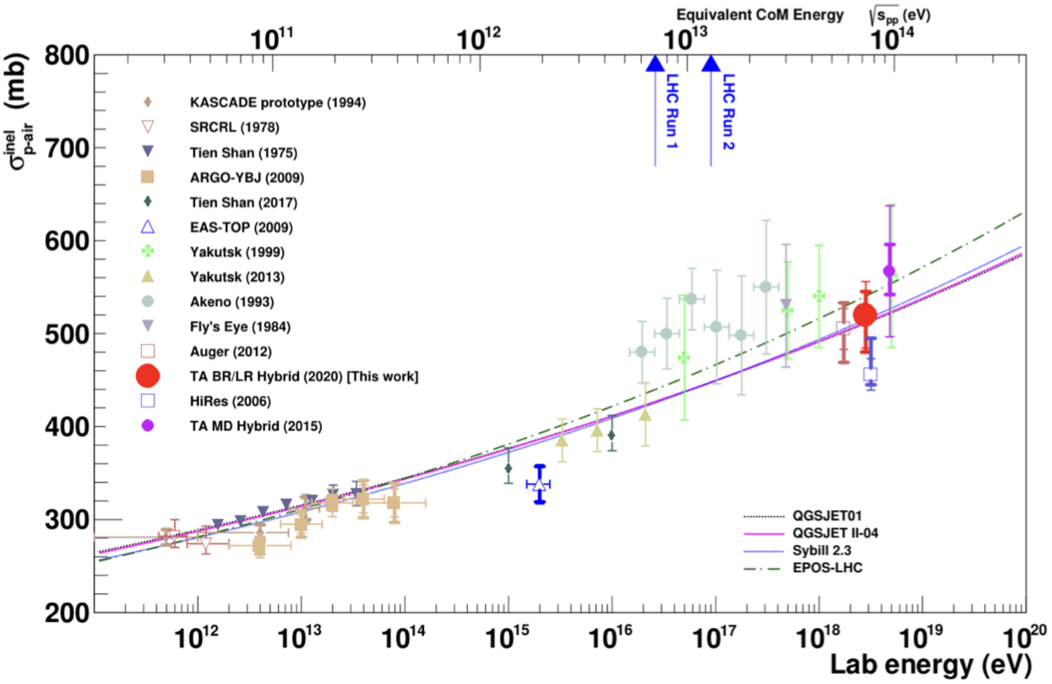

FIGURE 2.16: The proton-air cross section measured by various cosmic ray observatories [64].

2.6 Recent progress and goals to be solved in the next decade

As introduced, some observational progresses have advanced our understanding of sources and nature of the UHECR:

- **Energy spectrum**; the UHECR energy spectrum has been observed up to ∼ $10^{20.5}$ eV with the statistical uncertainties of ∼ 2% (∼ 1)% at 10^{19} eV, ∼ 7% (∼ 4)% at $10^{19.5}$ eV, and ∼ 22% (∼ 25)% at 10^{20} eV for the TA (PAO). The cutoff was observationally confirmed, although the nature of the cutoff has not been understood; both the energy loss during the propagation and the acceleration limit of sources possibly explain the current measurement. The steepening in the energy spectrum around $E \sim 10^{18.7}$ eV (ankle) has been observed. The ankle may indicate the transition from galactic to extragalactic cosmic rays [67]. Alternatively, the light component below the ankle might be produced by photodisintegration of more energetic heavy nuclei in the environment around extragalactic sources and form the ankle [57] [58]. The instep, softening of the spectrum around $10^{19.2}$ eV, observed by the PAO [13] can be reproduced by a model with an energy-dependent mass composition: light-to-intermediate mass nuclei [19]. In addition to the spectral features, spectral anisotropies have been reported. The difference between the northern sky observed by the TA experiment and the southern sky observed by the PAO in the highest-energy region ($E > 10^{19.5}$ eV) may be due to astrophysical origins, such as a model that explains the difference by a nearby source with a hard spectrum in the northern sky [24].

- **Arrival direction**; the large-scale anisotropy of UHECR indicates that UHECR with $E > 8 \times 10^{18} = 10^{18.9}$ eV are mainly of extragalactic origins [43]. The intermediate-scale anisotropies, such as the TA hotspot [26], are clues to identify UHECR sources. However, the statistics are not sufficient to confirm the anisotropy and reveal the origin of the anisotropy. The correlation between the arrival direction of UHECRs and nearby source candidates indicates the strongest correlation with starburst galaxies with the significance of 4.7σ [49].

- **Mass composition**; the mass composition has been estimated by measuring X_{max} by FDs. The TA reported subdominant light primary composition of UHECRs with their measurement up to $10^{19.5}$ eV [50]. The PAO reported a light composition of UHECRs below $10^{18.2}$ eV, becoming heavier as energy increases [51]. Both measurements are consistent within their uncertainties [52]. The energy spectrum and mass composition combination constrain source models [19]. In addition, the combination of the anisotropy and the mass composition is ongoing; an indication of anisotropy of X_{max} was reported by the PAO [68]. The study reported the heavier component in the Galactic plane $|b| < 30^\circ$ compared with the off-plane for $E > 10^{18.7}$ eV with a significance of 3.3σ. It indicates the mixed composition of UHECR and that the galactic magnetic field impacts UHECR measurements with an observable level. The statistics to estimate the mass composition are not yet sufficient, especially at the highest-energy region, due to the low duty cycle of the FD. The machine learning approach using SD data would enhance the statistics for the analyses.

2.6.1 The goals in the next decade of the UHECR measurement

A next-generation experiment of UHECR, the Global Cosmic Ray Observatory (GCOS), is in progress and planned to start observation in the 2030s with an observational area of 40,000 km^2 [69]. The TA×4 experiment and the AugerPrime should operate at least in the next decade. The following are expected to be achieved with the TA×4 experiment and the AugerPrime in the next decade:

- Statistical confirmation of the TA hotspot and further analyses on TA hotspot with large statistics to understand its nature; The TA×4 SD array is significant to achieve this goal. In Sec. 9.2, we describe a future projection on the observation of the TA hotspot. Other anisotropies, such as the PPSC excess [46] and spectral anisotropies [23], may be able to be confirmed with more statistics. A future projection on spectral anisotropy is described in Sec. 9.1.2.

- Analyses in the whole sky using both the TA and PAO data, such as spectral anisotropy; To achieve such analyses, understanding the experimental differences between them is significant. In the case of the energy spectrum, confirmation of the consistency in the energy spectra in the common declination band with a large number of events is important. The energy spectra in the common band are discussed in Chap. 8. The increase in the number of events in the northern sky by the TA×4 experiment is especially important for these analyses on a whole-sky basis since the number of events observed so far in the northern sky is smaller than those in the southern sky.

- Analyses in the highest-energy region; Since there are not sufficient events in the highest-energy region ($\sim$ 70 events for $E > 10^{20}$ eV combining recent TA and PAO data), the nature of the highest-energy cosmic rays is not specifically understood. The TA experiment observed the second-highest-energy cosmic ray in history in May 2021 [70]. No plausible candidates are around the arrival direction, even considering the galactic magnetic field. The paper mentions no indication of anisotropy for $E > 10^{20}$ eV. The isotropy indicates heavy nuclei of the highest-energy cosmic rays [71] or stronger magnetic fields than models. Alternatively, physics beyond the standard model may be possible. With the larger number of events in the highest-energy region observed by the TA×4 experiment and the PAO, we can advance our understanding of the highest-energy cosmic rays. The increase in the number of events measured by FDs at the highest-energy region will improve our understanding of the acceleration mechanism of the highest-energy cosmic rays and the nature of the cutoff. Machine learning techniques using SD data would increase the statistics to estimate the mass composition. A future projection on the number of events expected to be observed by the TA×4 SD array will be given in Chap. 9.

- Event-by-event discrimination of the mass of the UHECR by the AugerPrime; Such event-by-event mass estimation will enable us to conduct the anisotropy study considering rigidity and energy spectrum for each mass.

Chapter 3

The Telescope Array experiment

The Telescope Array (TA) experiment observes UHECR-induced air showers to elucidate the origins of UHECRs with two types of detectors: 507 surface detectors (SDs) placed in a 1.2 km square grid covering approximately 700 km^2 and 38 fluorescence detectors (FDs) which overlook the TA SD array to detect air showers simultaneously with SDs. The TA experiment was constructed in Utah, USA, at latitude 39.1° north and longitude 112.9° west and altitude $\sim$1400 m above sea level, which corresponds to 876 g/cm^2 vertical column density of the atmosphere. The configuration of the TA experiment is shown in Fig. 3.1.

3.1 Surface detectors of the TA experiment

The TA experiment consists of 507 plastic scintillator counters covering approximately 700 km^2. In this paper, we call these 507 SDs in the TA experiment TA SDs to distinguish them from surface detectors additionally deployed for the TA×4 experiment (TA×4 SDs) described in Chap. 4. The basic design of the TA SD and the TA×4 SD are the same, and the basic trigger system is the same. The detailed description of the design and trigger system of the TA×4 SD, including the difference from those of TA SD, are described in Chap. 4. The event reconstructions (energy and arrival direction) are described in Chap. 5. Since the energy estimated by the SD array is based on an MC simulation as described in Sec. 6.4, the energy estimated by the SD array is calibrated to the energy estimated by the FD (Sec. 3.3).

The TA SD array consists of three sub-arrays: the SK (Smelter Knoll) sub-array, the BR (Black Rock) sub-array, and the LR (Long Ridge) sub-array (Fig. 3.1). Each TA SD communicates with the communication tower of the sub-array to which the SD belongs. The TA SD array started data acquisition on 11th May 2008.

3.2 Fluorescence detectors of the TA experiment

There are three FD stations in the TA experiment: the BRM (Black Rock Mesa) station, the LR (Long Ridge) station, and the MD (Middle Drum) station.

Each of the BRM and LR stations has 12 FDs, newly designed for the TA experiment [73]. Each FD camera has 256 PMTs (R9508; Hamamatsu) located at the focal plane of 18 segments of spherical mirrors with a diameter of 3.3 m. The total field of view of each station is 108° in azimuthal angle and from 3° to 33° in elevation angle.

On the other hand, the MD station consists of 14 FDs [74], which were initially used for HiRes-I and HiRes-II experiments. Each FD camera has 256 PMTs (9974KAFL; EMI and XP3062/FL; Philips) and four segments of spherical mirrors whose total area is 5.2 m^2. The field of view of each FD camera is 15.5° in azimuthal

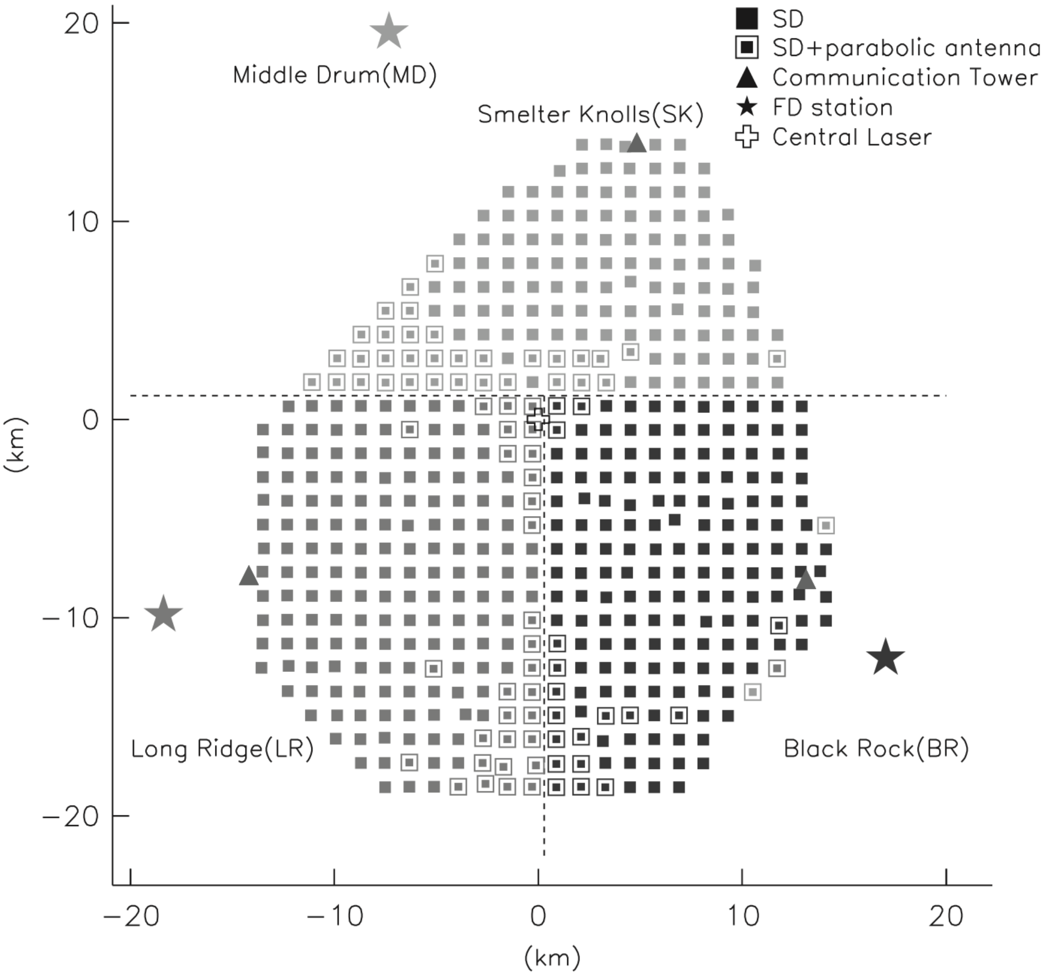

FIGURE 3.1: The configuration of the Telescope Array experiment, taken from [72]. The squares represent surface detectors (SDs), and the stars represent fluorescence detector (FD) stations. The SD array consists of three sub-arrays: Smelter Knolls (SK), Long Ridge (LR), and Black Rock (BR) sub-arrays. The triangles represent the communication towers of the corresponding sub-arrays.

angle and 14° in elevation. Figure 3.2 shows FDs at the BRM station and FDs at the MD station.

FIGURE 3.2: The photographs of the exterior of the Black Rock Mesa (BRM) FD station (left) and the Middle Drum (MD) FD station (right).

An Ultra-Violet (UV) transparent filter (BG3; Schott) is attached to the front of the PMTs to cut background photons.

The PMT signal is sent to FD-electronics, which issues triggers and records waveforms. The trigger system judges air shower events at each communication tower by selecting events where a cluster of PMTs has recorded signals above a certain threshold within a specific time window. Figure 3.3 shows an example of an air shower event observed by FDs.

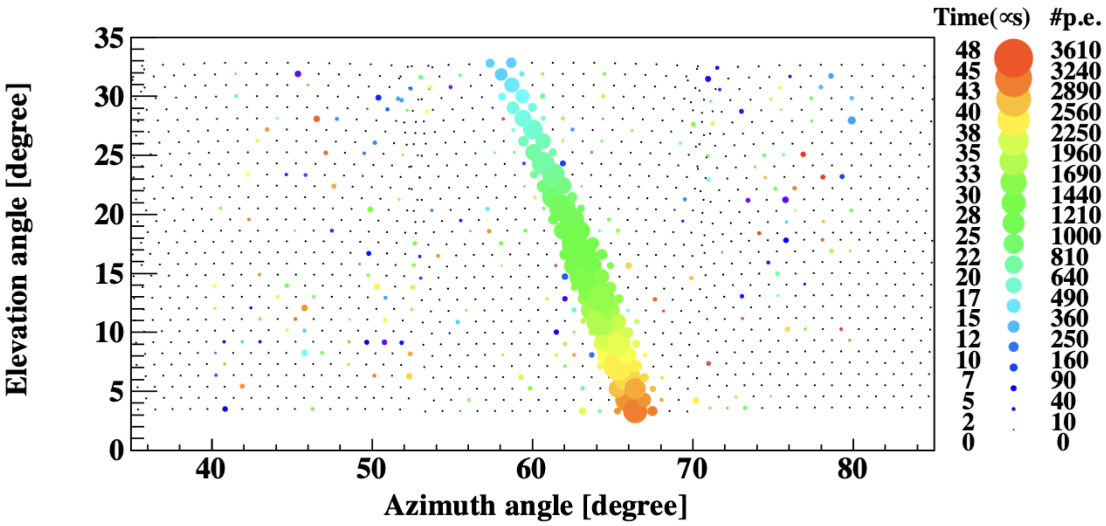

FIGURE 3.3: An example of the air shower event observed by the FD, taken from [75]. The size and the color of each circle indicate the signal size and the signal timing of the corresponding PMT.

TABLE 3.1: The systematic uncertainty of the energy measured by the TA FD [79].

Item	Uncertainty	Contributions
Detector sensitivity	10%	PMT (8%), mirror (4%) aging (3%), filter (1%)
Atmospheric collection	11%	aerosol (10%) Rayleigh (5%)
Fluorescence yield	11%	model (10%) humidity (4%) atmosphere (3%)
reconstruction	10%	model (10%) missing energy (5%)
Sum in quadrature	21%	

3.2.1 Event reconstruction of TA FD

PMT selections are performed for the recorded events to remove PMTs that recorded noise signals at first. After the PMT selections, geometry reconstruction, longitudinal profile reconstruction, and energy reconstruction are performed.

In the geometry reconstruction, the air shower's core position and arrival direction are determined from the hit timing, signal size, and position of selected PMTs.

After determining the geometry, the longitudinal profile of the air shower is determined using the Inverse Monte Carlo (IMC) method [76]. The IMC method iteratively simulates air showers, whose geometry is as determined by the geometry reconstruction, and searches for the optimum Gaisser-Hillas function [77] parameters X_{max} and N_{max} which best reproduce the observed results. Other parameters of the Gaisser-Hillas function are fixed: $\lambda = 70\ \mathrm{g/cm^2}$ and $X_0 = 0\ \mathrm{g/cm^2}$. In the IMC method, the fluorescence light and the Cherenkov light are considered.

At last, energy reconstruction is performed. The calorimetric energy E_{cal} is estimated by integrating the Gaisser-Hillas function with the optimum X_{max} and N_{max} and mean ionization loss rate $\alpha_{\mathrm{eff}}(X)$, which is a function of atmospheric depth X and is calculated using CORSIKA [78]. After calculating E_{cal}, missing energy E_{miss}, such as energy carried by neutral particles, is corrected. The missing energy is calculated using the simulation. The energy reconstructed by the FD is described as

$$E_{\mathrm{FD}}^{\mathrm{rec}} = \int_{X_0}^{\mathrm{inf}} N_e(X; N_{\mathrm{max}}, X_{\mathrm{max}}, X_0, \lambda)\alpha_{\mathrm{eff}}(X)dX + E_{\mathrm{miss}}. \tag{3.1}$$

The uncertainties of the energy reconstructed by the TA FDs are listed in Tab. 3.1 [79]. The overall uncertainty is 21%, almost independent of energy. This uncertainty is propagated to the uncertainty of energy estimated by the SD array since the SD-energy is calibrated to the FD-energy.

3.3 Hybrid detection of the TA experiment

Since FDs overlook the TA SD array, the TA experiment can observe air showers simultaneously by SDs and FDs. By using the SDs data, the FDs can more accurately determine the core position of the air shower. Therefore, the energy and shower profile can be derived with better accuracy.

In addition to the more accurate measurement, the hybrid detection enables us to calibrate SD-energy by FD-energy, which is calorimetrically measured. Such a comparison showed a linear relationship between SD-energies and FD-energies, with SD estimating on average 27% greater energy than FD [80]. Figure 3.4 shows the relation between FD-energy and SD-energy after scaling by a factor of 1/1.27. From this measurement, $E_{\mathrm{SD}}^{\mathrm{rec}} = E_{\mathrm{SD}}^{\mathrm{rec,\ table}}/1.27$ is used as SD-energies for the TA SD array.

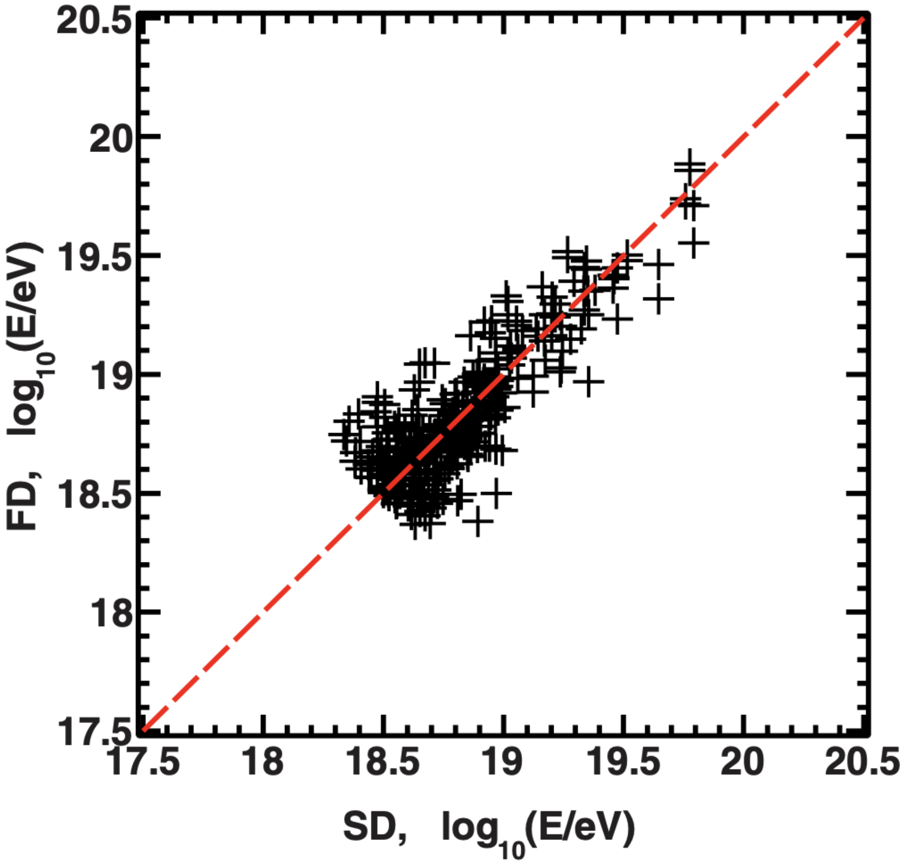

FIGURE 3.4: Comparison between the energy estimated by the TA SD divided by 1.27 and that reconstructed by the TA FD [80].

3.4 The TA×4 experiment

The TA×4 experiment is the extension of the TA experiment focusing on observing UHECRs with energies greater than 5.7×10^{19} eV, which is the energy threshold of the TA hotspot search [26], by quadrupling the observation area. We refer to the experiment including the original detectors and the extended detectors as TA×4. The spacing of the extended SD array (2.08 km) is broader than that of the TA SD array (1.2 km). Therefore, the energy threshold where the trigger efficiency is $\sim$ 100% of the extended SD array ($\sim 10^{20}$ eV) is higher than that of the TA SD array ($\sim 10^{19}$ eV).

The expansion at the first stage was completed with 257 additional surface detectors and two additional fluorescence detector stations in 2019. The expansion of the 257 additional SDs is approximately half of the final plan. Figure 3.5 shows the configuration of the TA×4 experiment. There are two extended SD arrays on the northern side of the TA SD array (TA×4 North) and the southern side of the TA SD array (TA×4 South). Hereafter, we refer to the SD arrays added for the extension as TA×4 SD array unless otherwise noted. The area of the TA×4 SD array is approximately 1000 km^2, which is approximately 1.5 times the area of the TA SD array ($\sim$ 700 km ^{2}). TA×4 North and South each has one FD station, which overlooks the corresponding TA×4 SD array.

3.4.1 Surface detectors of the TA×4 experiment

The TA×4 SD array started stable observation in Oct. 2019 with 130 SDs in TA×4 North and 127 SDs in TA×4 South. TA×4 North and TA×4 South consist of 3 subarrays: Keg Mountain (KM), Desert Mountain (DM), and Smelter Knolls North (SN) for the North, and Black Rock FD (BF), South Cricket (SC), and Sand Ridge (SR) for the South (Fig. 4.1).

The details of the TA×4 SDs, including their design, performance, and operations, are described in Chap. 4.

3.4.2 Fluorescence detectors of the TA×4 experiment

Two FD stations are constructed for the TA×4 experiment. One is the TA×4 FD at the Middle Drum site (TA×4 MDFD) station at the TA×4 North, and the other is the TA×4 FD at the Black Rock site (TA×4 BRFD) station at the TA×4 South (Fig. 3.5). The MDFD station consists of 4 FDs viewing $3^\circ - 17^\circ$ in elevation and $12^\circ - 76^\circ$ in azimuth (clockwise from North). The BRFD station consists of 8 FDs viewing $3^\circ - 17^\circ$ in elevation and $238^\circ - 350^\circ$ in azimuth [81] [82]. Figure 3.6 shows the photographs of the stations. The spherical mirrors used in the FDs were reconditioned from the previous HiRes experiment [83]. The MDFD station has been taking data regularly since June 2018, and the BRFD station has been taking data regularly since June 2020.

As well as the TA SD array, the TA×4 SD array can observe air shower events in hybrid mode.

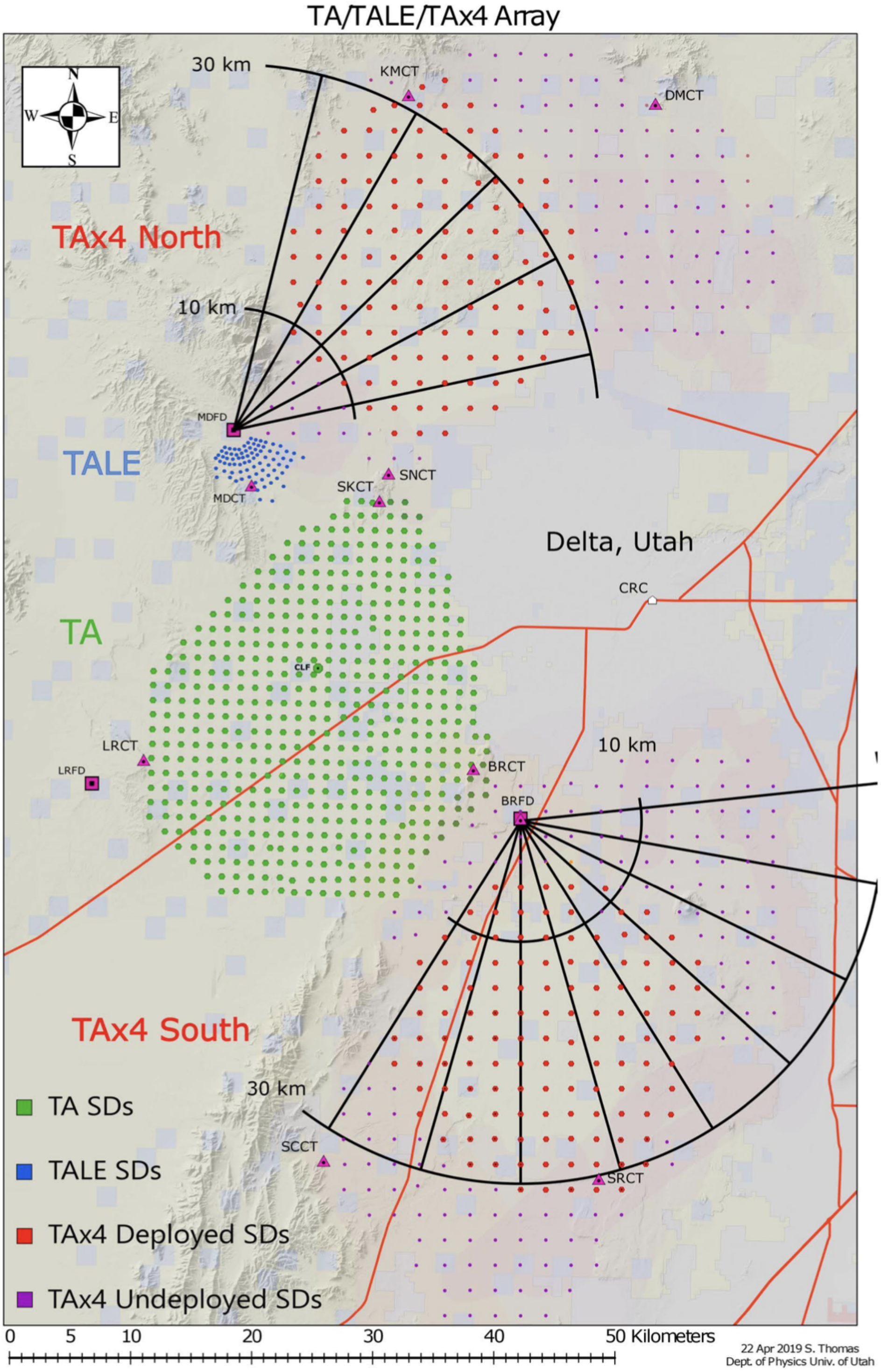

FIGURE 3.5: The configuration of the TA×4 experiment. The green circles represent 507 TA SDs (TA SD array). The red circles represent newly deployed 257 SDs for the TA×4 experiment. The purple dots represent the planned 243 SDs to be deployed to complete the TA×4 experiment. Two FD stations are constructed for the TA×4 experiment: the TA×4 FD at the Middle Drum site (TA×4 MDFD) station at the TA×4 North and the TA×4 FD at the Black Rock site (TA×4 BRFD) station at the TA×4 South. The blue circles represent SDs for the Telescope Array Low energy Extension (TALE) experiment, which aims to observe cosmic rays below 10^{18} eV.

FIGURE 3.6: The photographs of the exterior of the FD stations for the TA×4 experiment: the TA×FD at the Black Rock site (TA×4 BRFD) station (left) and the TA×4 FD at the Middle Drum site (TA×4 MDFD) station (right), taken from [84].

Chapter 4

The TA×4 surface detectors

This chapter describes the design of the additionally deployed SDs (TA×4 SDs) along with the differences from the TA SDs. The trigger system, running status, and aperture of the TA×4 SD array are also described.

4.1 The TA×4 surface detector

4.1.1 Design of the TA×4 SD

The basic design of the TA×4 SD is the same as that of the TA SD [86]. In this section, the design of the TA SD is described first. Subsequently, the design of the TA×4 SD, especially the difference from the TA SD, is described.

The design of the TA SD

The TA SD [72] was designed to operate solely for more than ten years in the desert where the detector temperature ranges from -30C° to 50C°. Figure 4.2 shows an outside view of a TA SD. The TA SD consists of a scintillator box, a stainless box that contains a battery (DCS100; C&D technologies, Inc.) and electronics, a solar panel (KC125TJ; KYOCERA Corp.), a WLAN antenna (ADAF2414; ADTEC Co.), and a GPS antenna.

The TA SD scintillator box contains two layers of plastic scintillators. Each layer has eight scintillator slabs, each 150 cm long, 25 cm wide, and 1.2 cm thick. The total area of each layer is 3 m^2. Polyvinyl toluene (C_9H_{10}, 1.032 g/cm^2) is basic material of the plastic scintillator. The scintillation light of each layer is collected to a photomultiplier tube (PMT) (9124SA; Electron Tubes Ltd.) via wavelength shifting (WLS) fibers (Y-11; Kuraray Co. Ltd.). The arrangements of the scintillators, PMTs, and WLS fibers inside the scintillator box of the TA SD are shown in Fig. 4.3.

The signals from PMTs are sent to the SD-electronics, which consists of a motherboard, wireless LAN modem, and a charge controller. The signals are digitized by a 12-bit flash analog-to-digital converter (FADC) (AD9235RU-65; Analog Devices Co.) with a 50 MHz sampling rate. It means the PMT signals are digitized in time bins with a width of 20 ns. Figure 4.4 shows the SD-electronics and the arrangements in the stainless box. The electronics are charged by a battery inside a tucker box in the stainless box. The battery is powered by a solar panel in the daytime. The SDs operate on 100% solar energy.

Each SD communicates with the corresponding communication tower with 2.4 GHz wireless LAN communication by the antenna.

The details of the TA SD are described in [72].

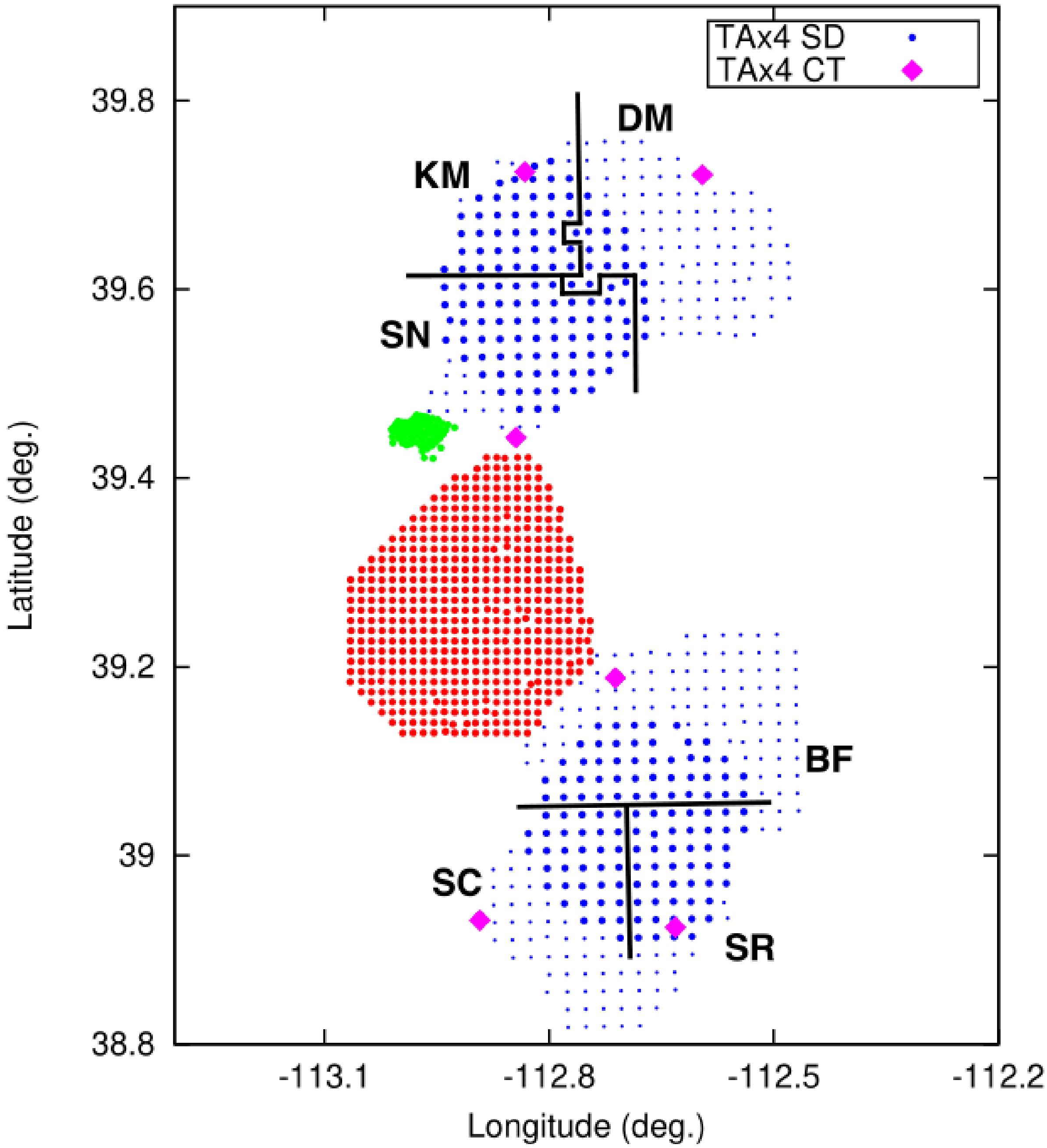

FIGURE 4.1: The layout of the TA×4 experiment. The red circles represent 507 TA SDs (TA SD array). The blue circles are newly deployed 257 SDs for the TA×4 experiment in 2019. The northern array (TA×4 North array) consists of 3 sub-arrays: Keg Mountain (KM), Desert Mountain (DM), and Smelter Knolls North (SN). The southern array (TA×4 South array) also consists of 3 sub-arrays: Black Rock FD (BF), South Cricket (SC), and Sand Ridge (SR). The solid black lines indicate the boundary of the sub-arrays. The blue dots are SDs planned to be deployed for the TA×4 experiment in the future. The light green circles represent SDs for the TALE experiment [85], which aims to observe cosmic rays below 10^{18} eV. The pink diamonds show the communication towers for the TA×4 northern array and southern array.

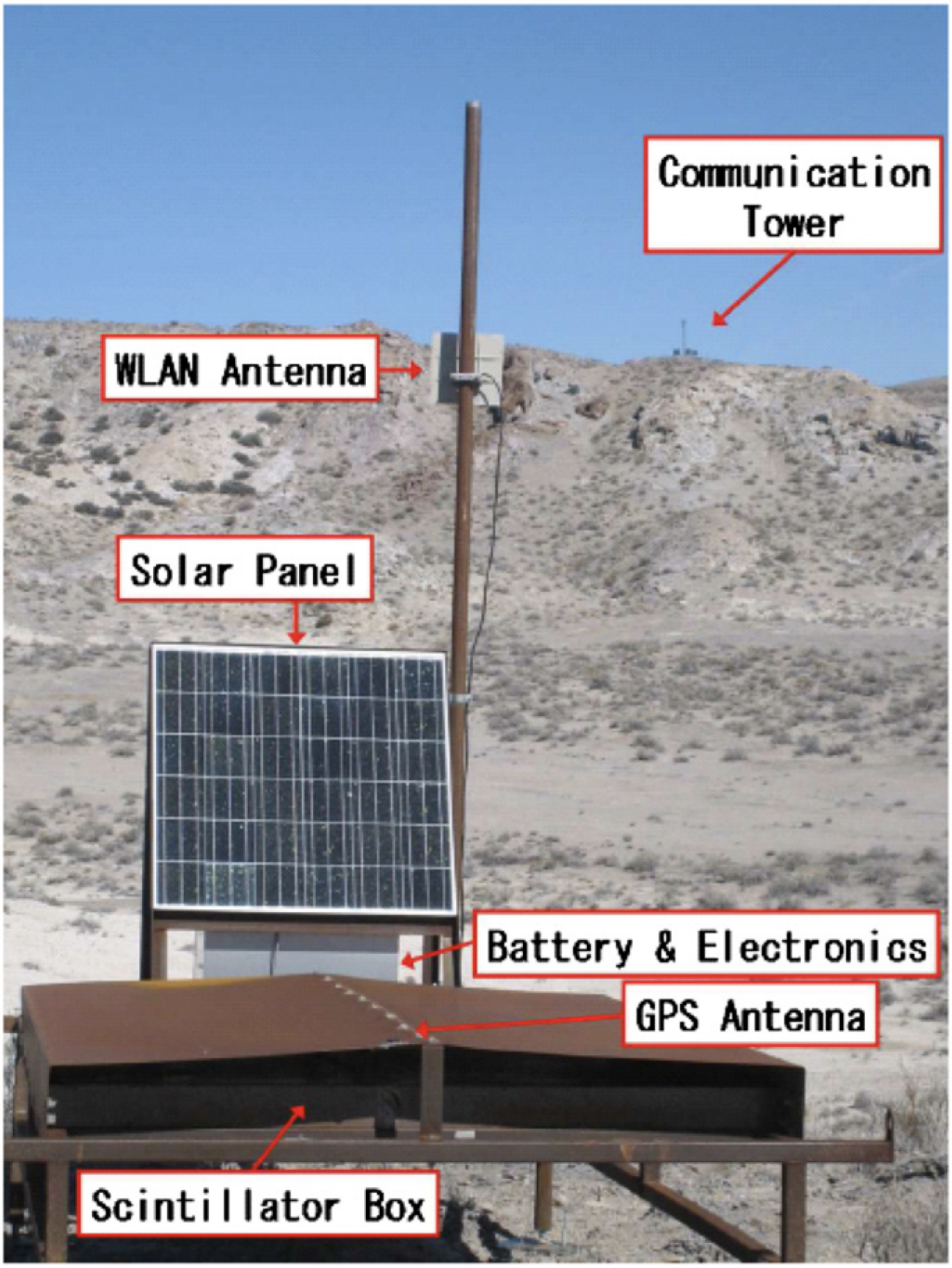

FIGURE 4.2: Outside view of a deployed TA SD. The scintillator box is on the iron frame and covered by the iron roof. The stainless box containing a battery and an electronics is under the solar panel.

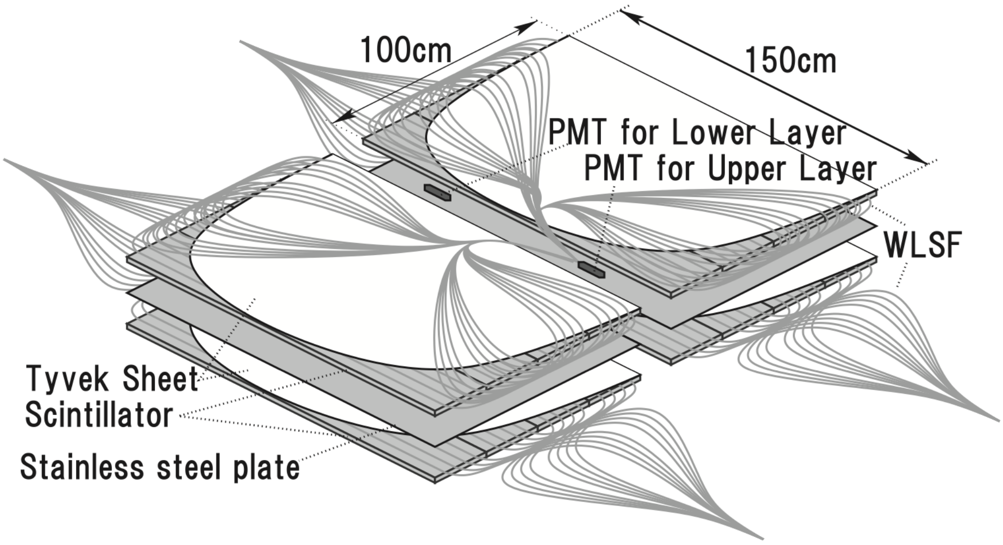

FIGURE 4.3: Schematic view of the inside of the scintillator box of the TA SD, taken from [72]. On each layer, 104 WLS fibers are laid. The length of the WLS fiber is 5 m, and laid with a spacing of 2 cm.

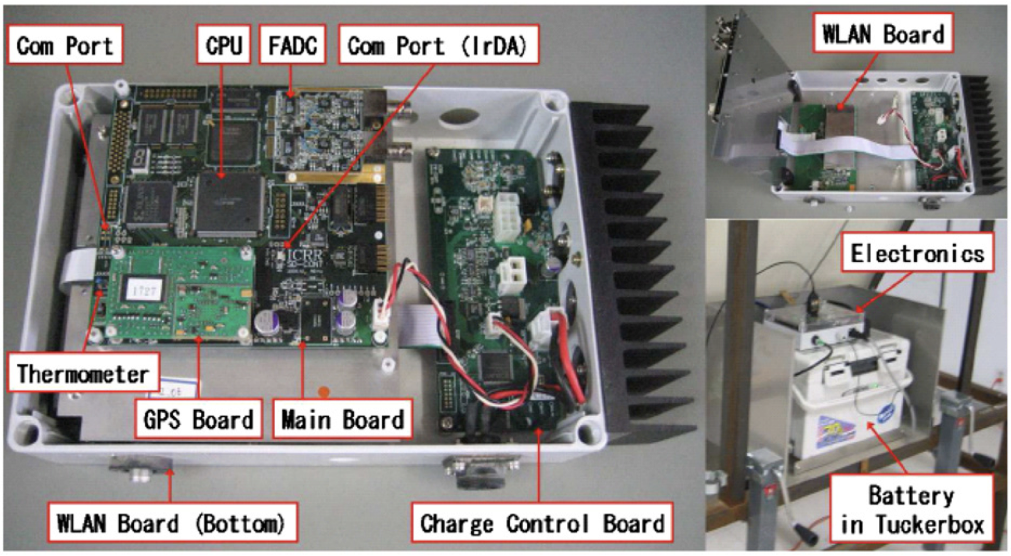

FIGURE 4.4: The SD-electronics and the arrangement inside the stainless box, which is located under the solar panel.

The design of the TA×4 SD and the difference from the TA SD

Figure 4.5 shows an outside view of a TA×4 SD. The basic design of the TA×4 SD is the same as that of the TA SD described above. However, the following points are improved from TA SDs:

- R8619 (Hamamatsu) is used as PMT in a TA×4 SD. R8619 (Hamamatsu) has higher quantum efficiency and better linearity than 9124SA (Electron Tubes Ltd), which is used in the TA SD. The results of the PMT linearity test are shown in Fig. 4.6.
- The interval of the WLS fibers, which collect scintillation light and send it to the photocathode of the PMT, is enlarged from 2 cm to 4 cm. The length of the fibers is extended from 5 m to 6.1 m, and the number of fibers is reduced from 104 to 28 on each layer. Arrangements of the TA×4 SD and TA SD are shown in Fig. 4.7 and Fig. 4.3, respectively. The total length of the WLS fibers in a TA×4 SD is 67% shorter than that in a TA SD [86]. Hence, the cost per detector was reduced.
- The material of the plastic holder of the WLS fiber bundle attached to the PMT surface was changed from optically transparent acrylic to white polyacetal resin. This change increased the amount of light sent to a PMT by 11%. Since the higher quantum efficiency of the PMTs in the TA×4 SD (approximately 10% higher than PMT of the TA SD) and the change of the plastic holders of the WLS fibers, the average number of photoelectrons from the PMTs and the uniformity of the signal are the same level as the TA SD despite the reduced length of the WLS fibers [86] [87].
- The solar panel used for the TA×4 SD is KD150SX-UFU (Kyocera) or KD145SX- UFU (Kyocera) or DS-A18-135 (DASOL), which is different from the solar panel used in the TA SD. The maximum power of the solar panels used in the TA×4 SDs is between 135 Watts and 150 Watts. It is higher than that used in the TA SD: 120 Watts.
- Reboot timers (ZEN-10C3DR-D-V2; omron) are installed to all TA×4 SDs. The SD electronics would occasionally hang, requiring a manual reboot when that occurred. The reboot timer automatically reboots the electronics once a week, eliminating the need for local access in case of hang-up. At the same time as the introduction of the reboot timer, a Low Voltage Disconnect Module (LVDM, D1077; CZH-LABS) was incorporated into the circuitry to automatically disconnect the battery from the electronics when the battery voltage drops below 10 V. This is to prevent excessive power consumption by the reboot timer in the event that power supply is interrupted, such as by a solar panel failure.
- Bird spikes, plates covering the side of the scintillator box, and cable-protector tubes are added to protect the SD from damage caused by animals in the field.
- To prevent PMTs from being damaged during transportation, PMTs were more firmly secured in aluminum cases [87].

The details of the design and performance of the TA×4 SD are described in [86].

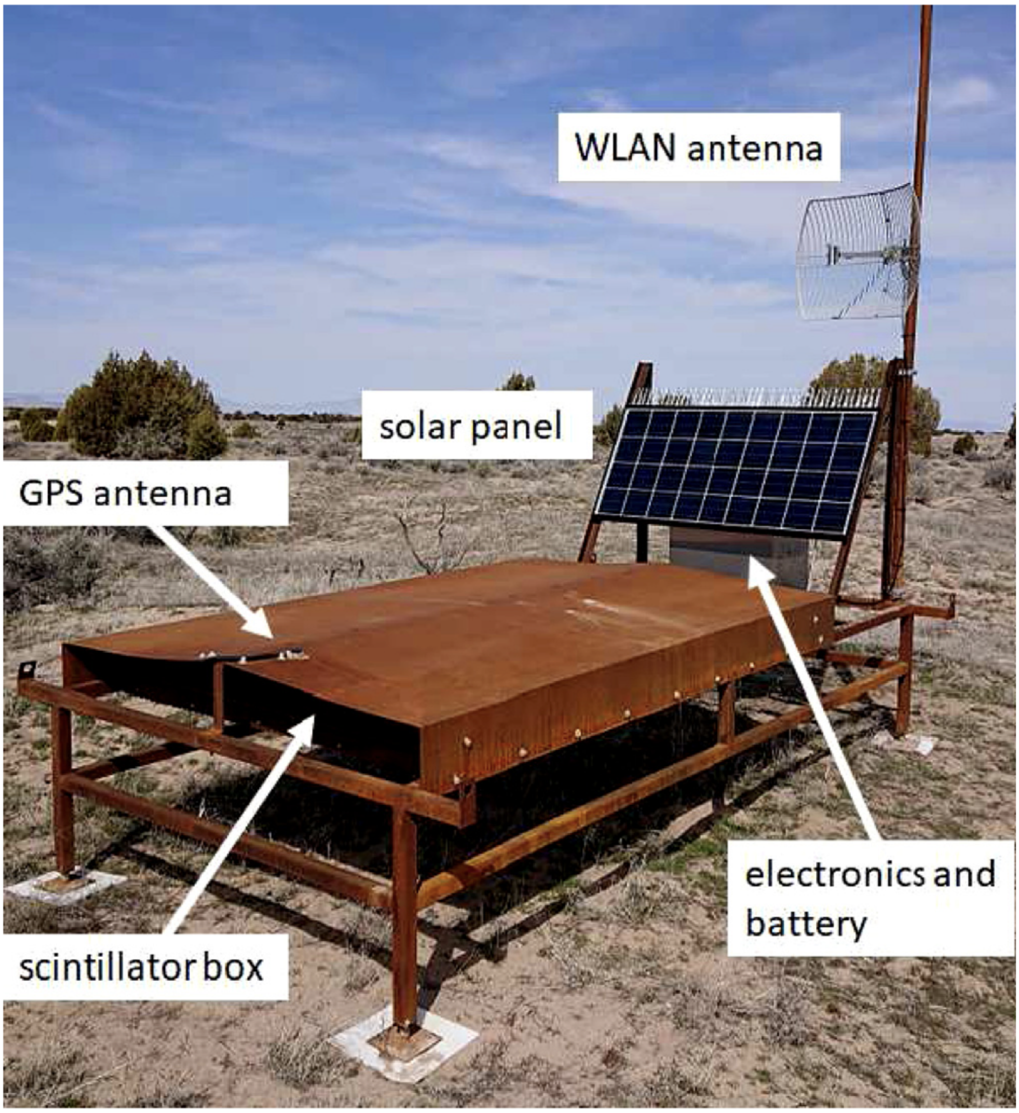

FIGURE 4.5: Outside view of a deployed TA×4 SD. The basic design is the same as the TA SD (Fig. 4.2). The bird spike is mounted on the solar panel.

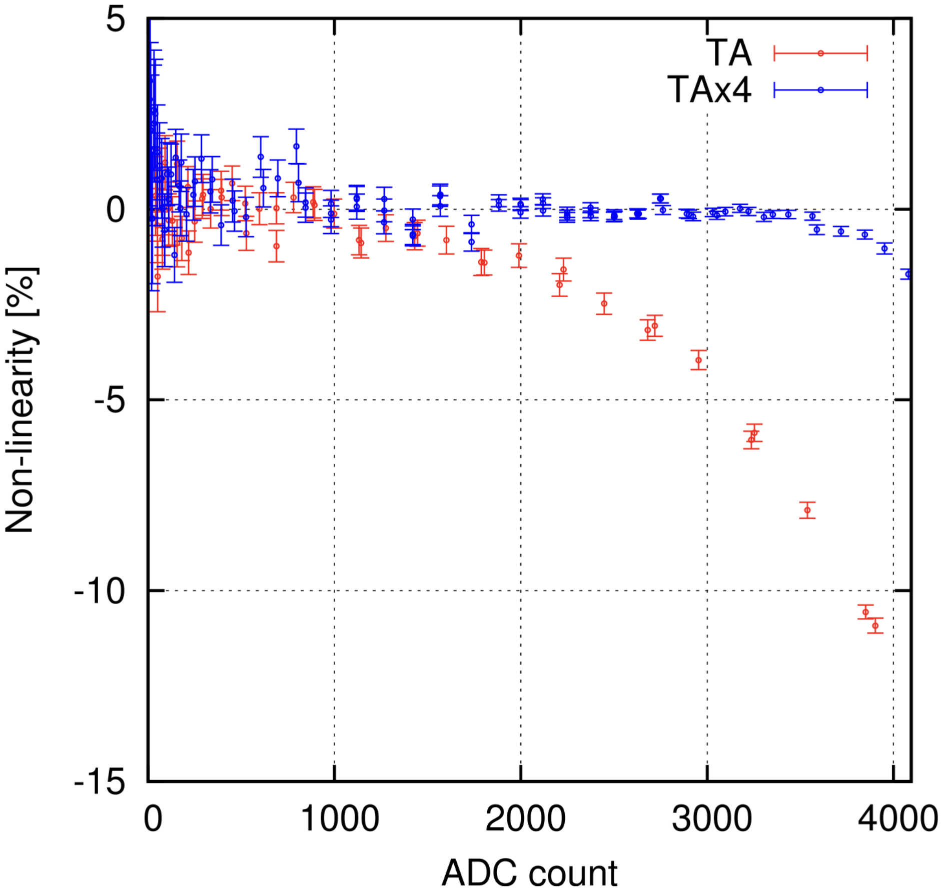

FIGURE 4.6: The nonlinearity of the typical PMT used for TA×4 SDs (blue) and TA SDs (red) [86]. Each FADC count corresponds to 0.01 mA.

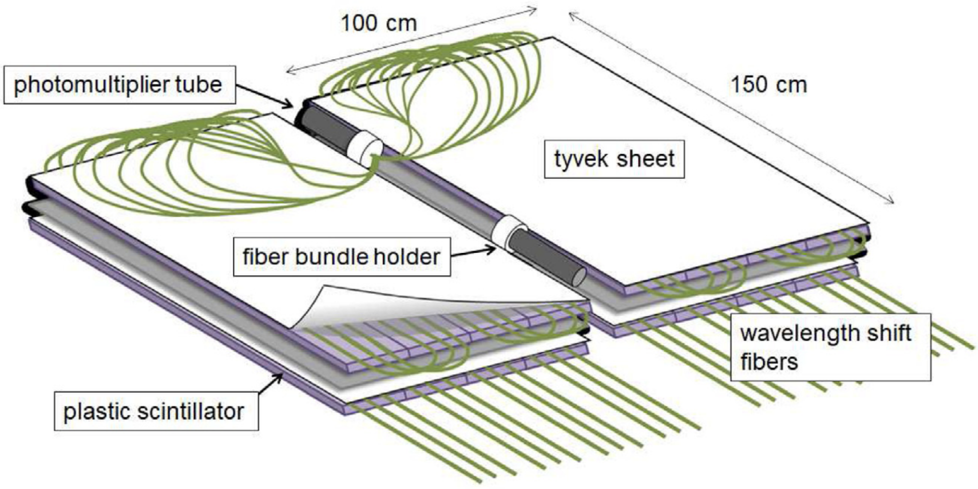

FIGURE 4.7: Schematic view of the inside of the scintillator box of the TA×4 SD, taken from [86]. On each layer, 28 WLS fibers are laid. The length of the WLS fiber is 6 m, and laid with the spacing of 4 cm. Compared with the TA SD (Fig. 4.3), the total length of the WLS fibers per one SD is reduced by 67%.

4.2 The trigger system of the TA×4 surface detectors

Each SD records waveforms when specific triggers are issued. There are three types of trigger: Level-0 trigger, Level-1 trigger, and Level-2 trigger. Level-0 and Level-1 triggers are judged by each SD-electronics. Level-2 trigger, which corresponds to a trigger to record air shower events, is judged by the electronics installed in the communication towers or FD stations. In this section, these trigger systems are described in detail.

4.2.1 Level-0 trigger

Level-0 trigger is issued when both of the two layers record more than 15 FADC counts, which corresponds to approximately 0.3 minimum ionizing particles (MIPs) within 160 ns. When Level-0 was issued, the SD records waveforms within 2.56 μs (from 0.64 μs before the trigger time to 1.92 μs after the trigger time) to a synchronous dynamic random access memory along with the trigger time. Since the one-time bin of the FADC is 20 ns, each of the recorded waveforms consists of $(2.56 \times 10^{-6})/(20 \times 10^{-9}) = 128$ time bins. The typical rate of the Level-0 trigger is about 750 Hz.

4.2.2 Level-1 trigger

The criteria of the Level-1 trigger are the same as that of the Level-0 trigger except for the FADC threshold: 150 FADC counts for the Level-1 trigger, which corresponds to approximately 3 MIPs. The lists of the Level-1 triggers are sent to the corresponding communication tower every second. The typical rate of Level-1 trigger is about 20 Hz.

4.2.3 Level-2 trigger

The TA×4 SD array has two types of Level-2 trigger system. One is the SD-self trigger, which is generated by the communication tower. The other one is the hybrid trigger, which is generated by the FD station.

No matter which type of Level-2 trigger is issued, all waveforms of SDs that issue Level-0 trigger within ± 32 μs of the Level-2 trigger time in the array are collected. The set of the waveforms with their timestamps is recorded as an event. The description of the recorded shower event is given in Sec. 4.3.2.

SD-self trigger

When any adjacent 3 SDs (see Fig. 4.8) in an array issue Level-1 trigger within 14 μs, all waveforms of SDs which issue Level-0 trigger within ± 32 μs of the Level-2 trigger time in the array are collected. This trigger method is the same as the TA SD except for the time window, which is 8 μs for TA SD. The ratio of the time window is defined as the ratio of the SD spacing (14 μs/8 μs $\simeq$ 2.08 km / 1.2 km). Before the implementation of the inter-tower trigger described below, the judgment of Level-2 trigger and waveform collection were performed independently in each of the six sub-arrays.

Inter-tower trigger

The judgment of the adjacent condition of the Level-2 trigger for the events at the boundary region among sub-arrays requires data transfer of Level-1 trigger time

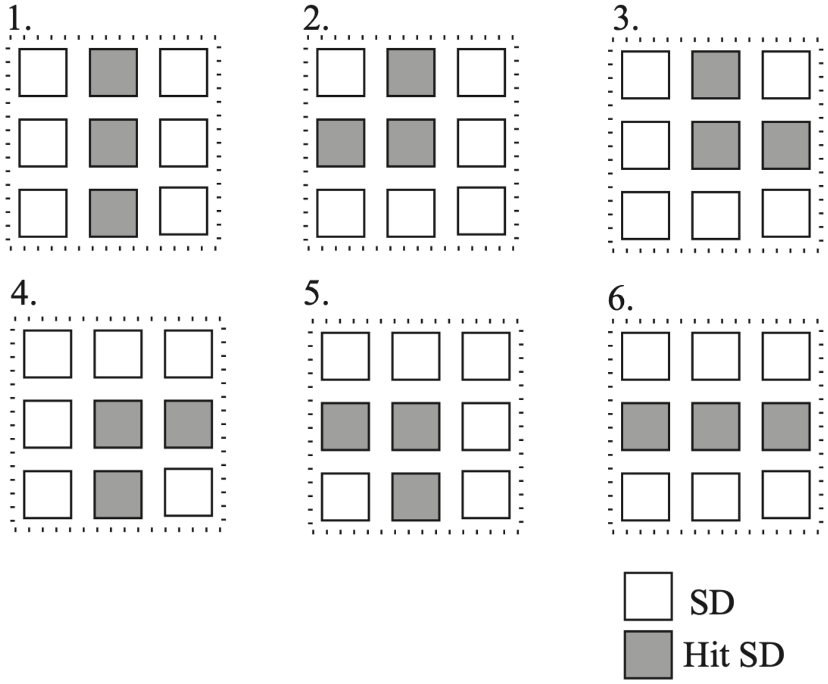

FIGURE 4.8: The trigger pattern of the SD-self trigger. Any three adjacent SDs issue the Level-1 trigger (represented by a shaded square), and the Level-2 trigger is issued, taken from [72].

between communication towers. Therefore, we additionally implemented the data transfer and the inter-tower trigger software to the data acquisition program for the SD-self trigger [88]. Inter-tower wireless communication of 5 GHz band [89] is used for data transfer. The data rate of the inter-tower wireless communication is approximately several tens of Mbps. On the other hand, the data rate of the Level-1 trigger time in the whole SD array is approximately several tens of kbps, much smaller than the inter-tower wireless communication data rate. Therefore, we implemented a simple data transfer of all the Level-1 trigger timing from non-central towers (KM and DM for the TA×4 North array, and SC and SR for the TA×4 South array) to the central tower (SN for the TA×4 North array, and BF for the TA×4 South array) every second for the inter-tower triggers. Figure 4.9 shows a time chart of the data transformation of the inter-tower trigger.

The inter-tower trigger is conducted in the following way.

1. All the Level-1 trigger time stamps of SR (KM) and SC (DM) are sent to the central tower BF (SN) every second.
2. Level-2 trigger conditions are judged in the Level-1 trigger timing of the whole South (North) array.
3. If there are additional Level-2 triggers to the current Level-2 triggers at the central tower, requests to take waveforms are sent to all the towers.
4. If there are duplicated requests of taking waveforms or no waveform in the time window, the requests are canceled at each tower.

The inter-tower trigger has been partially working since the implementation on 1 November 2022; when the Level-2 trigger is issued only in the central tower, waveforms are not collected from the non-central towers. The full inter-trigger system

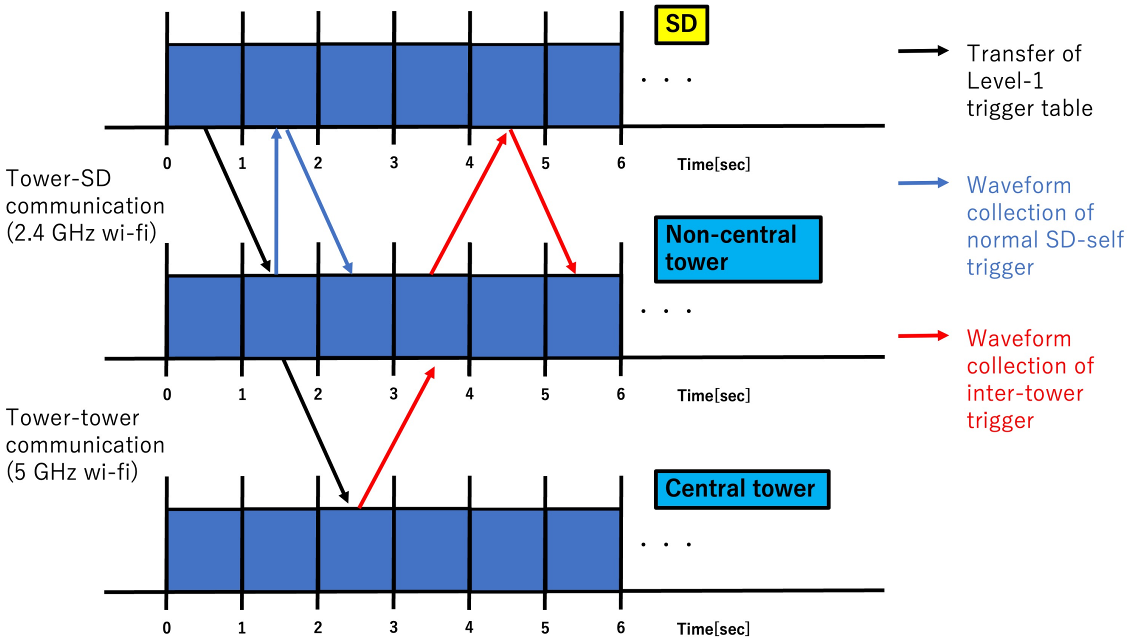

FIGURE 4.9: Schematic view of the data transfer of the inter-tower trigger. Each block represents one DAQ cycle of 1 second period. The black arrows represent the transfer of the Level-1 trigger table. The waveform collection and instruction issued by the normal SD-self trigger within each sub-array are represented by blue arrows, and those by the inter-tower trigger are represented by red arrows.

was implemented on 23rd November 2023. Hereafter, the former and the latter inter-tower trigger systems are referred to as *partial inter-tower trigger* and *full inter-tower trigger*, respectively. The evaluation of the difference in the efficiency between both inter-tower trigger systems is given in Sec. 7.2.2. A flowchart of both inter-tower trigger systems is shown in Fig. 4.10.

With the full inter-tower trigger, the whole TA×4 North (South) array, consisting of three sub-arrays, works as a single array.

Hybrid trigger

The TA×4 MDFD (TA×4 BRFD) station that covers the TA×4 North (South) array began observation in June 2018 (June 2020). When an FD triggers a shower, the trigger time information is sent to SDs, and SDs record waveforms. This trigger system is called the hybrid trigger. The hybrid trigger is issued for the TA×4 North and TA×4 South, independently. An example of a hybrid-triggered event is shown in Fig. 4.11.

4.3 Low level data

4.3.1 Calibration data

Each SD accumulates FADC values when the Level-0 trigger is issued over a 10-minute period, and it sends them to the corresponding communication tower every 10 minutes. The waveform recorded by the Level-0 trigger is integrated over 12 bins (240 ns) from four bins before to eight bins after the peak of the waveform and saved

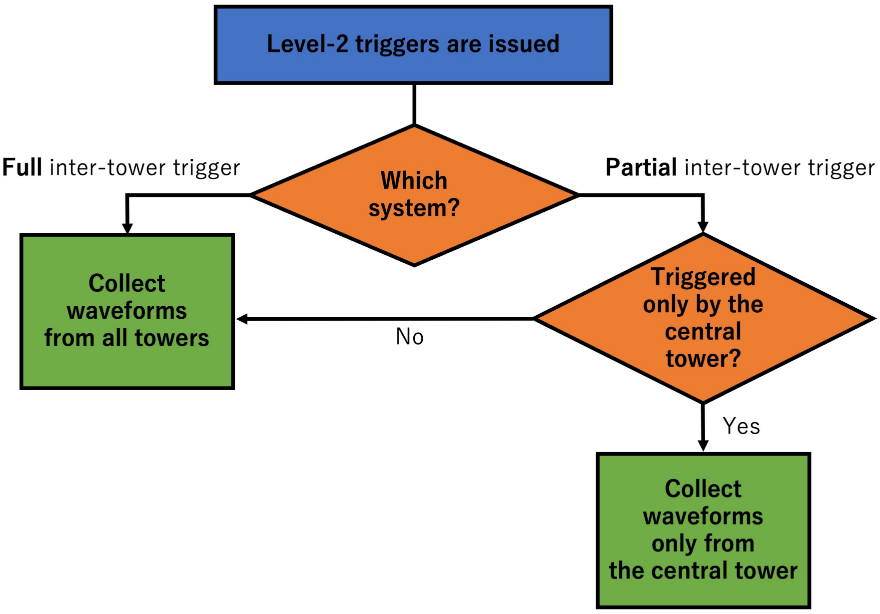

FIGURE 4.10: A flowchart of the two inter-tower trigger systems (the full inter-tower trigger and the partial inter-tower trigger).

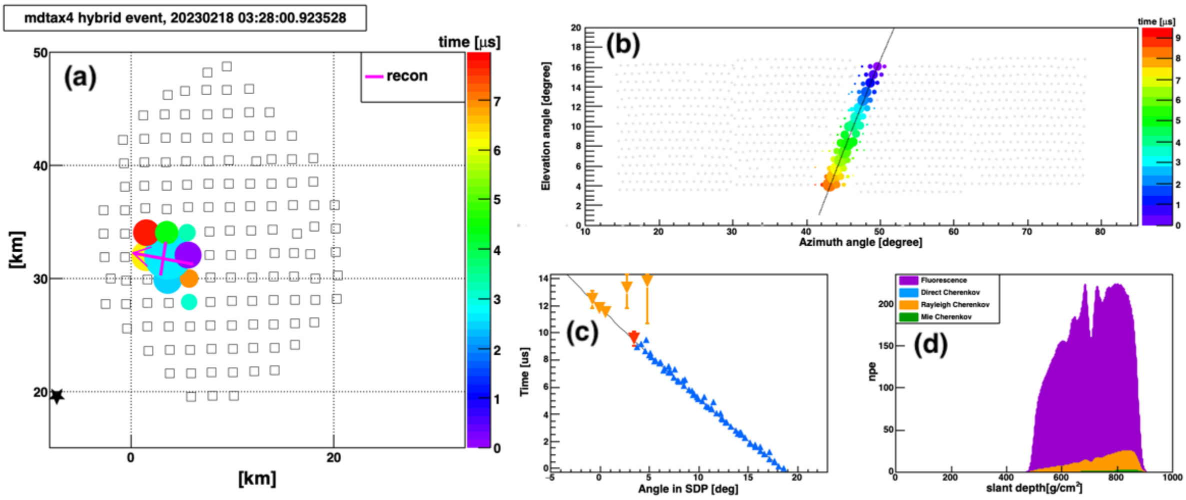

FIGURE 4.11: An example of the hybrid-triggered event in the TA×4 North on 18th February 2023: (a) the SD footprint of the event, (b) the shower track observed by the FD PMT, (c) the SD-FD combined time fit of the event, and (d) the reconstructed shower profile.

as a 1-MIP histogram. The 1-MIP histogram is fitted to obtain the 1-MIP peak for that 10-minute period. All FADC counts are integrated over every eight bins and saved into a pedestal histogram, which is fitted to obtain the pedestal level and pedestal fluctuation for that 10-minute period. Figure 4.12 shows an example of the 1-MIP histogram and pedestal histogram for a 10-minute period (see Sec. 6.1).

When we reconstruct observed data, the corresponding values are used as 1-MIP value and pedestal level. These values are reflected in the MC simulation described in Sec. 5.2 as well to reproduce actual SD conditions in the MC simulation.

In addition to the 1-MIP histogram and pedestal histograms, each SD also records other data: GPS information, trigger rate, battery condition, communication condition, etc. It allows us to grasp the running status of SD remotely (see Sec. 4.4.1) as well as to remove bad SD (see Sec. 6.2.1), such as SD, whose pedestal fluctuation is very high when we reconstruct air shower events. They are monitored (Fig. 4.14) and used to check the running status of the SDs.

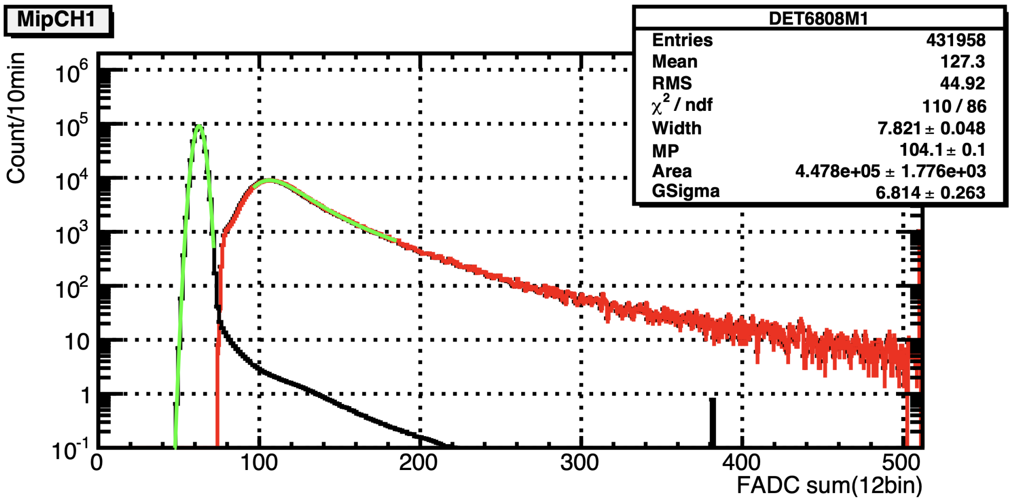

FIGURE 4.12: 1-MIP histogram (red) and pedestal histogram (black) for a 10-minute period of the lower layer of the detector 6808. The light green lines are fit results.

4.3.2 Shower event data

When Level-2 trigger is issued, the waveforms of the SDs that issued the Level-0 triggers are sent to the corresponding communication tower and are recorded as shower event data. The following is an example of the shower event recorded on 22nd February 2023 in the BFCT:

```
E 00000000 1fb1ad24
W 4615 1
w 0 0 132
4053cf7c
03ee033f
00007005
01006004
...
02faeb19
5cf03027
W 4616 1
w 0 0 132
```

```
4053d0c1
05f60346
...
02faead2
5b202e28
### DONE 493545 1fb1ad24
```

The first line, started with "`E`," declares the start of the event data. The third term in the first line is the hexadecimal encoding of the trigger mode and the event time.

The following lines indicate the waveform information of each SD. The lines started with "`W`" or "`w`" are the header section of the corresponding SD. They include the information on the ID of the SD, the number of waveforms from the SD, and the number of retries in obtaining the waveform. The successive 132 lines include the information on the waveform. Four of the 132 lines include the information on the trigger timing, the trigger flag, and the debug information. The remaining 128 lines are the FADC counts of the corresponding time bin.

The last line started with "`### DONE`" declares the end of the event data.

The above data is the lowest-level shower event data. The data process and reconstruction of the shower event data are described in Chap. 6. Figure 4.13 shows an example of the display of a shower event recorded on 23rd March 2023 in the TA×4 North array.

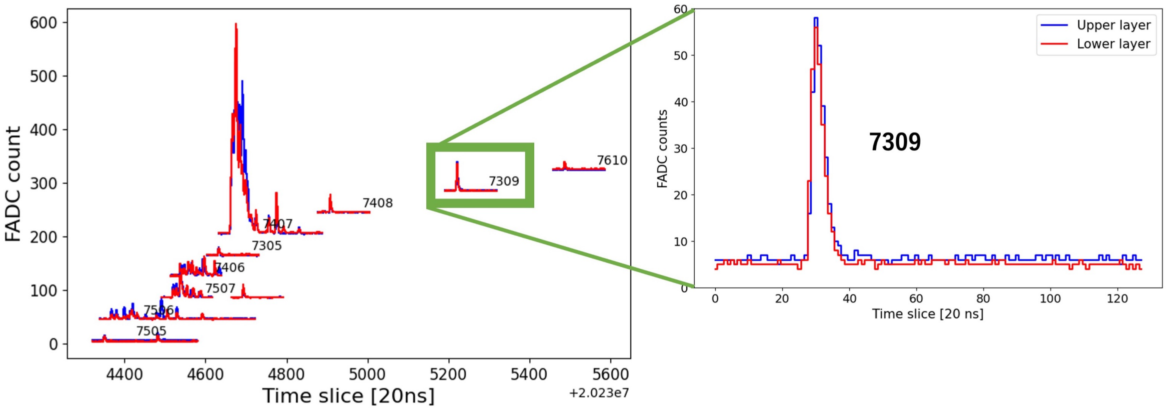

FIGURE 4.13: Display of a recorded shower event on 23rd March 2023 in the TA×4 North array. The left figure shows the recorded waveforms. The baseline of the waveforms is shifted for ease of viewing. Each waveform consists of 128-time bins of FADC counts. One SD may record multiple waveforms. The blue (red) line is the signal of the upper (lower) layer. The numbers written near the waveform indicate the corresponding detector ID. The right figure is an enlargement of the detector 7309 in the left figure.

4.4 Construction and running status of the TA×4 SD array

4.4.1 Construction

Assembly of TA×4 SD scintillator boxes began in Japan in 2016 and in Korea for 30 units in 2018. The assembled scintillator boxes were transported to the Cosmic-Ray Center in Delta City, Utah, USA. The final assembly (putting the scintillator box on a stand and installing electronics, batteries, solar panels, antennas, etc.) of 257 TA×4 SDs was performed at the Cosmic-Ray Center.

After assembly and tests to check if they work fine were completed in February 2019, the TA×4 SDs were transported by flatbed trucks to staging areas near the location of the SD deployment sites. The deployment sites were visited by buggy or helicopter in advance to check the postural stability of SD and line-of-sight to the communication towers. The SDs at staging areas were deployed to the corresponding deployment site one by one by helicopter in February 2019. After the deployment, the direction of the wireless LAN antenna of each deployed SD was optimized to achieve the best communication conditions.

The data acquisition started at the end of April 2019. There were problems in the communication tower operation and trigger systems in the first several months. After addressing those issues, steady-state operations began on October 8, 2019. The observational data from that date onward are used in analyses of this paper. The running status of the steady-state operation is described in the following section.

To maintain the stable observation of the TA×4 SDs, we have been doing remote operations from Japan. In the operation, we check the running status of each 257 TA×4 SD once a week by monitor plots (Fig. 4.14) and direct maintenance to researchers and technicians in Utah when problems are found. Problems caused by temporary malfunctions in electronics, such as HV configuration failures, were handled by rebooting remotely. We also adjusted high voltage of PMTs depending on temperature.

4.4.2 Running status

Running status

Figure 4.15 shows the number of live SDs in the TA×4 SD array from 8th October 2019 to 31st July 2023. The period is divided into four epochs, *Epoch-1*, *Epoch-2*, *Epoch-3*, and *Epoch-4* in terms of the running status. The running status and problems in each Epoch are described below.

Epoch-1: 8th October 2019 – 30th September 2022

Epoch-1, from 8th October 2019 to 30th September 2022, is the period before the first mass onsite maintenance in August 2022. In this period, travel was restricted due to COVID-19. After the relaxation of international travel in Japan, the first mass access was performed in August 2022, and the running status was improved, as seen in Fig. 4.15. The most serious and frequent problem in this period was the overcharging of batteries. This overcharging problem was caused by malfunctioning charge controllers and solved by installing a commercial charge controller (SunSaver SS-10L 12V; Morning star). Any SD with commercial charge controllers have not experienced overcharging since the installation.

In addition to the installation of the commercial charge controllers, we also installed amplifiers (SH2500P/SH24Gi4000P; Sunhans) to improve the wireless communication between an SD and its corresponding communication towers. We have installed 67 amplifiers on SDs whose communication was not good, and they improved their Received Signal Strength Indicator (RSSI) values, which indicates the strength of the received signal, by about 10 dBm to 20 dBm. There was no lack of power supply due to the amplifier power consumption.

In February 2022, we retrieved 11 TA×4 SDs which did not record muon signals to the Cosmic-Ray Center by helicopter. We repaired them by re-soldering the connection of the PMT signal circuit and replacing the broken PMTs, and then we returned them to their original locations.

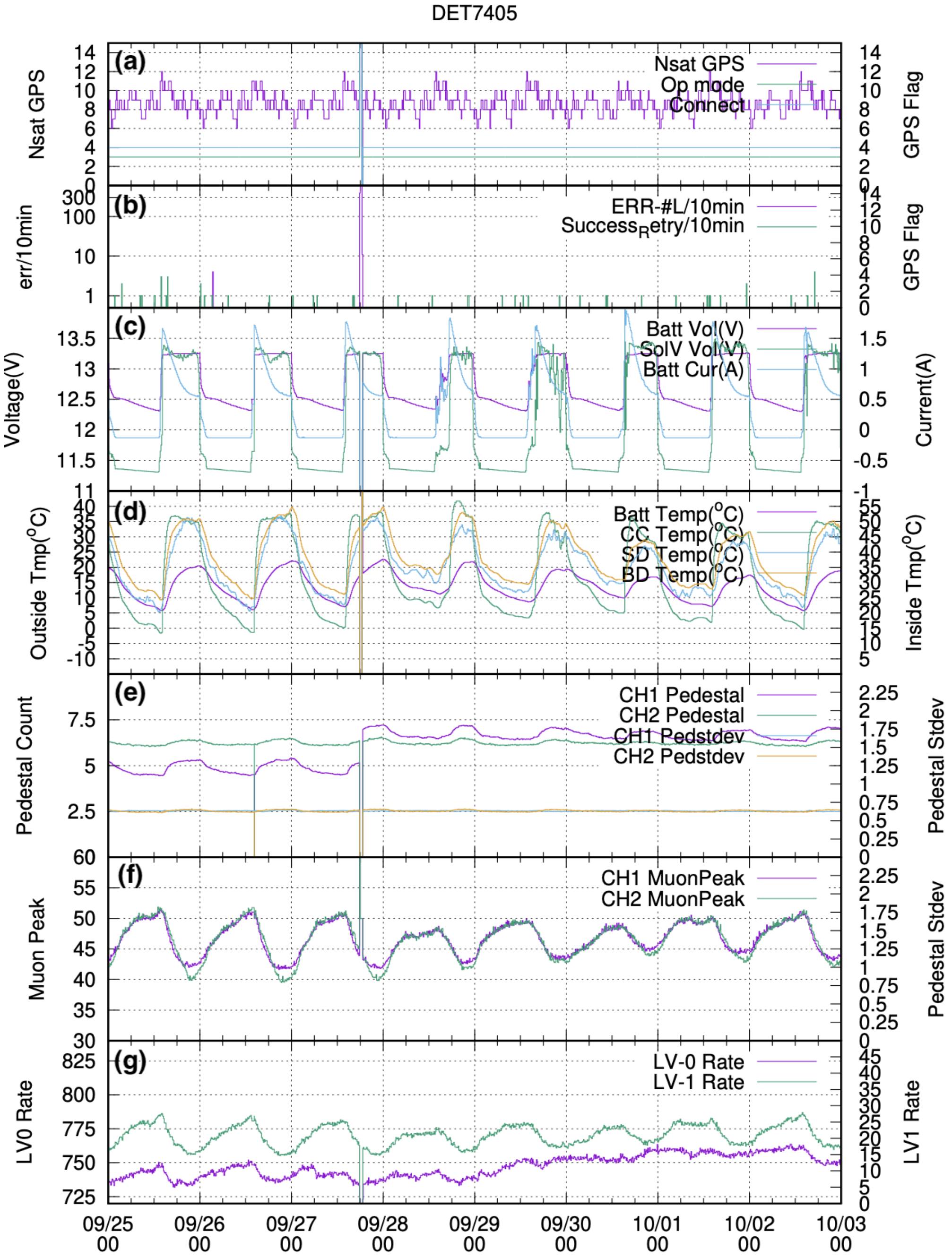

FIGURE 4.14: An example of monitor plot of a TA×4 SD (DET7405 in the KM sub-array). The x-axis is the time, where the resolution is 10 minutes. This plot is from 25th September to 3rd October 2022. Each panel corresponds to each status of the SD: (a) the GPS status, (b) the communication status, (c) the battery and solar panel status, (d) the temperature measured by each point (Batt: battery, CC: charge controller, SD: inside the scintillator box, BD: main board), (e) the pedestal level and fluctuation, (f) the muon peak, and (g) the trigger rate.

Epoch-2: 1st September 2022 – 31st October 2022

Epoch-2, from 1st September 2022 to 31st October 2022, is the period from the first mass access to the implementation of the inter-tower trigger. In this Epoch, the ratio of live SDs was above around 90%.

Epoch-3: 1st November 2022 – 30th June 2023

Epoch-3 is the period after the implementation of the inter-tower trigger. As seen in Fig. 4.15, the number of live SDs drastically decreased in December 2022. This was due to the overcharging and the malfunctioning of electronics on the TA×4 SDs. Delta, where the TA experiment is located, was experiencing heavy snowfall that winter, and the low temperature damaged the batteries and electronics. To address these problems, the batteries were successively replaced after January 2023, and the electronics were replaced between May and June.

Epoch-4: 1st June 2023 –

As a result of the maintenance in *Epoch-3*, the ratio of live SDs has been greater than 90% since June 2023. In October 2023, commercial charge controllers were installed before the winter arrived. Currently, 252 over 257 TA×4 SDs have commercial charge controllers after the installation.

4.4.3 Aperture and exposures

Using the Monte Carlo (MC) simulation (described later in Chap. 5), which reflects calibration data described in Sec. 4.3.1, two types of aperture of the TA×4 SD array are calculated for each Epoch.

One is the aperture α_{gen} as a function of generated energy. It is given as follows:

$$\alpha_{\mathrm{gen}}(E_i) = A_{\mathrm{gen}}\Omega_{\mathrm{gen}} \times \frac{N_{\mathrm{rec}}(E_{\mathrm{gen},\,i}/f)}{N_{\mathrm{gen}}(E_{\mathrm{gen},\,i}/f)}, \tag{4.1}$$

where A_{gen} and Ω_{gen} are the area and the solid angle of the generated MC events, respectively (see Sec. 5.3). $N_{\mathrm{rec}}(E_{\mathrm{gen},\,i}/f)$ is the number of events that are reconstructed and pass the event selection (described later in Sec. 6.5) in the i-th energy bin as a function of the generated energy scaled by the energy factor f (in the case of the TA×4 SD array, $f = 1.36$ as described later in Sec. 7.1). $N_{\mathrm{gen}}(E_{\mathrm{gen},\,i}/f)$ is the number of events that are generated in the MC simulation in the i-th energy bin as a function of $E_{\mathrm{gen},\,i}/f$. The energy $E_{\mathrm{gen},\,i}/f$ corresponds to the true energy of the generated cosmic ray (see Sec. 7.1 for details).

The other one is the aperture α_{rec} as a function of the reconstructed energy. It is given as follows:

$$\alpha_{\mathrm{rec}}(E_i) = A_{\mathrm{gen}}\Omega_{\mathrm{gen}} \times \frac{N_{\mathrm{rec}}(E_{\mathrm{rec},\,i})}{N_{\mathrm{gen}}(E_{\mathrm{gen},\,i}/f)}. \tag{4.2}$$

The difference from α_{gen} is the denominator of the efficiency: $N_{\mathrm{rec}}(E_{\mathrm{rec},\,i})$, which is the number of events in the i-th energy bin as a function of the reconstructed energy (including the energy scaling as described in $E_{\mathrm{rec},\,i}$, see Sec. 7.1 for details). This term includes the bin-to-bin migration effect due to the finite energy resolution of the SD array. Hence, this aperture $\alpha_{\mathrm{rec}}(E_i)$ corresponds to the number of events observed in the reconstructed energy bin. We have to assume the cosmic ray energy spectrum to calculate the migration effect.

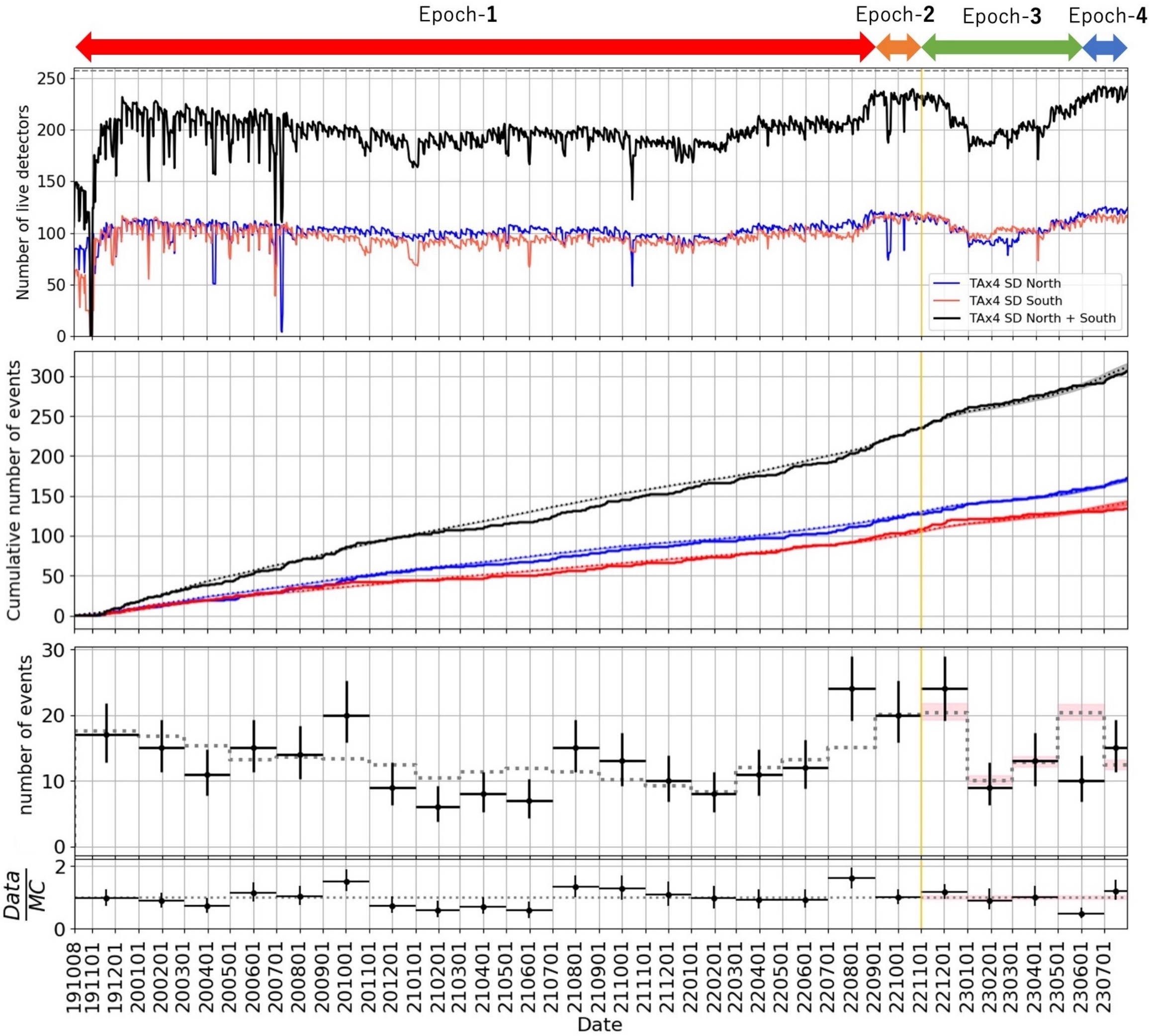

FIGURE 4.15: The number of live SDs (top), the cumulative number of events (middle), and the differential number of events and its ratio of the observation (black points) to the MC simulation (dotted line and histogram) (bottom) in the TA×4 North SD array (red), TA×4 South SD array (blue), and North SD array plus South SD array (black), respectively from 8th October 2022 to 31st July 2023. In the middle and the bottom figures, the dotted lines indicate the expectation by the MC simulation. The vertical yellow line indicates the date of the implementation of the inter-tower trigger. After the date, the expectation by the MC simulation is scaled by the factors, which correct the difference between the trigger systems implemented in real and that implemented in the MC simulation as described in Sec. 7.2.2, and the uncertainties of the factors are shown by the bands. The gray dashed-horizontal line in the top figure indicates the total number of deployed TA×4 SDs: 257. The arrows indicate the Epochs described in the text.

The aperture $\alpha_{\mathrm{rec}}(E_i)$ as a function of the reconstructed energy is usually shown as the effective aperture for the TA SD. In this paper, we show both of the apertures of the TA×4 SD array since the TA×4 SD array has worse energy resolution than TA SD, and the migration effect is larger than that of TA SD. The TA SD energy spectrum with 11 years of data [90] is used as the input energy spectrum here.

The two types of aperture are shown for each Epoch in Fig. 4.16, Fig. 4.17, Fig. 4.18, and Fig. 4.19. The comparison of the apertures of the four Epochs is shown in Fig. 4.20. As seen in Fig. 4.20, the apertures are different among Epochs. The number of live SDs is important not only for the low-efficiency energy region but also for the high-efficiency energy region: several tens of percent effect on the energy region of $E > 10^{20}$ eV (Fig. 4.21). We introduced the inter-tower trigger and performed maintenance. As a result, the best performance of the *Epoch-4* was achieved.

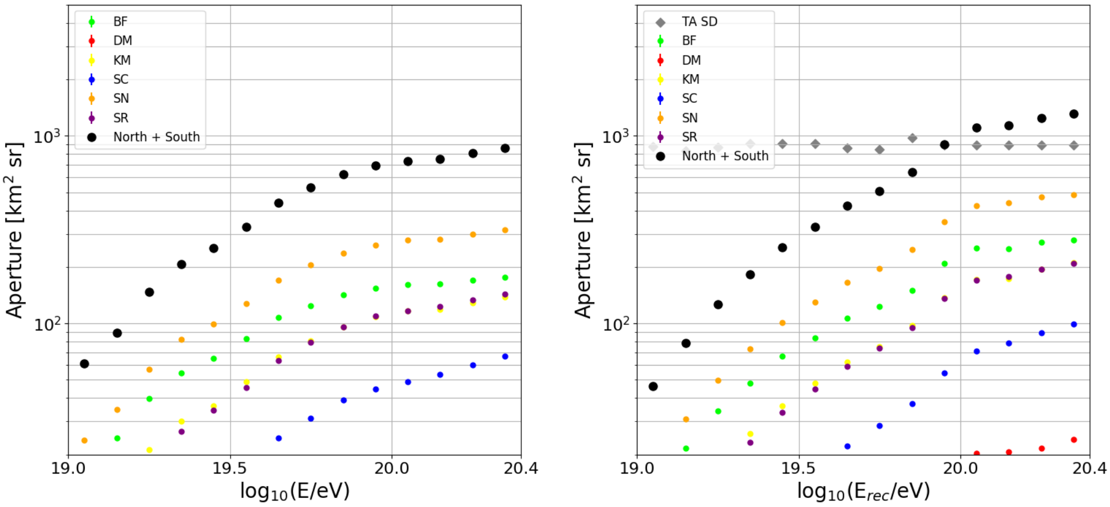

(A) The aperture α_{gen} as a function of the generated energy.

(B) The aperture α_{rec} as a function of the reconstructed energy.

FIGURE 4.16: The aperture as a function of the generated energy (left) and the reconstructed energy (right) for *Epoch-1*. The aperture for the six sub-arrays and their sum are shown. In the right figure, the aperture of the TA SD [91] is shown by the gray diamonds.

4.4.4 Effect of the full inter-tower trigger

Figure 4.22 shows the comparison between the aperture with the full inter-tower trigger and that without the inter-tower trigger. They are calculated for the same period (November 2022). Therefore, the running status is the same between them, and only the difference in the trigger system is reflected. The full inter-tower trigger enhances the aperture by approximately 50%. This enhancement is less dependent on energy.

4.4.5 Exposure

The exposure as a function of the reconstructed energy is given by $\alpha(E_{\mathrm{rec},\,i}) \times T$, where T is the observation period. Figure 4.23 shows the exposures of the TA×4 SD array and the TA SD array. With the first three years of the observational period without the inter-tower trigger (*Epoch-1* + *Epoch-2*), the total exposure of the TA ×4 North array plus the TA×4 South array is approximately 30% of that of the TA SD of

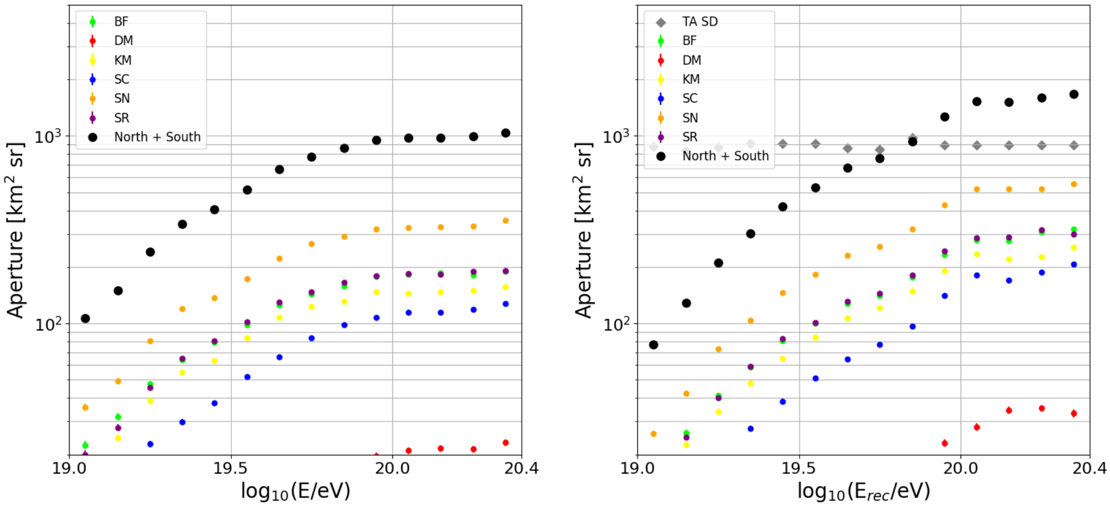

(A) The aperture α_{gen} as a function of the generated energy.

(B) The aperture α_{rec} as a function of the reconstructed energy.

FIGURE 4.17: Same as Fig. 4.16, but for *Epoch-2*.

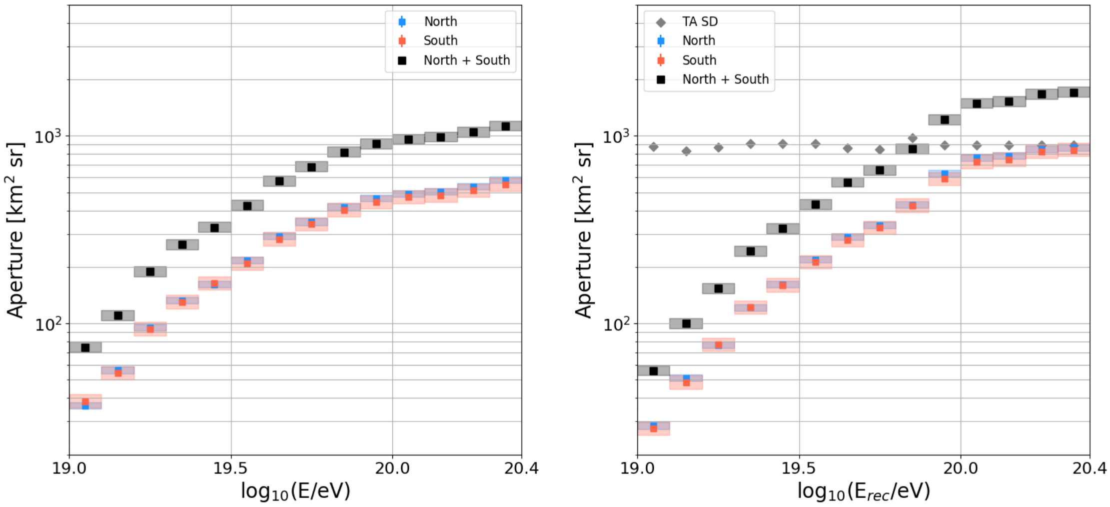

(A) The aperture α_{gen} as a function of the generated energy.

(B) The aperture α_{rec} as a function of the reconstructed energy.

FIGURE 4.18: Same as Fig. 4.16, but for *Epoch-3*. The bands indicate the uncertainty of the estimation of the partial inter-tower trigger aperture from the full inter-tower trigger (see Sec. 7.2.2 for details).

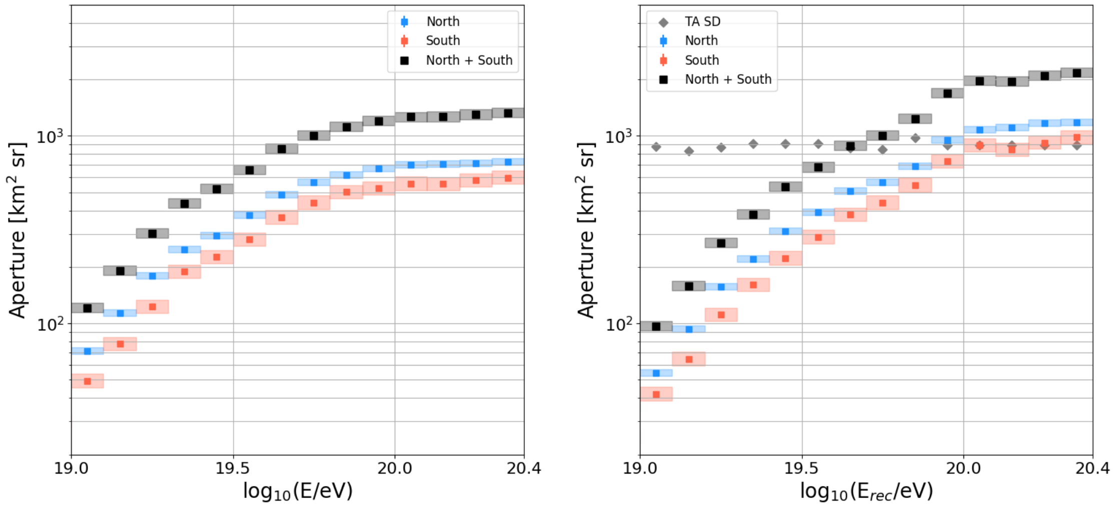

(A) The aperture α_{gen} as a function of the generated energy.

(B) The aperture α_{rec} as a function of the reconstructed energy.

FIGURE 4.19: Same as Fig. 4.18, but for the period of *Epoch-4*.

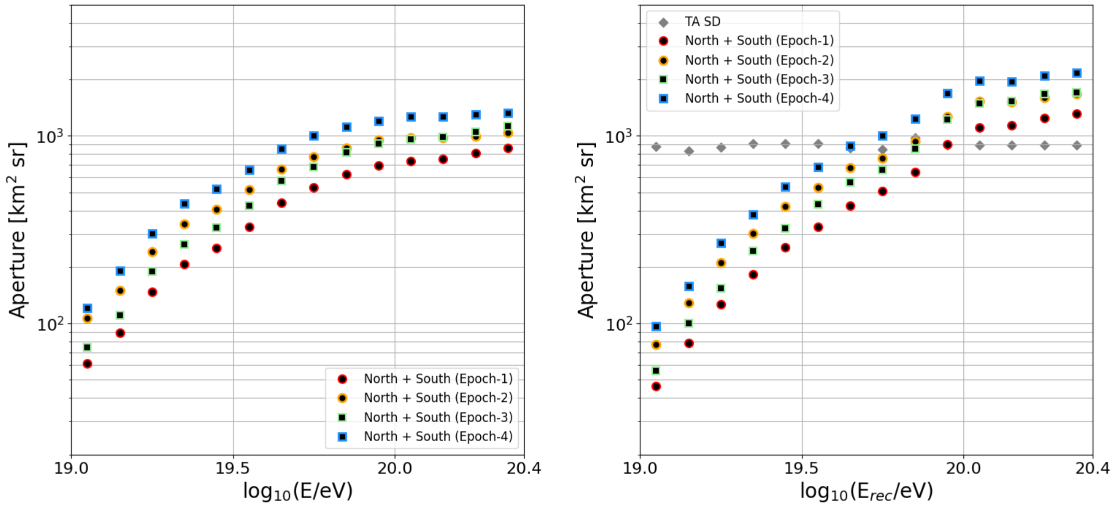

(A) The aperture α_{gen} as a function of the generated energy.

(B) The aperture α_{rec} as a function of the reconstructed energy.

FIGURE 4.20: The comparison of the apertures of the North + South array as a function of the generated energy (left) and the reconstructed energy (right) for each Epoch.

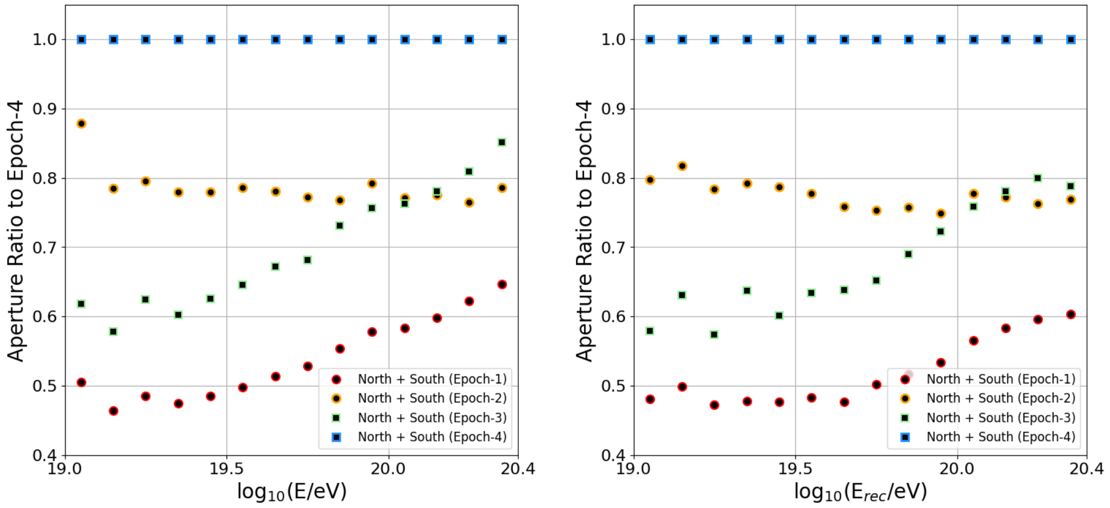

(A) The aperture α_{gen} ratio to *Epoch-4* as a function of the generated energy.

(B) The aperture α_{rec} ratio to *Epoch-4* as a function of the reconstructed energy.

FIGURE 4.21: The apertures ratio to the *Epoch-4* as a function of the generated energy (left) and the reconstructed energy (right).

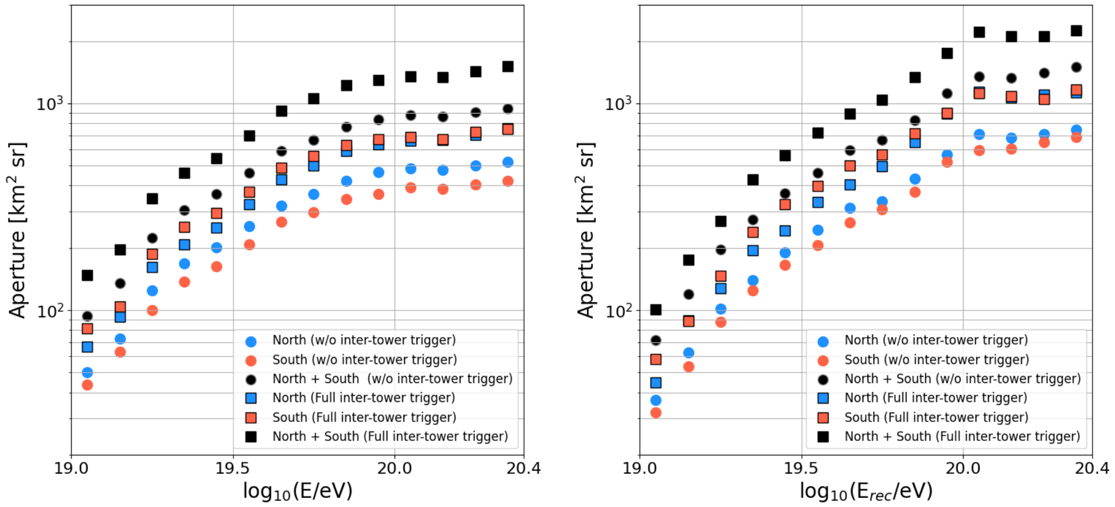

(A) The aperture α_{gen} as a function of the generated energy.

(B) The aperture α_{rec} as a function of the reconstructed energy.

FIGURE 4.22: The apertures with the full inter-tower trigger (squares) and without the inter-tower trigger (circles). They are calculated with the same SD status: the status between 1st November 2022 and 31st November 2022.

14 years of the observational period for energies greater than 10^{20} eV. With another nine months (*Epoch-3* + *Epoch-4*), the exposure of the TA ×4 North array plus the TA×4 South array is approximately 40% of that of the TA SD array.

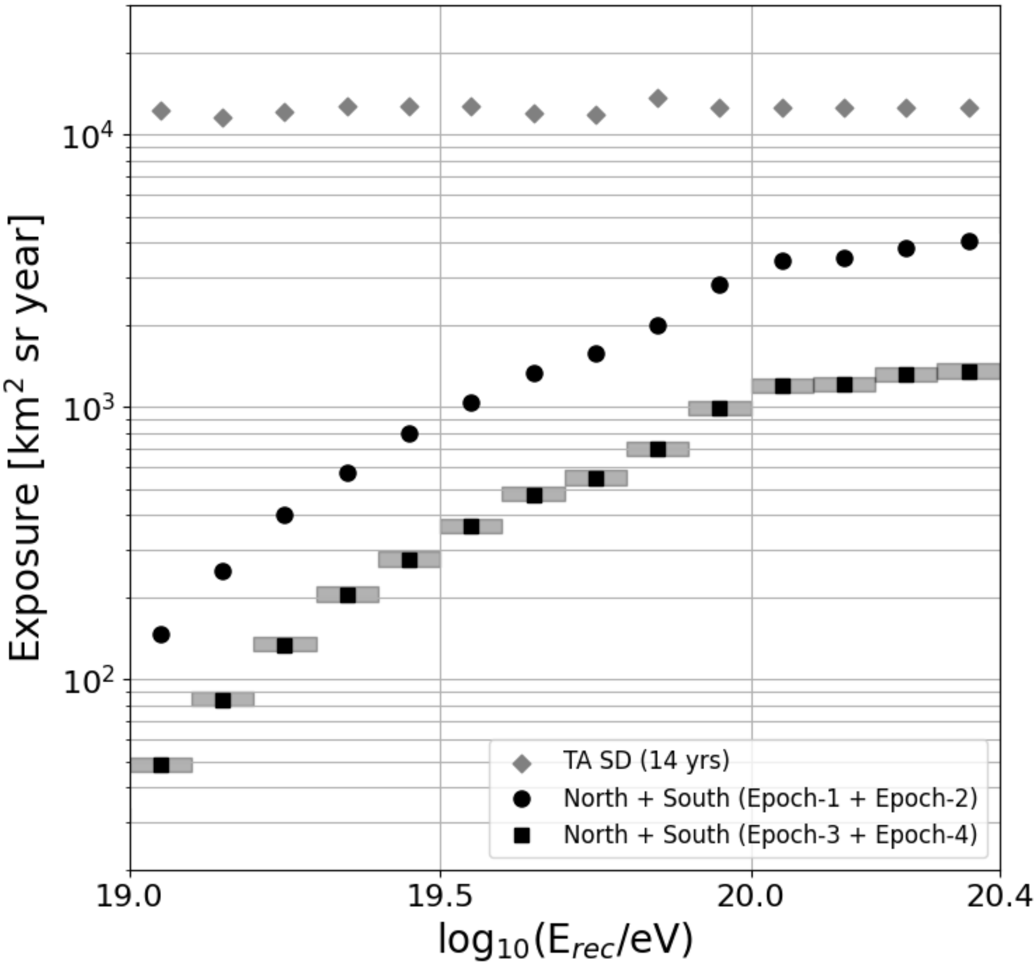

FIGURE 4.23: The exposure of the TA×4 (black circles for the period without the inter tower trigger and black squares for the period with the partial inter-tower trigger) and the TA SD for 14 years of the observational period [91] as a function of the reconstructed energy.

4.5 Summary and data set used in the following analyses

The 257 TA×4 SDs were additionally deployed with 2.08 km spacing on the northern and southern sides of the TA SD array in 2019. The TA×4 SD North and South arrays started regular observation in October 2019. The partial inter-tower trigger was implemented in November 2022, and the full inter-tower trigger was implemented on November 23rd, 2023. In the first three years of the observation without the inter-tower trigger (Epoch-1 and Epoch-2), the six sub-arrays operated independently.

In this work, we present the analysis results of the UHECR energy spectrum using the data of Epoch-1 and Epoch-2 in Chap. 7. The future prospects, including the periods with the inter-tower trigger, are given in Chap. 9.

Chapter 5

Monte Carlo simulation of the TA×4 surface detectors

We use a Monte Carlo (MC) simulation software, which was developed for the TA SD [92], to calculate the aperture of the TA×4 SD array, develop the energy estimation, and determine event selection criteria. The MC simulation comprises air shower simulation, detector response, and trigger simulation. The MC simulation software for the TA×4 SD is basically the same as the original one. However, the following are different:

- The time window of the Level-2 trigger (TA SD: 8 μs, TA×4 SD: 14 μs),
- The configuration of SDs,
- The linearity of the PMT,
- The hadronic interaction model used in the shower generation (TA SD: QGSJET II-03, TA×4 SD: QGSJET II-04).

In this section, the details of the MC simulation software are described first. Then, the generated MC event set and the weighting technique are described.

5.1 Air shower generation

Firstly, we simulate air showers with CORSIKA (COsmic Ray SImulations for KAscade) program [78]. The CORSIKA can simulate hadronic interactions and electromagnetic interactions of particles in an air shower with given interaction models, and it can track trajectories of all particles in the air shower up to a given observational level. For the simulation of the TA×4 SDs, we use distributions of the air shower particles at the detector level. Specifically, the arrival position at the detector level, particle type, zenith angle, and energy of all the air shower particles are what we use for the successive detector simulations.

We used QGSJET II-04 [61] and FLUKA [93] as hadronic interaction models for $E > 80$ GeV and $E < 80$ GeV, respectively, and EGS4 [94] as the electromagnetic interaction model in the air shower simulation. The energy range generated goes from $10^{17.5}$ eV up to $10^{20.5}$ eV, and 160 to 180 showers are generated for each $\Delta \log_{10}(\mathrm{E/eV}) = 0.1$ bin (totally 31 energy bins). The zenith angles (θ) are simulated following a $\sin\theta\cos\theta$ distribution at the detector level. The $\sin\theta$ denotes the isotropy of cosmic rays arriving at the earth, and $\cos\theta$ means that a flat SD array has a smaller area by a factor of $\cos\theta$ when viewed from cosmic rays arriving at a zenith angle of θ. Therefore, the zenith angle distribution of $\sin\theta\cos\theta$ means the isotropic arrival direction of cosmic rays seen by the SD array. The primary particles generated for this study are all protons. Table 5.1 summarizes the input parameters of air showers generated by CORSIKA.

5.1.1 Thinning method

The UHECR-induced air shower simulation requires vast computer power and calculation time. To reduce the required computation time, a technique called *thinning* [95] has been used. The thinning does not track all particles but tracks representative particles and assigns weights to them to account for the removed particles to reduce the calculation time. The left figure in Fig. 5.1 shows a schematic illustration of the thinning method. In the thinning method, air shower particles with energies below a thinning factor given by a user, multiplied by the primary cosmic ray energy, are grouped as the weighted particle at every interaction probabilistically. In this study, the thinning factor is 10^{-6}. It is the same as the simulation of the TA SDs.

After the air shower generation with the thinning method, the trajectories of the air shower particles are restored by a technique called the *dethinning* method. The right figure in Fig. 5.1 shows a schematic illustration of the dethinning method. In the dethinning method, the weighted particles are smeared into particles with the number of the weight. The energies of the restored particles follow a Gaussian distribution averaging the energy of the weighted particle, and the direction follows a Gaussian distribution centered on the trajectory of the weighted particle. The parameters of the Gaussian distributions are chosen so that air showers generated with the thinning-dethinning method reproduce air showers without the thinning approximation. Figure 5.2 shows that the lateral distributions of the energy deposition of the air shower particles agree between thinned-dethinned air showers and non-thinned air showers [92]. In addition to the lateral distributions, the agreements of the energy spectra of air shower particles, their number density, and their arrival time distributions are reported in [96]. The comparisons were tested up to 60° of the zenith angle of the primary cosmic rays. Therefore, we can use the thinning-dethinning method in air shower simulation as an approximation up to 60° of the zenith angle. In the air shower simulation for the TA×4 SDs, the thinning-dethinning method is used.

TABLE 5.1: The summary of CORSIKA inputs for this study.

Parameter	**Description**
Primary particle	proton
Energy E_{gen}	From $10^{17.5}$ eV to $10^{20.5}$ eV with $\Delta \log_{10}(E_{\mathrm{gen}}/\mathrm{eV}) = 0.1$ intervals
Zenith angle θ	θ [deg] $\in [0, 60]$, isotropic distribution
Azimuthal angle ϕ	ϕ [deg] $\in [0, 360]$, isotropic distribution
Number of air showers	from 160 to 180 for each energy bin $(\Delta \log_{10}(E_{\mathrm{gen}}/\mathrm{eV}) = 0.1)$
Hadronic interaction model	QGSJET II-04 (E > 80 GeV), FLUKA (E < 80 GeV)
Electromagnetic interaction model	EGS4
Thinning factor	10^{-6}

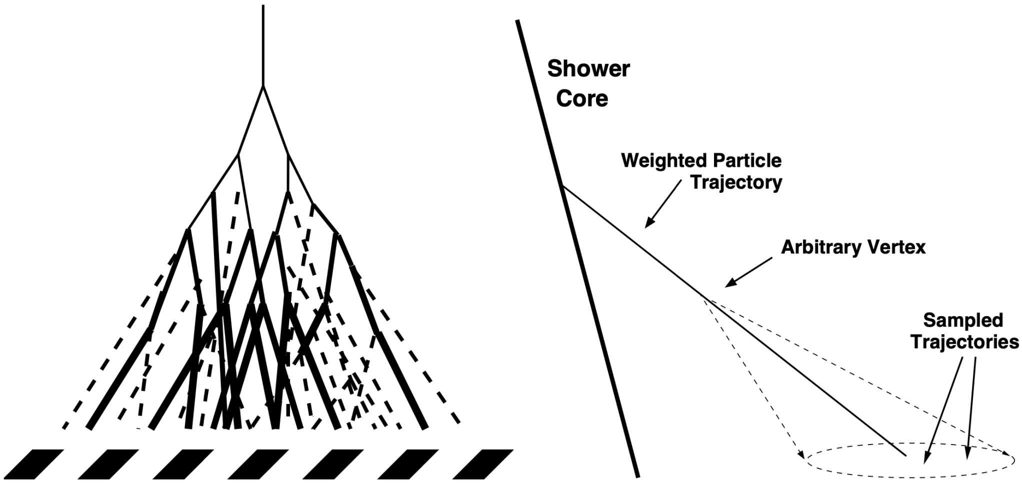

FIGURE 5.1: (Left) Schematic view of the thinning method, taken from [97]. The dashed lines represent the discarded particles, and the solid lines represent the weighted particles, where the thickness of the lines corresponds to the weight of the particles. (Right) The schematic view of the dethinning method is taken from [96].

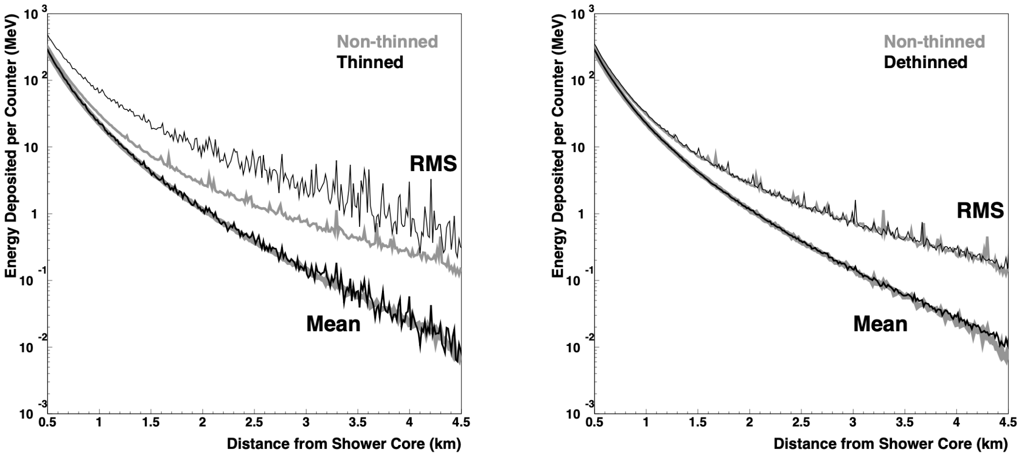

FIGURE 5.2: The mean and root mean square of energy deposition by the air shower particles as a function of lateral distance for a non-thinned shower (black thin lines in both figures), thinned shower with 10^{-6} as the thinning factor without dethinning (gray thick lines in the left figure), and thinned-dethinned shower (gray thick lines in the right figure) [92].

5.2 The Monte Carlo simulation for the TA×4 surface detectors

The next step of the simulation is detector response. This step consists of three parts: (1) calculation of energy deposition on SD (Sec. 5.2.1), (2) conversion from the energy deposition waveform to FADC value waveform (Sec. 5.2.2), and (3) trigger simulation (Sec. 5.2.3).

5.2.1 (1) Energy deposition

At first, the lateral distribution of the air shower particles at the detector level is spatially divided into 2800×2800 tiles each with a 6-meter × 6-meter square, and temporally into 20 ns time bins. One SD is located at the center of each tile (see Fig. 5.3), and energy depositions on both scintillator layers of the SD are calculated for each tile. Figure 5.4 shows the structure of the SD in the GEANT4 simulation [98]. We use detector response tables, which were developed using the GEANT4 package for the TA SD [97], to calculate the energy depositions. The detector response table was developed for each particle type (γ, $e^{\pm}$, $\mu^{\pm}$, p, n, and $\pi^{\pm}$), energy, and zenith angle as follows:

1. Sample random point (X, Y) in the square tile and random azimuthal angle (Fig. 5.3).
2. Generate the particle trajectory with the zenith angle θ, azimuthal angle ϕ which passes (X, Y) point at the ground of the tile.
3. Simulate the particle interaction with all of the material shown in Fig. 5.4 using the GEANT4 package and store energy deposit (from the initial particle and secondary particles) on the upper and lower scintillator layers.
4. Repeat the above procedures for 1.2×10^6 times.

The energy bins of the detector response tables are from $10^{4.7}$ eV to 10^{11} eV with $\Delta \log_{10} E = 0.1$ intervals for γ, from 10^6 eV to $10^{10.9}$ eV for $\pi^{\pm}$, and from 10^6 eV to 10^{11} eV for $e^{\pm}$, $\mu^{\pm}$, p, and n. The bin of the zenith angle is from $\sec\theta = 1.0$ to $\sec\theta = 4.0$ with $\Delta(\sec\theta) = 0.5$ intervals. Figure 5.5 shows examples of the detector response tables.

The tables are probability functions. We calculate the energy depositions on the upper and lower scintillator layers of the SD located at the center of each tile in the following procedure:

1. Choose the detector response table according to the type, energy, and zenith angle of the incident particle.
2. Generate a random number and choose the pair of values from the table according to the generated random number. The chosen pair of values is the pair of energy deposits for the upper and lower layers by the incident particle.
3. Repeat the above procedures for all incident particles in the tile.

Figure 5.6 shows an example of the energy deposition by an air shower of $10^{19.5}$ eV proton with zenith angle of 7.7°. The left figure in Fig. 5.7 shows an example of the energy deposition waveform of a tile.

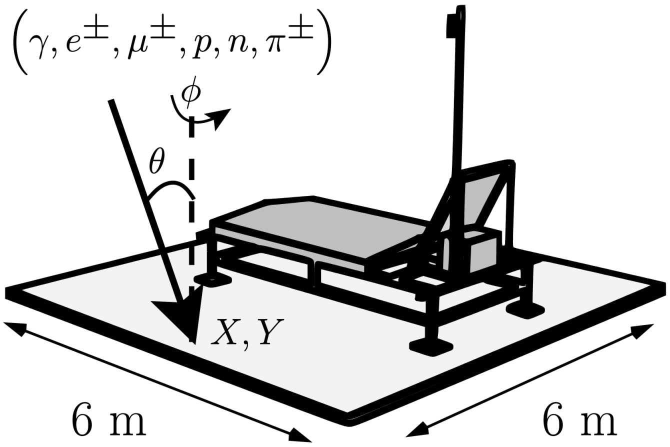

FIGURE 5.3: Schematic view of the tile of the detector response simulation, taken from [97].

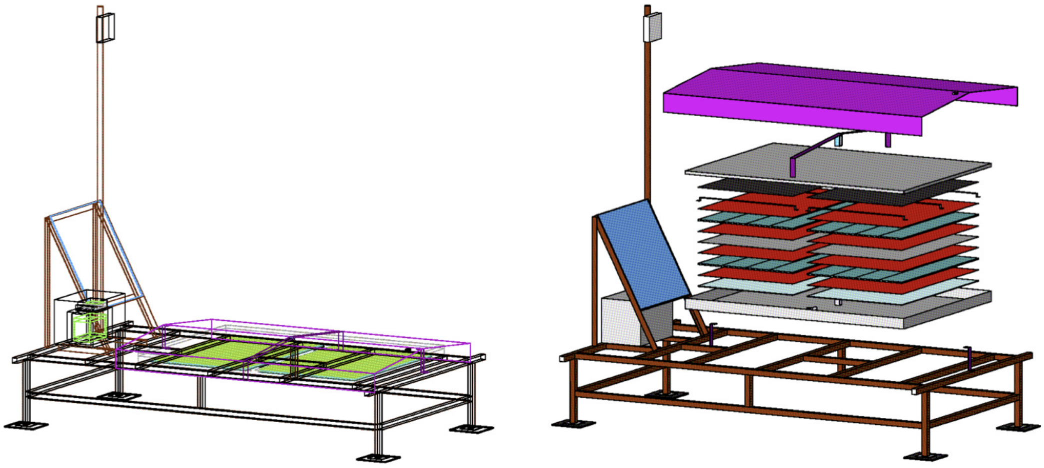

FIGURE 5.4: The SD structure in the GEANT4 simulation, taken from [99].

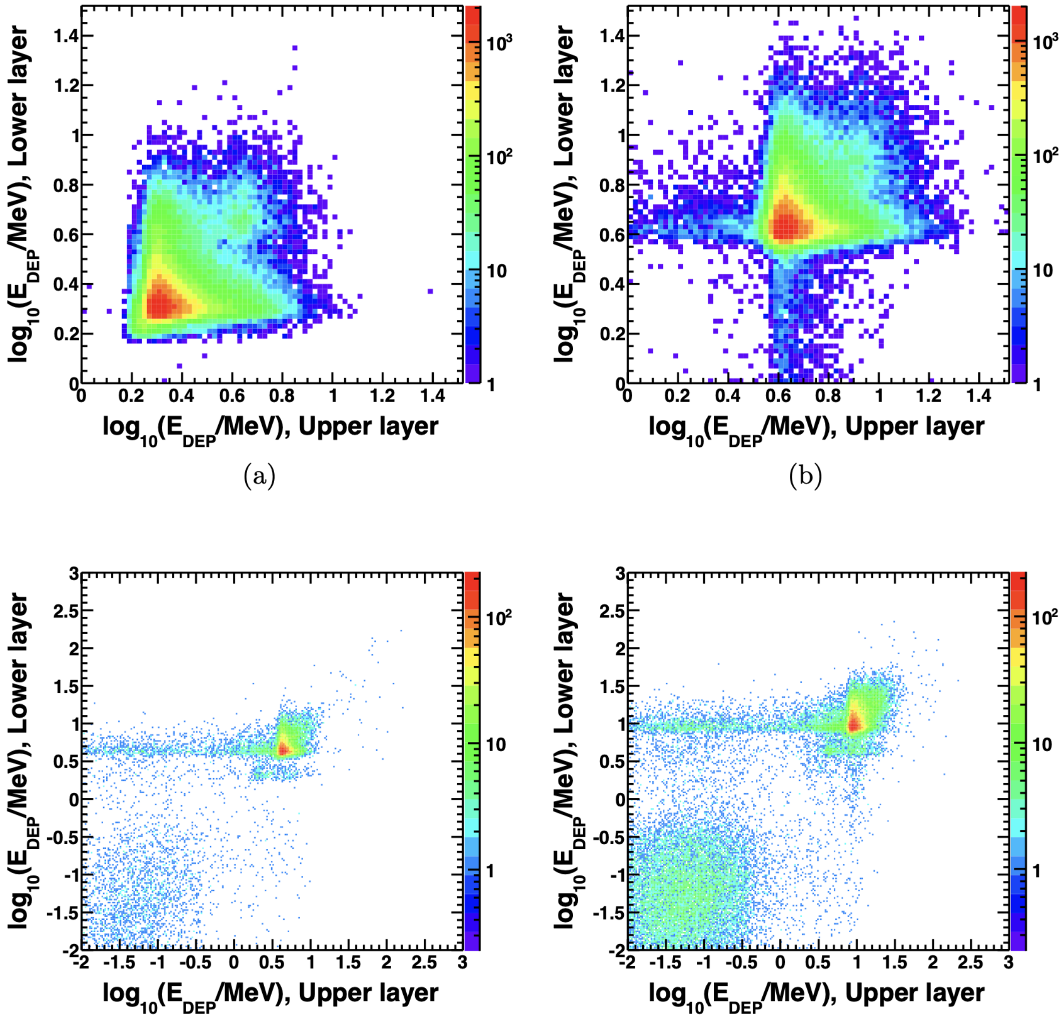

(a) (b)

(c) (d)

FIGURE 5.5: Examples of the detector response tables, taken from [97]. The x-axes and y-axes are energy deposition on the upper and lower scintillator layers, respectively. The z-axes shown by colors represent frequency. (a): μ^+, $\theta = 0^\circ$, $E = 1$ GeV, (b): μ^+, $\theta = 60^\circ$, $E = 1$ GeV, (c): γ, $\theta = 0^\circ$, $E = 1$ GeV, and (d): γ, $\theta = 60^\circ$, $E = 1$ GeV.

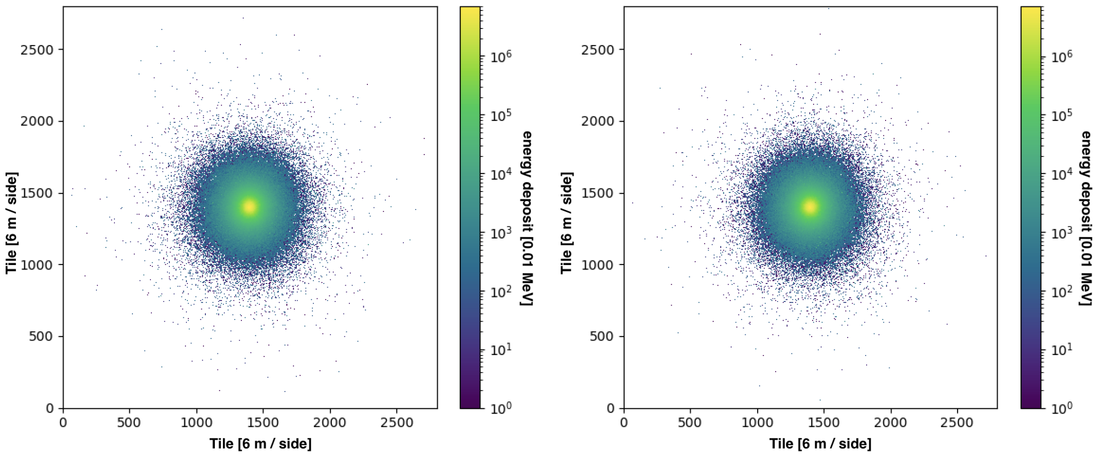

FIGURE 5.6: An example of lateral distribution of energy deposition on scintillator layers by an air shower of $10^{19.5}$ eV proton with zenith angle of 7.7°. The left and right figures correspond to the upper and lower scintillator layers, respectively. The color of each tile represents time-integrated energy deposition.

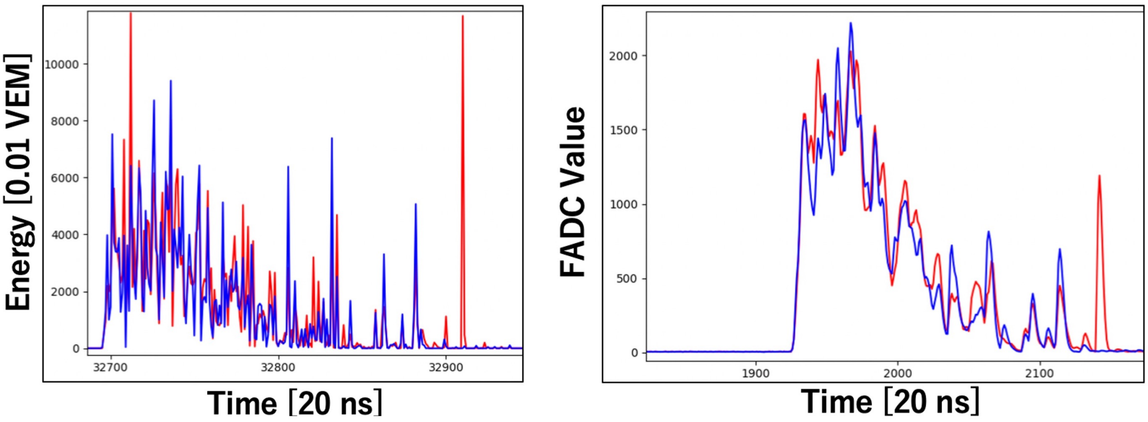

FIGURE 5.7: An example of a waveform in the MC simulation. (Left) The energy deposit waveform. (Right) The FADC count waveform which is converted from the left figure considering the calibration data of the corresponding SD. See Sec. 5.2.2 for details of the conversion. The blue and the red lines indicate the upper and lower layers, respectively.

5.2.2 (2) Conversion from the energy deposition to FADC value waveform

The energy depositions on the scintillator layers are converted to FADC count waveforms considering actual detector status, such as PMT gain and pedestal.

Assignment of the SD array configuration and determination of the azimuthal angle and the core position of the air shower

At first, we assign the configuration of the SD array to the MC simulation to consider the actual detector status. By selecting tiles properly, we can simulate any SD array configurations (with 6 m spatial resolution). In this step, the azimuthal angle and the core position of the air shower can be varied by rotating and moving the array in parallel with respect to the tiles. In our simulation, the generated air showers are reused many times (for energies greater than $10^{18.5}$ eV, about 50×[months of the simulated period] times) to reduce calculation time and avoid storage of computers.

Conversion to FADC counts using calibration data taken from the real SDs

After the assignment of the array configuration, we have a set of selected tiles where energy deposition per 20 ns on scintillator layers is assigned. We assign the calibration data from the real SDs, summarized in Tab. 5.2, to the corresponding tile. The calibration data is summarized for each 10-minute time bin, allowing the detector response simulation that reflects actual SD conditions with a 10-minute time resolution. After choosing the time and assigning the corresponding calibration data to the tiles, the energy deposition is converted to the FADC counts in the upper and lower layers as follows;

1. Add energy deposit due to random atmospheric muon whose rate follows the Level-0 trigger rate of the TA SDs to the original energy deposition in the tile file. The total energy deposition is smeared by a Poisson distribution, which describes the fluctuation of the photo-electrons in the PMT. The non-linearity of the PMT is simulated in the TA SD simulation. On the other hand, the non-linearity is not simulated in the TA×4 SD simulation since the PMTs used for the TA×4 SDs have good linearity up to the maximum FADC value.

2. Convert energy deposit to FADC counts using the information of the 1-MIP peak of the SD and add pedestal which follows a Gaussian distribution whose mean value and standard deviation follow the mean and the standard deviation of the pedestal, respectively, in the calibration data of the corresponding 10 minutes time bin.

3. Convolute the FADC counts S_i with a response function of the electronics R_i, where i denotes the index of the time bin (Fig. 5.8). The convoluted FADC counts $\tilde{S}_i$ is described as $\tilde{S}_i = \Sigma_{j=0}^{11} S_{i-j} R_j$.

4. Consider the saturation. If the FADC counts in a time bin exceed 4095, the FADC counts are set to 4095.

The right panel in Fig. 5.7 shows an example of FADC count waveform, which is converted from energy deposition waveform (the left panel in Fig. 5.7) by the above procedures.

TABLE 5.2: The parameters in the calibration data used in the SD simulation.

Index	Parameter name	Description
0	ta_period	time from 17th April 2008 (1bin = 10 minutes)
1	detector index	detector index
2	dontUse	detector status
3, 4	mevpoisson	conversion factor from energy deposition to photo-electrons in upper (lower) layer
5, 6	one_mev	conversion factor from energy deposition to FADC counts in upper (lower) layer
7, 8	mip	single muon peak in upper (lower) layer
9, 10	fadc_ped	average of pedestal in upper (lower) layer
11, 12	fadc_noise	standard deviation of pedestal in upper (lower) layer
13, 14	pchped	peak of pedestal in upper (lower) layer
15, 16	lpchped	left side half width at half maximum for pedestal in upper (lower) layer
17, 18	rpchped	right side half width at half maximum for pedestal in upper (lower) layer
19, 20	mftndof	degree of freedom of single muon peak fitting in upper (lower) layer
21, 22	mftchi2	χ^2 of single muon peak fitting in upper (lower) layer
23	site	the sub-array to which the SD belongs
24, 25	sat	maximum linearity range of PMT in an upper (lower) layer, which is 4095 for the TA×4 SD

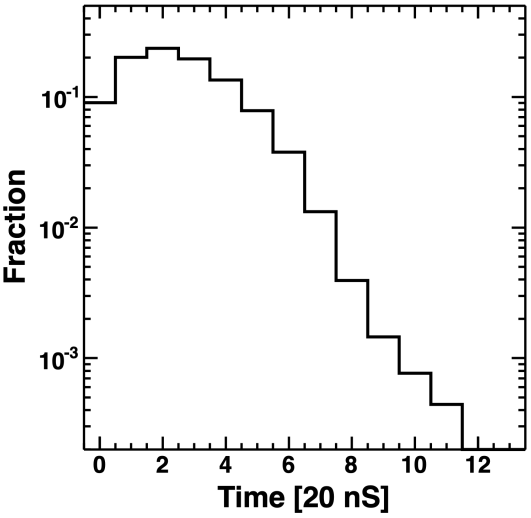

FIGURE 5.8: The response function of the SD electronics R_i, taken from [97]. The FADC counts in one time bin are smeared to 12 consecutive bins.

5.2.3 (3) Trigger simulation

At last, the trigger simulation is performed. The trigger algorithm is the same as the SD-self trigger described in Sec. 4.2.3.

As described in Sec. 4.2.3, the partial inter-tower trigger has worked since 1st November 2022. However, the whole TA×4 North (or South) SD array was treated as one sub-array in the MC simulation. It means that the trigger system in the MC simulation is the full inter-tower trigger, not the partial trigger. Implementing the partial inter-tower trigger on the MC simulation has not yet been done. Therefore, we have to estimate the performance of the partial inter-tower trigger from the MC simulation in which the full inter-tower trigger is implemented. The estimation is described in Sec. 7.2.2.

After the trigger simulation, we have an MC event set in which the input parameters of the simulation, such as energy and arrival direction of a primary cosmic ray, and outputs, such as FADC count waveforms of hit SDs, are stored. Not-triggered events are also recorded in the MC event set so that we can calculate the efficiency of the SD array.

The data format of the MC event sets is the same as that of the observed event sets. Therefore, the exact reconstruction program can be used for both event sets.

5.3 Generated MC event sets

We performed the MC simulation for the period before and after the implementation of the inter-tower trigger according to the observation period to be analyzed. Table 5.3 and Tab. 5.4 summarize the generated condition of the MC event sets. Figure 5.9 and Fig. 5.10 show a 2-dimensional thrown core position histogram for each sub-array and TA×4 North (South) array, respectively. Outside the thrown region, the trigger efficiency is $\sim$ 0% at $10^{20.5}$ eV, which is the maximum energy generated in the MC simulation.

TABLE 5.3: The area in which the MC events are generated (shown in Fig. 5.9) and the observational period for each sub-array before implementation of the inter-tower trigger.

Sub-array	**Area: A_{gen} [km^2]**	**Time period (days: T)**
KM	330.0	8th Oct. 2019 to 31st Oct. 2022 (1120)
DM	251.3	26th Oct. 2019 to 31st Oct. 2022 (1102)
SN	486.4	8th Oct. 2019 to 31st Oct. 2022 (1120)
BF	418.0	4th Nov. 2019 to 31st Oct. 2022 (1093)
SC	283.0	8th Oct. 2019 to 31st Oct. 2022 (1120)
SR	344.9	8th Oct. 2019 to 31st Oct. 2022 (1120)

TABLE 5.4: The areas where the MC events are generated (shown in Fig. 5.10) and the observational periods for the TA×4 North SD array and the TA×4 South SD array after implementing the inter-tower trigger.

Array	**Area: A_{gen} [km^2]**	**Time period (days: T)**
TA×4 North	1023	1st Nov. 2022 to 31st Jul. 2023 (273)
TA×4 South	898.0	1st nov. 2022 to 31st Jul. 2023 (273)

The validation of the MC simulation by comparing parameters of the MC events and the observed events is described in Sec. 7.2.

5.3.1 Weighting events according to the cosmic ray energy spectrum

The energy distributions of the generated MC event sets (the right panel of Fig. 5.11) do not follow the cosmic ray energy spectrum. In the previous TA SD analysis [97], the generated events were thinned out so that the energy distribution followed the energy spectrum measured by the HiRes experiment [18]. On the other hand, a weighting method was developed alternatively for the TA×4 SD simulation. In the weighting method, no event is thinned out, but weight is assigned to each event according to their energy E_{gen}. This weighting method has two advantages: (1) we can simulate any energy spectra as an input; hence, analyses less dependent on spectral assumptions are possible, such as the forward-folding method described in Sec. 7.3.1. (2) The number of MC events can be maintained, especially in the highest energy region. Figure 5.11 shows the simulated energy distributions before and after weighting, assuming the energy spectrum measured by the TA SD [90] as an input spectrum.

Since we know the aperture of the generated cosmic rays, we can calculate the number of events expected to arrive at an SD array in a certain observational period under a particular cosmic ray energy spectrum by weighting events properly. We can also calculate the number of events expected to be observed by the SD array in the observational period (the right panel in Fig. 5.11).

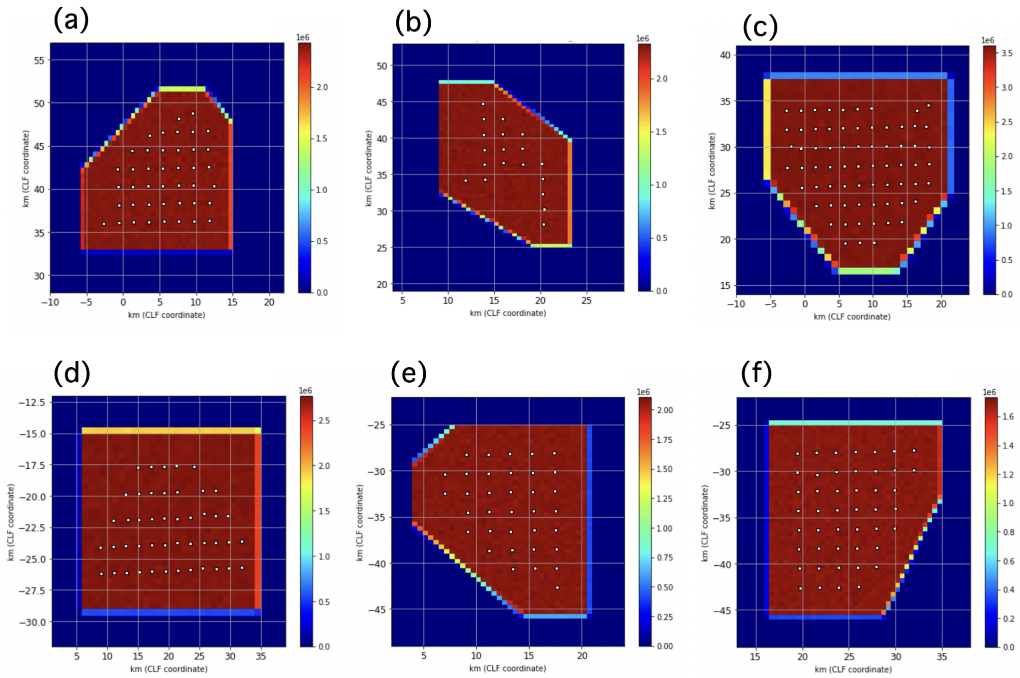

FIGURE 5.9: Thrown core position two-dimensional histograms for (a): KM, (b): DM, (c): SN, (d): BF, (e): SC, and (f): SR sub-arrays. The white squares represent SDs. The color indicates the number of events in the corresponding bin.

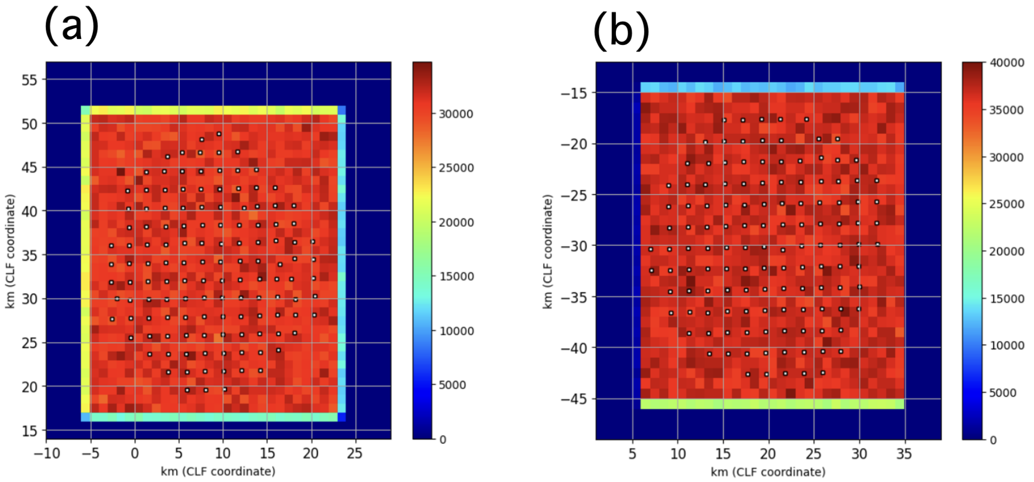

FIGURE 5.10: Thrown core position two-dimensional histograms for (a): TA×4 North and (b): TA×4 South. The white squares represent SDs. The color indicates the number of events in the corresponding bin.

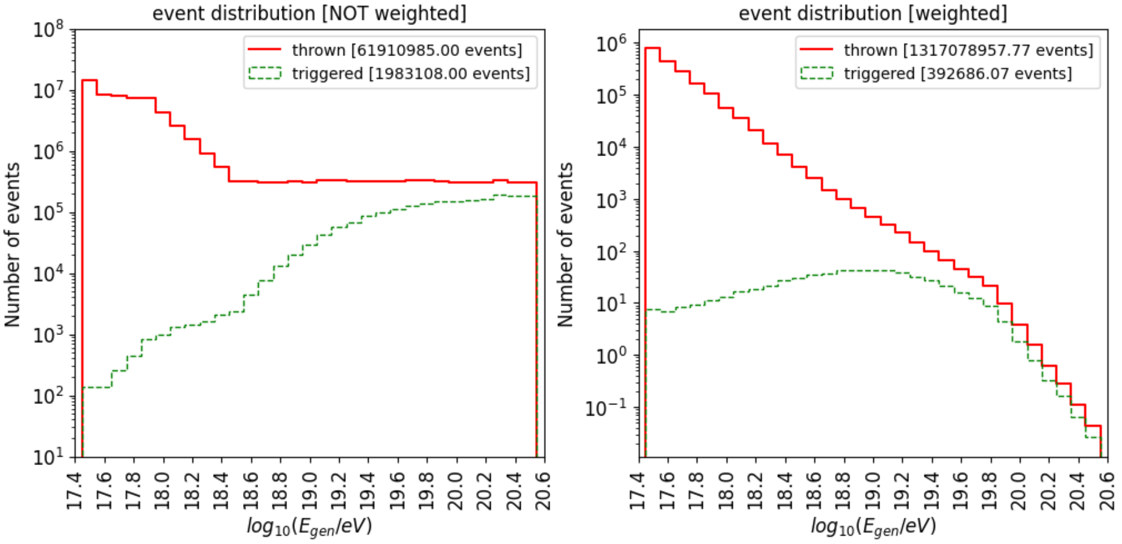

FIGURE 5.11: (Left) The number of events generated by the MC simulation for the SN sub-array for three years of observational period in each energy bin. The red solid histogram indicates the thrown events, including both triggered and not-triggered events in the MC simulation, and the green dashed histogram indicates the triggered events. The thrown area is shown in the figure (c) in Fig. 5.9. (Right) The number of events expected to come to the SN sub-array for three years of observation in each energy bin, assuming the cosmic ray energy spectrum measured by the TA SD. The distributions are calculated by weighting the original distributions in the left figure.

Chapter 6

The reconstruction of air shower events

This section describes the event reconstruction methods for the TA×4 SD array. The signal process and the reconstruction method are the same as the TA SD [97]. The event selection criteria and the energy estimation table are newly developed for the TA×4 SD array in this study.

At first, the signal is extracted for each triggered SD, and the hit timing and the signal size are determined (Sec. 6.1). Second, bad-status SDs and SDs which only record accidental muons are excluded (Sec. 6.2). Thirdly, the event reconstructions are performed; the geometry fit (Sec. 6.3.1) determines the geometry of the air shower from the hit timing of the SDs, and the lateral distribution fit (Sec. 6.3.2) determines the lateral distribution of the air shower particle density. Finally, the primary energy is determined from $S800$, which is the signal density at 800 m from the air shower axis, and the zenith angle using a look-up table developed for the TA×4 SD array (Sec. 6.4).

The resolution of the energy and the arrival direction of the TA×4 SD array are shown in Sec. 6.6.

6.1 Signal process

6.1.1 Signal extraction

An event observed by the TA×4 SD array consists of FADC waveforms with their time stamps as described in Sec. 4.3.2. To reconstruct the observed air shower event, the signal extraction is performed for each waveform recorded in each SD at first in the following procedures;

1. Scan FADC counts with 4-time bins (= 80 ns) width. If all of the 4-time bins exceed 5σ (1σ is the root mean square of the pedestal per 1-time bin) in both upper and lower layers, the signal is regarded as starting. The first time bin is called the *leading edge* of the signal. When FADC counts in all of the scanned 4-time bins are no longer above 5σ, the signal is considered to be over, and the first time bin of the 4-time bins is set as the end of the signal. Figure 6.1 shows an example of the signal extraction.

2. Repeat the above procedure until the end of the waveform.

After the signal extraction, an FADC count waveform recorded by an SD would be separated into multiple signals. If a triggered SD consists of multiple waveforms and the leading edges of the waveforms are separated by more than 50 time bins (= 10 μs) in both upper and lower layers, the waveforms are considered different signals. Otherwise, the waveforms are considered to be the same signal.

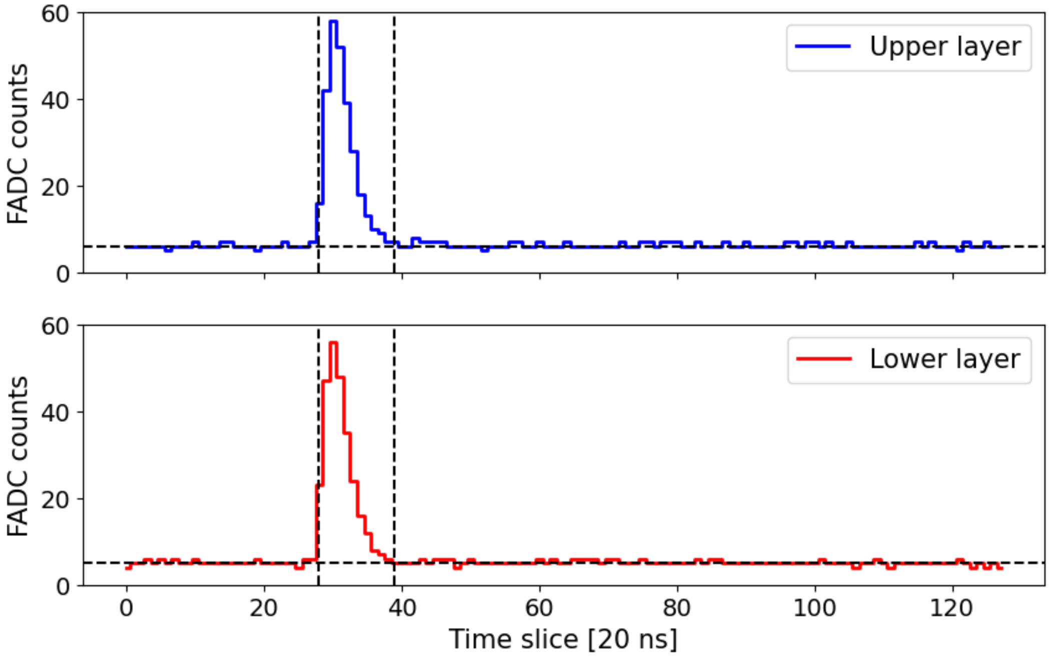

FIGURE 6.1: An example of the signal extraction. The upper and lower panels show waveforms of the upper and lower layers, respectively. The left vertical dashed line indicates the leading edge of the signal. The right vertical dashed line indicates the end of the signal. The horizontal dashed lines indicate the pedestal level of the upper and lower layers.

6.1.2 Conversion from FADC counts to VEM

The signal size is calculated by integrating all FADC counts of the signal, subtracting the pedestal from the integration, and averaging over the upper and lower layers. The signal size in FADC counts, S_{FADC}, is then converted to the energy deposit in Vertical Equivalent Muon (VEM) by $S_{\mathrm{VEM}} = S_{\mathrm{FADC}}/[p \times \cos(35^{\circ})]$, where 35° is the mean zenith angle of random muons, and p is the fitted peak of the 1-MIP histogram at that time in the calibration data (Sec. 4.3.1).

6.2 Classification of signals

After the signal process, the event consists of a set of signals, each of which consists of the hit timing and the energy deposition in VEM. The signals are then classified to exclude accidental backgrounds that can not be used for the event reconstructions.

6.2.1 Excluding signals of bad SD

A bad SD selection is performed according to the monitor data described in Sec. 4.3.1. If any of the following conditions are satisfied, the signal is not used in the event reconstruction;

- The SD does not have GPS information, or the error of GPS clock count is larger than 100 ns.
- The average of the pedestal histogram (integration of 8 time bins) is smaller than 1 FADC count or larger than 20 counts.
- The peak of the MIP histogram is smaller than 12 FADC counts or larger than 500 FADC counts.
- The χ^2/ndof of the MIP peak fit is greater than 4, or the fit failed.
- The Level-0 trigger rate is smaller than 10 Hz or higher than 1000 Hz.

6.2.2 Excluding random muon signals

The second selection excludes random muon signals, which are not components of a UHECR-induced air shower. The selection procedures are as follows;

1. Exclude signals whose signal sizes of both upper and lower layers are smaller than 1.4 VEM.
2. Group into sets of signals whose SD positions are continuous in horizontal, vertical, and diagonal directions. Exclude signals not belonging to the largest set of signals (*space cluster*).
3. Calculate the hit time differences of pairs of adjacent signals in the *space cluster* and group them into time clusters, in which the time difference of any adjacent signals does not exceed l/c, where c is the speed of light, and l is the distance between the SDs. Exclude signals not belonging to the largest set of signals (*space-time cluster*).

The excluded signals in the above procedures are regarded as random muon signals and are not used in event reconstructions. Figure 6.2 shows an example a result of the signal exclusion.

If an SD has multiple signals in the space-time cluster, they are combined by summing the signal sizes. After the combination, each SD has a set of signal density and the hit timing.

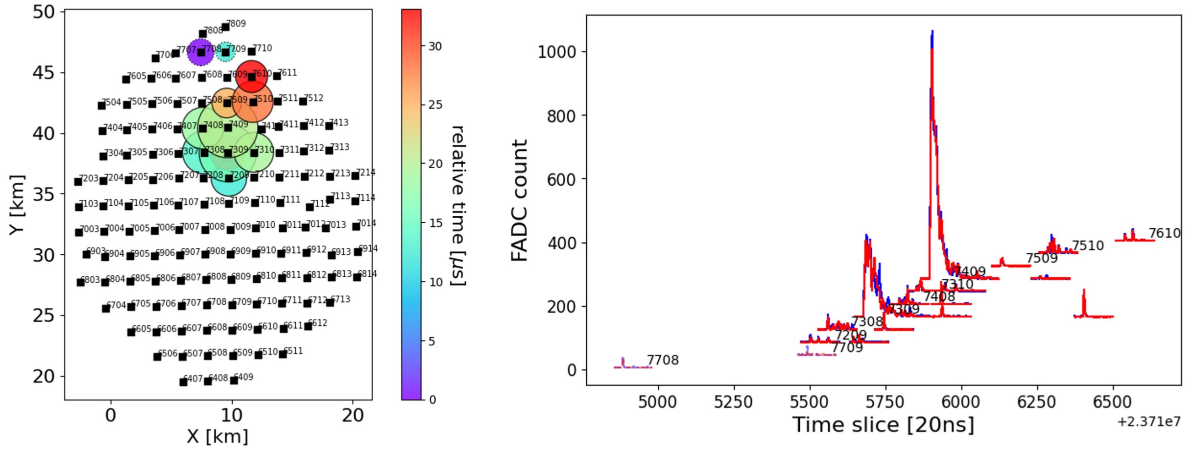

FIGURE 6.2: An example of the signal exclusion. (Left) The footprint of the air shower. The size and the color of the circle indicate the signal size and the hit timing of the corresponding SD, which recorded the signal by issuing the Level-0 triggers. The dashed circles (DET7708 and DET7709) indicate signals which are judged to be due to random muons since these waveforms are not in the *space-time cluster* of the air shower event. (Right) Triggered waveforms, consisting of 128 time bins (= 2.56 μs). The waveforms of DET7708 and DET7709 (shown in light blue and red) are judged to be due to random muons.

6.3 Fitting: determination of arrival direction and lateral distribution of an air shower

Fitting is performed to reconstruct the arrival direction and energy of the primary UHECR. The fitting consists of the geometry fit (Sec. 6.3.1) and the lateral distribution fit (Sec. 6.3.2). After these fits, the combined fit is finally performed (Sec. 6.3.3). The combined fit gives the final values used as reconstruction parameters.

The coordinate used in the reconstruction is the central laser facility (CLF) frame [97]. The origin of the frame is the position of the CLF; the latitude is 39.30°, the longitude is -112.91°, and the altitude is 1370 m above the sea level. The CLF is located in the middle of the TA SD array (Fig. 3.1). Figure 6.3 illustrates the CLF frame. The X-axis of the CLF frame points toward the east, the Y-axis points toward the north, and the Z-axis points upwards. The zenith angle is the angle between the Z-axis and the arrival direction. The azimuthal angle is the angle between the X-axis and the X-Y projection of the arrival direction, measured counterclockwise with respect to the X-axis. Let θ and ϕ denote the zenith angle and azimuthal angle of the air shower, respectively.

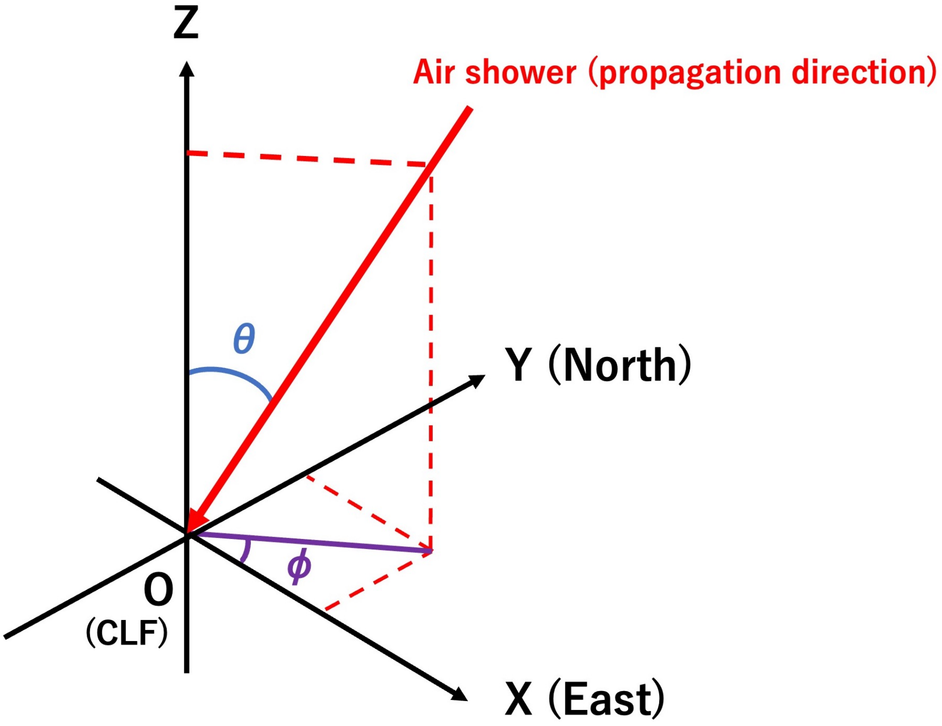

FIGURE 6.3: The central laser facility (CLF) coordinate. The origin is the position of the CLF; the latitude is 39.30°, the longitude is -112.91°, and the altitude is 1370 m above sea level. The X-axis and Y-axis point east and north, respectively. The Z-axis points upwards. The zenith angle, θ, is the angle between the Z-axis and the arrival direction. The azimuthal angle, ϕ, is the angle between the X-axis and the X-Y projection of the arrival direction of the air shower, measured counterclockwise with respect to the X-axis.

6.3.1 Geometry fit

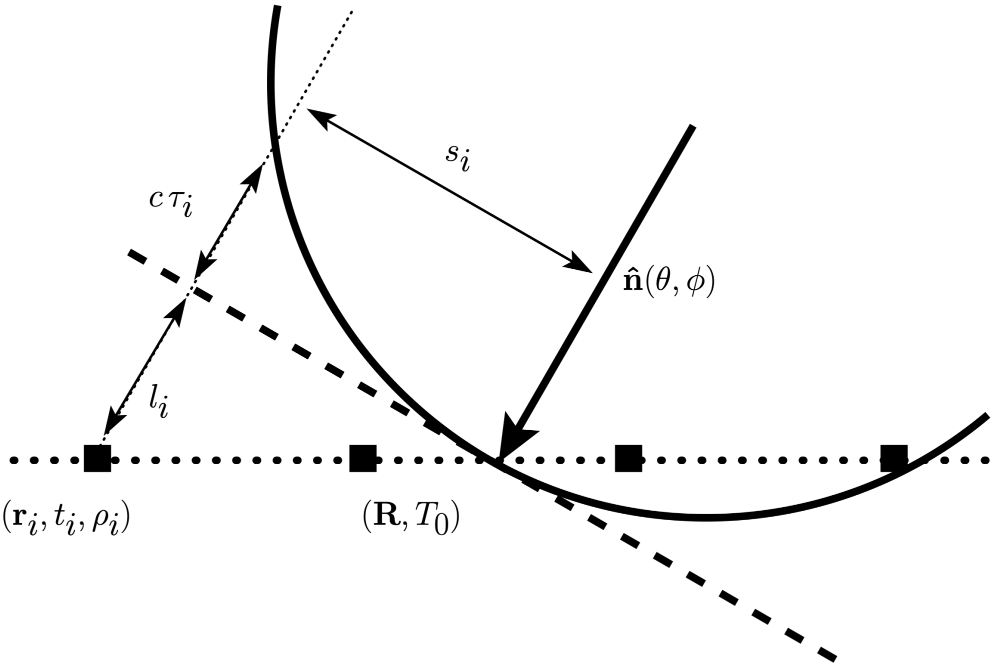

FIGURE 6.4: A schematic view of the air shower front (shown in bold line), taken from [97]. The black-filled squares represent surface detectors. **R** represents the core position of the air shower, and T_0 represents the time when the core passes through the detector level shown in the dotted line. $\mathbf{r}_i$, t_i, and ρ_i represent the position, hit time, and signal density of the i-th SD, respectively. l_i and s_i are the distance from the air shower front plane at time T_0 in shower propagation direction and the perpendicular distances from the air shower axis of the i-th SD. τ_i is the time delay due to the air shower front curvature.

The hit timing of SDs determines the geometry of the air shower: the location where the shower core hits the ground, the hit timing, and the shower core axis. Figure 6.4 shows a schematic view of the air shower front and SDs. The unit vector along the direction of the shower propagation denoted by $\hat{\mathbf{n}}(\theta,\phi)$ is expressed as

$$\hat{\mathbf{n}}(\theta,\phi) = \begin{pmatrix} -\sin\theta\cos\phi \\ -\sin\theta\sin\phi \\ \cos\theta \end{pmatrix}. \tag{6.1}$$

First, consider the simplest case where the air shower front is a plane ($\tau = 0$ in Fig. 6.4). Denoting the core position and the time when the shower core passes through the X-Y plane by $\mathbf{R} = (R_x, R_y, 0)$ and T_0, respectively, the hit timing with respect to T_0 of the i-th SD (denoted as $\Delta t_i = t_i - T_0$) is geometrically expressed as

$$\Delta t_i = \frac{(\mathbf{r}_i - \mathbf{R}) \cdot \hat{\mathbf{n}}(\theta,\phi)}{c}, \tag{6.2}$$

where $\mathbf{r}_i$ is the three-dimensional position vector of the i-th SD. The propagation speed of the shower front is the speed of light c since particles in the shower front have sufficiently large energy.

In reality, however, the shower front is not a plane. Denoting the time delay of the i-th SD due to the shower front curvature as τ_i (see Fig. 6.4), the hit timing with a plane shower front approximation (Eq. 6.3) can be modified as

$$\Delta t_i = \frac{(\mathbf{r}_i - \mathbf{R}) \cdot \hat{\mathbf{n}}(\theta, \phi)}{c} + \tau_i. \tag{6.3}$$

Modified Linsley time delay function

We use the Linsley time delay function [100] [101] modified for the TA SD [97] to describe the time delay τ:

$$\tau = a\left(1 - \frac{l}{1200\text{ m}}\right)^{1.05}\left(1 + \frac{s}{30\text{ m}}\right)^{1.35}\left(\frac{\rho}{1\text{VEM/m}^{-2}}\right)^{-0.5}[\mu\text{s}]\,, \tag{6.4}$$

$$\sigma_\tau = (1.56 \times 10^{-3})\left(1 - \frac{l}{1200\text{ m}}\right)^{1.05}\left(1 + \frac{s}{30\text{ m}}\right)^{1.5}\left(\frac{\rho}{1\text{VEM/m}^{-2}}\right)^{-0.3}[\mu\text{s}]\,, \tag{6.5}$$

where $l = \begin{pmatrix} r_x - R_x \\ r_y - R_y \end{pmatrix} \cdot \begin{pmatrix} -\sin\theta\cos\phi \\ -\sin\theta\sin\phi \end{pmatrix}$ is the distance between $\mathbf{r} = (r_x, r_y)$ and the core position along with the shower propagation direction (l_i in Fig. 6.4), $s = \sqrt{\mathbf{r}^2 - l^2}$ is the perpendicular distance between $\mathbf{r}$ and the shower axis (s_i in Fig. 6.4), and ρ is the signal density at $\mathbf{r}$. σ_τ is the uncertainty of the time delay τ.

Time fit

A set of geometry parameters (θ, ϕ, T_0, R_x, R_y, a) are determined by minimizing the following χ^2_{geom}:

$$\chi^2_{\text{geom}} = \sum_i \frac{(t_i - t_i^{\text{Fit}})^2}{\sigma_{t_i}^2} + \frac{(\mathbf{R} - \mathbf{R}_{\text{COG}})^2}{\sigma_{\mathbf{R}_{\text{COG}}}^2}. \tag{6.6}$$

In Eq. 6.6, t_i is the measured hit time of the i-th SD and $t_i^{\text{Fit}} = T_0 + \frac{(\mathbf{r}_i - \mathbf{R}) \cdot \hat{\mathbf{n}}(\theta,\phi)}{c} + \tau_i$ is the hit time of the i-th SD predicted by the time delay function (Eq. 6.5).

The hit time uncertainty $\sigma_{t_i} = \sqrt{\sigma_\tau^2 + \sigma_{\text{e}}^2}$ is a quadratic sum of σ_τ in Eq. 6.5 and the time bin width $\sigma_{\text{e}} = 20$ ns.

The second term in Eq. 6.6 is an empirical one that gives weight to the signal center of gravity position $\mathbf{R}_{\text{COG}} = \Sigma_i \rho_i \mathbf{r}_i / \Sigma_i \rho_i$ so that the core position does not diverge. $\sigma_{\mathbf{R}_{\text{COG}}} = 150$ m is the uncertainty of the signal center of gravity position. Note that the z-coordinate of the core position is fixed at the CLF elevation (=1370 m).

Excluding SDs which make fit worse

After the geometry fit is performed, one of the SDs used for the fit is removed, and the fit is performed again with the remaining SDs. If the SD's removal improves χ^2_{geom} by more than 10 compared with the fit without removal, that SD is removed. Repeat this procedure for all SDs used for the fit, and the value fitted with the remaining SDs is used as the final result of the geometry fit.

6.3.2 Lateral distribution fit

The lateral distribution of the particle density is determined after the geometry fit. The lateral distribution function modified by the AGASA experiment [102] is used for the fit:

$$\begin{aligned}\rho &= A\left(\frac{s}{91.6\,\mathrm{m}}\right)^{-1.2}\left(1+\frac{s}{91.6\,\mathrm{m}}\right)^{-\eta(\theta)+1.2}\left[1+\left(\frac{s}{1000\,\mathrm{m}}\right)^{2}\right]^{-0.6} \qquad (6.7)\\ &\qquad [\mathrm{VEM/m^2}],\\ \eta(\theta) &= 3.97-1.79[\sec\theta-1]. \qquad (6.8)\end{aligned}$$

We determine a set of parameters (A, R_x, R_y) by minimizing the following χ^2_{LDF}:

$$\chi^2_{\mathrm{LDF}}=\sum_i\frac{(\rho_i-\rho_i^{\mathrm{Fit}})^2}{\sigma^2_{\rho_i}}+\frac{(\mathbf{R}-\mathbf{R}_{\mathrm{COG}})^2}{\sigma^2_{\mathbf{R}_{\mathrm{COG}}}}, \qquad (6.9)$$

where the uncertainty of the signal density of the i-th SD is $\sigma_{\rho_i}=0.53\sqrt{2\rho_i+(0.15\rho_i)^2}$. Note that the core position is determined again by the lateral distribution fit. In the fit, SDs which satisfy the following conditions are used:

- Not saturated.
- Not excluded by the SD selection in the geometry fit (Sec. 6.3.1).
- More than 600 m away from the shower axis determined by the geometry fit.

6.3.3 Combined fit

A combined fit is performed after the geometry fit and the lateral distribution fit using the results of the previous two fittings as initial values. In the combined fit, a set of parameters (θ, ϕ, T_0, R_x, R_y, a, A) is determined by minimizing the following χ^2_{Comb}:

$$\chi^2_{\mathrm{Comb}}=\sum_i\left(\frac{(\rho_i-\rho_i^{\mathrm{Fit}})^2}{(0.82)^2\sigma^2_{\rho_i}}+\frac{(t_i-t_i^{\mathrm{Fit}})^2}{(0.82)^2\sigma^2_{t_i}}\right)+\frac{(\mathbf{R}-\mathbf{R}_{\mathrm{COG}})^2}{\sigma^2_{\mathbf{R}_{\mathrm{COG}}}}. \qquad (6.10)$$

In this work, the values obtained by the combined fit are used as the reconstructed values.

6.4 First energy estimation

When the geometry and lateral distribution of the event are successfully reconstructed, the signal density at 800 m from the shower axis $S800=\rho(800\,\mathrm{m})$ is determined using Eq. 6.7. The reconstructed parameter set ($S800$, $\sec\theta$) is then converted to the first estimated energy $E_{\mathrm{TA\times4\,SD}}$. The conversion table $f(S800,\sec\theta)=E_{\mathrm{TA\times4\,SD}}$ is generated using the MC simulation. The conversion table estimates the energy as follows:

1. Assign to $\sec\theta$ bins with respect to the reconstructed zenith angle. The bin width is $\Delta(\sec\theta)=0.02$.
2. Estimate energy by $E_{\mathrm{TA\times4\,SD}}=a_2\times(S800)^2+a_1\times S800+a_0$, where the parameters ($a_2$, a_1, and a_0) are fixed values in each $\sec\theta$ bin.

We developed a conversion table for the TA×4 SD array using an MC event set summarized in Tab. 6.1 after the event selection described in Sec. 6.5. Figure 6.5 shows the conversion table.

TABLE 6.1: The summary of the MC event set used to develop the conversion function (proton primaries).

Parameter	**Description**
Primary particle	proton
Energy E_{gen}	From $10^{18.5}$ eV to $10^{20.5}$ eV with $\Delta \log_{10}(E_{\mathrm{gen}}/\mathrm{eV}) = 0.1$ intervals
Zenith angle θ	θ [deg] $\in$ [0,60], isotropic distribution
Azimuthal angle ϕ	ϕ [deg] $\in$ [0,360], isotropic distribution
Number of air showers	$\sim$350 for each energy bin ($\Delta \log_{10}(E_{\mathrm{gen}}/\mathrm{eV}) = 0.1$)
Hadronic interaction model	QGSJET II-04 (E > 80 GeV), FLUKA (E < 80 GeV)
Electromagnetic interaction model	EGS4
Thinning factor	10^{-6}
SD array configuration	BF sub-array
Simulated period	4th Nov. 2019 to 7th Oct. 2022

This energy $E_{\mathrm{TA\times4\,SD}}$ is just the first estimation since the energy estimation method possibly has some systematic biases due to the hadronic interaction model used in the air shower simulation. Therefore, the first estimated energy E_{SD} has to be calibrated. In the case of the TA SD array, $E_{\mathrm{TA\,SD}}$ was calibrated to the energy measured by fluorescence detectors, and the scaled energy $E_{\mathrm{TA\,SD}}/1.27$ is used as the final value as explained in Sec. 3.3. However, in the case of the TA×4 SDs, there are not yet sufficient hybrid events to calibrate $E_{\mathrm{TA\times4\,SD}}$. An alternative calibration method is proposed in Sec. 7.1.

6.5 Event selection criteria

The observational data includes not only UHECR-induced air shower events but also backgrounds from random muons. Event selection is necessary to exclude such background and poorly reconstructed events. In cosmic ray observations, the migration of low-energy events to the high-energy side has a significant effect since the energy spectrum follows a power law. The determination of the event selection criteria is a compromise among the reconstruction accuracy, background rejection, and efficiency.

Due to the large detector spacing of the TA×4 SD array, the ratio of the number of triggers due to the random muon to that of UHECR-induced air shower events is higher than the ratio of the TA SD array. In particular, there is an excess in the lower energy region ($E < 10^{19}$ eV) in observation. The excess cannot be explained by the current MC simulation, which does not consider air shower events with $E_{\mathrm{gen}} < 10^{17.5}$ eV and events triggered only by random muons.

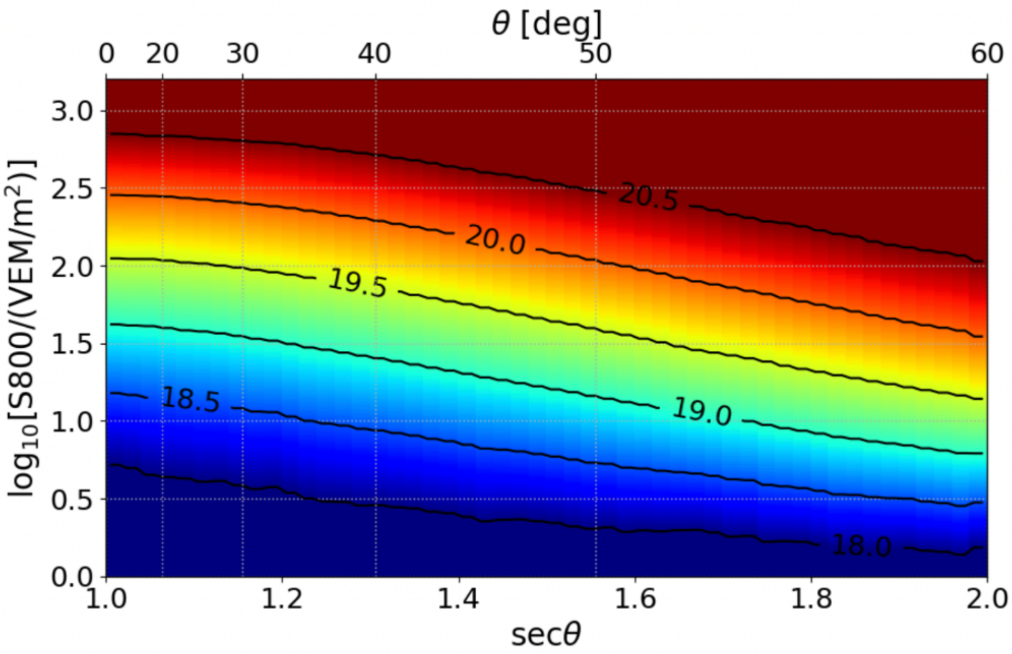

FIGURE 6.5: The energy conversion table of the TA×4 SDs. The x-axis is the secant of the reconstructed zenith angle, and the y-axis is the logarithm of $S800$. The colors indicate the energy, E. Typical values of the logarithm of E are indicated by black solid lines. The description of the MC events used to generate the table is summarized in Sec. 6.1.

Therefore, we made the following condition mandatory: the number of events in the observation and that of the MC simulation have to be consistent in two energy regions: all energies and $E_{\mathrm{TA}\times4\,\mathrm{SD}} > 10^{19}$ eV.

The event selection criteria were determined to meet the above requirements while increasing efficiency and not significantly worsening resolutions of energy and arrival direction.

We use six parameters for event selection criteria, which are the same as those used in the TA SD array [97]: (1) the number of SDs used in the fitting, (2) zenith angle, (3) relative uncertainty of $S800$: $\sigma_{S800}/S800$, (4) the distance of the shower core from the edge of the SD array, (5) the uncertainty of the reconstructed direction, and (6) reduced chi-square of the fitting. Table 6.2 summarizes the event selection criteria used in this study.

The number of events in the observation and the MC simulation is calculated for various combinations of event selections and shown in Fig. 6.7. The sets of event selections are summarized in Tab. 6.3. In the figure, the combinations of the parameters are sorted in descending order by the number of observed events for all energies (indicated by the light-blue thick line in Fig. 6.7). The figure shows that the number of events in the observation and that of the MC simulation are consistent with the event selection described in Tab. 6.2 (indicated by the vertical dashed line in the figure) or tighter selections. The figure also shows that the efficiency is kept high with the determined event selection. The detailed comparison between the observed and MC events is described in Sec. 7.2. The effects of each parameter are described in the following.

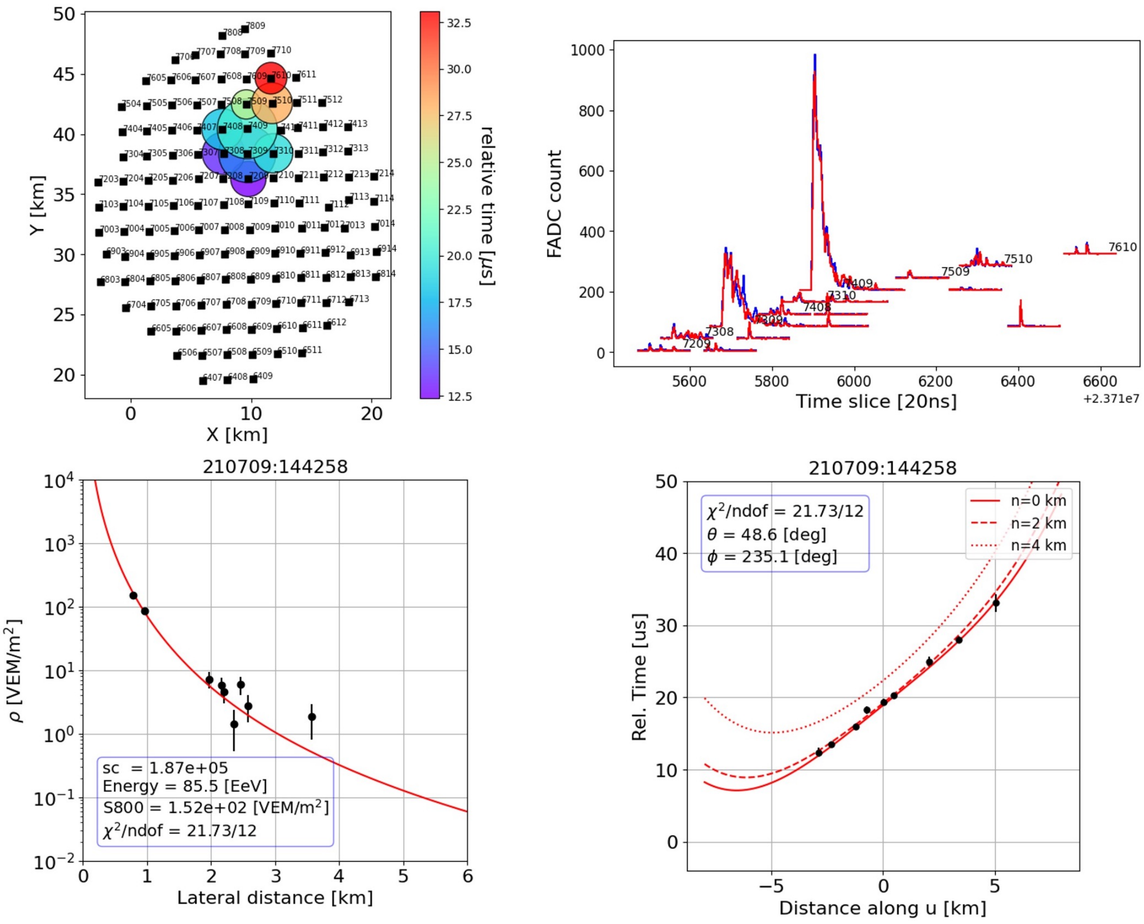

FIGURE 6.6: An example of the reconstructed event observed on 9th July 2021 in the KM sub-array. It is the same event as in Fig. 6.2. The energy is estimated to be 86.5 EeV. The zenith angle is estimated to be 48.6°. (Upper left) The footprint of the air shower. The size and the color of the circle indicate the signal size and the hit timing of the corresponding SD, which recorded the signal and was used for the combined fit. (Upper right) Waveforms are used for the combined fit. (Lower left and right) The fit results of the combined fit. The left figure shows the lateral distribution, and the right figure shows the geometry fit result. Each point indicates the SD signals.

TABLE 6.2: The event selection criteria used for this study.

Parameter	**Condition**
Number of SDs used for the combined fit (N_{SD})	$N_{\mathrm{SD}} \geq 5$
Zenith angle (θ)	$\theta \leq 55°$
Reduced chi-square of the combined fit (χ^2/ndof)	$\chi^2/\mathrm{ndof} \leq 4$
Uncertainty of the reconstructed arrival direction (σ_{dir})	$\sigma_{\mathrm{dir}} \leq 6°$
Relative uncertainty of the $S800$ ($\sigma_{S800}/S800$)	$\sigma_{S800}/S800 \leq 0.5$
Distance of the shower core from the border of the SD array (D_{border})	$D_{\mathrm{border}} \geq 400$ m

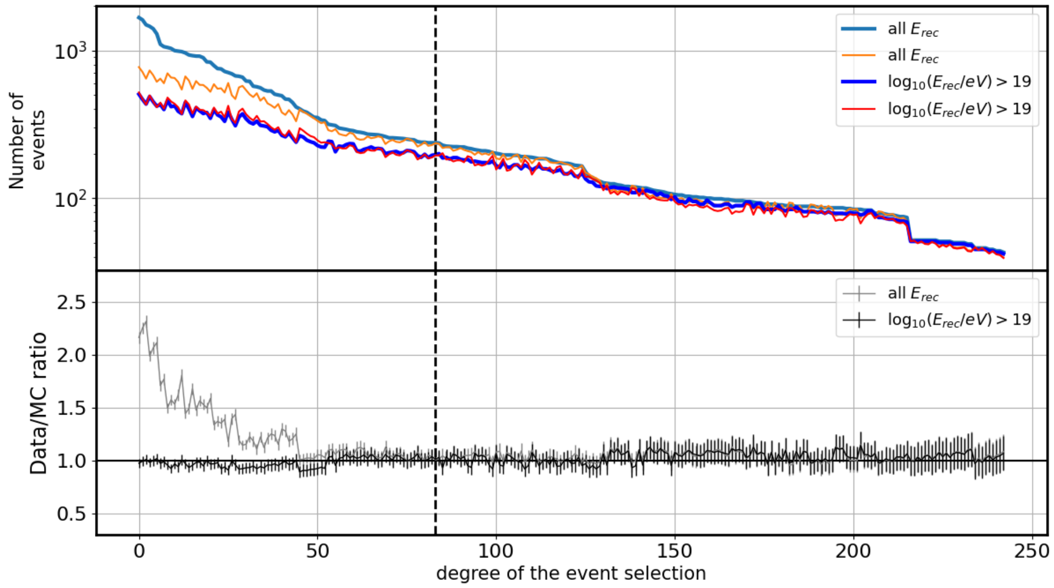

FIGURE 6.7: (Top) The number of events in the observation for all energies (energies greater than 10^{19} eV) represented by light-blue thick line (blue thick line) and that of the MC simulation for all energies (energies greater than 10^{19} eV) represented by orange thin line (red thin line). (Bottom) The ratio of the number of events in the observation to that of the MC simulation (gray for all energies and black for energies greater than 10^{19} eV). The x-axis represents the degree of the event selection, which is sorted in descending order by the number of observed events for all energies. The conditions used here are summarized in Tab. 6.3. The vertical dashed line represents the event selection used in this study (Tab. 6.2).

TABLE 6.3: The event selections used in Fig. 6.7. Totally $3 \times 3 \times 3 \times 3 \times 3 = 243$ conditions were used. In Fig. 6.7, The 243 conditions are sorted in descending order according to the number of observed events for all energies. Zenith angle selection is fixed at $\theta < 55°$. The bold values are those used in this analysis.

Parameter		**Values**
N_{SD}	$\geq$	[4, **5**, 6]
$\chi^2/ndof$	$\leq$	[5, **4**, 3]
σ_{dir} [deg]	$\leq$	[8, **6**, 4]
$\sigma_{S800}/S800$	$\leq$	[0.7, **0.5**, 0.3]
D_{border} [m]	$\geq$	[0, **400**, 800]

Number of SDs used for fit, reduced chi-square of the fit, relative uncertainty of $S800$, and uncertainty of the reconstructed arrival direction

These four parameters significantly affect the rejection of the low-energy background events. They also affect the efficiency, energy resolution, and angular resolution. The efficiency has to be decreased by more than around 30% to improve the energy resolution by more than 5% for $E_{\rm rec} > 10^{19}$ eV in quadrature.

Zenith angle

The zenith angle cut is $\theta_{\rm rec} < 55^\circ$. This criterion was determined regarding the maximum zenith angle generated by CORSIKA (up to 60°). The MC events with large zenith angle region $\theta > 60^\circ$ can not be used yet for two major reasons: (i) the validation of the thinning-dethinning method was confirmed up to $\theta = 60^\circ$ [96], and (ii) the detector response tables (described in Sec. 5.2.1) were generated up to $\sec\theta = 4.0$, which corresponds to $\theta = 75.5^\circ$.

Distance from the border

Events where a portion of the air shower was observed at the edge of the SD array tend to be underestimated in energy. The $D_{\rm border}$ selection excludes such events by selecting events whose core positions are enough inside the array. This selection directly relates to the aperture of the array.

In the case of the TA SD, $D_{\rm border} \geq 1200$ m, which corresponds to the spacing of the TA SD, is used. The TA×4 SDs, on the other hand, operated without the inter-tower trigger for the first three years, and a detector-spacing selection ($D_{\rm border} \geq 2080$ m) decreases the aperture by 60% for this period. In addition to that, the occupancy rate of the TA×4 SD for more than half of the first three years is less than 80%. Tighter $D_{\rm border}$ cuts do not always result in better energy resolutions due to bad SDs inside the array (for example, detector 7407, which had not worked until the replacement of the PMT in February 2022, is in the center of the KM sub-array).

In this study, we use $D_{\rm border} \geq 400$ m for all sub-arrays. Tighter cuts do not improve the energy resolution by more than 1%. Looser cut such as $D_{\rm border} \geq 0$ m is not used to avoid a more considerable bias toward underestimating energy. The same selection is applied for events in the period after the implementation of the inter-tower trigger in this work.

6.6 Resolutions of the energy and arrival direction

6.6.1 Energy resolution

Figure 6.8 shows histograms of $\ln\left(E_{{\rm TA}\times 4\,{\rm SD}}/E_{\rm gen}\right)$ for three energy ranges: (A) $10^{19.0}$ eV $< E_{\rm gen}/1.36 < 10^{19.5}$ eV, (B) $10^{19.5}$ eV $< E_{\rm gen}/1.36 < 5.7 \times 10^{19}$ eV, and (C) 5.7×10^{19} eV $< E_{\rm gen}/1.36$. The factor 1.36 is the energy resolution of the TA×4 SD array, discussed later in Sec. 7.1. The scaled energy $E_{\rm gen}/1.36$ corresponds to the true energy of the generated cosmic ray (see Sec. 7.1 for details). The histograms are fitted with Gaussian distributions, and the energy resolutions σ_E are evaluated by:

$$\sigma_E = \exp(\sigma_{\ln E}) - 1, \tag{6.11}$$

where $\sigma_{\ln E}$ is the standard deviation of the Gaussian fit. It is the same evaluation of the energy resolution as the TA SD array [97]. The energy resolutions are 43% for

$10^{19.0}$ eV $< E_{\rm gen}/1.36 < 10^{19.5}$ eV, 32% for $10^{19.5}$ eV $< E_{\rm gen}/1.36 < 5.7 \times 10^{19}$ eV, and 28% for 5.7×10^{19} eV $< E_{\rm gen}/1.36$.

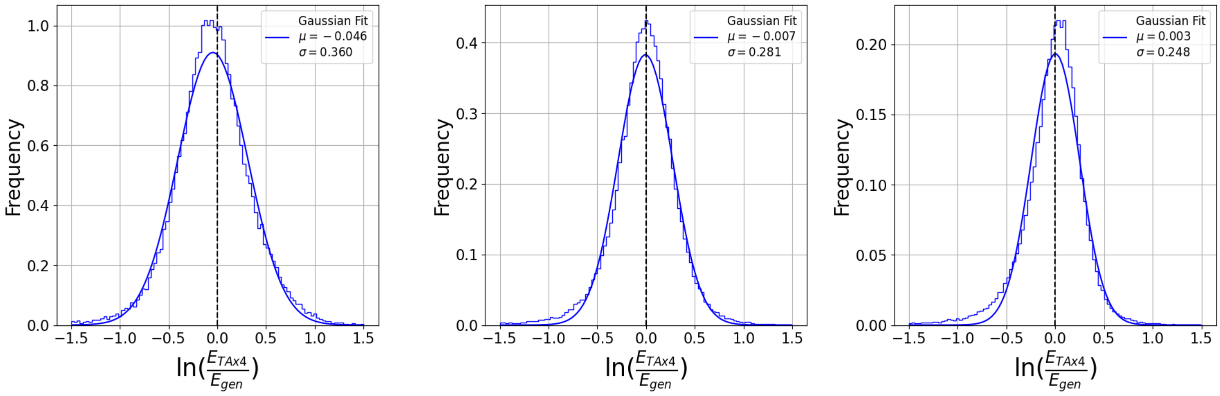

(A) $10^{19.0}$ eV $< E_{\rm gen}/1.36 < 10^{19.5}$ eV

(B) $10^{19.5}$ eV $< E_{\rm gen}/1.36 < 5.7 \times 10^{19}$ eV

(C) 5.7×10^{19} eV $< E_{\rm gen}/1.36$

FIGURE 6.8: The histograms of $\ln(E_{\rm TA\times4\,SD}/E_{\rm gen})$ for three energy ranges: (A) $10^{19.0}$ eV $< E_{\rm gen}/1.36 < 10^{19.5}$ eV, (B) $10^{19.5}$ eV $< E_{\rm gen}/1.36 < 5.7 \times 10^{19}$ eV, and (C) 5.7×10^{19} eV $< E_{\rm gen}/1.36$. The solid line indicates a Gaussian fit. The TA SD energy spectrum [90] is assumed here.

Figure 6.9 shows the peak and width of the Gaussian fit to $\ln(E_{\rm TA\times4\,SD}/E_{\rm gen})$ histogram. In the figure, the peak is $\exp(\mu_{\ln E}) - 1$, the upward error bar is $\exp(\mu_{\ln E} + \sigma_{\ln E}) - \exp(\mu_{\ln E})$, and the downward error bar is $\exp(\mu_{\ln E}) - \exp(\mu_{\ln E} - \sigma_{\ln E})$, where $\mu_{\ln E}$ and $\sigma_{\ln E}$ are the mean and the standard deviation of the Gaussian fit, respectively.

6.6.2 Angular resolution

The angular resolution is calculated by choosing a 68.3% point of a cumulative histogram of the opening angle, which is expressed as

$$\delta_{\rm angular} = \arccos(\hat{\mathbf{n}}_{\rm rec} \cdot \hat{\mathbf{n}}_{\rm gen}), \tag{6.12}$$

where $\hat{\mathbf{n}}_{\rm rec}$ and $\hat{\mathbf{n}}_{\rm gen}$ are reconstructed arrival direction and generated arrival direction, respectively. In this section, the following values ($\theta_{\rm eval}$, $\phi_{\rm eval}$) are used to evaluate the angular resolution:

$$\theta_{\rm eval} = \begin{cases} \theta_{\rm Comb,\,mod} & (\theta_{\rm Comb,\,mod} < 20^\circ) \\ \theta_{\rm geom,\,mod} & (\theta_{\rm Comb,\,mod} \geq 20^\circ) \end{cases} \tag{6.13}$$

$$\phi_{\rm eval} = \begin{cases} \phi_{\rm Comb} & (\theta_{\rm Comb,\,mod} < 20^\circ) \\ \phi_{\rm geom} & (\theta_{\rm Comb,\,mod} \geq 20^\circ), \end{cases} \tag{6.14}$$

$$\tag{6.15}$$

where

$$\begin{aligned} \theta_{\rm Comb,\,mod} &= 1.2059 + 0.95820\theta_{\rm Comb} + 3.3046 \times 10^{-3}\theta_{\rm Comb}^2 - 4.6604 \times 10^{-5}\theta_{\rm Comb}^3 \\ \theta_{\rm geom,\,mod} &= 1.2971 + 0.91132\theta_{\rm geom} + 3.0011 \times 10^{-3}\theta_{\rm geom}^2 - 3.2212 \times 10^{-5}\theta_{\rm geom}^3, \end{aligned}$$

$\theta_{\rm Comb}$ and $\phi_{\rm Comb}$ are the results of the combined fit, and $\theta_{\rm geom}$ and $\phi_{\rm geom}$ are the results of the geometry fit. These functional forms are based on the MC simulation to

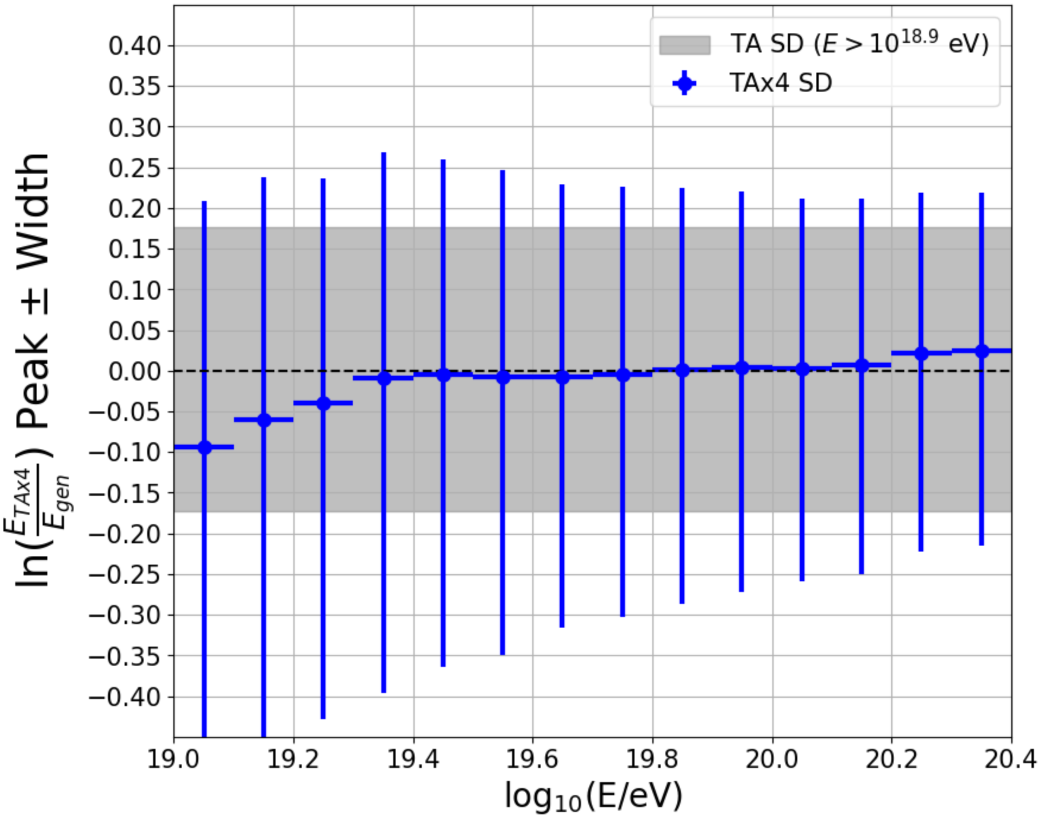

FIGURE 6.9: The energy resolution of the TA×4 SDs for each energy bin. The blue point and errorbar represent the mean and standard deviation of a Gaussian fit of $\ln(E_{\mathrm{TA\times4\,SD}}/E_{\mathrm{gen}})$ in each energy bin, respectively. The x-axis is the scaled energy: $E_{\mathrm{gen}}/1.36$. The hatched area represents the energy resolution of the TA SD $E_{\mathrm{gen}}/1.27$ for energy above $10^{19}/1.27 = 10^{18.9}$ eV [97].

reduce systematic bias dependent on the zenith angle. In this work, arrival distribution is not discussed. The modified zenith and azimuthal angles are used only to evaluate the angular resolution.

Figure 6.10 shows cumulative histograms of the opening angles and the angular resolution (represented by the vertical dashed lines) for three energy ranges: 3.0° for $10^{19.0}$ eV $< E_{\mathrm{gen}}/1.36 < 10^{19.5}$ eV, 2.5° for $10^{19.5}$ eV $< E_{\mathrm{gen}}/1.36 < 5.7 \times 10^{19.0}$ eV, and 2.1° for $5.7 \times 10^{19.0}$ eV $< E_{\mathrm{gen}}/1.36$.

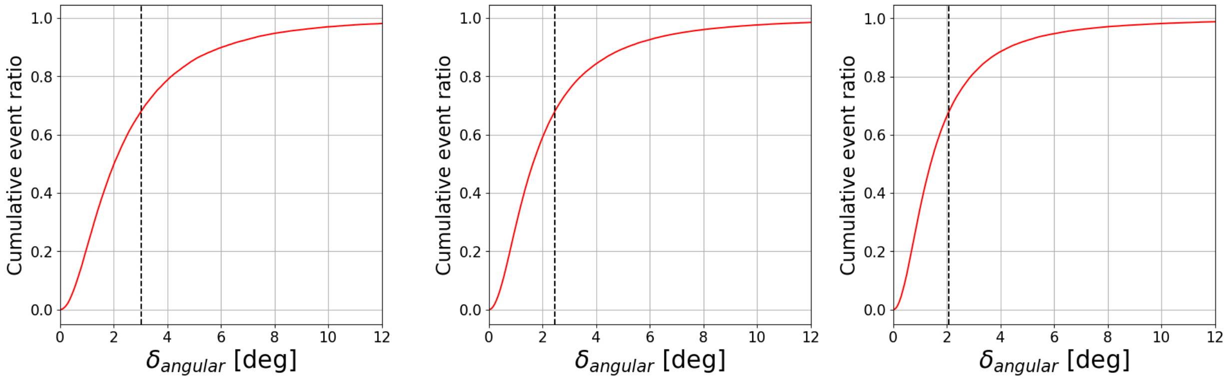

(A) $10^{19.0}$ eV $< E_{\mathrm{gen}}/1.36 < 10^{19.5}$ eV (B) $10^{19.5}$ eV $< E_{\mathrm{gen}}/1.36 < 5.7 \times 10^{19}$ eV (C) 5.7×10^{19} eV $< E_{\mathrm{gen}}/1.36$

FIGURE 6.10: The cumulative histograms of opening angle (Eq. 6.12) for three energy ranges: (A) $10^{19.0}$ eV $< E_{\mathrm{gen}}/1.36 < 10^{19.5}$ eV, (B) $10^{19.5}$ eV $< E_{\mathrm{gen}}/1.36 < 5.7 \times 10^{19}$ eV, and (C) 5.7×10^{19} eV $< E_{\mathrm{gen}}/1.36$. The vertical dashed lines indicate 68.3% confidence limits, which contain 68.3% of all events in the energy ranges. The TA SD energy spectrum [90] is assumed here.

Figure 6.11 shows the angular resolution in each energy bin.

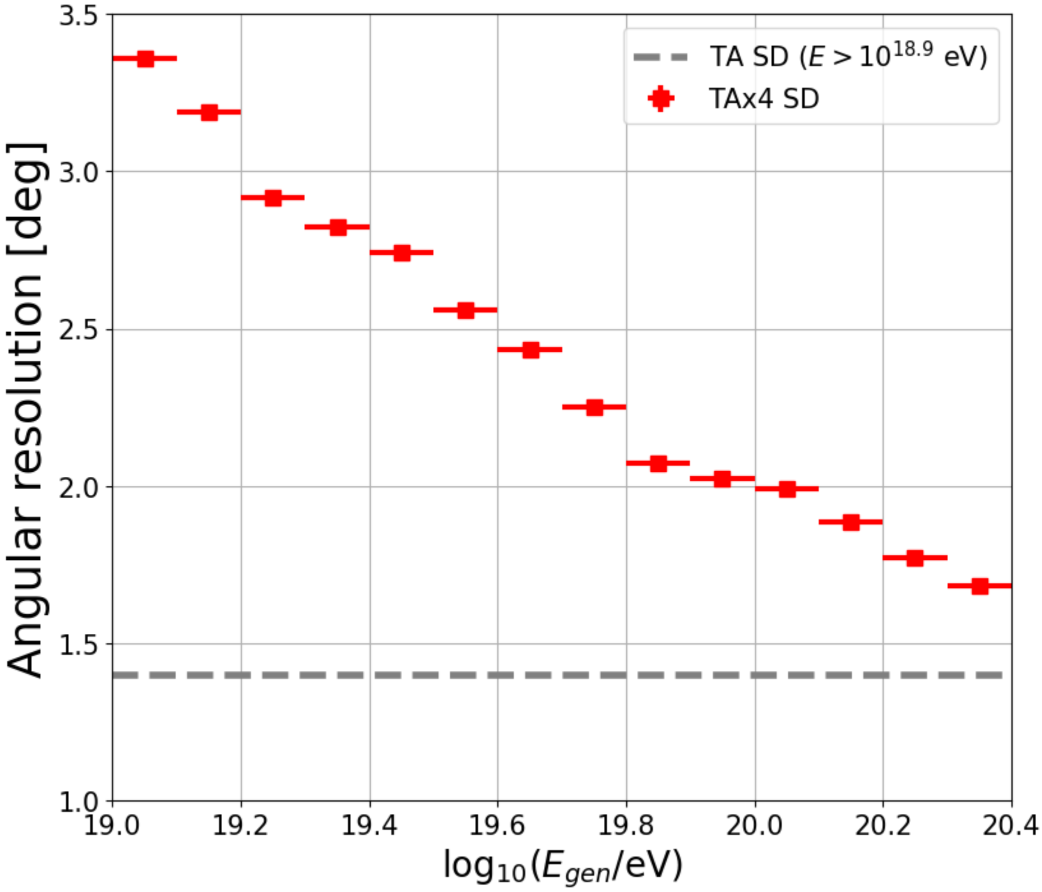

FIGURE 6.11: The angular resolution of the TA×4 SD array for each energy bin. The dashed line represents the angular resolution of the TA SD $E_{\mathrm{gen}}/1.27$ for energy above $10^{18.9}$ eV [97].

Chapter 7

The UHECR energy spectrum measurement

7.1 Energy scale

Surface detectors estimate the energies of primary UHECRs from the lateral distributions of the particle density of the air showers. Hence, the energy estimation possibly has systematic biases, such as the hadronic interaction model used in the air shower simulations. On the other hand, the energy estimation by fluorescence detectors is calorimetric. Therefore, the FD-energy can be used to calibrate the energy reconstructed by SDs using hybrid events simultaneously observed by both SDs and FDs. In the case of the TA SD array, it was reported that the energy estimated by TA SDs, $E_{\mathrm{TA\,SD}}$ agrees with the linearly scaled energy reconstructed by TA FDs, $E_{\mathrm{FD}} \times f_{\mathrm{TA\,SD}}$, where $f_{\mathrm{TA\,SD}} = 1.27$ [80], as described in Sec. 3.3.

In the case of the TA×4 SD array, however, there are insufficient numbers of hybrid events to calibrate energy estimation of SDs since the energy threshold of the TA×4 SD array is much higher than the TA SD array. Thus, we propose another method to determine the energy scale. In this section, the formalization of the energy scale and the method to determine the energy scale of the TA×4 SD array assuming the energy spectrum observed by the TA SD array [90] are explained.

7.1.1 Formalization of energy scale

We use the following denotation:

- E_{gen}: the energy of the primary particle that generates the air shower in the MC simulation.
- $E_{SD}^{int,\,A}$: the energy estimated by the conversion table (see Sec. 6.4) of the SD array (SD-table-energy). The hadronic interaction model and the primary particle used to construct the table are *int* and *A*, respectively.
- E_{FD}: the energy reconstructed by the FD (FD-energy).
- E_{true}: the true energy of the UHECR.
- $E_{\mathrm{rec}} = E_{SD}^{int,\,A} / f_{SD}^{int,\,A}$: the scaled SD-table-energy. This value is finally used as the reconstructed energy of the SD array.

We assume the following:

1. The FD can estimate the true energy without any bias: $E_{\mathrm{FD}} = E_{\mathrm{true}}$

2. The relation between the SD-table-energy and the FD-energy is linear: $f_{SD}^{int,\ A} \times E_{\mathrm{FD}} = E_{SD}^{int,\ A}$.

We do not consider the resolutions of the SD and FD for simplification here.

Using the above two assumptions, we obtain

$$E_{\mathrm{true}} = E_{\mathrm{FD}} = E_{SD}^{int,\ A} / f_{SD}^{int,\ A}. \tag{7.1}$$

In the case of the TA SD array, the above equation is

$$\begin{aligned} E_{\mathrm{true}} = E_{\mathrm{FD}} &= E_{\mathrm{TA\ SD}}^{\mathrm{QGSJET\ II\text{-}03,\ p}} / f_{\mathrm{TA\ SD}}^{\mathrm{QGSJET\ II\text{-}03,\ p}} \\ &= E_{\mathrm{TA\ SD}}^{\mathrm{QGSJET\ II\text{-}03,\ p}} / 1.27, \end{aligned} \tag{7.2}$$

where $f_{\mathrm{TA\ SD}}^{\mathrm{QGSJET\ II\text{-}03,\ p}} = 1.27$ is experimentally determined using hybrid events [80]. Therefore, the TA SD uses $E_{\mathrm{rec,\ TA\ SD}} = E_{\mathrm{TA\ SD}}^{\mathrm{QGSJET\ II\text{-}03,\ p}}/1.27$ as the reconstructed energy. Note that the effects of the hadronic interaction model (*int*) and the primary particle (A) used in the MC simulation are included in the energy scale $f_{\mathrm{TA\ SD}}^{\mathrm{QGSJET\ II\text{-}03,\ p}} = 1.27$ since the energy scale factor is determined by hybrid events, which reflect the actual mass composition of UHECRs. Therefore, $E_{\mathrm{rec,\ TA\ SD}}$ is independent of the hadronic interaction model and the primary particle used in the MC simulation.

Energy scale in the air shower simulation

The conversion table to estimate SD-table-energy is constructed based the simulation, hence $E_{SD}^{int,\ A} = E_{\mathrm{gen}}$. The linear scale between E_{true} and $E_{SD}^{int,\ A}$ means that there is also linear scale between E_{true} and E_{gen}:

$$E_{\mathrm{gen}} = E_{SD}^{int,\ A} = E_{\mathrm{true}} \times f_{SD}^{int,\ A}. \tag{7.3}$$

Therefore, we have to scale the energy by $f_{SD}^{int,\ A}$ when we generate air showers in the MC simulation. In Sec. 4.4.3 and Sec. 6.6, we scaled E_{gen} by the energy scale factor for this reason.

Energy distribution as a function of the energy scale

Here, we discuss the differential number of events expected to be observed by the SD array in the MC simulation in the energy bin of $[E_{SD}^{int,\ A} - \Delta E,\ E_{SD}^{int,\ A} + \Delta E]$, denoted by $N^{\mathrm{MC}}(E_{SD}^{int,\ A})$. In this discussion, we introduce the energy migration by $\kappa(E_{\mathrm{output}}\,; E_{\mathrm{input}})$, which describes the probability distribution of the estimated energy E_{output} as a function of the true energy E_{input}, i.e., $\int dE_{\mathrm{output}} \kappa(E_{\mathrm{output}}\,; E_{\mathrm{input}}) = 1$ holds.

$N^{\mathrm{MC}}(E_{SD}^{int,\ A})$ is given by:

$$\begin{aligned} N^{\mathrm{MC}}(E_{SD}^{int,\ A}) &= \int_{E_{SD}^{int,\ A}-\Delta E}^{E_{SD}^{int,\ A}+\Delta E} d\tilde{E}_{SD}^{int,\ A} \int d\tilde{E}_{\mathrm{gen}} \int dA \int d\Omega \int dt\ J(\tilde{E}_{\mathrm{true}}) \\ &\quad \times \epsilon(\tilde{E}_{\mathrm{gen}}) \times \kappa(\tilde{E}_{SD}^{int,\ A}\,; \tilde{E}_{\mathrm{gen}}) \\ &= A_{\mathrm{gen}} \Omega_{\mathrm{gen}} T \int_{E_{SD}^{int,\ A}-\Delta E}^{E_{SD}^{int,\ A}+\Delta E} d\tilde{E}_{SD}^{int,\ A} \int d\tilde{E}_{\mathrm{gen}}\ J(\tilde{E}_{\mathrm{gen}} / f_{SD}^{int,\ A}) \\ &\quad \times \epsilon(\tilde{E}_{\mathrm{gen}}) \times \kappa(\tilde{E}_{SD}^{int,\ A}\,; \tilde{E}_{\mathrm{gen}}), \end{aligned} \tag{7.4}$$

where the $J(E)$ is the differential cosmic ray energy spectrum, $A_{\mathrm{gen}}\Omega_{\mathrm{gen}}$, T are geometrical aperture and time period of the generated MC events (described in Sec. 5.3), and $\epsilon(E)$ is the efficiency. $N^{\mathrm{MC}}(E_{SD}^{int,\,A})$ is calculated as a function of $f_{SD}^{int,\,A}$ assuming the cosmic ray energy spectrum $J(E)$. Note that integration with respect to E_{true} yields the same result as the integration with respect to E_{gen}. An essential point in the above equation is that E_{gen} must be scaled relative to E_{true} to reflect the lateral distribution of particle density at the detector level.

By comparing $N^{\mathrm{MC}}(E_{SD}^{int,\,A})$ with the number of events actually observed, we can estimate the energy factor. In particular, we determined $f_{\mathrm{TA\times4\,SD}}^{\mathrm{QGSJET\ II\text{-}04},\,p}$ so that $N^{\mathrm{MC}}(E_{\mathrm{TA\times4\,SD}}^{\mathrm{QGSJET\ II\text{-}04},\,p} > 10^{18}\ \mathrm{eV})$, which is calculated by Eq. 7.4 assuming the TA SD energy spectrum [90] in $J(E)$, with $N^{\mathrm{Obs}}(E_{\mathrm{TA\times4\,SD}}^{\mathrm{QGSJET\ II\text{-}04},\,p} > 10^{18}\ \mathrm{eV})$, which is the observed number of events. The data period used here is *Epoch-1* and *Epoch-2*, the first three years of the data before the implementation of the inter-tower trigger (see Sec. 4.4.2).

Figure 7.1 shows the ratio $N^{\mathrm{Obs}}/N^{\mathrm{MC}}$ as a function of $f_{\mathrm{TA\times4\,SD}}^{\mathrm{QGSJET\ II\text{-}04},\,p}$. The figure shows that it is equal to 1 with $f_{\mathrm{TA\times4\,SD}}^{\mathrm{QGSJET\ II\text{-}04},\,p} = 1.36 \pm 0.05$. Hereafter, we use it as the energy scale factor of the TA×4 SD array. The uncertainty of the energy scale is determined by the statistical uncertainty of the observed number of events. The uncertainty of the energy scale factor corresponds to the energy uncertainty of $[1/(1.36-0.05)]/[1/1.36]-1 = +3.8\%$ and $1-[1/1.36]/[1/(1.36+0.05)] = -3.7\%$. The energy threshold was chosen low enough not to be significantly affected by the assumed energy spectrum. Note that this energy scale is determined relative to the FD-energy. Therefore, the uncertainty of the energy scale is relative to the FD-energy of the TA experiment. The effects of the hadronic interaction model and the mass of the primary particle in the MC simulation are included in the energy scale factor as well as the energy scale of the TA SD array. In other words, if we use another hadronic interaction model or primary particle in the MC simulation, the energy scale factor f will change, but the reconstructed energy E_{rec} will not change.

7.1.2 Comparison of the energy scales

The energy scale of the TA×4 SD array determined in this work ($f_{\mathrm{TA\times4\,SD}}^{\mathrm{QGSJET\ II\text{-}04},\,p} = 1.36 \pm 0.05$) is greater than that of the TA SD array ($f_{\mathrm{TA\ SD}}^{\mathrm{QGSJET\ II\text{-}03},\,p} = 1.27$). Here, we discuss this relation ($f_{\mathrm{TA\times4\,SD}}^{\mathrm{QGSJET\ II\text{-}04},\,p} = 1.36 > 1.27 = f_{\mathrm{TA\ SD}}^{\mathrm{QGSJET\ II\text{-}03},\,p}$) qualitatively. Figure 7.2 shows a previous study in the TA group [103] which shows the energy scales as functions of the primary energy, hadronic interaction model and primary particle. The energy scales shown in the figure are relative to $f_{\mathrm{TA\ SD}}^{\mathrm{QGSJET\ II\text{-}03},\,p}$ since the energy estimation table of the TA SD array is based on air showers generated with QGSJET II-03 proton. The horizontal green line in the figure ($\ln(E_{\mathrm{REC}}/E_{\mathrm{THR}}) \sim 0.25$) indicates the energy scale of the TA SD array ($e^{0.25} \sim 1.27$). In the case of the QGSJET II-04 proton, the ratio is $\ln(E_{\mathrm{REC}}/E_{\mathrm{THR}}) \sim 0.07$. Therefore, the energy scale of the TA SD array with QGSJET II-04 proton would be $1.27/e^{0.07} \sim 1.18$ almost independent of the energy. It means that the air showers generated with QGSJET II-04 proton agree with the air showers in real better than QGSJET II-03 proton in terms of the energy measurement by the TA SD array. The energy scale expected from the previous study (1.18) is smaller than 1.27, and this is contrary to this work; the determined energy scale (1.36) is greater than 1.27.

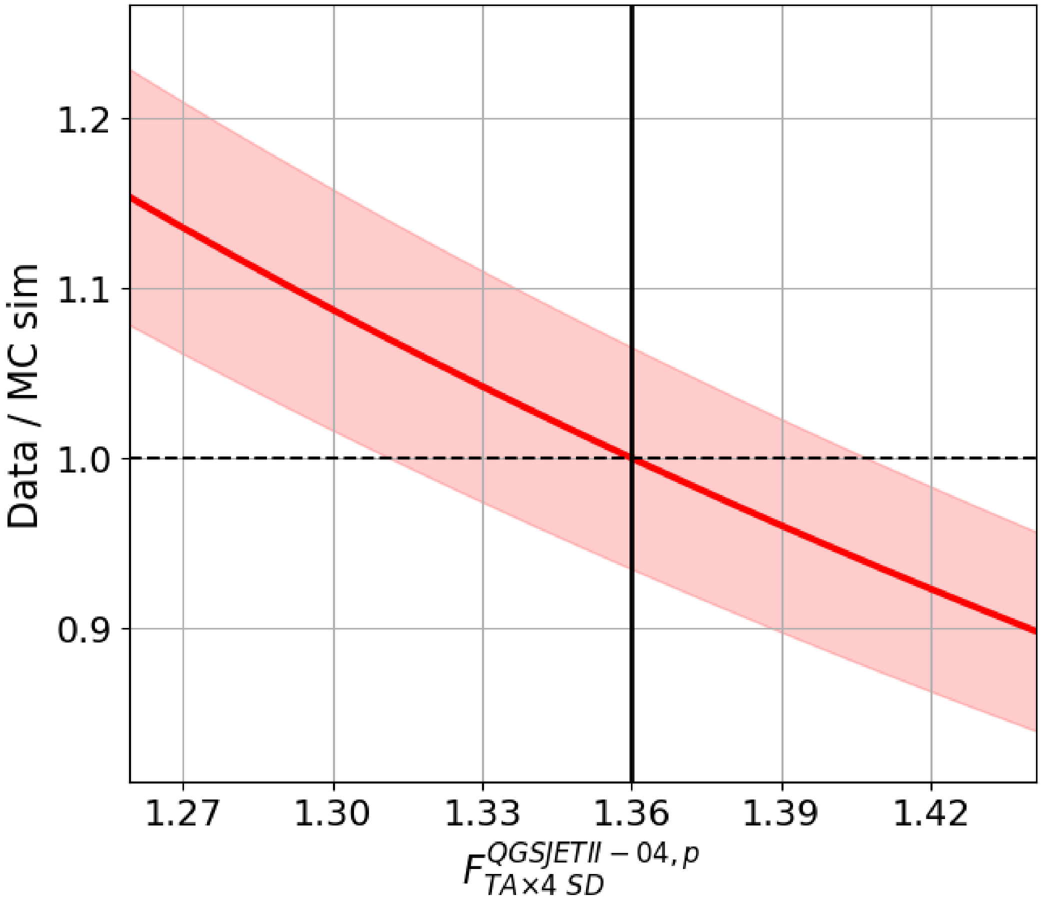

FIGURE 7.1: The ratio of the number of events with energies greater than 10^{18} eV expected by the MC simulation to that of the observation as a function of the energy scale factor. The band indicates the statistical uncertainty of the number of observed events.

TABLE 7.1: The nine parameters compared between the observation and the MC simulation.

Parameter	Description
E_{rec}	Reconstructed energy
$S800$	Signal density at 800 m from the distance
$\sigma_{S800}/S800$	Relative uncertainty of $S800$
N_{SD}	Number of events used in the combined fit
θ_{rec}	Reconstructed zenith angle
ϕ_{rec}	Reconstructed azimuthal angle
X_{rec}	Reconstructed core position of the X-axis (West-East)
Y_{rec}	Reconstructed core position of the Y-axis (South-North)
χ^2/ndof	Reduced chi-square of the combined fit

The possible source of this difference is the detector spacing: 1.2 km for the TA SD array and 2.08 km for the TA×4 SD array. The ratio of hit SDs at a greater distance from the air shower axis in the TA×4 SD array is greater than that in the TA SD array (Fig. 7.3). Due to the difference, lateral distribution fit (Sec. 6.3.2) of the TA×4 SD array is more affected by SDs at a greater distance from the air shower axis. This effect does not matter as long as the lateral distributions of the air shower particles generated in the simulation agree with those in real observation. However, a discrepancy in the lateral distribution was recently reported by the TA experiment [104]. The bottom right panel in Fig. 7.4 shows the discrepancy especially at the distance farther than 2500 m from the air shower axis. This discrepancy is thought to be due to the muon excess in the observation (as explained in Sec. 2.5.1). The excess of the signal density at the greater distance is more effective in the TA×4 SD array than the TA SD array. In particular, the TA×4 SD array can overestimate the signal density of the air shower in observation due to the signal density excess at the greater distance and estimate the energy of the UHECR greater than the TA SD array in real observation. This effect possibly increases the energy scale of the TA×4 SD.

7.2 Data/MC comparison

It is necessary to confirm that the MC simulation reproduces the real observation accurately. The running status differs depending on observational Epochs as explained in Sec. 4.4.2, so the comparisons are performed for each Epoch. The parameters summarized in Tab. 7.1 are compared for events after the event selection described in Sec. 6.5, with reconstructed energies greater than 10^{18} eV.

7.2.1 The comparisons for periods before the implementation of the inter-tower trigger

The TA×4 SD array operated without the inter-tower trigger for the first three years (up through 31st October 2022). This period is divided into two periods in terms of the occupancy rate of the SDs as explained in Sec. 4.4.2; *Epoch-1* is from 8th October

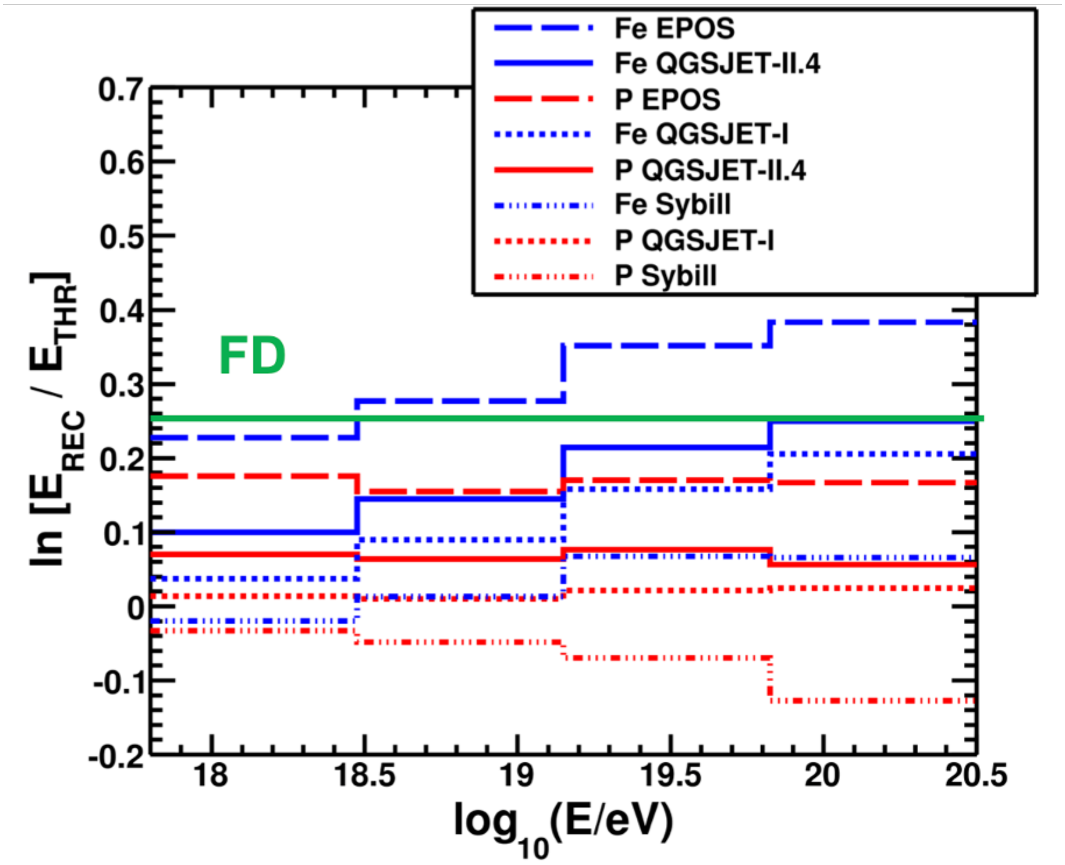

FIGURE 7.2: The relation between the energy of air showers produced by various hadron interaction models (denoted by E_{THR}) and the energy estimated from them by the TA SD array with the energy estimation table developed with QGSJET II-03 proton (denoted by E_{REC}) [103]. The hadronic interaction models of QGSJET I [60] (dotted line), QGSJET II-04 [61] (solid line), Sibyll [105] (dash-dotted line), and EPOS [106] (dashed line) with the primary particles of proton (red) and iron (blue) are compared. The solid green line shows the air shower in real; $\ln(E_{\mathrm{REC}}/E_{\mathrm{THR}}) \sim 0.25$ means the energy scale of the TA SD array with QGSJET II-03 proton is $e^{0.25} \sim 1.27$.

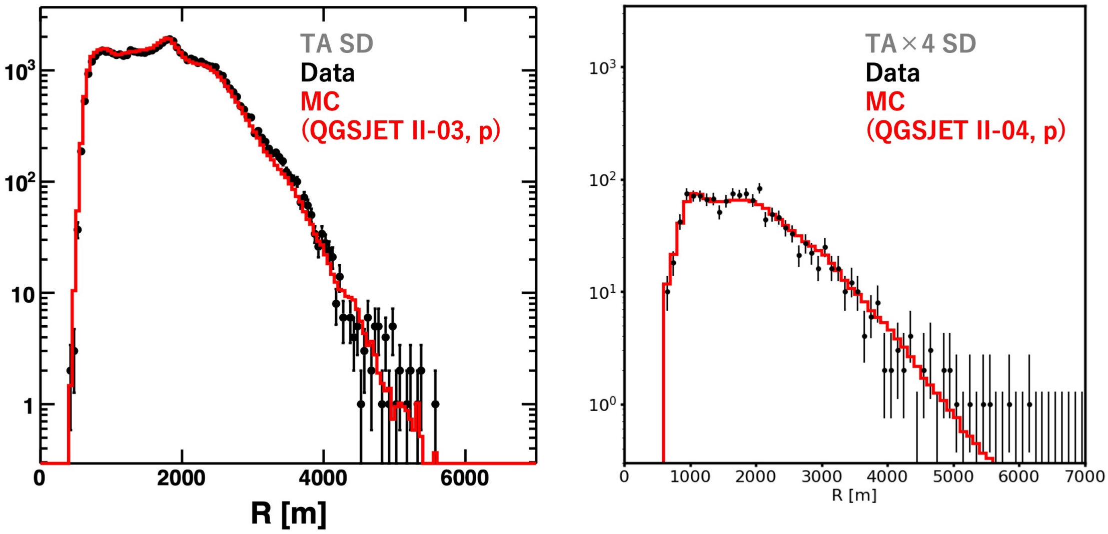

FIGURE 7.3: The histograms of the distance R between the SD used for the lateral distribution fit and the air shower axis for the TA SD array (left) [97] and the TA×4 SD array (right). In both panels, the red histogram is the simulated events, and the black error bars are the observed events.

2019 through 31st August 2022, and *Epoch-2* is from 1st September 2022 through 31st October 2022. The comparison is performed in each period.

Figure 7.5 and Fig. 7.6 show the comparisons for *Epoch-1* and *Epoch-2*, respectively. In each figure, the p-values of the chi-square test of distributional comparisons are also shown in green. As shown in the figures, there is no statistical discrepancy between the parameters of observed events and those simulated in both Epochs. It shows that the MC simulation accurately reproduces the observation, including the real running status of the SDs.

7.2.2 The comparisons for periods after the implementation of the inter-tower trigger

Similarly to *Epoch-1* and *Epoch-2*, Data/MC comparison is performed for *Epoch-3*+*Epoch-4*, where the partial inter-tower trigger described in Sec. 4.2.3 has been implemented. However, the full inter-tower trigger is implemented alternatively on the MC simulation as described in Sec. 5.2.3. Therefore, we have to estimate the performance of the partial inter-tower trigger from the MC simulation of the full inter-tower trigger.

The estimation of the performance of the partial inter-tower trigger

The difference between the partial inter-tower trigger and the full inter-tower trigger is, as shown in Fig. 4.10, the treatment when a Level-2 trigger is issued only by the central tower (SN for the North array and BF for the South array). The full inter-tower trigger collects all waveforms when the Level-2 trigger is issued only by the central tower, while the partial inter-tower trigger collects only the central tower waveforms in that case. Therefore, the effective aperture is smaller with the partial inter-tower trigger than the full inter-tower trigger.

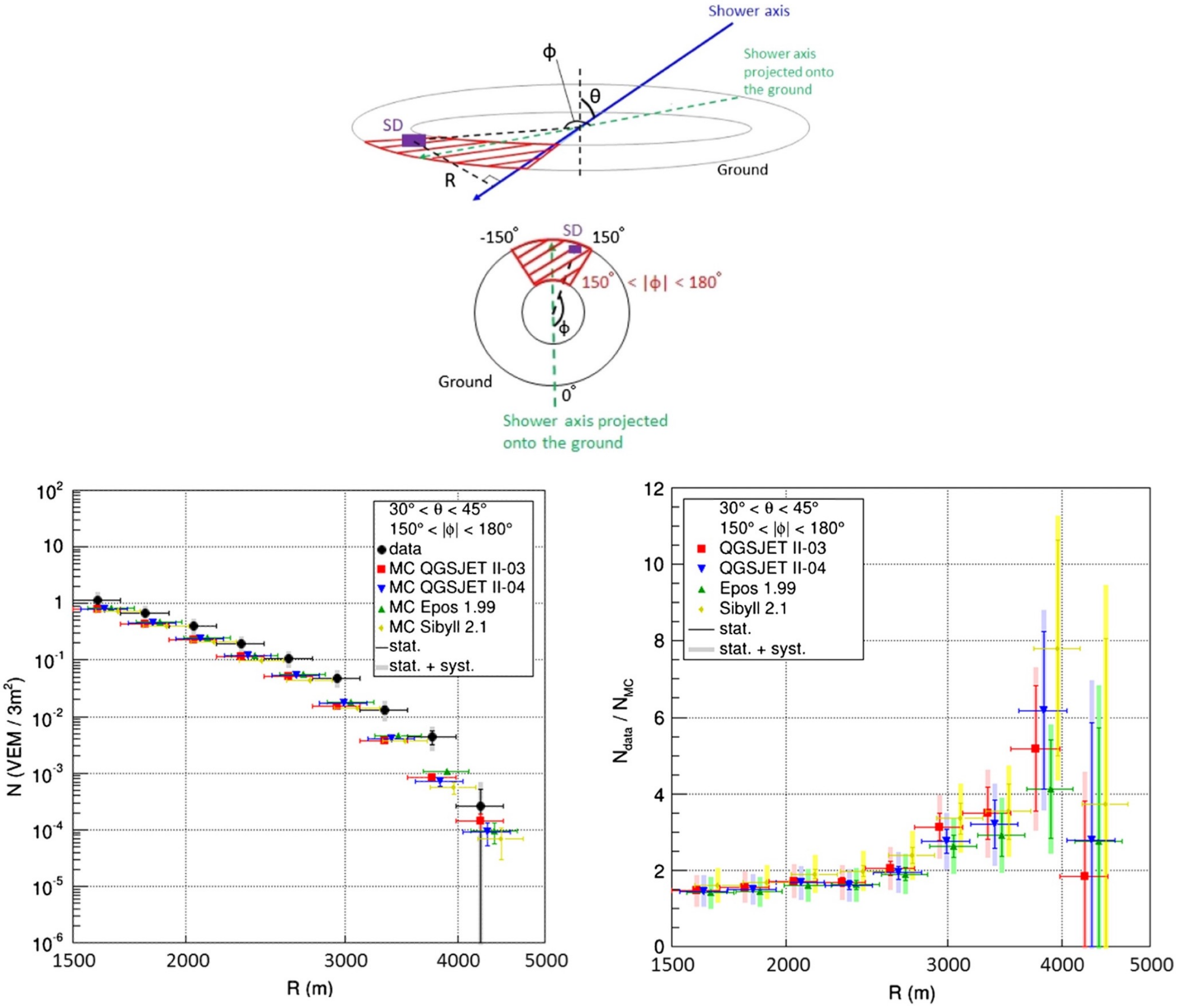

FIGURE 7.4: The signal density with respect to the distance from the air shower axis measured with the TA SD array [104]. (Top) The geometrical definition for the study. The SDs in the hatched area in red are used to calculate the signal density. (Bottom left) The average signal density with respect to the distance from the air shower axis for the events with zenith angle θ from 30° to 45°. The black points indicate the observation, and the others represent the MC simulation: QGSJET II-03 (red square), QGSJET II-04 (blue down triangle), EPOS 1.99 (green up triangle), and Sibyll 2.1 (yellow diamond). Primary particle of the MC simulation is proton. (Bottom right) The ratio of the average signal density of the observation to those of the MC simulation for the hadronic interaction models.

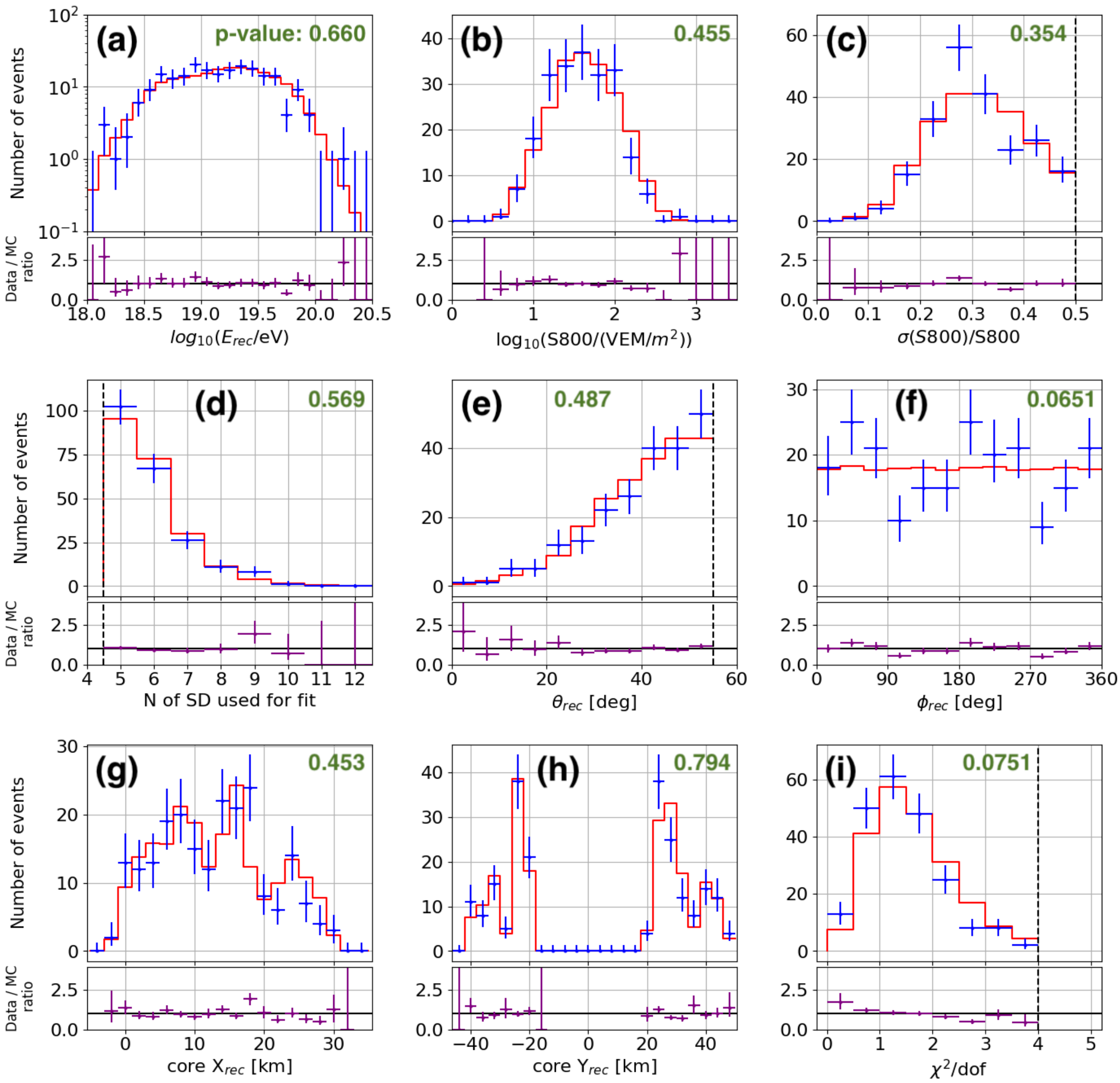

FIGURE 7.5: Comparisons between the observed events (blue points) and the events generated by the MC simulation (red histogram) in *Epoch-1*. The MC simulation histogram is normalized in terms of the number of expected events with 1.36 as the energy scale factor. Chi-square test p-values of the parameters are also shown in green. The compared parameters are (a) reconstructed energy, (b) $S800$, (c) $\sigma_{S800}/S800$, (d) the number of hit SDs, (e) zenith angle, (f) azimuthal angle, (g)(h) core positions (west-east direction and south-north direction), and (i) χ^2/ndof of fit. The dashed vertical lines indicate the thresholds of the event selection criteria. The lower panel of each parameter comparison shows the ratio of the number of observed events to that of simulated events.

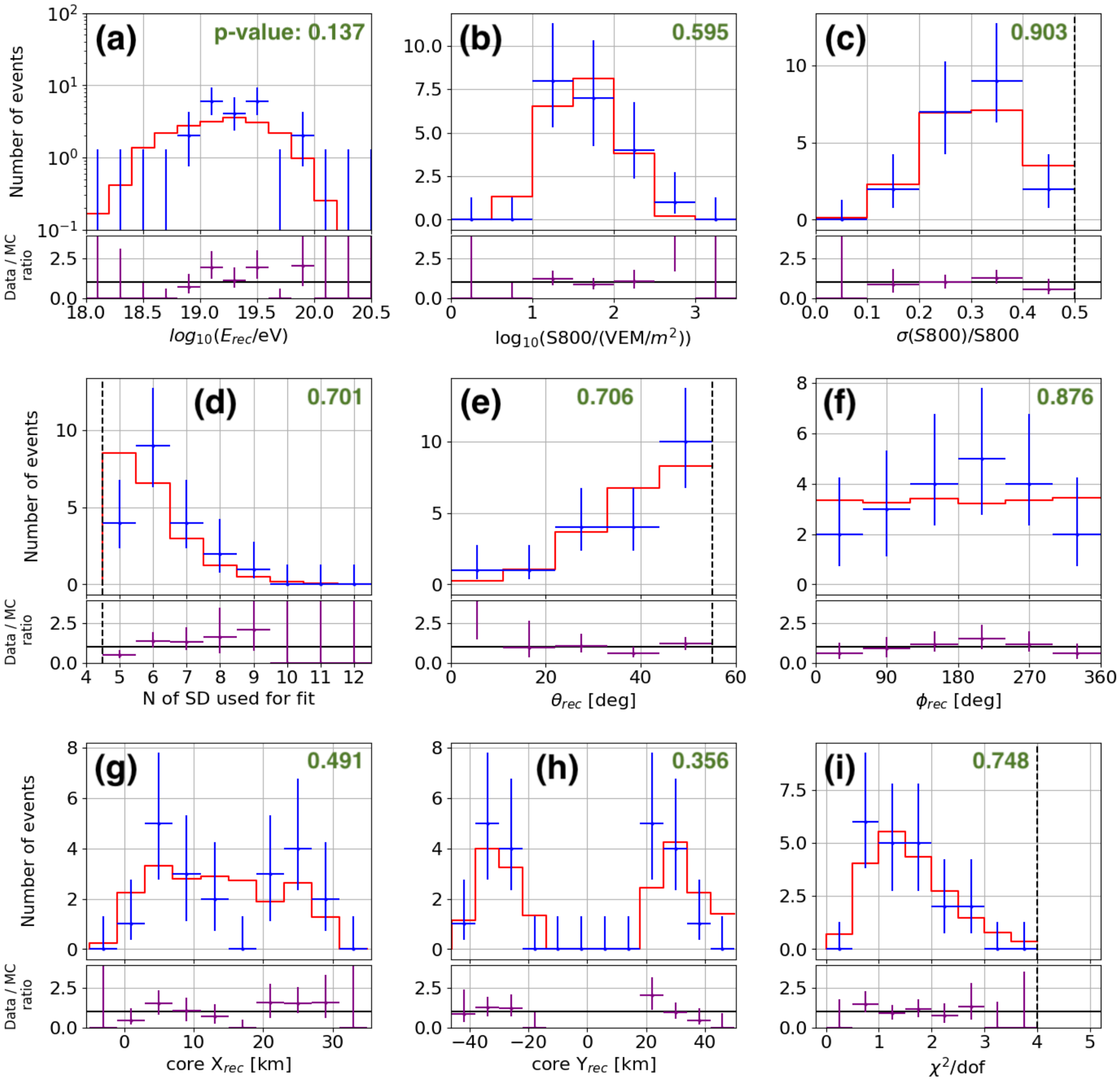

FIGURE 7.6: Same as Fig. 7.5, but comparison in *Epoch*-2.

Denoting the effective aperture of the TA×4 North (South) array with the partial inter-tower trigger and the full inter-tower trigger as $\alpha^{\text{part}}_{\text{North (South)}}$ and $\alpha^{\text{full}}_{\text{North (South)}}$, respectively, they can be given in the following equations:

$$\alpha^{\text{part}}_{\text{North (South)}} = \alpha^{\text{part}}_{\text{SN (BF)}} + \alpha^{\text{full}}_{\text{KM (SC)}} + \alpha^{\text{full}}_{\text{DM (SR)}} \tag{7.5}$$

$$\alpha^{\text{full}}_{\text{North (South)}} = \alpha^{\text{full}}_{\text{SN (BF)}} + \alpha^{\text{full}}_{\text{KM (SC)}} + \alpha^{\text{full}}_{\text{DM (SR)}}, \tag{7.6}$$

where $\alpha^{\text{part}}_{\text{sub-array}}$ is the aperture of the sub-array, which operates independently, and $\alpha^{\text{full}}_{\text{sub-array}}$ is the contribution of the sub-array to the total aperture with the full inter-tower trigger. Using the equations Eq. 7.5 and Eq. 7.6, we get the following equation:

$$\alpha^{\text{part}}_{\text{North (South)}} = \alpha^{\text{full}}_{\text{North (South)}}\left(1 + R^{\text{part}}_{\text{SN (BF)}} - R^{\text{full}}_{\text{SN (BF)}}\right), \tag{7.7}$$

where $R^{\text{part}}_{\text{SN (BF)}} = \alpha^{\text{part}}_{\text{SN (BF)}}/\alpha^{\text{full}}_{\text{North (South)}}$ and $R^{\text{full}}_{\text{SN (BF)}} = \alpha^{\text{full}}_{\text{SN (BF)}}/\alpha^{\text{full}}_{\text{North (South)}}$.

$R^{\text{part}}_{\text{SN (BF)}}$ can be easily estimated using the MC simulation of SN (BF) and the MC simulation of the full inter-tower trigger as follows:

$$\begin{aligned} R^{\text{part}}_{\text{SN (BF)}} &= \frac{\alpha^{\text{part}}_{\text{SN (BF)}}}{\alpha^{\text{full}}_{\text{North (South)}}} \\ &= \frac{A^{\text{gen}}_{\text{SN (BF)}}\Omega^{\text{gen}} \times \frac{N^{\text{rec}}_{\text{SN (BF)}}}{N^{\text{gen}}_{\text{SN (BF)}}}}{A^{\text{gen}}_{\text{North (South)}}\Omega^{\text{gen}} \times \frac{N^{\text{rec}}_{\text{North (South)}}}{N^{\text{gen}}_{\text{North (South)}}}}, \end{aligned} \tag{7.8}$$

where $A^{\text{full}}_{\text{array}}$ (summarized in Tab. 5.3 and Tab. 5.4) and Ω^{gen} are the area and the solid angle used in the MC simulation. $N^{\text{gen}}_{\text{array}}$ and $N^{\text{rec}}_{\text{array}}$ are the number of events generated in the MC simulation and that remain after the event selection, respectively. Both of them are calculated by the available MC events for the same period for the one month of November 2022.

On the other hand, $R^{\text{full}}_{\text{SN (BF)}}$ can not be exactly estimated since the contribution of the sub-array to the full array $A^{\text{full}}_{\text{sub-array}}$ is ambiguous. Here, we estimate $R^{\text{full}}_{\text{SN (BF)}}$ as follows:

$$\begin{aligned} R^{\text{full}}_{\text{SN (BF)}} &= \frac{\alpha^{\text{full}}_{\text{SN (BF)}}}{\alpha^{\text{full}}_{\text{North (South)}}} \\ &= \frac{A^{\text{gen}}_{\text{North (South))}}\Omega^{\text{gen}} \times \frac{N^{\text{rec}}_{\text{SN (BF)}}}{N^{\text{gen}}_{\text{North (South)}}}}{A^{\text{gen}}_{\text{North (South)}}\Omega^{\text{gen}} \times \frac{N^{\text{rec}}_{\text{North (South)}}}{N^{\text{gen}}_{\text{North (South)}}}}. \end{aligned} \tag{7.9}$$

This equation approximates the contribution of SN (BF) with the term $A^{\text{gen}}_{\text{North (South))}}\Omega^{\text{gen}} \times \frac{N^{\text{rec}}_{\text{SN (BF)}}}{N^{\text{gen}}_{\text{North (South))}}}$. In the above equation, the definition of the SN (BF) area in the whole array is ambiguous. We use a geometrical area of the sub-array (the green and blue regions in Fig. 7.7) as its area. The ambiguity of the contribution to the whole array is evaluated by using different areas where the boundary region is widened by 0.5 detector spacing (or narrowed by 0.5 detector spacing), as shown in Fig. 7.7.

The calculated values are summarized in Tab. 7.2. As seen in the table, the reduction in effective aperture due to the partial inter-tower trigger instead of the full

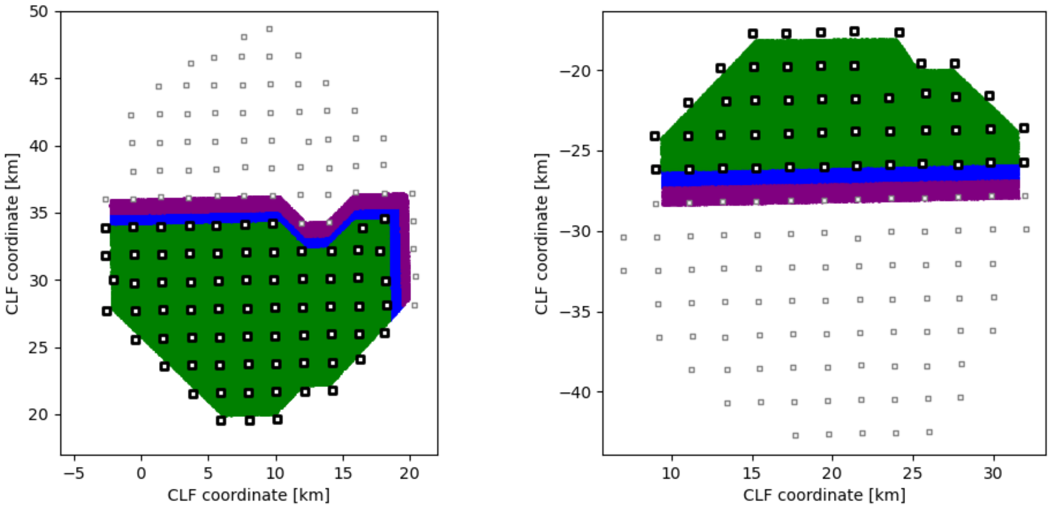

(A) TA×4 North array.

(B) TA×4 South array.

FIGURE 7.7: The regions to calculate the contribution of the central towers (SN, BF) to the overall North (South) array. The SDs of the central towers are shown with thick squares. The region in green and blue is used as their contribution area. The narrowed region (the green region) and the widened region (the green region plus the blue and purple regions) are also used to evaluate the uncertainty of the contribution.

TABLE 7.2: The contribution of the central tower to the overall array for the partial inter-tower trigger and the full inter-tower trigger.

Parameter	**Value**
$R^{\mathrm{full}}_{\mathrm{SN}}$	$0.593^{+0.041}_{-0.034}$
$R^{\mathrm{part}}_{\mathrm{SN}}$	0.509
$R^{\mathrm{full}}_{\mathrm{BF}}$	$0.410^{+0.063}_{-0.072}$
$R^{\mathrm{part}}_{\mathrm{BF}}$	0.222

inter-tower trigger is estimated to be $8.4^{+4.1}_{-3.4}$% for the North array and 19^{+6}_{-7}% for the South array. The percentage of the SN sub-array occupying the North array is larger than that of the BF sub-array occupying the South array. Hence, the difference between the partial inter-tower and full inter-tower triggers has a greater impact on the South array than the North sub-array.

As well as the period of *Epoch-1* and *Epoch-2*, we performed the Data/MC comparison for the period *Epoch-3* for both the TA×4 North and South arrays to see the effect of the partial inter-tower trigger on both arrays (Fig. 7.8 and Fig. 7.9). In both figures, the MC events are scaled by the factors of $(1 + R^{\mathrm{part}}_{\mathrm{SN\,(BF)}} - R^{\mathrm{full}}_{\mathrm{SN\,(BF)}})$ following Eq. 7.7.

As seen in the figures, the MC simulation reproduces well the observation for both the North and South arrays. The MC data set used here is for the period of the first month after the implementation of the inter-tower trigger (November 2022), and the working status of SDs is not constant, as seen in Fig. 4.15. Therefore, this

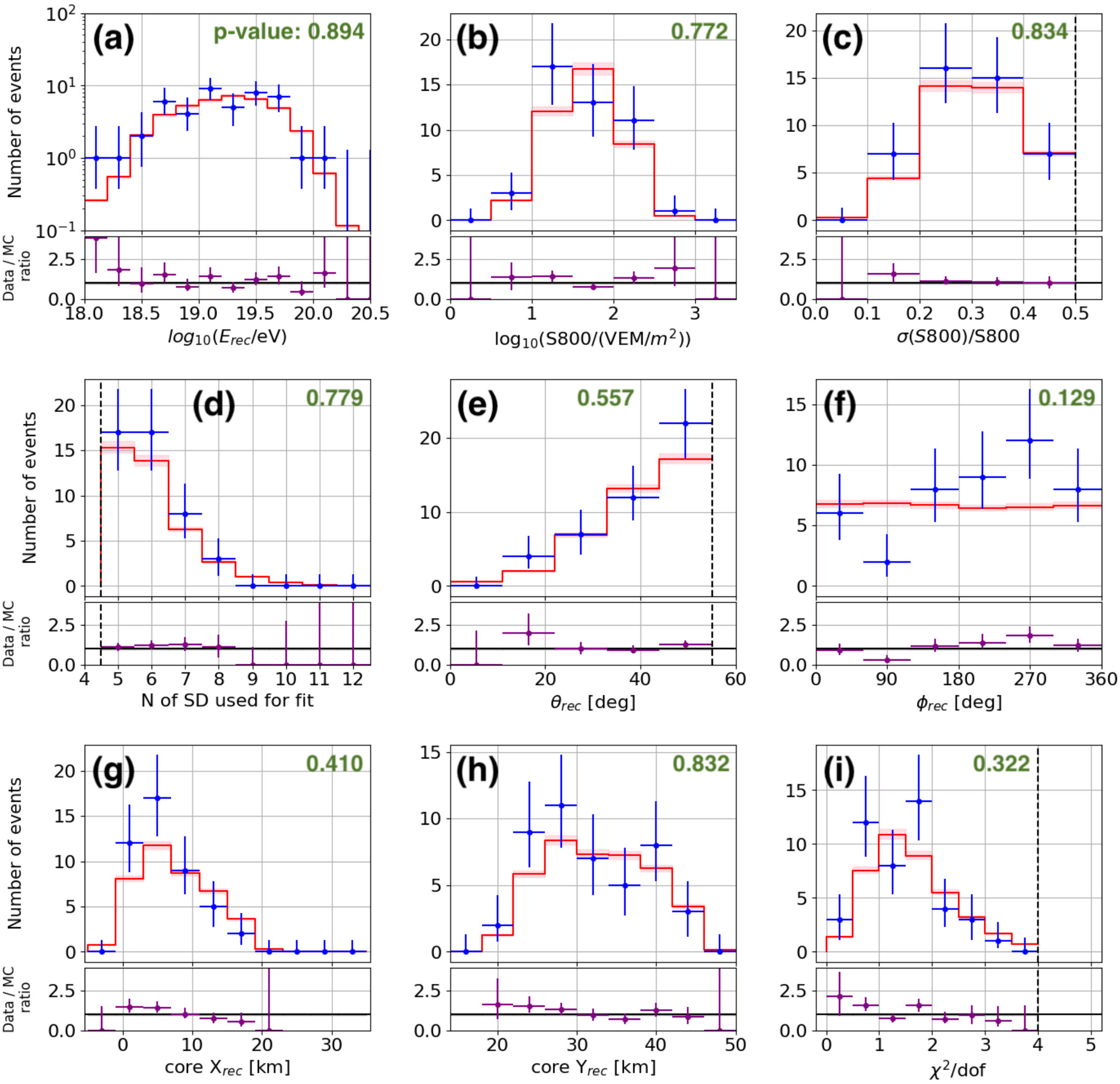

FIGURE 7.8: Comparisons between the observed events (blue points) and the events generated by the MC simulation (red histogram) in *Epoch-3* + *Epoch-4* for the TA×4 North array. The MC simulation histogram is normalized regarding the number of expected events with 1.36 as the energy scale factor. The MC histograms are scaled following by the factor $(1 + R_{\mathrm{SN}}^{\mathrm{part}} - R_{\mathrm{SN}}^{\mathrm{full}})$ (see Tab. 7.2 and the text for details), and its uncertainty is shown by the pink regions. Chi-square test p-values of the parameters without considering the uncertainty of the factor are also shown in green.

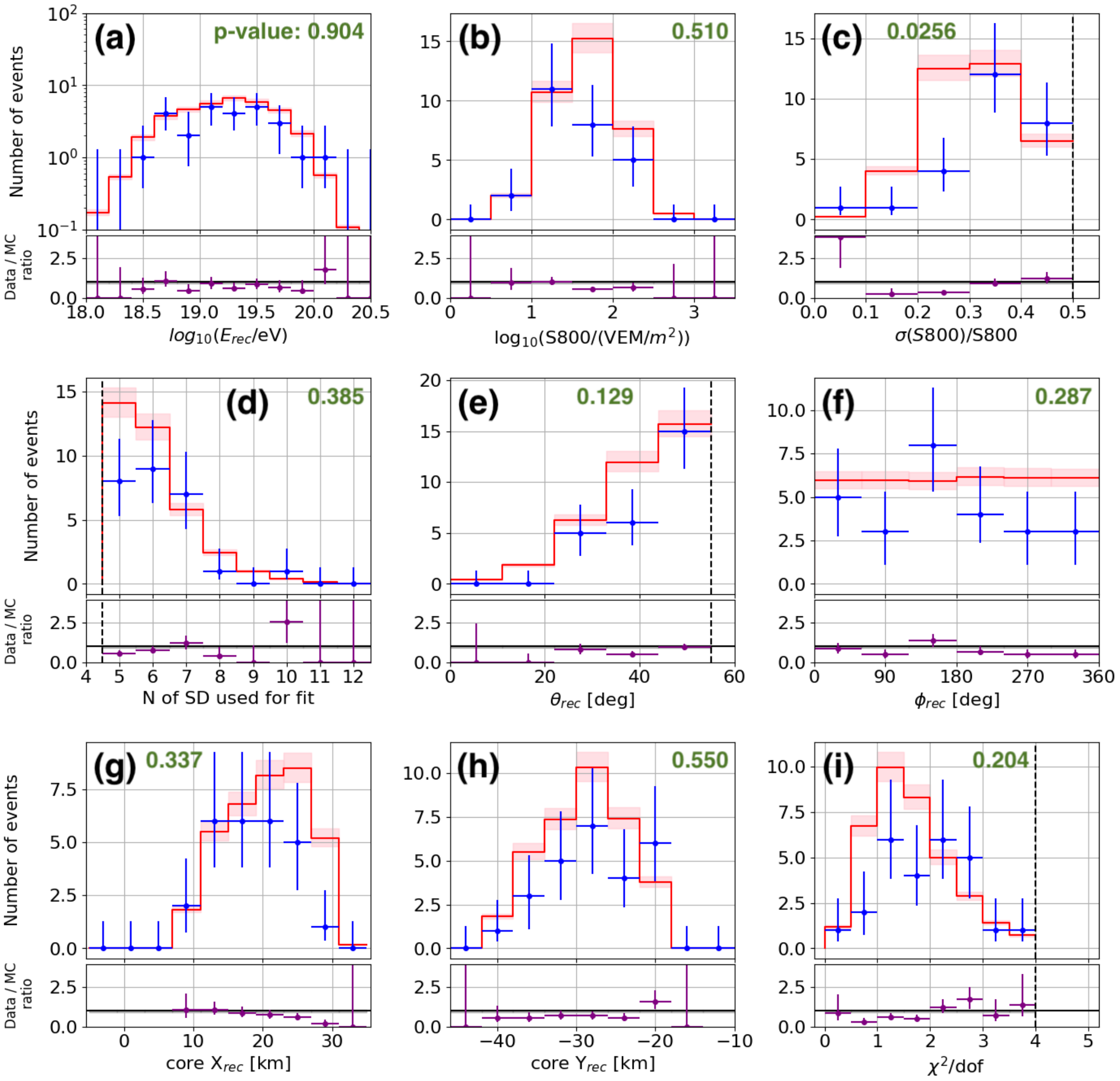

FIGURE 7.9: Same as Fig. 7.8, but comparison in *Epoch-3* + *Epoch-4* for the TA×4 South array.

estimation is just a rough approximation. The accurate evaluation of the array performance for this period will be studied by performing the MC simulation for the period after implementing the partial inter-tower trigger to the MC simulation.

In the following analysis, the data set for *Epoch-1* and *Epoch-2*, where all subarrays operated independently, are used.

7.3 Cosmic ray energy spectrum

In this section, the cosmic ray energy spectrum for energies greater than $10^{19.0}$ eV is determined with the TA×4 SD array for the first time. The *forward-folding* method, which is less dependent on the assumption of the shape of the cosmic ray energy spectrum compared with the method used in the analysis of the TA SD array, is described first. Then, the energy spectrum observed with the first three years of data of the TA×4 SD array is shown. The consistency with the TA SD observation and the significance of the observation of the cutoff in the energy spectrum are discussed at the end of this section.

The differential cosmic ray energy spectrum is defined as:

$$J = \frac{dN}{dA d\Omega dT dE} \tag{7.10}$$

where dN is the number of particles in energy range dE and time interval dT, passing through an area dA and solid angle $d\Omega$ in the reference frame of an observer.

If we have a detector with area A and solid angle Ω with 100% efficiency, and it detects N_i events in energy range ΔE_i with the time interval of the observation T, where i is a label of the energy bin, the cosmic ray energy flux in the i-th energy bin is expressed as

$$J^{\text{Ideal}}(E_i) = \frac{N_i}{A\Omega T \Delta E_i}, \tag{7.11}$$

where N_i is the number of events observed by the detector in the energy range ΔE_i.

By estimating the efficiency of the detector using the MC simulation, we calculate the cosmic ray energy spectrum by the following equation:

$$J^{\text{Raw}}(E_i) = \frac{N_i}{\epsilon(E_i) \times A_{\text{gen}}\Omega_{\text{gen}} T \Delta E_i}, \tag{7.12}$$

where $\epsilon(E_i)$ is the efficiency at the energy bin E_i, and $A_{\text{gen}}\Omega_{\text{gen}}$ are the geometric aperture in which the MC events are generated (described in Sec. 5.3).

7.3.1 Forward-folding

In addition to not being 100% efficiency, actual detectors have finite energy resolutions, which produce bin-to-bin migrations. We must extract the bin-to-bin migration effect to estimate the true cosmic ray energy spectrum. In the case of the TA SD array, bin-by-bin correction unfolding method has been used [97] [91]. This method assumes an input cosmic ray energy spectrum and estimates the bin-to-bin migration effect and efficiency using the MC simulation. The estimated migration effect is corrected for exposure of each energy bin. This method is valid as far as the migration effect is less dependent on the input energy spectrum.

In the case of the TA×4 SD array, the bin-to-bin migration effect is larger than that of the TA SD array due to the worse energy resolution as shown in Fig. 6.9, and the efficiency of the TA×4 SD array is much lower than that of the TA SD array. Therefore, the dependence on the input energy spectrum is larger than the TA SD array.

Therefore, an alternative method, *forward-folding method* inspired by [13], is used in this study. The forward-folding method assumes the functional form of the energy spectrum with a set of free parameters. The set of the parameters **s** is determined to minimize the deviance:

$$D = 2\Sigma_i \left([N^{\mathrm{MC}}_{\mathrm{rec}}(g(\mathbf{s}))]_i - [N^{\mathrm{Data}}_{\mathrm{rec}}]_i + [N^{\mathrm{Data}}_{\mathrm{rec}}]_i \ln\left(\frac{[N^{\mathrm{Data}}_{\mathrm{rec}}]_i}{[N^{\mathrm{MC}}_{\mathrm{rec}}(g(\mathbf{s}))]_i} \right) \right), \tag{7.13}$$

where $[N^{\mathrm{MC}}_{\mathrm{rec}}(g(\mathbf{s}))]_i$ is the number of events expected by the MC simulation with the input energy spectrum $g(\mathbf{s})$ in the i-th energy bin as a function of the reconstructed energy $E_{\mathrm{rec}} = E^{\text{QGSJET II-04, } p}_{\mathrm{TA\times4\,SD}} / f^{\text{QGSJET II-04, } p}_{\mathrm{TA\times4\,SD}}$, and $[N^{\mathrm{Data}}_{\mathrm{rec}}]_i$ is the number of observed events in the i-th energy bin as a function of reconstructed energy. The deviance D approximately behaves as χ^2 with the number of degrees of freedom of $(n_{\mathrm{bins}} - n_{\mathrm{params}})$ [107], where n_{bins} is the number of energy bins and n_{params} is the number of parameters in the model. D is used instead of χ^2 since the number of events in each bin is not always large enough. Two types of function of the cosmic ray energy spectra are tested in this study. One is the single power law (SPL) function:

$$J_{\mathrm{SPL}}(E) = K_{\mathrm{SPL}}(E/\mathrm{EeV})^{p_{\mathrm{SPL}}}, \tag{7.14}$$

where K_{SPL} and p_{SPL} are free parameters. The other is the broken power law with one breakpoint (1-BPL):

$$J_{\text{1-BPL}}(E) = K_{\text{1-BPL}}[\theta(E_1 - E) \times (E/\mathrm{EeV})^{p_1} + \theta(E - E_1) \times (E_1/\mathrm{EeV})^{p_1 - p_2} \times (E/\mathrm{EeV})^{p_2}], \tag{7.15}$$

where $K_{\text{1-BPL}}$, E_1, p_1, and p_2 are free parameters, and $\theta(E)$ is a step function.

When the optimum parameter set $\mathbf{s}_{\mathrm{opt}}$ is determined, the correction factor is calculated for each i-th energy bin:

$$c_i(g(\mathbf{s}_{\mathrm{opt}})) = [N^{\mathrm{MC}}_{\mathrm{gen}}(g(\mathbf{s}_{\mathrm{opt}}))]_i / [N^{\mathrm{MC}}_{\mathrm{rec}}(g(\mathbf{s}_{\mathrm{opt}}))]_i, \tag{7.16}$$

where $[N^{\mathrm{MC}}_{\mathrm{gen}}(g(\mathbf{s}_{\mathrm{opt}})]_i$ is the number of events expected by the MC simulation with $g(\mathbf{s}_{\mathrm{opt}})$ as the input energy spectrum in the i-th energy bin as a function of scaled generated energy $E_{\mathrm{gen}}/f^{\text{QGSJET II-04, } p}_{\mathrm{TA\times4\,SD}}$. The correction factor accounts for the bin-to-bin migration effect. Using the correction factor, the measured cosmic ray energy spectrum can be described as

$$J(E_i) = c_i \times J^{\mathrm{Raw}}(E_i) = \frac{c_i \times [N^{\mathrm{Data}}_{\mathrm{rec}}]_i}{\epsilon(E_i) \times A_{\mathrm{gen}}\Omega_{\mathrm{gen}} T \times \Delta E_i} \tag{7.17}$$

The geometrical area of the MC events A_{gen} and observation period T are summarized in Tab. 5.3 for each sub-array. As explained in Sec. 5.3, we generated air showers with zenith angles which follow isotropic distribution up to 60°, so the geometrical aperture $A_{\mathrm{gen}}\Omega_{\mathrm{gen}}$ is $\int_0^{2\pi} d\phi \int_0^{\pi/3} d\theta \sin\theta \cos\theta A_{\mathrm{gen}} = \frac{3\pi}{4} A_{\mathrm{gen}}$.

7.3.2 Measured energy spectrum

We calculated the cosmic ray energy spectrum with observational data of *Epoch-1+Epoch-2*, in which the inter-tower trigger has not been implemented. The energy

TABLE 7.3: Best fit parameters and the goodness of fit for two models. The uncertainties are evaluated for 1 d.o.f; all but one parameter of interest is fixed, and the uncertainty of the parameter of interest is evaluated when D increases (decreases) by 1 from the minimum value of D. AICc (given in Eq. 7.20) indicates how well a model reproduces data [108]. The model with a relatively small AICc is considered better.

Function	**Parameter**	**Best fit value**	**D/ndof**	**p-value**	**AICc**
Broken power law	$K_{\text{1-BPL}}[\text{m}^{-2}\text{sr}^{-1}\text{s}^{-1}\text{eV}^{-1}]$	$1.74^{+0.14}_{-0.24} \times 10^{-30}$	14.79/10	0.140	23.06
	p_1	$-2.90^{+0.08}_{-0.09}$			
	$\log_{10}(E_1/\text{eV})$	$19.86^{+0.08}_{-0.07}$			
	p_2	$-6.4^{+1.7}_{-4.2}$			
Single power law	$K_{\text{SPL}}[\text{m}^{-2}\text{sr}^{-1}\text{s}^{-1}\text{eV}^{-1}]$	$3.69^{+1.02}_{-0.87} \times 10^{-30}$	19.32/12	0.0811	23.40
	p_{SPL}	$-3.16^{+0.34}_{-0.34}$			

threshold used for the fit is $E_{\text{rec}} > 10^{19}$ eV since it is safe not to use the energy region where the efficiency is tiny (< 5%), and there are background events not reproduced by the MC simulation when we apply loose event selections.

Forward-folding with a broken power law function

The optimum parameters of the broken power law with one breaking point (Eq. 7.15) are shown in Tab. 7.3, and the best-fit function is shown in Fig. 7.10a. The two-dimensional deviance map is shown in Fig. 7.11. The optimum parameters are consistent with the measurement of the TA SD with 14 years of the observation [91]. The consistency of the cutoff position between the TA×4 SD measurement and the TA SD measurement implies that the energy scale factor of the TA×4 SD is determined correctly.

The measured cosmic ray energy spectrum is shown in Fig. 7.12 along with the previous TA SD and PAO measurements. In the figure, the systematic uncertainties of the energy scale of the FD-energy of the TA experiment (21% [79]) and the TA×4 SD are shown as well. Note that the uncertainty of the energy scale of the TA×4 SD array is relative to the FD-energy of the TA experiment. The total uncertainty of the energy scale of the TA×4 SD array is a quadratic sum of them ($\sim \sqrt{0.21^2 + 0.038^2} \sim$ 21.3%).

Forward-folding with a single power law function

We also performed the forward-folding with the single power law function (Eq. 7.14) to test if the TA×4 SD array observed the cutoff in the energy spectrum independent of the TA SD array. The optimum parameters are listed in Tab. 7.3, and the best-fit function is shown in Fig. 7.10b. Figure 7.13 shows the two-dimensional deviance map. Figure 7.14 shows the measured cosmic ray energy spectrum.

Cutoff observed by the TA×4 experiment

To evaluate two models (the single power law model and the broken power law model), we compared reduced deviance and the Akaike Information Criterion with

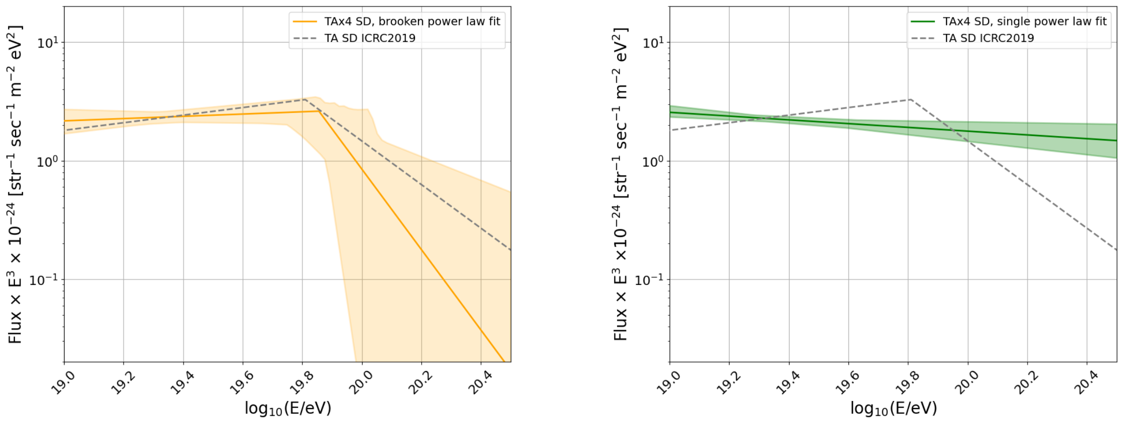

(A) The best-fit broken power law of the TA×4 SD observation (orange solid line).

(B) The best-fit single power law of the TA×4 SD observation (green solid line).

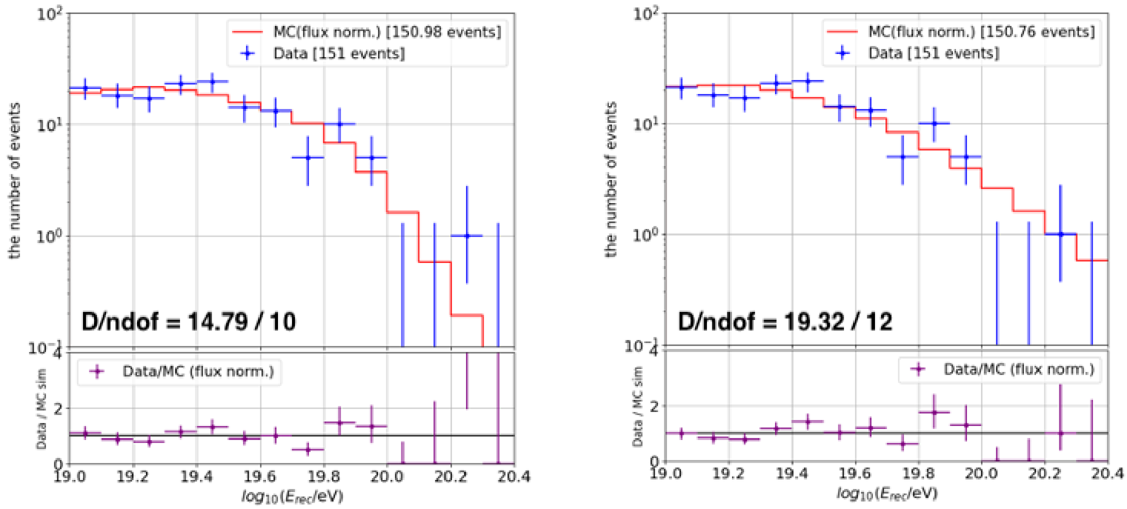

(C) The energy distribution of the observation and the expectation with the best-fit broken power law function (the upper panel).

(D) The energy distribution of the observation and the expectation with the best-fit single power law function (the upper panel).

FIGURE 7.10: (Top) The best-fit functions of a broken power law (top left) and a single power law (top right). The dashed lines are the best-fit function of TA SD observation [90]. (Bottom) The energy distributions of the observation (blue points) and the expectation by the MC simulation (red histograms) with the best-fit broken power law function (bottom left) and the best-fit single power law function (bottom right).

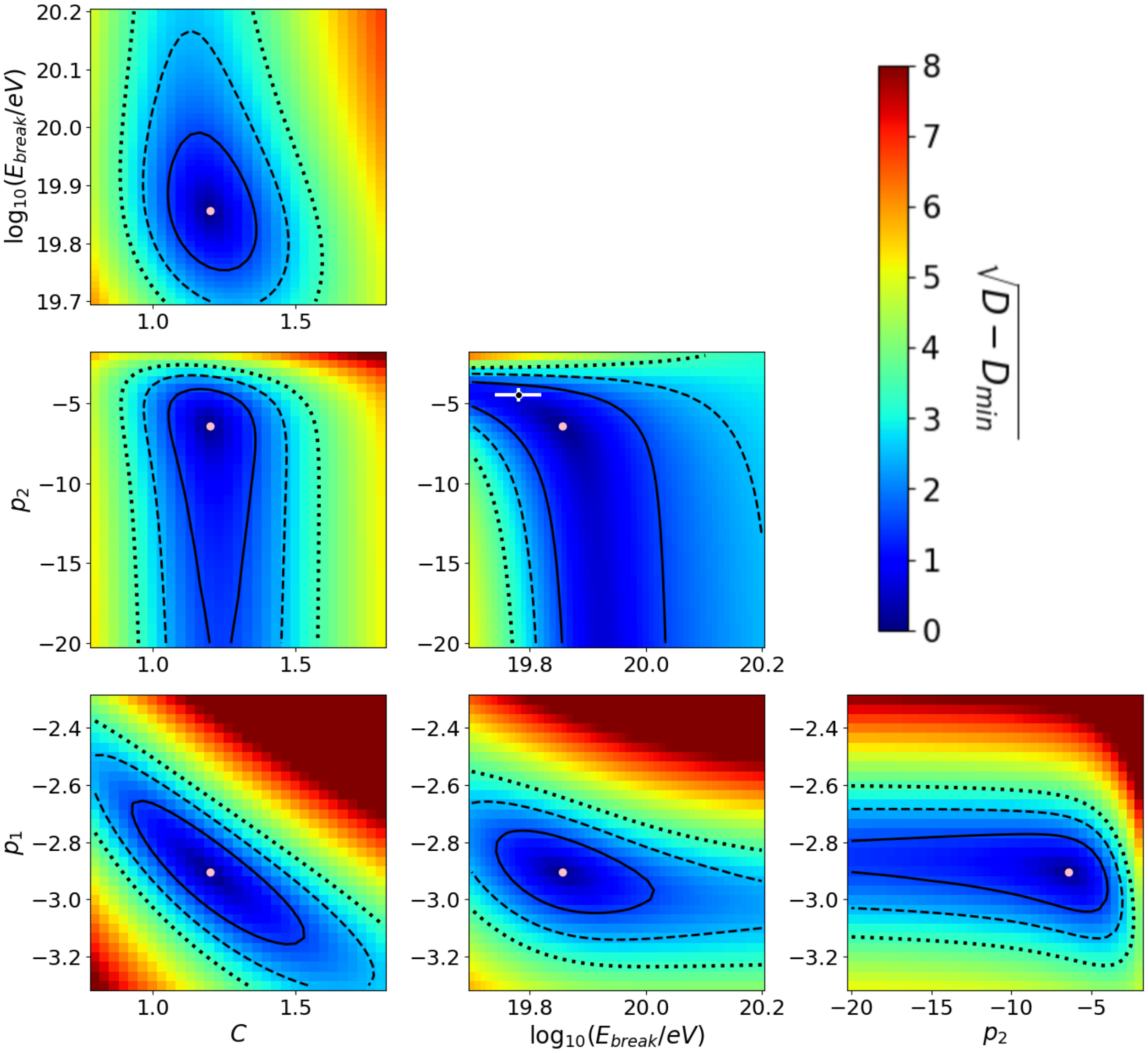

FIGURE 7.11: The two-dimensional deviation map of the broken power law fit with the three years of the TA×4 SD data. The color indicates the square root of the difference of D from the minimum deviance D_{min}. The contours represent 1σ, 2σ, and 3σ. The pink points indicate the best-fit parameters. The black point with a white error bar in the E_{break}-p_2 plot is the best-fit value and its uncertainty of the TA SD measurement [91]. The parameter C corresponds to the parameter $K_{\text{1-BPL}}$ in Eq. 7.15 by the following equation:

$$K_{\text{1-BPL (SPL)}} = 2.24 \times C \times 10^{-11-p_{1\,\text{(SPL)}}}\,[\mathrm{m^{-2}sr^{-1}s^{-1}eV^{-1}}] \qquad (7.19)$$

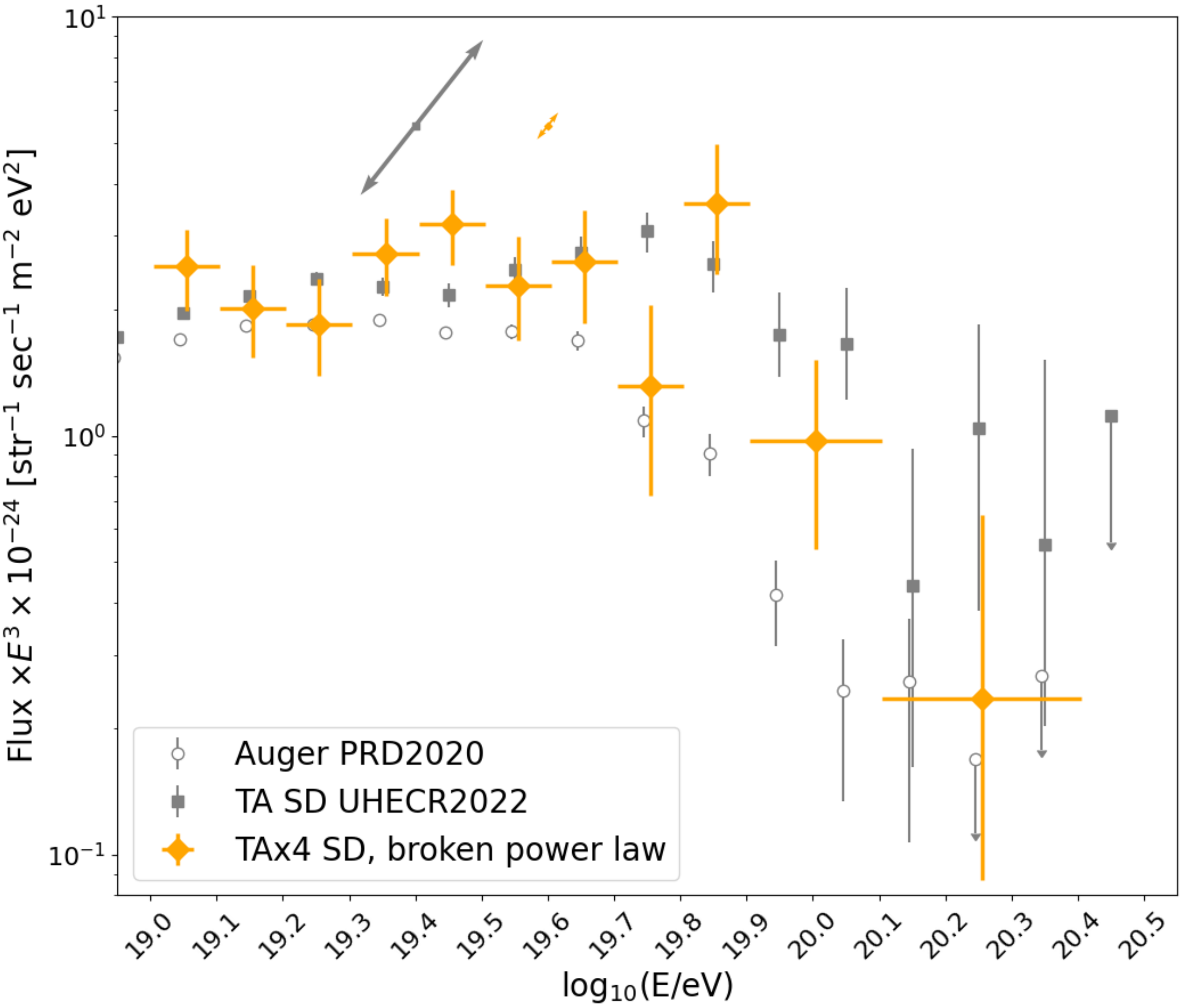

FIGURE 7.12: The cosmic ray energy spectrum measured by the TA×4 SD array with three years of observation with a broken power law function as an input spectral function (orange diamonds). Those measured by the TA SD [91] (gray squares) and the PAO [13] (open circles) are also shown. Each point is slightly shifted horizontally for better visibility. The thick gray arrow represents the uncertainty of the energy scale of the TA experiment. The thin orange arrow represents the uncertainty of the energy scale of the TA×4 SD array with respect to the TA energy scale.

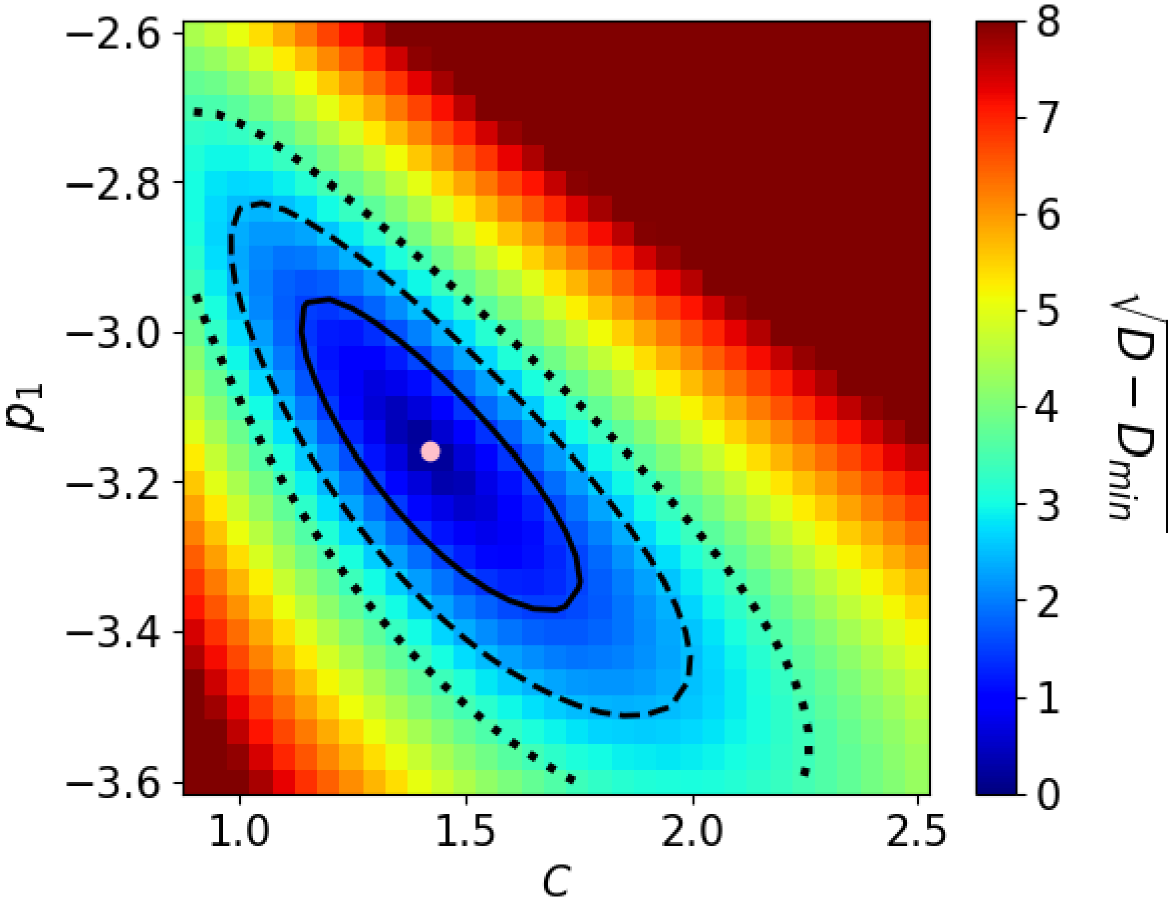

FIGURE 7.13: The two-dimensional deviation map of the single power law fit with the three years of the TA×4 SD data. The color indicates the square root of the difference of D from the minimum deviance D_{min}. The contours represent 1σ, 2σ, and 3σ. The pink point indicates a set of parameters (C, p_1) for the best fit. The parameter C corresponds to the parameter K_{SPL} in Eq. 7.14 by Eq. 7.19.

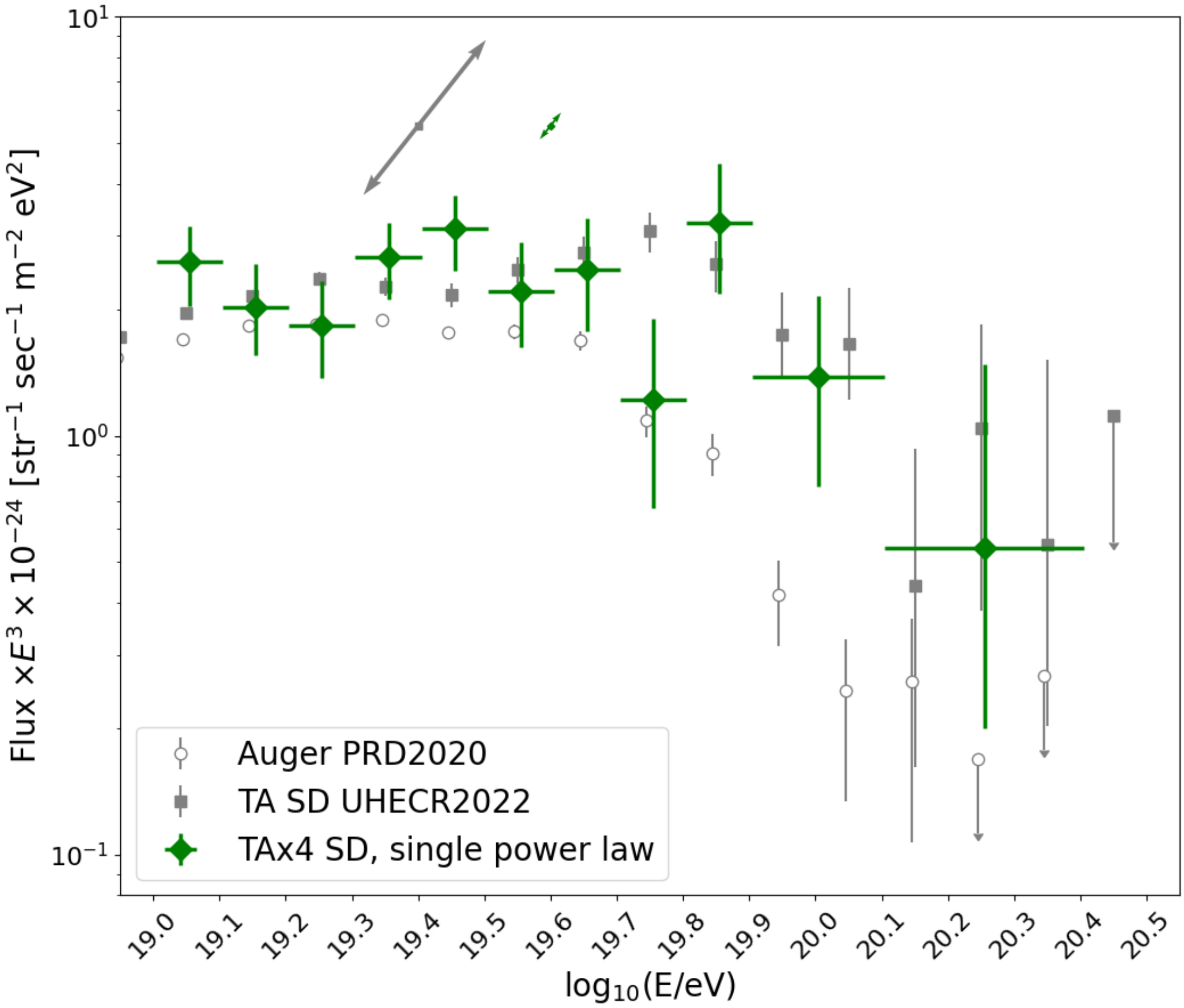

FIGURE 7.14: The cosmic ray energy spectrum measured by the TA×4 SD array with three years of observation with a single power law function as an input spectral function (green diamonds). Those measured by the TA SD [91] (gray squares) and the PAO [13] (open circles) are also shown. Each point is slightly shifted horizontally for better visibility. The thick gray arrow represents the uncertainty of the energy scale of the TA experiment. The thin green arrow represents the uncertainty of the energy scale of the TA×4 SD array with respect to the TA energy scale.

correction (AICc) [108] between the two models. AICc is calculated as follows:

$$\mathrm{AICc} = D + 2k + \frac{2k(k+1)}{n-k-1}, \tag{7.20}$$

where D is the deviance between the observation and the expectation by the MC simulation defined by Eq. 7.13, k is the number of free parameters ($k = 4$ for the broken power law function, and $k = 2$ for the single power law function), and n is the number of bins. The AICc is one of the indicators used to test how well a model reproduces data, and models with relatively small AICc are considered better.

Figure 7.10 shows the best-fit functions of the models, the energy distributions of the observation, and the expectation by the MC simulation with the best-fit functions. Table 7.3 shows the deviances and AICc of the two models. As seen in Tab. 7.3, the broken power law fit (p-value: 0.140, AICc: 23.06) is preferred compared with the single power law fit (p-value: 0.0811, AICc: 23.40). It indicates that the TA×4 SD array observed the cutoff of the cosmic ray energy spectrum independent of the TA SD, while neither of them is ruled out by this test.

7.3.3 Combined cosmic ray energy spectrum

In this subsection, we show the cosmic ray energy spectrum using the three years of TA×4 SD observational data and the 14 years of TA SD observational data using the forward-folding method. In this combined fitting, I do not weigh event-by-event as described in Sec. 5.3.1. Alternatively, I made E_{gen}/f vs. E_{rec} two-dimensional histograms for the TA SD array and six sub-arrays in the TA×4 SD array (Fig. 7.15). Each E_{gen}/f vs. E_{rec} two-dimensional histogram is made by binning MC events of the corresponding array with E_{gen}/f and E_{rec}. The bin widths of the two-dimensional histograms are $\Delta \log(E/\mathrm{eV}) = 0.02$ for both E_{gen}/f and E_{rec}, which is 1/5 of the bin width of the E_{rec} histograms to be fitted. The MC events are not weighted per event but per bin in the two-dimensional histograms. This method is introduced to reduce computation time.

As with the TA×4 SD analysis, the forward-folding is performed on multiple model functions: the broken power law with two and three breaks. The broken power law (BPL) function with n breaks ($n \geq 0$) is given as follows:

$$J_{\text{n-BPL}}(E) = K \sum_{i=0}^{n} \left[\theta(E_{i+1} - E)\theta(E - E_i)\big(E/\mathrm{EeV}\big)^{p_{i+1}} \prod_{j=0}^{i} \big(E_j/\mathrm{EeV}\big)^{p_j - p_{j+1}} \right], \tag{7.21}$$

where $E_0 = 0$, $E_{n+1} = \infty$, and $p_0 = 0$. The number of free parameters of the n-BPL function is $2n + 2$. The two break points in the 2-BPL function correspond to the ankle and the cutoff of the energy spectrum. The additional break point in the 3-BPL corresponds to the instep feature [13].

The energy regions used for the fit are $\log_{10}(E_{\mathrm{rec}}/\mathrm{eV}) > 19$ for the TA×4 SD and $\log_{10}(E_{\mathrm{rec}}/\mathrm{eV}) > 18.2$ for the TA SD. The uncertainty of the energy scale of the TA×4 SD relative to the TA energy scale is not considered here.

The best-fit values, the deviance, the p-value, and the AICc for each model are summarized in Tab. 7.4. The energy spectra calculated by Eq. 7.17 and the energy distributions of the observation and the expectation by the MC simulation with the best-fit functions are shown in Fig. 7.16 and Fig. 7.17. The two-dimensional deviance maps are shown in Fig. 7.18 and Fig. 7.19.

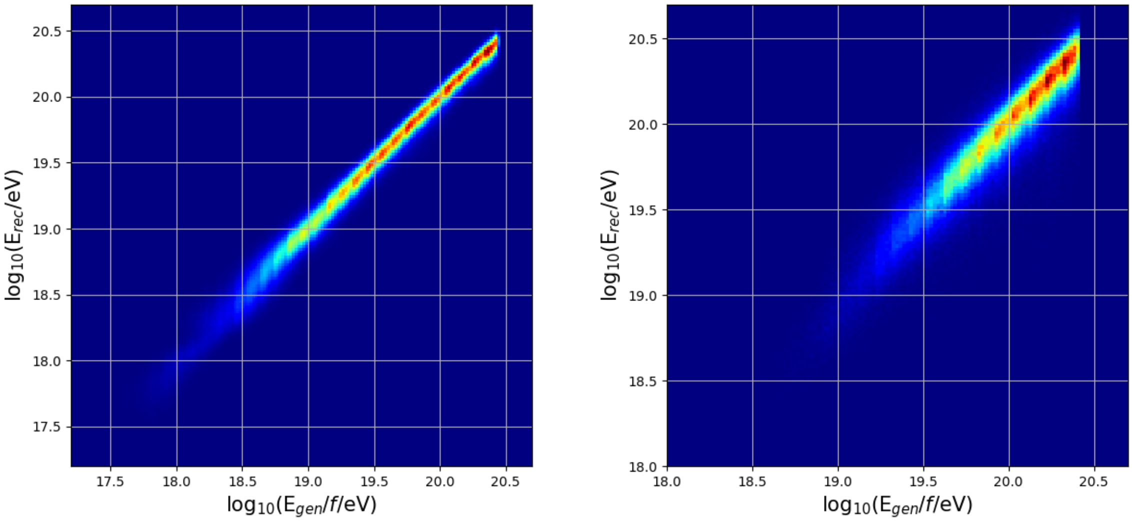

FIGURE 7.15: The E_{gen}/f vs. E_{rec} two-dimensional histograms of the TA SD array (left) and the SN sub-array in the TA×SD array (right). In each panel, the x-axis is the scaled generated energy (E_{gen}/f), the y-axis is the reconstructed energy E_{rec}, and the color is the number of events in the bin. The bin width of both axes is 0.02.

The table shows that the 3-BPL function (p-value: 0.246, AICc: 321) is preferred over the 2-BPL model (p-value: 0.0329, AICc: 478). It means that the UHECR energy spectrum in the northern sky also has a feature that corresponds to the instep feature reported in the southern sky by the PAO [13], which might indicate the interplay of light-to-intermediate nuclei following the rigidity-dependent acceleration at UHECR sources. The combined statistics of 15 years of the TA SD data and three years of the TA×4 SD data in the highest energy region are about double the nine years data of the TA SD, which was used in the recent combined fit of the energy spectrum and mass composition [20]. The combined fit of the energy spectrum and mass composition with the increasing statistics will allow us to estimate the characteristics of the UHECR sources, especially for the highest energy region, where the different source distribution between the northern and southern skies could be observed.

Cutoff significance

To calculate the significance of the cutoff in the energy spectrum, we use a test model, which is the same as the best-fit of the 2-BPL model except for the existence of the cutoff as shown in the left panel of Fig. 7.20. We calculate the number of events expected to be observed by the TA SD array and the TA×4 SD array with the test model in the energy range of $E_{\mathrm{rec}} > 10^{19.8}$ eV. In the energy range, 105 events are observed, while 188.7 events are expected to be observed with the test model without cutoff. The deviation corresponds to a significance of 8.2σ. It is the confirmation of the cutoff structure with the largest statistics in the Northern Hemisphere.

Systematic uncertainty due to calculation method

To check the systematic uncertainty due to the calculation method, we compared energy spectra using 14 years of the TA SD data with the previous analysis [91], which

TABLE 7.4: Best fit parameters and the goodness of fit for broken power law functions with n breaks (n-BPL). The uncertainties are evaluated for 1 d.o.f.

Function	**Parameter**	**Best fit value**	D**/ndof**	**p-value**	**AICc**
2-BPL	$K[\mathrm{m^{-2}sr^{-1}s^{-1}eV^{-1}}]$	$2.28^{+0.01}_{-0.01} \times 10^{-30}$	45.74/30	0.0329	478
	p_1	$-3.31^{+0.01}_{-0.01}$			
	$\log_{10}(E_1/\mathrm{eV})$	$18.64^{+0.01}_{-0.01}$			
	p_2	$-2.70^{+0.01}_{-0.01}$			
	$\log_{10}(E_2/\mathrm{eV})$	$19.78^{+0.03}_{-0.03}$			
	p_3	$-4.42^{+0.26}_{-0.28}$			
3-BPL	$K[\mathrm{m^{-2}sr^{-1}s^{-1}eV^{-1}}]$	$2.20^{+0.01}_{-0.01} \times 10^{-30}$	32.63/28	0.246	321
	p_1	$-3.27^{+0.01}_{-0.01}$			
	$\log_{10}(E_1/\mathrm{eV})$	$18.72^{+0.01}_{-0.01}$			
	p_2	$-2.53^{+0.02}_{-0.02}$			
	$\log_{10}(E_2/\mathrm{eV})$	$19.13^{+0.03}_{-0.03}$			
	p_3	$-2.87^{+0.03}_{-0.03}$			
	$\log_{10}(E_3/\mathrm{eV})$	$19.85^{+0.04}_{-0.03}$			
	p_4	$-4.55^{+0.36}_{-0.38}$			

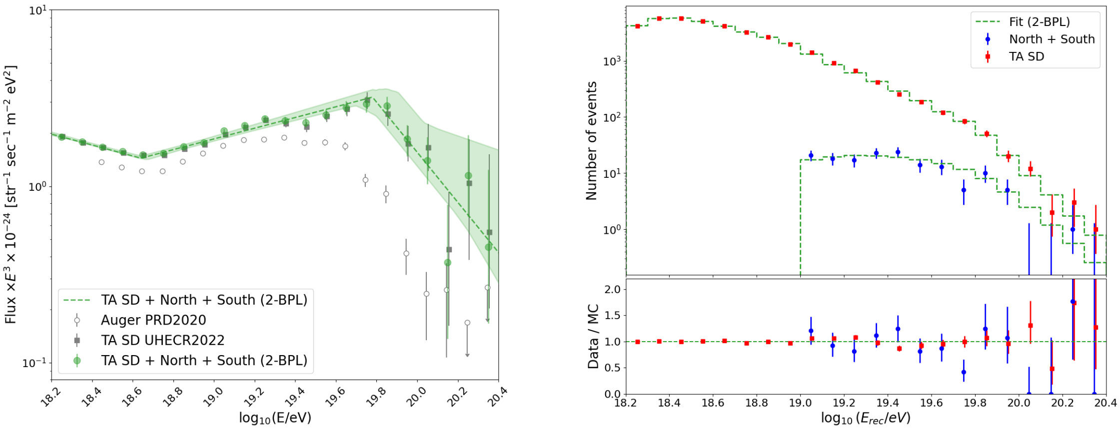

(A) The energy spectrum with the 2-BPL model.

(B) The event distributions with the 2-BPL model.

FIGURE 7.16: (Left) The energy spectrum measured combined with the 14 years of the TA SD data and the three years of the TA×4 SD data using the 2-BPL model. (Right) The energy distributions of the observation (blue for the TA×4 SD and red for TA SD) and the expectation by the MC simulation (histogram) with the best-fit function. The ratio of the number of observed events to that of expectation is shown at the bottom of the right figure.

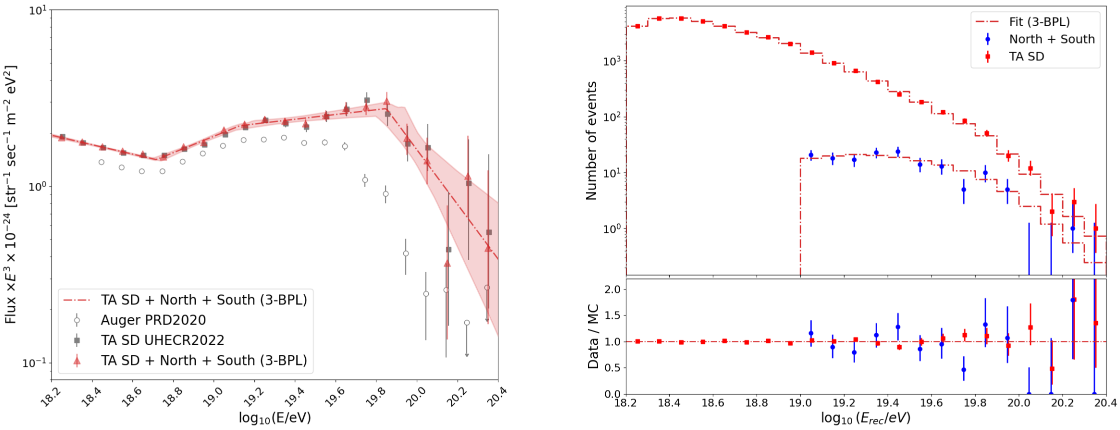

(A) The energy spectrum with the 3-BPL model.

(B) The event distributions with the 3-BPL model.

FIGURE 7.17: Same as Fig. 7.16, but for the 3-BPL model.

used the same data set of the TA SD. Figure 7.21 shows the systematic uncertainty dependent on the input spectrum. As seen in the figure, the systematic difference between the previous and this work's results is comparable to the statistical uncertainty below $10^{19.3}$ eV (up to around 5%). The systematic uncertainty due to the functional form in the forward-folding method is the same level or smaller than the systematic difference from the previous work. These results indicate that the systematic uncertainty due to the unfolding method is not very significant compared with statistical uncertainty in the highest energy region ($E > 10^{19.5}$ eV), where the energy spectrum difference between the TA and the PAO has been recognized (Fig. 1.6).

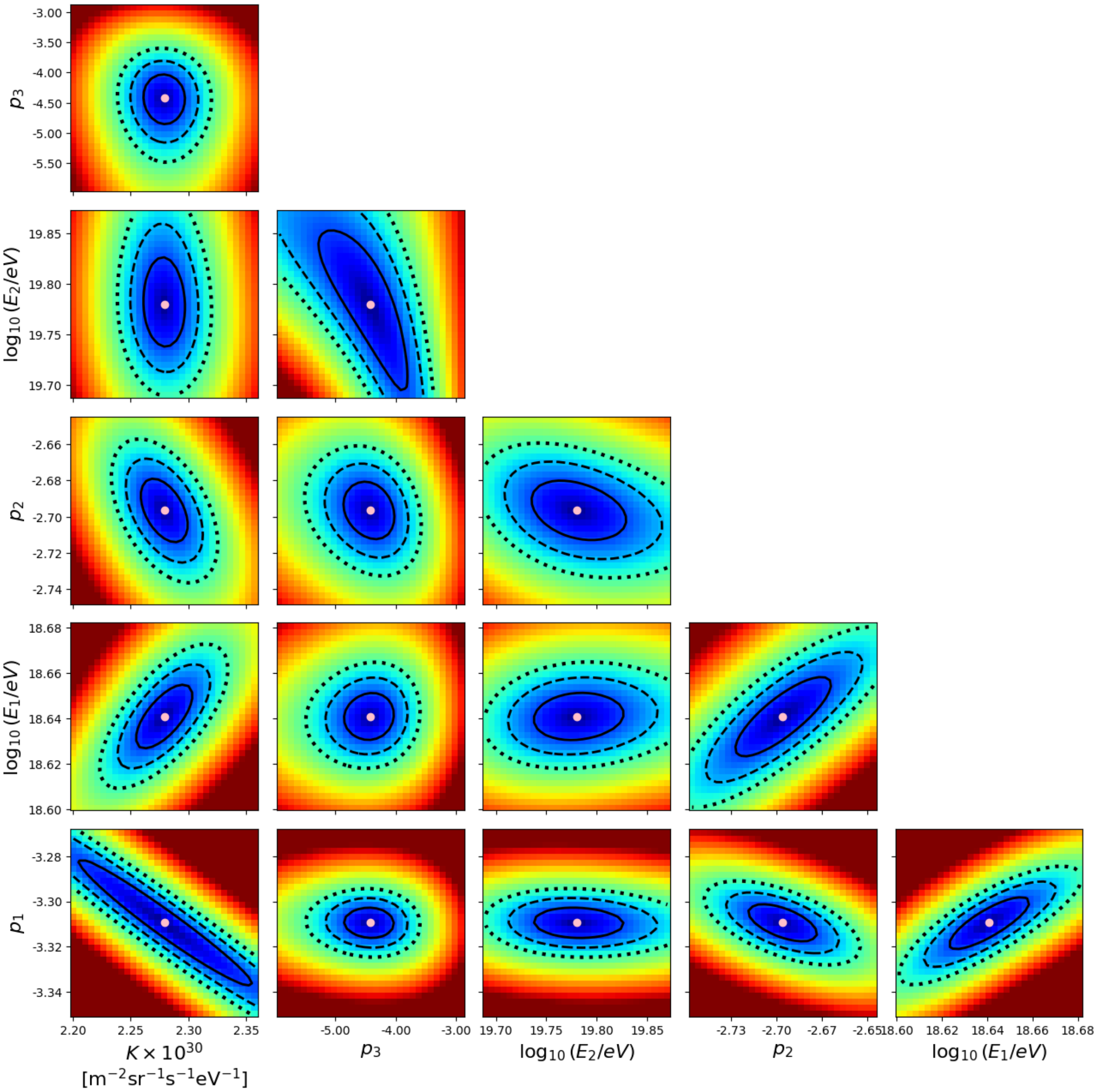

FIGURE 7.18: The two-dimensional deviation map of the 2-BPL model. The color indicates the square root of the difference of D from the minimum deviance D_{min}. The contours represent 1σ, 2σ, and 3σ. The pink points indicate the best-fit parameters.

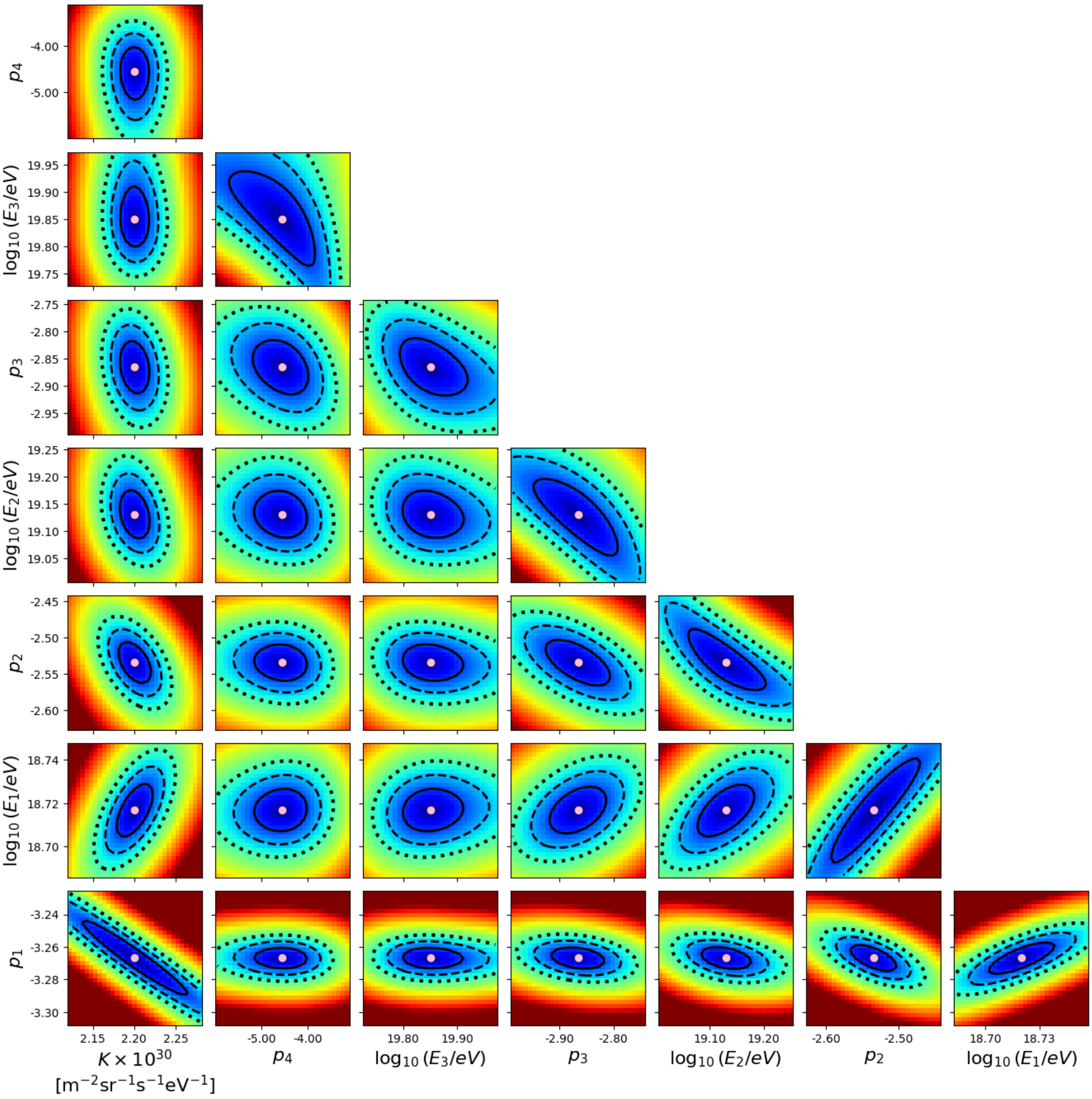

FIGURE 7.19: Same as Fig. 7.18, but for the 3-BPL model.

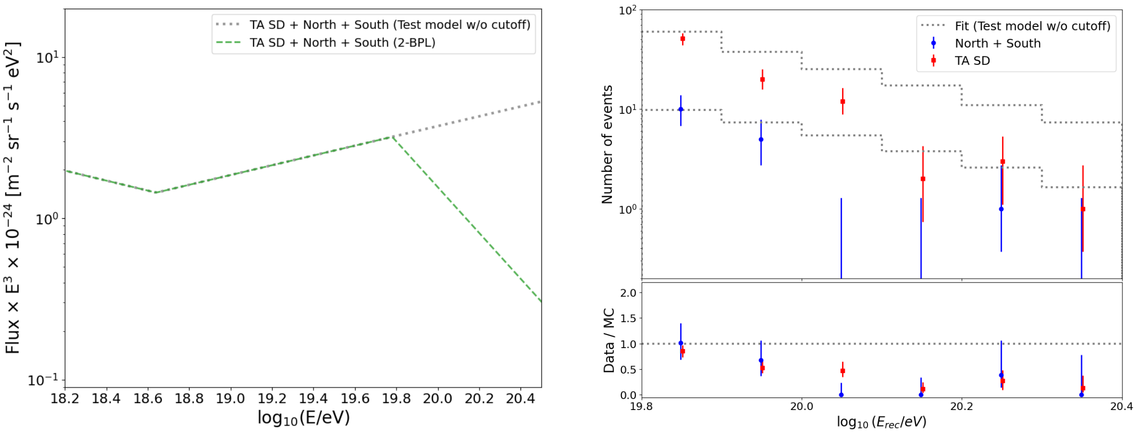

FIGURE 7.20: (Left) The test model without cutoff (gray dotted line) and the best-fit function of the 2-BPL model (green dashed line). (Right) The energy distribution of the observation (blue for the TA×4 SD and red for TA SD) and the expectation with the test model without cutoff (gray dotted histograms). The energy range is $E_{\rm rec} > 10^{19.8}$ eV.

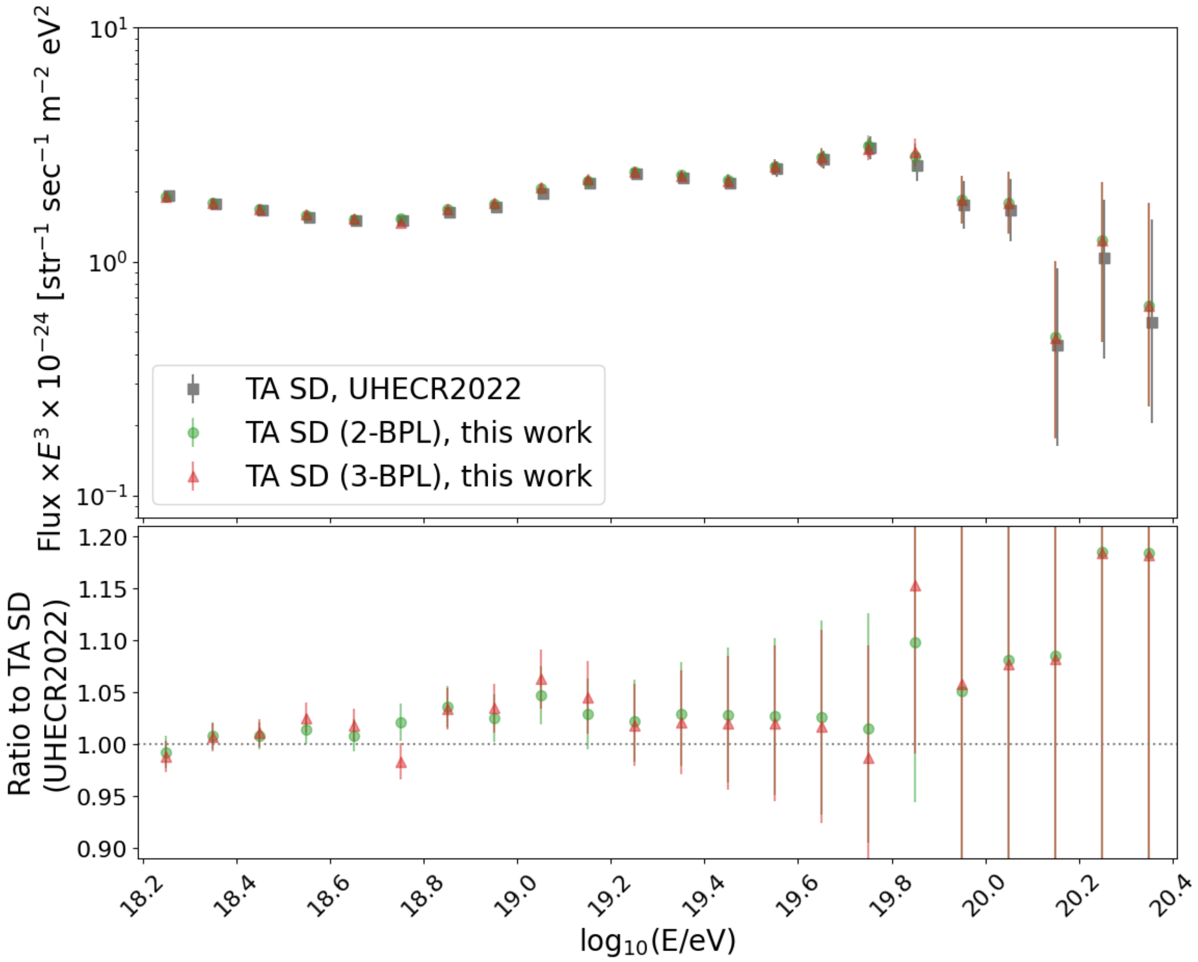

FIGURE 7.21: (Top) The energy spectra using the 14 years of the TA SD data. In the previous work (indicated by gray squares) [91], the energy spectrum observed by the HiRes experiment [18] is used as the input spectrum to calculate the bin-to-bin migration effect. Other energy spectra are calculated by the forward-folding method. (Bottom) The ratio of the energy spectra calculated by the forward-folding method to the previous work [91].

Chapter 8

The UHECR energy spectrum in the common declination band

Testing the anisotropy of the cosmic ray energy spectrum is an important mission of the TA×4 experiment, as well as testing the TA hotspot. In this chapter, we discuss the current topic of the spectral anisotropy: the difference of the UHECR energy spectrum in the declination band commonly observed by the TA experiment and the PAO.

As mentioned in Sec. 1.2.1, the difference between the shapes of the cosmic ray energy spectrum for $E > 10^{19.5}$ eV observed by the TA experiment and the PAO is under discussion. The difference might be due to the astrophysical origin: the different UHECR source distributions in the Northern sky, observed by the TA, and the Southern sky, observed by the PAO. To confirm that the difference is astrophysics, we must check if experimental uncertainties make the difference. One strategy to test and evaluate the experimental uncertainties of the TA and the PAO is performed by comparing the energy spectra in the common declination band, where both the TA and PAO observe. As reported in [21], there is a difference in the common declination band (Fig. 1.8).

However, the difference in exposure depending on the declination in the common declination band between the TA experiment and the PAO has not been considered in the previous study. The TA experiment observes the northern part of the common band more, while the PAO observes the southern part of the common band more (as described in Sec. 8.2). The energy spectra in the common band observed by both observatories could differ without considering the declination-dependent exposures if the energy spectrum in the common band depends on declination. In this work, we compare the UHECR energy spectra of both observatories, considering such declination dependence with a simple model for the first time. The data obtained by the TA SDs are used, and those obtained by the TA×4 SDs are not used in this chapter.

8.1 Directional exposure

The exposure of a cosmic ray observatory is a function on the celestial sphere, indicated by a set of right ascension α and declination δ, and it depends on the location of the observatory (longitude and latitude) if it is on the ground. We call the exposure as a function of (α, δ) as directional exposure denoted by $\omega(\mathbf{n})$, where $\mathbf{n}$ is the unit vector directed to (α, δ). The total exposure $X_{\rm tot}$ is expressed as

$$\begin{aligned} X_{\rm tot} &= \int d\mathbf{n}\omega(\mathbf{n}) \\ &= \int d\alpha \int d\delta\omega(\alpha,\delta)\sin(\pi-\delta). \end{aligned} \tag{8.1}$$

As far as we discuss exposure on a unit of sidereal day, the directional exposure ω is uniform with respect to the right ascension. Therefore, Eq. 8.1 can be simplified as

$$X_{\rm tot} = 2\pi \int d\delta\omega(\delta)\cos(\delta). \tag{8.2}$$

The functional form of $\omega(\delta)$ of an observatory which observes up to the zenith angle of $\theta_{\rm max}$ with full efficiency at latitude a_0 was derived by [109] as

$$\omega(\delta) = A \times T \times (\cos a_0 \cos\delta \sin\alpha_{\rm m} + \alpha_{\rm m} \sin a_0 \sin\delta), \tag{8.3}$$

where A and T are the area and the observational period of the observatory, respectively, and $\alpha_{\rm m}$ is given by

$$\alpha_{\rm m} = \begin{cases} 0 & \text{if } \xi > 1 \\ \pi & \text{if } \xi < 1 \\ \arccos\xi & \text{otherwise,} \end{cases} \tag{8.4}$$

$$\xi = \frac{\cos\theta_{\rm max} - \sin a_0 \sin\delta}{\cos a_0 \cos\delta}. \tag{8.5}$$

8.2 Directional exposure of the TA experiment and the Pierre Auger Observatory

Figure 8.1 shows the relative directional exposure $\tilde{\omega}(\delta) = \omega(\delta)/(A \times T)$ of the TA experiment ($a_0 = 39.3^\circ$, $\theta_{\rm max} = 55^\circ$) and the PAO ($a_0 = -35.2^\circ$, $\theta_{\rm max} = 60^\circ$). Similarly, Fig. 8.2 shows $\tilde{\omega}(\delta) \times \cos\delta$, which is proportional to the exposure at the declination (δ). $\tilde{\omega}(\delta) \times \cos\delta$ (Fig. 8.2) is proportional to the event distribution with respect to the declination if the cosmic rays are isotropic. The figures indicate that the exposure depends on declination, and the dependence on declination differs between the experiments. For example, Fig. 8.2 shows that only 5% of the number of events observed by the TA in the common band is expected to be from $\delta < -10^\circ$. On the other hand, the PAO is expected to observe 22% of the number of events in the common band from $\delta < -10^\circ$. In general, the TA observes the northern part of the common band more, and the PAO observes the southern part more. If the energy spectrum of the common declination band varies with declination, the energy spectra of the common band observed by the TA and PAO could be different without considering the declination-dependent exposures. The evaluation of the difference without considering the declination-dependent exposures is given in Sec. 8.3.1. The hypothesis that the energy spectrum of the common declination band varies with declination is reasonable since the declination-dependent anisotropy of the energy spectrum was reported by the TA experiment [23].

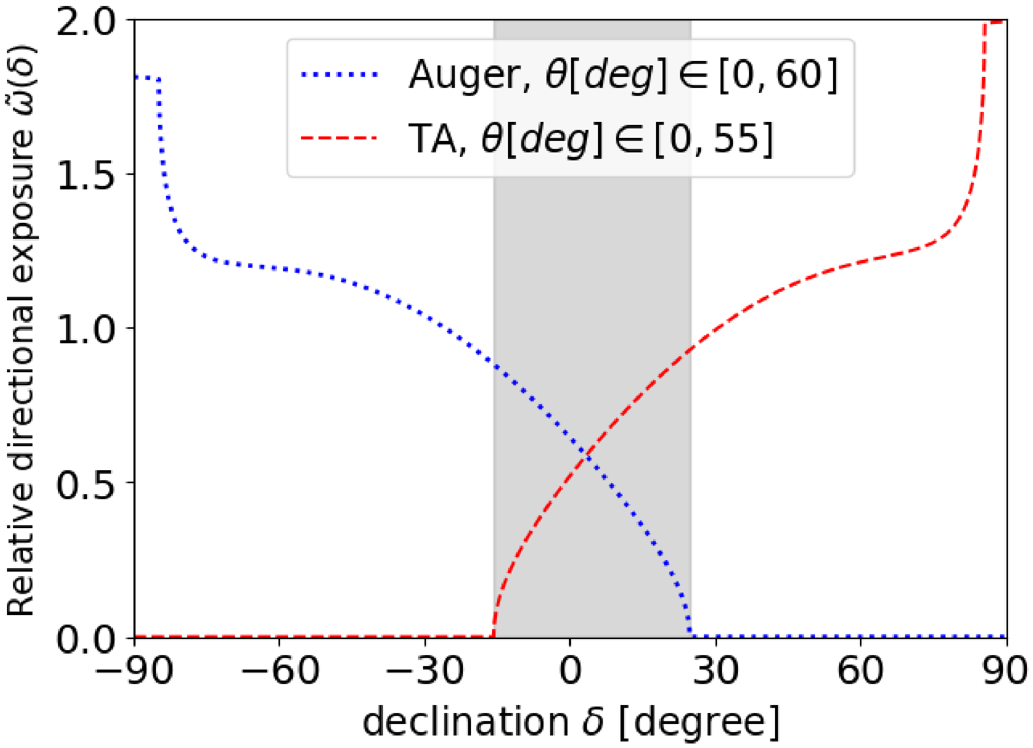

FIGURE 8.1: The relative directional exposure $\tilde{\omega}(\delta) = \omega(\delta)/(A \times T) = \cos a_0 \cos\delta \sin\alpha_{\mathrm{m}} + \alpha_{\mathrm{m}} \sin a_0 \sin\delta$ of the TA experiment (red dashed line) and the PAO (blue dotted line), where $\omega(\delta)$, A, and T are the directional exposure, aperture and observational period of the experiment. The common declination band, which is observed by both observatories ($\delta \in [-15.7°, 24.8°]$), is shown by a gray band.

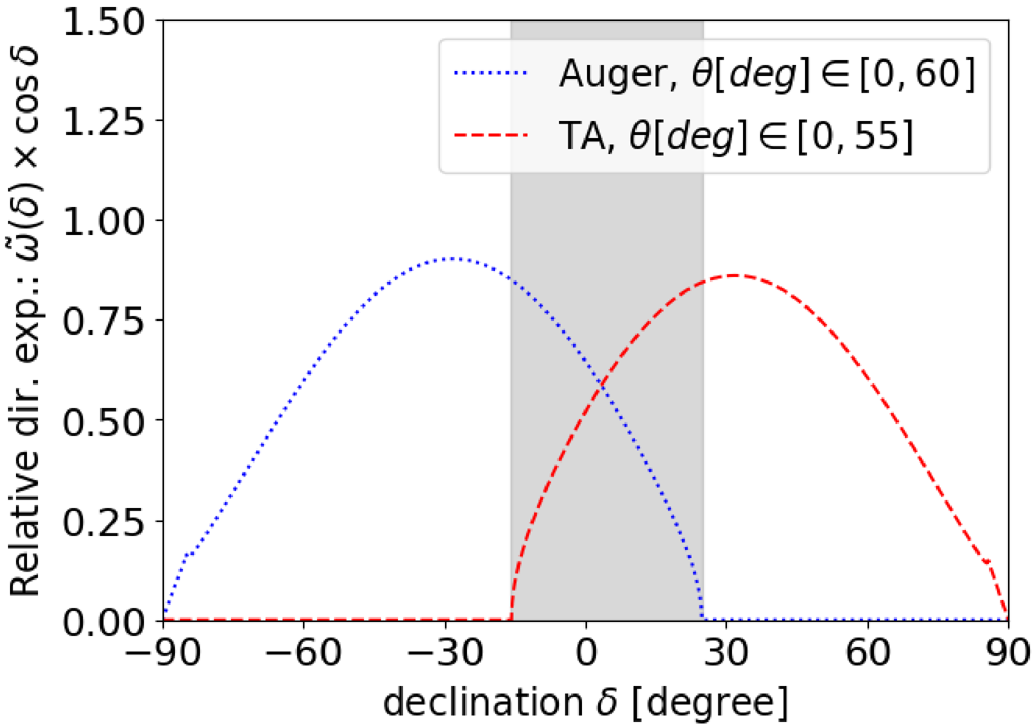

FIGURE 8.2: The relative directional exposure $\tilde{\omega}(\delta)$ multiplied by $\cos\delta$ of the TA experiment (red dashed line) and the PAO (blue dotted line). The arrival direction distribution in declination of UHECRs follows $\tilde{\omega}(\delta) \times \cos\delta$ if they arrive isotropically. The common declination band, which is observed by both observatories ($\delta \in [-15.7°, 24.8°]$), is shown by a gray band.

a

8.3 Comparison of the UHECR energy spectra in common declination band

8.3.1 Comparison without considering declination-dependent exposure

At first, we compare the energy spectra in the common declination band in the same way as the previous study [21] with the updated data set of the TA SD: 14 years of the observational data (from 11th May 2008 to 10th May 2022). The energy spectrum of the PAO is taken from the data shared by the Auger-TA co-working group. The data set of the PAO is the same data set as [13] (collected from 1st January 2004 to 31st December 2017).

Figure 8.3 shows the energy spectrum of each observation in the common declination band. The energy scale of the TA experiment is shifted by $(1.045)^2 = 1.092$, which is within the absolute energy scale uncertainty of each experiment (21% for the TA experiment and 14% for the PAO). This energy-independent shift ($\pm 4.5\%$ shift for both the TA and the PAO) was used in the previous study [21] to match the energy spectra below $10^{19.5}$ eV within the systematic uncertainty quoted by the experiments. In this study, only the energy of the TA experiment is shifted since we only have the event set of the TA SDs. The TA energy spectrum is shown above $10^{18.9}$ eV since the efficiency of the TA SD is 100% above this energy.

A chi-square test was performed to test the difference in the energy spectra in the common band. The chi-square was calculated by

$$\chi^2_{\text{prev}} = \sum_i \frac{[F^{\text{TA, common}}(E_i) - F^{\text{PAO, common}}(E_i)]^2}{\sigma^2_{i\,\text{TA, PAO}}}, \tag{8.6}$$

where $F^{\text{TA, common}}$ and $F^{\text{PAO, common}}$ are cosmic ray flux observed by the TA and PAO in the common band, respectively, and $\sigma_{i\,\text{TA, PAO}}$ is the summation of the statistical uncertainties of the TA and the PAO in quadrature. The index i is from the bin $E = 10^{18.95}$ eV to $E = 10^{20.15}$ eV (13 bins) where the efficiency is 100% and there is at least one event in the bin for both experiments. $\chi^2_{\text{prev}}/\text{ndof}$ is 36.28/13, and the p-value is 5.37×10^{-4}, corresponding to a significance of 3.5σ. There is a difference between the energy spectra in the common declination band even after energy-independent scaling without considering exposure dependence on declination. The exposure dependence on declination must be tested.

8.3.2 Simple mixing model in the common declination band

To consider the declination-dependent exposure as seen in Fig. 8.2, we introduce a simple model in which the energy spectrum in the common declination band is a mixture of the TA energy spectrum on the northern side and the PAO energy spectrum on the southern side, bounded by a certain declination δ_{border}. In particular, the energy spectra outside of the common band are used for the mixing: the cosmic ray flux observed by the TA ($24.8^\circ < \delta < 90^\circ$) denoted as $F^{\text{TA}, \delta > 24.8^\circ}$ on the northern side and the PAO ($-90^\circ < \delta < -15.7^\circ$) denoted as $F^{\text{PAO}, \delta < -15.7^\circ}$ on the southern side (see Fig. 8.4), bounded by δ_{border}. With this simple mixing model, we can calculate the number of events in the i-th energy bin observed by the TA and the PAO in

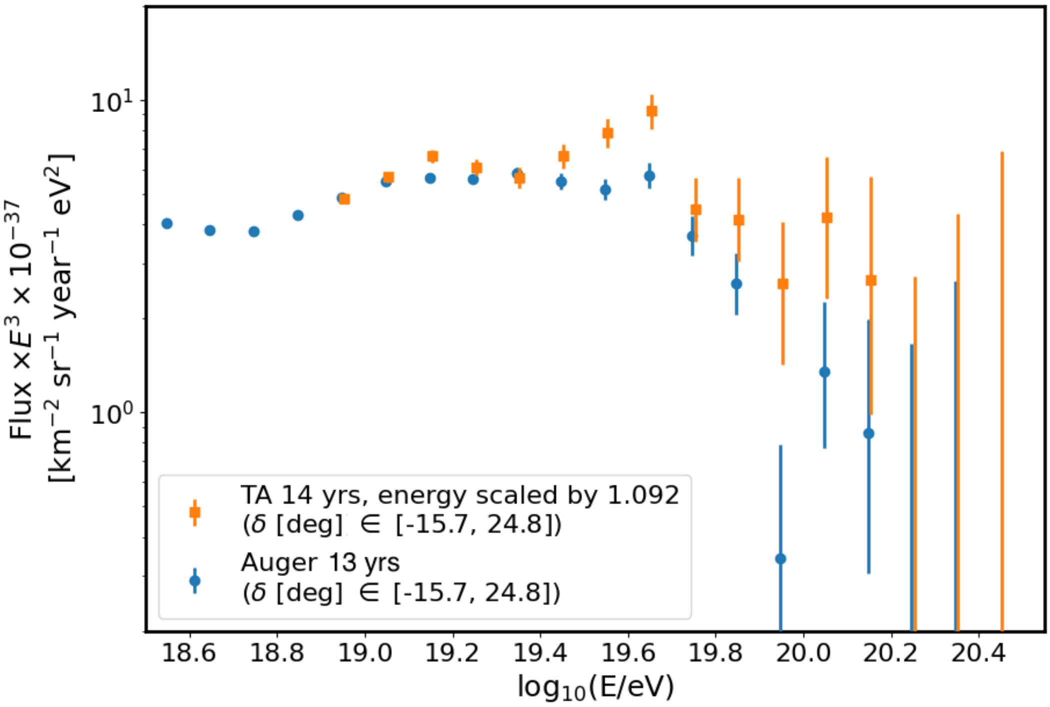

FIGURE 8.3: The cosmic ray energy spectra measured by the TA experiment (orange square) and the PAO (blue circle) in the common declination band.

the common band as a function of δ_{border} as follows:

$$\begin{aligned} N_i^{\text{TA, exp}} &= [f_{\text{south}}^{\text{TA}}(\delta_{\text{border}}) F^{\text{PAO}, \delta<-15.7^\circ}(E_i) + (1 - f_{\text{south}}^{\text{TA}}(\delta_{\text{border}})) F^{\text{TA}, \delta>24.8^\circ}(E_i)] \\ &\quad \times \Delta E_i \times X^{\text{TA, common}}(E_i) \qquad (8.7) \\ N_i^{\text{PAO, exp}} &= [f_{\text{south}}^{\text{PAO}}(\delta_{\text{border}}) F^{\text{PAO}, \delta<-15.7^\circ}(E_i) + (1 - f_{\text{south}}^{\text{PAO}}(\delta_{\text{border}})) F^{\text{TA}, \delta>24.8^\circ}(E_i)] \\ &\quad \times \Delta E_i \times X^{\text{PAO, common}}(E_i) \qquad (8.8) \end{aligned}$$

where $X^{\text{TA(PAO), common}}(E_i)$ is the exposure of the TA (PAO) of the i-th energy bin whose bin width is ΔE_i. The exposure fraction of the south side $f_{\text{south}}^{\text{TA (PAO)}}(\delta_{\text{border}})$ in the equations is given by

$$f_{\text{south}}^{\text{TA (PAO)}}(\delta_{\text{border}}) = \int_{-15.7^\circ}^{\delta_{\text{border}}} d\delta\, \tilde{\omega}^{\text{TA (PAO)}}(\delta) \cos(\delta). \qquad (8.9)$$

The optimum δ_{border}, with which the difference in the energy spectra in the common band is minimized in this model, is determined by minimizing the following chi-square:

$$\begin{aligned} \chi^2 &= \chi^2_{\text{TA}} + \chi^2_{\text{PAO}} \\ &= \sum_{m \in [\text{TA,PAO}]} \sum_i \frac{[N_i^{m,\text{obs}} - N_i^{m,\text{exp}}]^2}{\sigma^2_{i,m,\text{obs}} + \sigma^2_{i,m,\text{exp}}}, \qquad (8.10) \end{aligned}$$

where $N_i^{m,\text{obs}}$ and $\sigma^2_{i,m,\text{obs}}$ are the number of events of observation $m \in [\text{TA}, \text{PAO}]$ of the i-th energy bin and its statistical uncertainty, respectively. The uncertainty of the

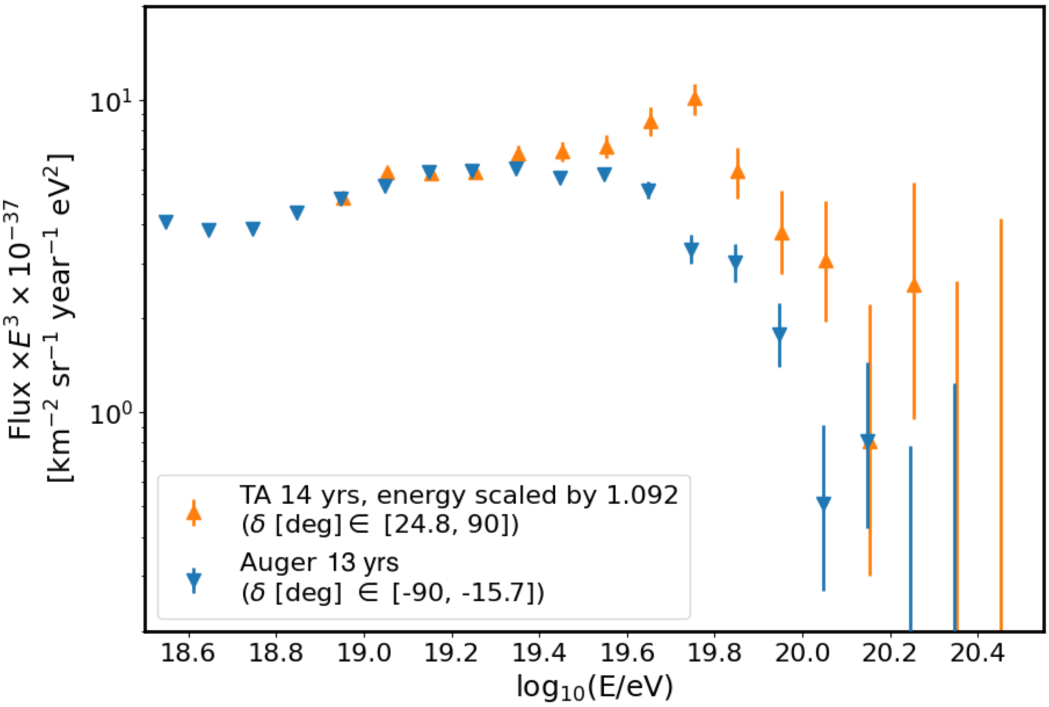

FIGURE 8.4: The comic ray energy spectra in the region excluding the common declination band of the TA (orange upward triangle) and the PAO (blue downward triangle). The energy of the TA is scaled by 1.092.

TABLE 8.1: The chi-squares and p-values of two tests: the previous model (described in Sec. 8.3.1) and the simple mixing model (described in Sec. 8.3.2).

model	χ^2	**ndof**	**p-value (corresponding significance)**
Previous model	36.28	13	5.37×10^{-4} (3.5σ)
Simple mixing model	41.03	25	2.28×10^{-2} (2.2σ)

expected number of events $N_i^{m,\,\mathrm{exp}}$ given by Eq. 8.7 and Eq. 8.8 is from the statistical uncertainty of the cosmic ray flux $F^{\mathrm{TA},\,\delta>24.8^\circ}$ and $F^{\mathrm{PAO},\,\delta<-15.7^\circ}$.

We found that the optimum δ_{border} is 18.15°, and the chi-squares are $\chi^2_{\mathrm{TA}} = 22.24$, $\chi^2_{\mathrm{PAO}} = 18.79$. The summation χ^2 is 41.03 with $13 \times 2 - 1 = 25$ degrees of freedom. The p-value is 2.28×10^{-2}, which corresponds to a significance of 2.2σ. Figure 8.5 shows the comparisons of the number of events with the optimum declination. Table 8.1 shows the results of the test of comparison for two models: the previous model (not considering the declination-dependent exposure) and the simple mixing model.

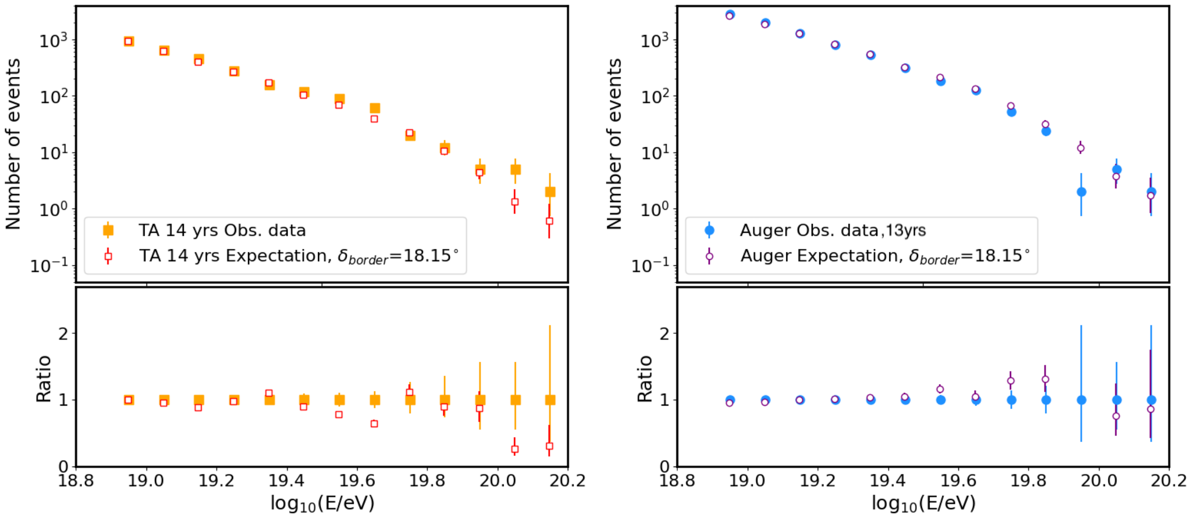

FIGURE 8.5: The number of events expected by the best fit of the simple mixing model (opened points) and those of the observation (filled points) for the TA experiment (left) and the PAO (right). The bottom figures show the ratio of the expectation to the observation.

8.4 Summary and conclusion of this chapter

A difference between the energy spectra observed in the full fields of view of the TA and PAO is recently known, however, the reason of the difference is not understood. The spectral anisotropy might reflect the different UHECR source distributions in the fields of view of the experiments. It is necessary to confirm that there is no systematic bias between the experiments. One strategy to check the systematic effect is the comparison of the energy spectra in the common field of view (common band). If there is no systematic bias between the experiments, the energy spectra in the common band should agree. However, the statistical significance of the difference in the energy spectra in the common band is found to be 3.5σ with the previous comparison method. It indicates that there are systematic effects which might cause the spectral difference in the full fields of view of the experiments.

In this work, we have compared the energy spectra in the common band considering one of the possible systematic effects: the declination-dependent exposure, which has not been considered in the previous comparison, with the simple mixing model. With the model, the statistical significance of the spectral difference in the common band is reduced to be 2.2σ. The significance of 2.2σ is still not small, and it does not fully explain the spectral difference in the full fields of view of the TA and the PAO shown in Fig. 1.4. We still need to understand the source of 2.2σ difference with other systematic effects or with more sophisticated model, but the reduction of the statistical significances (3.5σ and 2.2σ) with the simple model indicates that the effect of the declination-dependent exposure is important when we compare the energy spectra in the common declination band.

This study is the first step to consider the declination-dependent exposure for the first time with the simple model. In future, comparisons with more realistic model or model-independent comparisons have to be performed. For example, a model-independent comparison can be performed by weighting observed events on event-by-event basis according to the declination of the observed events to exclude the effect of the declination-dependent exposure; the weights are smaller for the north and larger for the south in the case of the TA, and larger for the north and smaller for the south in the case of the PAO. In addition to the improvements on the analysis method, the TA×4 SD data will increase the statistics and make statistically more precise comparisons possible.

Chapter 9

Future projections

In this chapter, we discuss the future projections of the observational results, expected to be measured by the extended SD array — the TA×4 SD array — and the TA SD array based on the performance described in this paper. Topics that have to be pursued by the TA×4 experiment, the spectral anisotropy and the TA hotspot, are discussed. Note that the TA×4 SD array means the extended surface detector array, consisting of the TA×4 North array and the TA×4 South array (Fig. 4.1). In the following calculation, we assume the following status;

- The TA×4 SD array completes its construction and starts observation on 1st November 2025. Before the date, the performance of the TA×4 SD array is the average status of the TA×4 SD array with the full inter-tower trigger from 1st June 2023 to 31st July 2023, where above 90% of the SDs work fine. After the date when the expansion is completed, the event rate of the TA×4 SD array is twice the rate before the date.
- The status of the TA SD array is the average of that over the 15 years.

Following the above scenario, the number of events expected to be observed by the TA×4 North and South arrays as of October 2025 and October 2030 are shown in the left panel of Fig. 9.1. The expectation of the sum of the TA×4 North, South, and TA SD arrays are shown in the right panel of Fig. 9.1. In the expectation, the TA SD energy spectrum [90] is assumed. As seen in the right panel of Fig. 9.1, the number of events with energies greater than $10^{19.5}$ eV observed by the TA×4 SD array and TA SD array is expected to be about three times the current number in 2030.

9.1 Projections of the energy spectrum

In this section, projections of the observation of the cosmic ray energy spectrum are discussed in terms of two points: (1) the cutoff significance measurement by the TA×4 SD array and (2) the spectral anisotropy observed by the TA experiment. Figure 9.2 shows the cosmic ray energy spectrum with expected statistical uncertainties, which are calculated by the number of events (Fig. 9.1).

9.1.1 Cutoff significance expected to be measured by the TA×4 SD

In Sec. 7.3, we showed that the cosmic ray energy spectrum with energies greater than 10^{19} eV measured by the TA×4 SD array favors the broken power law model whose cutoff position is consistent with the previous TA SD observation over the single power law model (Tab. 7.3). However, the single power law model is not statistically ruled out by only the TA×4 SD array. The p-values of the single power law model expected to be measured by the TA×4 SD array are shown in Tab. 9.1.

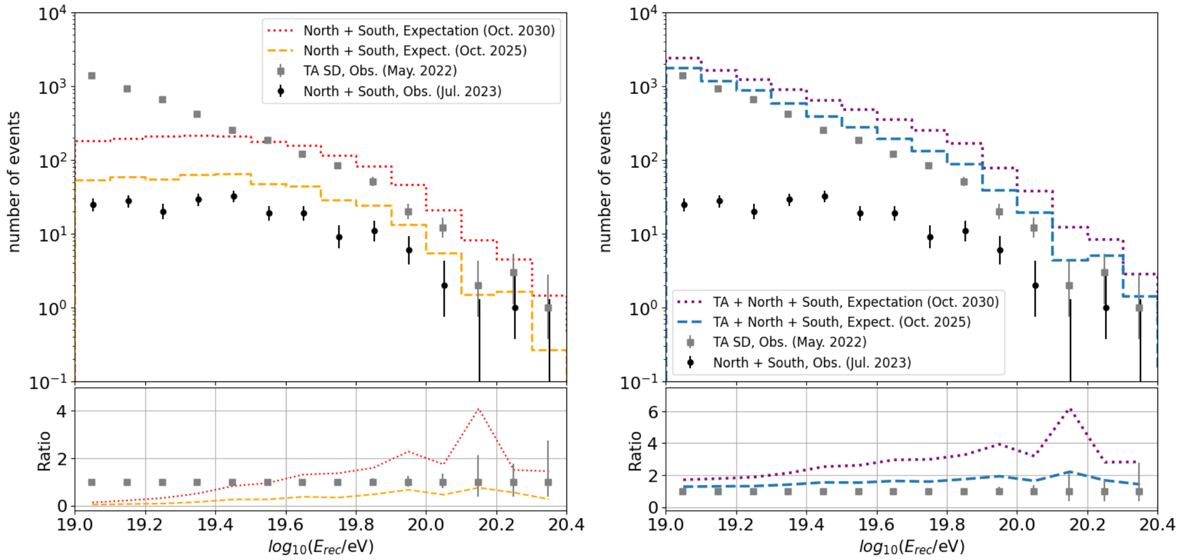

FIGURE 9.1: (Left) The numbers of events to be observed by the TA×4 SD North and South arrays as of October 2025 (dashed orange) and October 2030 (dotted red). (Right) Same as left, but the expectation of the sum of TA×4 SD North, South, and TA SD arrays. In both figures, the numbers of events observed by the TA SD (gray squares) and the TA×4 SD North and South arrays (black circles) are shown. The bottom figures show the ratio of the expected number of events to the number of events observed by the TA SD array.

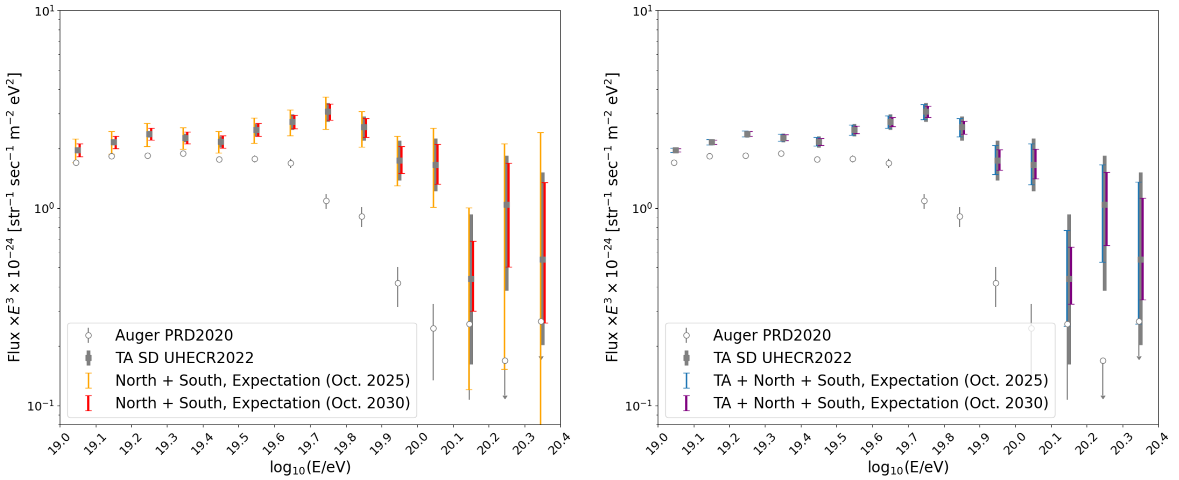

FIGURE 9.2: The energy spectrum observed by the TA×4 North and South SD arrays (left) and the sum of the TA×4 North, South, and the TA SD arrays (right) with expected statistical uncertainties.

TABLE 9.1: The deviance D and p-value of the fit with single power law model expected to be measured by the TA×4 SD array for three observational periods: until October 2025, October 2028, and October 2030.

Period	D/ndof	p-value (corresponding significance)
- Oct. 2025	17.7/12	0.13 (1.5σ)
- Oct. 2028	33.1/12	9.2×10^{-4} (3.3σ)
- Oct. 2030	46.9/12	4.9×10^{-6} (4.6σ)

The calculation method is the same forward folding method described in Sec. 7.3.1. As seen in the Tab. 9.1, the single power law model would be disfavored with a significance of above 3σ with the TA×4 SD data in 2028.

9.1.2 Spectral anisotropy

As described in Sec. 1.2.1, the anisotropy of the cosmic ray energy spectrum in the field of view of the TA experiment has been reported [23]; the energy spectrum differs between the common declination band ($\delta \in [-15.7°, 24.8°]$) and the TA-only declination band ($\delta \in [24.8°, 90°]$). In this subsection, we discuss the spectral anisotropy observed by the TA SD array and expected to be observed by the TA SD array and the TA×4 SD array.

To test the significance of the spectral difference, we simultaneously fit two data sets of the different declination bands to test a null hypothesis that there is no difference between the energy spectra in the two declination bands. The forward-folding method is used for the fitting. The fitted energy range is $E > 10^{18.9}$ eV.

Figure 9.3 shows the energy spectra in the two declination bands observed by the TA experiment with 14 years of the observational data. In the figure, the solid black line is the best-fit function to simultaneously fit the two data sets. The deviance is $D = 49.2$, and the number of degrees of freedom is 26 (the right panel of Fig. 9.3). The p-value of the chi-square test for the null hypothesis that there is no spectral difference between the two declination bands is approximately 3.94×10^{-3}, which corresponds to a significance of 3.4σ.

In 2025, the statistics of the combined data of the TA SD and TA×4 SD arrays would be around 1.6 times larger than the current statistics of the TA SD array, as seen in the right panel of Fig. 9.1. Therefore, the deviance would be expected to be $D \sim 49 \times 1.6 \sim 78$ with 26 degrees of freedom, assuming that the difference actually exists. The p-value of the chi-square test would be $\sim 4.3 \times 10^{-7}$, corresponding to a significance of $\sim 5.0\sigma$.

In 2030, the statistics would be about three times larger than the current statistics for $E > 10^{19.5}$ eV. With these statistics, we can search spectral anisotropy with more divided declination bands or areas. In particular, the spectral anisotropy test for six different sky regions would be possible with the same statistical power as the current analysis (a significance of $\sim 3\sigma$). We could test contributions from source candidates of UHECR more precisely with the test.

9.2 Projections of the TA hotspot

In this section, we calculate the expected number of events from the TA hotspot region with two models. One is the model where the event rate is constant averaged over the 15 years of the observation of the TA SD array, and the other one is the

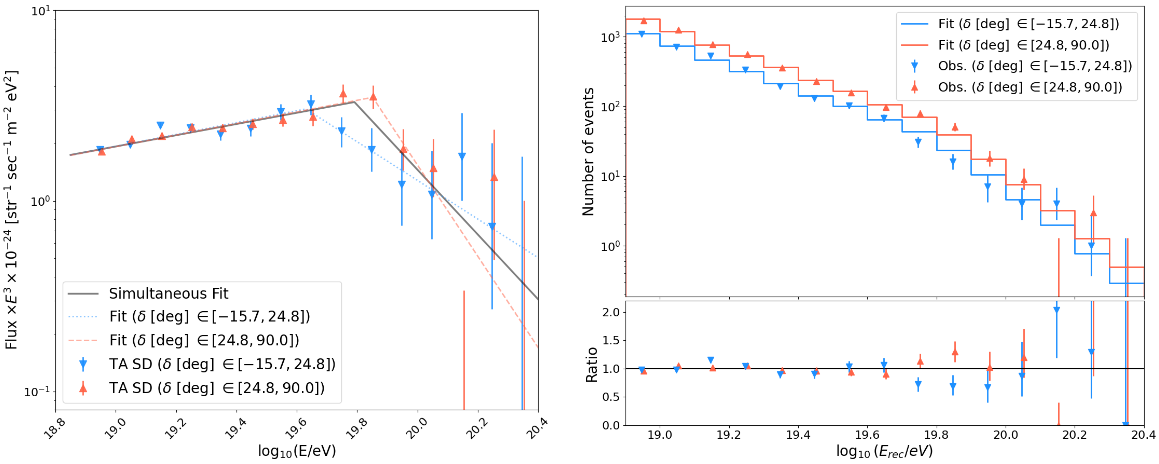

FIGURE 9.3: (Left) The energy spectra observed by the TA SD array with 14 years of the observation in the common declination band ($\delta \in [-15.7^\circ, 24.8^\circ]$) shown in blue and the TA-only declination band ($\delta \in [24.8^\circ, 90^\circ]$) shown in red. The dotted blue line and the dashed red line are the best-fit functions in the corresponding declination bands. The solid black line is the best-fit function to fit both declination bands simultaneously. (Right) The energy distribution of the observation (points) and the expectation with the simultaneous fit (histograms). The bottom panel of the right figure is the ratio of the observation to the expectation.

model with the event rate averaged over the last 8 years of observation of the TA SD array.

We consider the latter model since the event rate from the TA hotspot region appears to decrease in the last 8 years compared with the first 7 years until 2015 as seen in the left panel of Fig. 9.4. In particular, the significance of ruling out the hypothesis that the TA hotspot is stationary is 1.2σ with the 15 years of the TA SD observation. This significance is calculated as follows:

1. Calculate the maximum deviance D from the stationary-rate hypothesis by

$$D = 2\left(N_{\rm stat} - N_{\rm obs} + N_{\rm obs} \ln\left(\frac{N_{\rm obs}}{N_{\rm stat}}\right)\right), \tag{9.1}$$

   where $N_{\rm stat}$ and $N_{\rm obs}$ are the numbers of events inside the TA hotspot region expected from the stationary-rate hypothesis and that of the observation on a certain date, respectively. The maximum deviance of the observation is $D_{\rm max} = 5.23$ (the left panel of Fig. 9.4).

2. Generate 1 million event sets, each of which consists of the same number of the events as the observation (44 events) temporally random within the 15 years of the observation, and calculate $D_{\rm max}$ for each simulated event set.

3. There are 109,655 event sets that have the maximum deviances greater than 5.23 (the right panel of Fig. 9.4). The ratio of them to the generated event sets is 11.0%. This corresponds to a one-sided probability of 1.2σ.

This significance does not rule out the constant event rate from the TA hot spot region. However, we consider the model in this section as a pessimistic case.

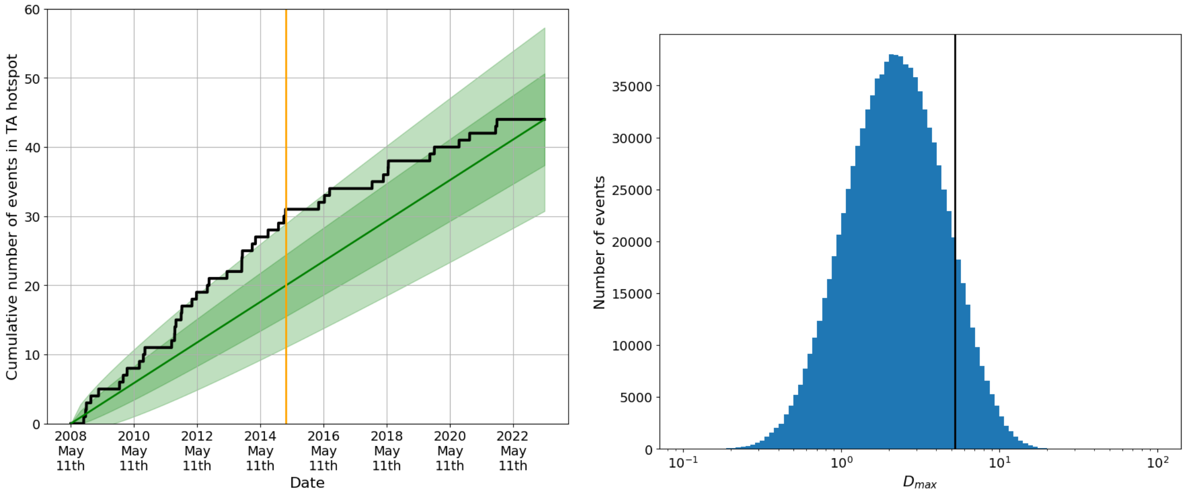

FIGURE 9.4: (Left) The cumulative number of events from the TA hotspot region observed by the TA SD. The green line indicates the stationary rate, and the green bands represent $\pm 1\sigma$ and $\pm 2\sigma$ statistical deviations from the stationary rate. The vertical line represents the maximum deviance $D_{\max} = 5.23$ from the stationary rate. (Right) The distribution of the maximum deviance $D_{\max}$ of 1 million event sets. Each event set consists of 44 events, distributed temporally randomly in the 15-year observational period. The vertical line indicates the observed maximum deviance $D_{\max} = 5.23$.

9.2.1 Projections of the significance of the TA hotspot

Figure 9.5 shows the expectation of the number of events from the TA hotspot region with energies greater than 5.7×10^{19} eV observed by the TA×4 SD array and the TA SD array. In the figure, two expectations are given; one is the constant rate averaged over the 15 years of the observation of the TA SD (the green dashed line in the figure), and the other is the constant rate averaged over the last 8 years of observation of the TA SD (the blue dash-dotted line in the figure).

With the former model, the number of events from the TA hot spot region will be doubled around 2028. With this model, the Li-Ma significance [110], which has been used to calculate the significance of the TA hot spot [26], given by

$$S_{LM} = \sqrt{2}\left[N_{\text{on}} \ln\left(\frac{(1+\eta)N_{\text{on}}}{\eta(N_{\text{on}}+N_{\text{off}})}\right) + N_{\text{off}} \ln\left(\frac{(1+\eta)N_{\text{off}}}{\eta(N_{\text{on}}+N_{\text{off}})}\right)\right]^{1/2} \tag{9.2}$$

is expected to be 7.7σ in October 2030. Assuming a penalty of the search, which considers chance probability to observe such Li-Ma significance anywhere in the sky, decreases the significance by 2σ following previous TA hotspot analyses [26] [27], the expected global significance is 5.7σ. This global significance is conservative one since it is assumed that the location and size of the hotspot are searched and penalized in the same way as the previous analyses.

9.2.2 Projections of the significance to rule out the scenario that TA hotspot is stationary

With the latter model, where the event rate from the TA hotspot is the average over the last 8 years observation of the TA SD, the expected Li-Ma significance of the TA

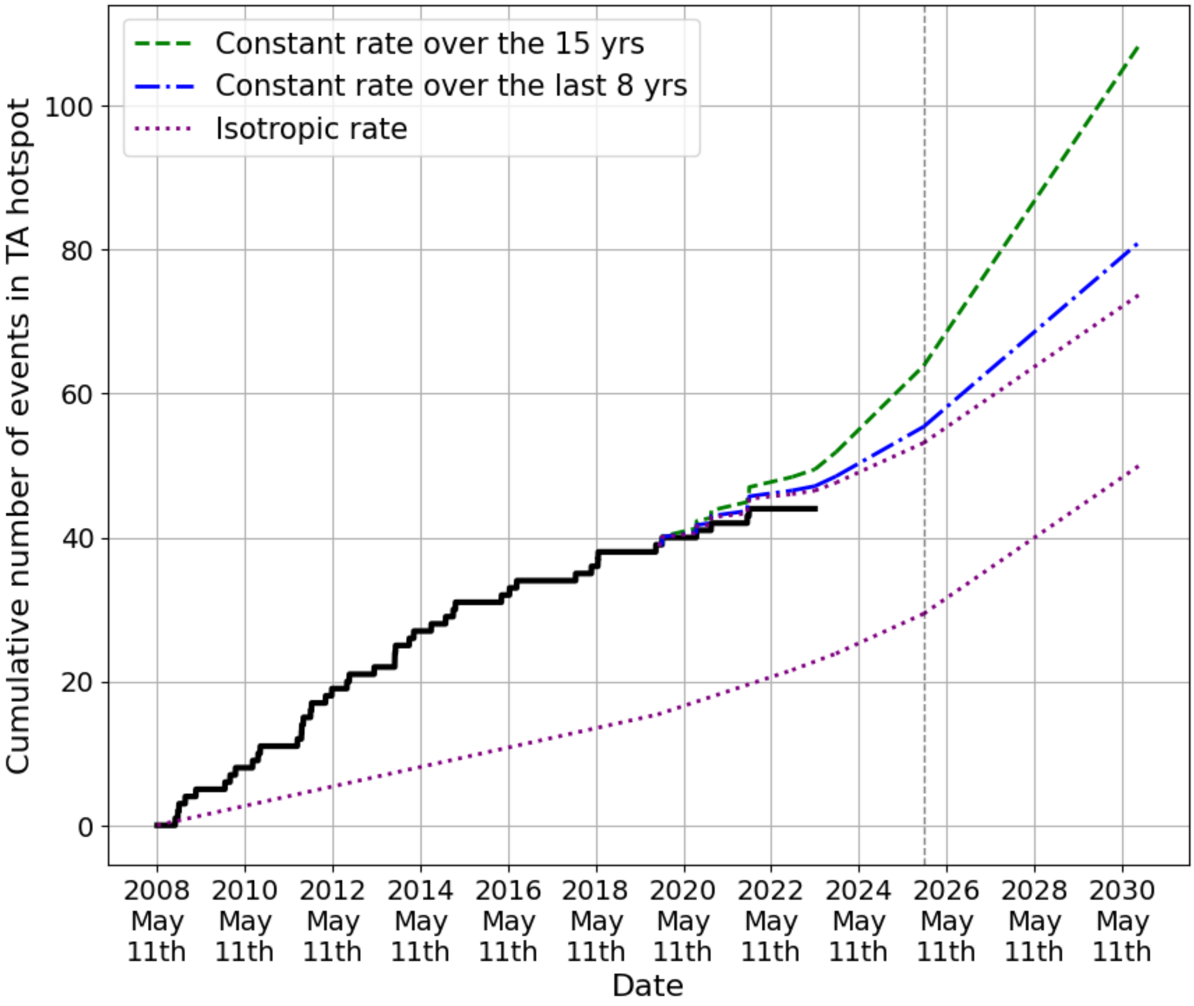

FIGURE 9.5: The expectation of the number of events with energies greater than 5.7×10^{19} eV inside the TA hot spot region (the circle centered at $\delta = 40.5°$, $\alpha = 144.0°$ with 25° radius). The black solid line is the observed events by the TA SD up to 11th May 2023. The green dashed line and the blue dash-dotted line represent the expected number of events by the TA×4 SD and the TA SD, assuming the constant rates of the 15 years and the last 8 years of observation of the TA SD, respectively. The dotted purple line represents isotropic expectation. The vertical dashed line represents the provisional date for the completion of the TA×4 SD array.

hotspot is 4.3σ in October 2030. Therefore, the global significance of the existence of the TA hotspot is conservatively 2.3σ.

Instead, the significance of ruling out the scenario that the TA hotspot is stationary is expected to be 2.8σ. It is calculated as follows; the maximum deviance expected to be observed in 2030 with this model is $D_{\mathrm{max}} = 13.3$ (the left panel of Fig. 9.6). One million event sets, each of which consists of the same number of events (81 events) expected by this model, are generated. In each event set, the dates of observation of 81 events are randomly assigned within the 22 years until 2030 according to the aperture (the green solid line in the left panel of Fig. 9.6), which means the constant rate from the TA hotspot region is assumed here as a null hypothesis. The maximum deviance D_{max} is calculated for the generated 1 million event sets, and 2,384 of the 1 million event sets have $D_{\mathrm{max}} > 13.3$ (the right panel of Fig. 9.6). The ratio is $2,384/1,000,000 = 0.24\%$, equivalent to a one-sided probability of 2.8σ.

In this case, the indication of the TA hotspot reported with the first 7 years of the observation is due to neither stationary UHECR sources nor stationary backgrounds with the significance of 2.8σ. One possibility of the decade-scale temporal variability is that we are observing a temporal tail from the nearby transient UHECR outburst [111]. According to the reference [111], UHECRs from the TA hotspot region are less deflected by the Galactic magnetic field, and temporal extent of UHECRs entering the Galaxy at the same time is smaller than UHECRs entering from other directions. Specifically, the temporal variability of the event rate of UHECRs entering the Galaxy at the same time with rigidity of $\sim$ 21 EV due to the Galactic magnetic field (using JF12Planck model [112]) in the direction of the TA hotspot is of the order of 10 years. The temporal variability due to the extragalactic magnetic field is more significant: 52 years and 5200 years for 0.1 nG and 1 nG, respectively, at a distance of 3.6 Mpc (distance to M82), according to [111]. It is difficult to explain the temporal variability of the event rate from the TA hotspot with the 10-year time scale considering both the Galactic and extragalactic magnetic fields, however, we would be able to study UHECR in terms of the temporal variability, which is a new perspective of the UHECR observation.

Assuming the constant rate over 15 years of the observation, the significance to rule out a hypothesis that the event rate from the TA hotspot region is stationary is expected to be 1.1σ (see Fig. 9.7). In this case, the stationary-rate hypothesis is not ruled out.

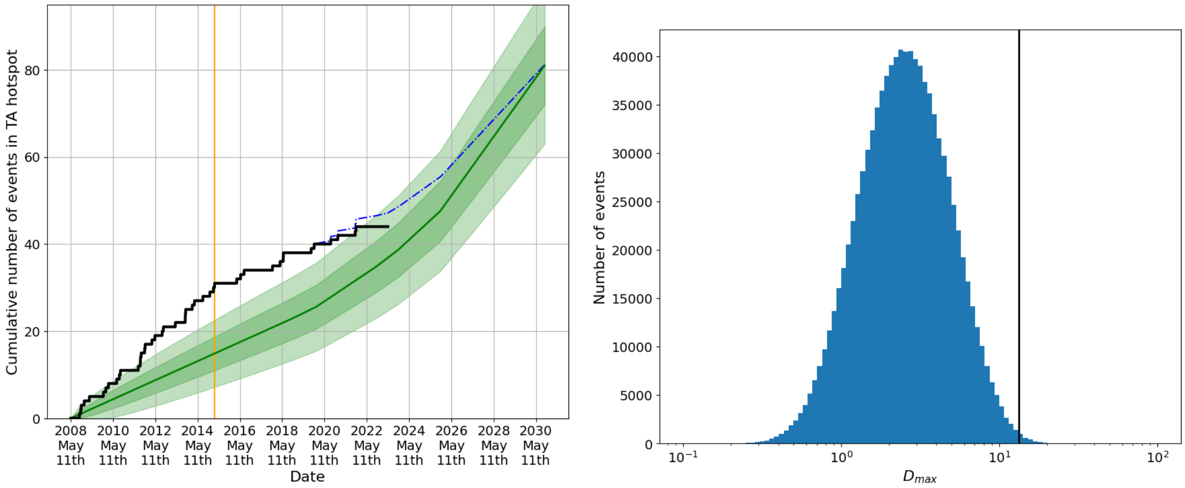

FIGURE 9.6: (Left) The cumulative number of events from the TA hotspot region expected to be observed by the TA×4 SD and the TA SD assuming the constant rate over the last 8 years of the TA SD observation (blue dash-dotted line). The black solid line is the observation of the TA SD. The green line with bands indicates the stationary rate of the expectation, which is the expected hypothetical constant rate from the TA hotspot region, assuming the constant rate over the last 8 years of the TA SD observation. Therefore, the slope of the green line is proportional to the total aperture for $E > 5.7 \times 10^{19}$ eV. The bands represent $\pm 1\sigma$ and $\pm 2\sigma$ statistical deviations from the expectation. The vertical line represents the date with the maximum deviance $D_{\rm max} = 13.3$ from the stationary rate. (Right) The distribution of the maximum deviance $D_{\rm max}$ of 1 million event sets. Each event set consists of 81 events, distributed following the stationary rate in the 22-year observational period. The vertical line indicates the observed maximum deviance $D_{\rm max} = 13.3$. There are 2,384 event sets on the right side of the vertical line.

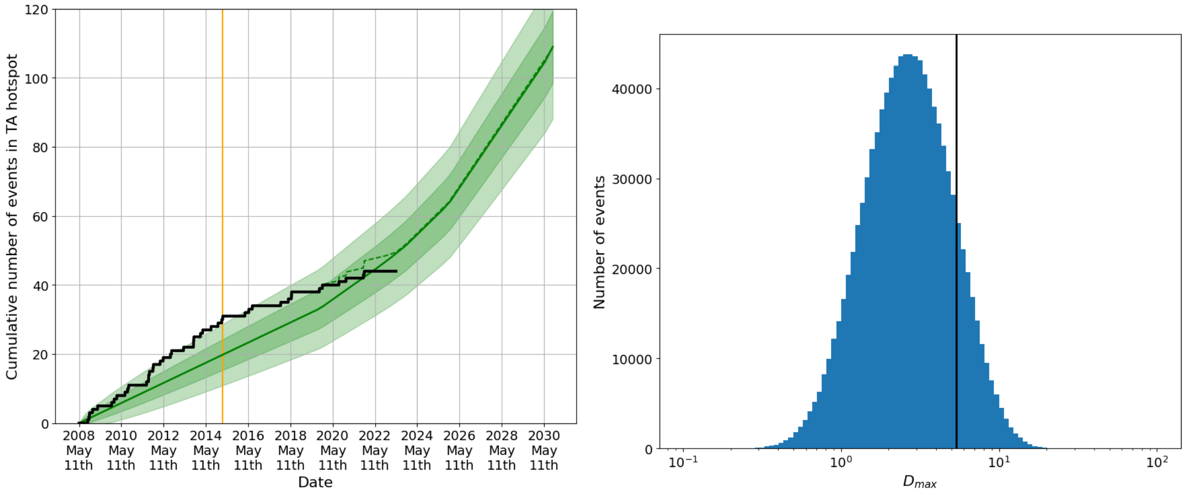

FIGURE 9.7: Same as Fig. 9.6, but assuming the constant rate over the 15 years of the observation.

Chapter 10

Conclusions

The origins of ultra-high-energy cosmic rays (UHECRs) have not been understood since their first discovery in the 1960s. There has been observational progress including some features in the UHECR energy spectrum, some anisotropies in arrival direction such as the TA hotspot, and the spectral difference between the northern sky and the southern sky. The TA×4 experiment began in 2019 with the addition of 257 surface detectors (SDs) with 2.08 km spacing and two fluorescence detector (FD) stations on the north and south sides of the TA SD array. With an additional observation area of approximately 1000 km^2, it expanded the largest air shower observatory in the Northern Hemisphere. One of the primary missions of the TA×4 experiment is testing the TA hotspot with additional statistics. The more precise measurements of the cosmic ray energy spectrum and the mass composition in the highest-energy region are also significant missions.

In this work, we established analysis methods for the extended surface detector array, the TA×4 SD array, reproduced the time-dependent running status of the TA×4 SD array by the established Monte Carlo (MC) simulation, and measured the highest-energy cosmic ray energy spectrum above 10^{19} eV with the TA×4 SD array for the first time. The running status of the TA×4 SD array has evolved from period to period over the first four years. Initially, it operated independently in the six sub-arrays until the implementation of the inter-tower trigger in November 2022. In addition to the trigger system, the number of working TA×4 SD has not been constant since the travel from Japan to the observational site was severely restricted due to the COVID-19 pandemic. I have been in charge of the operation of the TA×4 SD array since it started operation in April 2019. I have checked the status of the SDs, directed the onsite maintenance, fixed problems onsite, and maintained stable observation. Currently, more than 90% of SDs are working stably with the full inter-tower trigger.

The performance of the TA×4 SD array differs from the TA SD array since the detector spacing differs. I modified the Monte Carlo (MC) simulation method and the reconstruction method of the TA SD array to better model the TA×4 SD array. The observation by the TA×4 SD array is well reproduced by the MC simulation regardless of the running status, different trigger systems, and occupancy rates of SD by reflecting them in the MC simulation. I determined event selection criteria for the TA×4 SD array considering its performance. The exposure of the TA×4 SD array in the first three years of the observation is about 30% of that of the TA SD array in 14 years of the observation for $E > 10^{20}$ eV with the event selection.

Another difference between the TA×4 SD array and the TA SD array is the number of hybrid events to determine the energy scale. The energy scale is a factor to scale the energy reconstructed by the SD to match the energy reconstructed by the FD, which is calorimetrically determined. There has not been a sufficient number of hybrid events to determine the energy scale of the TA×4 SD array in the same way as the TA SD array due to the higher energy threshold and a short observational period of the TA×4 SD array. Therefor, I proposed a new method to determine the energy scale. In this method, the energy scale is determined by comparing the observed number of events with the number of events calculated in the MC simulation assuming the energy spectrum observed by the TA experiment. The energy scale factor was determined to be 1.36 ± 0.05.

With this energy scale, I calculated the highest-energy cosmic ray energy spectrum for energies greater than 10^{19} eV with the TA×4 SD array for the first time. The exposure of the TA SD array is calculated considering the bin-to-bin migration effect assuming an input energy spectrum. Since the energy resolution of the TA×4 SD array is not as good as the TA SD array and the exposure depends on assumptions, I introduced the forward-folding method, which is less dependent on the input energy spectrum than the method used in the TA SD array. With the forward-folding method, I tested two models of the energy spectrum: the broken power law model and the single power law model.

The broken power law model is preferred over the single power law model; the p-value of the broken power law model is 0.140, while that of the single power law model is 0.0811. This is the measurement of the cutoff in the energy spectrum by the TA×4 SD array independent of the TA SD array, although both models are acceptable. The best fit of the break energy of the broken power law model is consistent with the previous TA SD measurement. The consistency of the cutoff position implies that the energy scale is correctly determined.

Using the forward-folding method, we also calculated the UHECR energy spectrum by combining the three years of the TA×4 SD data and the 14 years of the TA SD data. It is the most statistically precise measurement of the UHECR energy spectrum in the northern sky. Two models are tested: the broken power law with two and three breaks. The three-break power law function is preferred over the two-break power law function; the p-values of the two-break and three-break models are 0.0329 and 0.246, respectively. It implies that the feature corresponding to the so called "instep" observed in the southern sky also exists in the northern sky. The cutoff significance is 8.2σ using the combined data.

We discussed the difference in the energy spectrum in the common declination band ($-15.7^\circ < \delta < 24.8^\circ$) observed by both the TA experiment and the PAO using the 14 years of the TA SD data. The difference is found to be a statistical significance of 3.5σ with the previous method in which the declination-dependent exposure is not considered. We introduce a simple model in which the energy spectrum changes at a particular declination: the TA energy spectrum at $\delta > 24.8^\circ$ and the PAO energy spectrum at $\delta < -15.7^\circ$ to consider the declination-dependent exposures. With the model, the difference decreased from 3.5σ to 2.2σ. The significance of 2.2σ is still not small, and this does not fully explain the difference in the energy spectra in the full fields of view of the experiments. It is the first time to compare the energy spectra in the common band considering the declination-dependent exposures with a simple model, and the reduction of the significance from 3.5σ to 2.2σ indicates the importance of the declination-dependent exposure. More sophisticated models or model-independent analyses will advance our understanding of the origin of the spectral difference between the northern sky observed by the TA and the southern sky observed by the PAO.

We discussed future results expected to be observed by the TA×4 SD array. It was assumed that the TA×4 SD array will work with about 90% of the working SDs, and the observation with additional ∼250 SDs (completing the TA×4 construction) beginning in November 2025. The number of events with energies greater than $10^{19.5}$

eV observed by the TA×4 SD array and TA SD array is expected to be about three times the current number in 2030. The TA×4 SD array alone will be able to reject the single power-law model with a significance of above 3σ in 2028. The difference in the energy spectra of the different declination bands would be tested to $\sim 5\sigma$ in 2025 using the TA×4 SD and TA SD data. In 2030, a spectral anisotropy test for six different sky regions would be possible with the same statistical power as the current two-region test. The TA hotspot can be confirmed with the global significance of 5.7σ, which is a conservative expectation, in 2030 using the data of the TA×4 SD and the TA SD if the event rate from the TA hotspot is constant: the average over the 15 years of the observation. If the event rate is lower, constant with the average over the last eight years, the significance would be 2.3σ. In this case, we could state that the event rate from the TA hotspot is not stationary with a significance of 2.8σ, and we would be able to study UHECR in terms of the temporal variability, which is a new perspective of the UHECR observation. Regardless of the scenarios, more statistically precise studies to reveal the nature of the TA hotspot, such as [28] [29] [31] [32], will be possible with the increased number of events from the TA hotspot region.

Bibliography

[1] V. Hess. “Über Beobachtungen der durchdringenden Strahlung bei sieben Freiballonfahrten”. In: *Phys. Z* 13 (Jan. 1912).

[2] Carmelo Evoli. *The Cosmic-Ray Energy Spectrum*. May 2023. DOI: `10.5281/zenodo.7948212`. URL: `https://doi.org/10.5281/zenodo.7948212`.

[3] John Linsley. “Evidence for a Primary Cosmic-Ray Particle with Energy 10^{20} eV”. In: *Phys. Rev. Lett.* 10 (4 1963), pp. 146–148. DOI: `10.1103/PhysRevLett.10.146`. URL: `https://link.aps.org/doi/10.1103/PhysRevLett.10.146`.

[4] M. Unger and G. Farrar. “Progress in the Global Modeling of the Galactic Magnetic Field”. In: *EPJ Web of Conferences* 210 (2019). Ed. by I. Lhenry-Yvon et al., p. 04005. DOI: `10.1051/epjconf/201921004005`. URL: `https://doi.org/10.1051%2Fepjconf%2F201921004005`.

[5] R. A. Batista et al. “Open Questions in Cosmic-Ray Research at Ultrahigh Energies”. In: *Frontiers in Astronomy and Space Sciences* 6 (2019). ISSN: 2296-987X. DOI: `10.3389/fspas.2019.00023`. URL: `https://www.frontiersin.org/articles/10.3389/fspas.2019.00023`.

[6] A. M. Hillas. “The Origin of Ultra-High-Energy Cosmic Rays”. In: *Annual Review of Astronomy and Astrophysics* 22.1 (1984), pp. 425–444. DOI: `10.1146/annurev.aa.22.090184.002233`. eprint: `https://doi.org/10.1146/annurev.aa.22.090184.002233`. URL: `https://doi.org/10.1146/annurev.aa.22.090184.002233`.

[7] A. Addazi et al. “Quantum gravity phenomenology at the dawn of the multi-messenger era—A review”. In: *Progress in Particle and Nuclear Physics* 125 (2022), p. 103948. ISSN: 0146-6410. DOI: `https://doi.org/10.1016/j.ppnp.2022.103948`. URL: `https://www.sciencedirect.com/science/article/pii/S0146641022000096`.

[8] Sangjin Lee, Angela V. Olinto, and Günter Sigl. “Extragalactic Magnetic Field and the Highest Energy Cosmic Rays”. In: *The Astrophysical Journal* 455.1 (1995), p. L21. DOI: `10.1086/309812`. URL: `https://dx.doi.org/10.1086/309812`.

[9] J. D. Bray and A. M. M. Scaife. “An Upper Limit on the Strength of the Extragalactic Magnetic Field from Ultra-high-energy Cosmic-Ray Anisotropy”. In: *The Astrophysical Journal* 861.1 (2018), p. 3. DOI: `10.3847/1538-4357/aac777`. URL: `https://dx.doi.org/10.3847/1538-4357/aac777`.

[10] H. Kawai et al. “Telescope Array Experiment”. In: *Nuclear Physics B - Proceedings Supplements* 175-176 (2008). Proceedings of the XIV International Symposium on Very High Energy Cosmic Ray Interactions, pp. 221–226. ISSN: 0920-5632. DOI: `https://doi.org/10.1016/j.nuclphysbps.2007.11.002`. URL: `https://www.sciencedirect.com/science/article/pii/S0920563207007992`.

[11] "The Pierre Auger Cosmic Ray Observatory". In: *Nuclear Instruments and Methods in Physics Research Section A: Accelerators, Spectrometers, Detectors and Associated Equipment* 798 (2015), pp. 172–213. ISSN: 0168-9002. DOI: `https://doi.org/10.1016/j.nima.2015.06.058`. URL: `https://www.sciencedirect.com/science/article/pii/S0168900215008086`.

[12] E. Fermi. "On the Origin of the Cosmic Radiation". In: *Phys. Rev.* 75 (8 1949), pp. 1169–1174. DOI: `10.1103/PhysRev.75.1169`. URL: `https://link.aps.org/doi/10.1103/PhysRev.75.1169`.

[13] The Pierre Auger Collaboration. "Measurement of the cosmic-ray energy spectrum above 2.5×10^{18} eV using the Pierre Auger Observatory". In: *Phys. Rev. D* 102 (6 2020), p. 062005. DOI: `10.1103/PhysRevD.102.062005`. URL: `https://link.aps.org/doi/10.1103/PhysRevD.102.062005`.

[14] R. L. Workman and Others. "Review of Particle Physics". In: *PTEP* 2022 (2022), p. 083C01. DOI: `10.1093/ptep/ptac097`.

[15] K. Greisen. "End to the Cosmic-Ray Spectrum?" In: *Phys. Rev. Lett.* 16 (17 1966), pp. 748–750. DOI: `10.1103/PhysRevLett.16.748`. URL: `https://link.aps.org/doi/10.1103/PhysRevLett.16.748`.

[16] G. T. Zatsepin and V. A. Kuzmin. "Upper limit of the spectrum of cosmic rays". In: *JETP Lett.* 4 (1966), pp. 78–80.

[17] M. Takeda et al. "Energy determination in the Akeno Giant Air Shower Array experiment". In: *Astroparticle Physics* 19.4 (2003), pp. 447–462. ISSN: 0927-6505. DOI: `https://doi.org/10.1016/S0927-6505(02)00243-8`. URL: `https://www.sciencedirect.com/science/article/pii/S0927650502002438`.

[18] R. U. Abbasi et al. "First Observation of the Greisen-Zatsepin-Kuzmin Suppression". In: *Phys. Rev. Lett.* 100 (10 2008), p. 101101. DOI: `10.1103/PhysRevLett.100.101101`. URL: `https://link.aps.org/doi/10.1103/PhysRevLett.100.101101`.

[19] A. Abdul Halim et al. "Constraining the sources of ultra-high-energy cosmic rays across and above the ankle with the spectrum and composition data measured at the Pierre Auger Observatory". In: *Journal of Cosmology and Astroparticle Physics* 2023.5, 024 (May 2023), p. 024. DOI: `10.1088/1475-7516/2023/05/024`. arXiv: `2211.02857 [astro-ph.HE]`.

[20] Douglas Bergman. "Telescope Array Combined Fit to Cosmic Ray Spectrum and Composition". In: *PoS* ICRC2021 (2021), p. 338. DOI: `10.22323/1.395.0338`.

[21] Yoshiki Tsunesada. "Measurement of UHECR energy spectrum with the Pierre Auger Observatory and the Telescope Array". In: *PoS* ICRC2023 (2023), p. 406. DOI: `10.22323/1.444.0406`.

[22] Shoichi Ogio. "A study of the systematic effects on the energy scale for the measurement of UHECR spectrum by the TA SD array". In: *PoS* ICRC2023 (2023), p. 400. DOI: `10.22323/1.444.0400`.

[23] R. U. Abbasi et al. *Evidence for Declination Dependence of the Ultrahigh Energy Cosmic Ray Spectrum in the Northern Hemisphere*. 2021. arXiv: `1801.07820 [astro-ph.HE]`.

[24] Pavlo Plotko et al. "Differences between the Pierre Auger Observatory and Telescope Array Spectra: Systematic Effects or Indication of a Local Source of Ultra-high-energy Cosmic Rays?" In: *The Astrophysical Journal* 953.2 (2023), p. 129. DOI: `10.3847/1538-4357/acdf59`. URL: `https://dx.doi.org/10.3847/1538-4357/acdf59`.

[25] Yoshiki Tsunesada et al. "Joint analysis of the energy spectrum of ultra-high-energy cosmic rays as measured at the Pierre Auger Observatory and the Telescope Array". In: *PoS* ICRC2021 (2021), p. 337. DOI: `10.22323/1.395.0337`.

[26] R. U. Abbasi et al. "Indications of Intermediate-scale Anisotropy of Cosmic Rays with Energy Greater Than 57 EeV in the Northern Sky Measured with the Surface Detector of the Telescope Array Experiment". In: *The Astrophysical Journal Letters* 790.2 (2014), p. L21. DOI: `10.1088/2041-8205/790/2/L21`. URL: `https://dx.doi.org/10.1088/2041-8205/790/2/L21`.

[27] Jihyun Kim et al. "Anisotropies in the arrival direction distribution of ultra-high energy cosmic rays measured by the Telescope Array surface detector". In: *PoS* ICRC2023 (2023), p. 244. DOI: `10.22323/1.444.0244`.

[28] Hao-Ning He et al. "Monte Carlo Bayesian search for the plausible source of the Telescope Array hotspot". In: *Phys. Rev. D* 93 (4 2016), p. 043011. DOI: `10.1103/PhysRevD.93.043011`. URL: `https://link.aps.org/doi/10.1103/PhysRevD.93.043011`.

[29] Ke Fang et al. "Is the Ultra-High Energy Cosmic-Ray Excess Observed by the Telescope Array Correlated with IceCube Neutrinos?" In: *Astrophys. J.* 794.2 (2014), p. 126. DOI: `10.1088/0004-637X/794/2/126`. arXiv: `1404.6237 [astro-ph.HE]`.

[30] Daniel N. Pfeffer, Ely D. Kovetz, and Marc Kamionkowski. "Ultrahigh-energy cosmic ray hotspots from tidal disruption events". In: *Mon. Not. Roy. Astron. Soc.* 466.3 (2017), pp. 2922–2926. DOI: `10.1093/mnras/stw3337`. arXiv: `1512.04959 [astro-ph.HE]`.

[31] Jihyun Kim et al. "Filaments of galaxies as a clue to the origin of ultrahigh-energy cosmic rays". In: *Science Advances* 5.1 (2019), eaau8227. DOI: `10.1126/sciadv.aau8227`. eprint: `https://www.science.org/doi/pdf/10.1126/sciadv.aau8227`. URL: `https://www.science.org/doi/abs/10.1126/sciadv.aau8227`.

[32] A. M. Taylor, J. H. Matthews, and A. R. Bell. "UHECR echoes from the Council of Giants". In: *Mon. Not. Roy. Astron. Soc.* 524.1 (2023), pp. 631–642. DOI: `10.1093/mnras/stad1716`. arXiv: `2302.06489 [astro-ph.HE]`.

[33] Ralph Engel, Dieter Heck, and Tanguy Pierog. "Extensive Air Showers and Hadronic Interactions at High Energy". In: *Annual Review of Nuclear and Particle Science* 61.1 (2011), pp. 467–489. DOI: `10.1146/annurev.nucl.012809.104544`. eprint: `https://doi.org/10.1146/annurev.nucl.012809.104544`. URL: `https://doi.org/10.1146/annurev.nucl.012809.104544`.

[34] Karl-Heinz Kampert and Michael Unger. "Measurements of the cosmic ray composition with air shower experiments". In: *Astroparticle Physics* 35.10 (2012), pp. 660–678. ISSN: 0927-6505. DOI: `https://doi.org/10.1016/j.astropartphys.2012.02.004`. URL: `https://www.sciencedirect.com/science/article/pii/S0927650512000382`.

[35] W. Heitler. *The quantum theory of radiation*. Vol. 5. International Series of Monographs on Physics. Oxford: Oxford University Press, 1936.

[36] J. Matthews. "A Heitler model of extensive air showers". In: *Astroparticle Physics* 22.5 (2005), pp. 387–397. ISSN: 0927-6505. DOI: `https://doi.org/10.1016/j.astropartphys.2004.09.003`. URL: `https://www.sciencedirect.com/science/article/pii/S0927650504001598`.

[37] C. Meurer et al. "Muon production in extensive air showers and its relation to hadronic interactions". In: *Czechoslovak Journal of Physics* 56.1 (2006), A211–A219. DOI: `10.1007/s10582-006-0156-9`. URL: `https://doi.org/10.1007/s10582-006-0156-9`.

[38] Jaime Alvarez-Muñiz et al. "Hybrid simulations of extensive air showers". In: *Phys. Rev. D* 66 (3 2002), p. 033011. DOI: `10.1103/PhysRevD.66.033011`. URL: `https://link.aps.org/doi/10.1103/PhysRevD.66.033011`.

[39] D. Newton, J. Knapp, and A.A. Watson. "The optimum distance at which to determine the size of a giant air shower". In: *Astroparticle Physics* 26.6 (2007), pp. 414–419. ISSN: 0927-6505. DOI: `https://doi.org/10.1016/j.astropartphys.2006.08.003`. URL: `https://www.sciencedirect.com/science/article/pii/S0927650506001216`.

[40] A Obermeier. "The Fluorescence Yield of Air excited by Electron measured with the AIRFLY Experiment". PhD thesis. 2007.

[41] Pablo M. Bauleo and Julio Rodríguez Martino. "The dawn of the particle astronomy era in ultra-high-energy cosmic rays". In: *Nature* 458.7240 (2009), pp. 847–851. DOI: `10.1038/nature07948`. URL: `https://doi.org/10.1038/nature07948`.

[42] Gioacchino Alex Anastasi. "AugerPrime: The Pierre Auger Observatory upgrade". In: *Nuclear Instruments and Methods in Physics Research Section A: Accelerators, Spectrometers, Detectors and Associated Equipment* 1044 (2022), p. 167497. ISSN: 0168-9002. DOI: `https://doi.org/10.1016/j.nima.2022.167497`. URL: `https://www.sciencedirect.com/science/article/pii/S0168900222007896`.

[43] The Pierre Auger Collaboration et al. "Observation of a large-scale anisotropy in the arrival directions of cosmic rays above 8×10^{18} eV". In: *Science* 357.6357 (2017), pp. 1266–1270. DOI: `10.1126/science.aan4338`. eprint: `https://www.science.org/doi/pdf/10.1126/science.aan4338`. URL: `https://www.science.org/doi/abs/10.1126/science.aan4338`.

[44] N Globus et al. "Cosmic ray anisotropy from large-scale structure and the effect of magnetic horizons". In: *Monthly Notices of the Royal Astronomical Society* 484.3 (Jan. 2019), pp. 4167–4173. ISSN: 0035-8711. DOI: `10.1093/mnras/stz164`. eprint: `https://academic.oup.com/mnras/article-pdf/484/3/4167/27747211/stz164.pdf`. URL: `https://doi.org/10.1093/mnras/stz164`.

[45] R. U. Abbasi et al. "Search for Large-scale Anisotropy on Arrival Directions of Ultra-high-energy Cosmic Rays Observed with the Telescope Array Experiment". In: *The Astrophysical Journal Letters* 898.2 (2020), p. L28. DOI: `10.3847/2041-8213/aba0bc`. URL: `https://dx.doi.org/10.3847/2041-8213/aba0bc`.

[46] Telescope Array Collaboration et al. *Indications of a Cosmic Ray Source in the Perseus-Pisces Supercluster*. 2021. arXiv: `2110.14827 [astro-ph.HE]`.

[47] P. Abreu et al. "Arrival Directions of Cosmic Rays above 32 EeV from Phase One of the Pierre Auger Observatory". In: *The Astrophysical Journal* 935.2 (2022), p. 170. DOI: `10.3847/1538-4357/ac7d4e`. URL: `https://dx.doi.org/10.3847/1538-4357/ac7d4e`.

[48] Cecilia Lunardini et al. "Are starburst galaxies a common source of high energy neutrinos and cosmic rays?" In: *Journal of Cosmology and Astroparticle Physics* 2019.10, 073 (Oct. 2019), p. 073. DOI: `10.1088/1475-7516/2019/10/073`. arXiv: `1902.09663 [astro-ph.HE]`.

[49] A. di Matteo et al. "2022 report from the Auger-TA working group on UHECR arrival directions". In: *EPJ Web of Conferences* 283 (2023). Ed. by I. De Mitri et al., p. 03002. DOI: `10.1051/epjconf/202328303002`. URL: `https://doi.org/10.1051%2Fepjconf%2F202328303002`.

[50] R. U. Abbasi et al. "Depth of Ultra High Energy Cosmic Ray Induced Air Shower Maxima Measured by the Telescope Array Black Rock and Long Ridge FADC Fluorescence Detectors and Surface Array in Hybrid Mode". In: *The Astrophysical Journal* 858.2 (2018), p. 76. DOI: `10.3847/1538-4357/aabad7`. URL: `https://dx.doi.org/10.3847/1538-4357/aabad7`.

[51] Eric Mayotte et al. *Measurement of the mass composition of ultra-high-energy cosmic rays at the Pierre Auger Observatory*. July 2023, p. 365. DOI: `10.22323/1.444.0365`.

[52] Bergman, Douglas et al. "Testing the Compatibility of the Depth of the Shower Maximum Measurements performed at Telescope Array and the Pierre Auger Observatory - Auger-TA Mass Composition Working Group Report". In: *EPJ Web Conf.* 283 (2023), p. 02008. DOI: `10.1051/epjconf/202328302008`. URL: `https://doi.org/10.1051/epjconf/202328302008`.

[53] R. U. Abbasi et al. "Mass composition of ultrahigh-energy cosmic rays with the Telescope Array Surface Detector data". In: *Phys. Rev. D* 99 (2 2019), p. 022002. DOI: `10.1103/PhysRevD.99.022002`. URL: `https://link.aps.org/doi/10.1103/PhysRevD.99.022002`.

[54] Adila Abdul Halim et al. "Mass Composition from 3 EeV to 100 EeV using the Depth of the Maximum of Air-Shower Profiles Estimated with Deep Learning using Surface Detector Data of the Pierre Auger Observatory". In: *PoS* ICRC2023 (2023), p. 278. DOI: `10.22323/1.444.0278`.

[55] Felix Riehn et al. "Hadronic interaction model sibyll 2.3d and extensive air showers". In: *Phys. Rev. D* 102 (6 2020), p. 063002. DOI: `10.1103/PhysRevD.102.063002`. URL: `https://link.aps.org/doi/10.1103/PhysRevD.102.063002`.

[56] B. Peters. "Primary cosmic radiation and extensive air showers". In: *Il Nuovo Cimento (1955-1965)* 22.4 (1961), pp. 800–819. DOI: `10.1007/BF02783106`. URL: `https://doi.org/10.1007/BF02783106`.

[57] Michael Unger, Glennys R. Farrar, and Luis A. Anchordoqui. "Origin of the ankle in the ultrahigh energy cosmic ray spectrum, and of the extragalactic protons below it". In: *Phys. Rev. D* 92 (12 2015), p. 123001. DOI: `10.1103/PhysRevD.92.123001`. URL: `https://link.aps.org/doi/10.1103/PhysRevD.92.123001`.

[58] Marco Stein Muzio, Glennys R. Farrar, and Michael Unger. "Probing the environments surrounding ultrahigh energy cosmic ray accelerators and their implications for astrophysical neutrinos". In: *Phys. Rev. D* 105 (2 2022), p. 023022. DOI: `10.1103/PhysRevD.105.023022`. URL: `https://link.aps.org/doi/10.1103/PhysRevD.105.023022`.

[59] Dennis Soldin. "Update on the Combined Analysis of Muon Measurements from Nine Air Shower Experiments". In: *PoS* ICRC2021 (2021), p. 349. DOI: `10.22323/1.395.0349`.

[60] N.N. Kalmykov, S.S. Ostapchenko, and A.I. Pavlov. "Quark-gluon-string model and EAS simulation problems at ultra-high energies". In: *Nuclear Physics B - Proceedings Supplements* 52.3 (1997), pp. 17–28. ISSN: 0920-5632. DOI: `https://doi.org/10.1016/S0920-5632(96)00846-8`. URL: `https://www.sciencedirect.com/science/article/pii/S0920563296008468`.

[61] S. Ostapchenko. "QGSJET-II: towards reliable description of very high energy hadronic interactions". In: *Nuclear Physics B - Proceedings Supplements* 151.1 (2006). VERY HIGH ENERGY COSMIC RAY INTERACTIONS, pp. 143–146. ISSN: 0920-5632. DOI: `https://doi.org/10.1016/j.nuclphysbps.2005.07.026`. URL: `https://www.sciencedirect.com/science/article/pii/S0920563205009175`.

[62] Eun-Joo Ahn et al. "Cosmic ray interaction event generator SIBYLL 2.1". In: *Phys. Rev. D* 80 (9 2009), p. 094003. DOI: `10.1103/PhysRevD.80.094003`. URL: `https://link.aps.org/doi/10.1103/PhysRevD.80.094003`.

[63] T. Pierog et al. "EPOS LHC: Test of collective hadronization with data measured at the CERN Large Hadron Collider". In: *Phys. Rev. C* 92 (3 2015), p. 034906. DOI: `10.1103/PhysRevC.92.034906`. URL: `https://link.aps.org/doi/10.1103/PhysRevC.92.034906`.

[64] R. U. Abbasi et al. "Measurement of the proton-air cross section with Telescope Array's Black Rock Mesa and Long Ridge fluorescence detectors, and surface array in hybrid mode". In: *Phys. Rev. D* 102 (6 2020), p. 062004. DOI: `10.1103/PhysRevD.102.062004`. URL: `https://link.aps.org/doi/10.1103/PhysRevD.102.062004`.

[65] The Pierre Auger collaboration et al. "Testing effects of Lorentz invariance violation in the propagation of astroparticles with the Pierre Auger Observatory". In: *Journal of Cosmology and Astroparticle Physics* 2022.01 (2022), p. 023. DOI: `10.1088/1475-7516/2022/01/023`. URL: `https://dx.doi.org/10.1088/1475-7516/2022/01/023`.

[66] Saikat Das, Kohta Murase, and Toshihiro Fujii. "Revisiting ultrahigh-energy constraints on decaying superheavy dark matter". In: *Phys. Rev. D* 107 (10 2023), p. 103013. DOI: `10.1103/PhysRevD.107.103013`. URL: `https://link.aps.org/doi/10.1103/PhysRevD.107.103013`.

[67] R. Aloisio, V. Berezinsky, and A. Gazizov. "Transition from galactic to extragalactic cosmic rays". In: *Astroparticle Physics* 39-40 (2012). Cosmic Rays Topical Issue, pp. 129–143. ISSN: 0927-6505. DOI: `https://doi.org/10.1016/j.astropartphys.2012.09.007`. URL: `https://www.sciencedirect.com/science/article/pii/S092765051200182X`.

[68] Mayotte, Eric and Fitoussi, Thomas. “Update on the indication of a mass-dependent anisotropy above $10^{18.7}$ eV in the hybrid data of the Pierre Auger Observatory”. In: *EPJ Web Conf.* 283 (2023), p. 03003. DOI: `10.1051/epjconf/202328303003`. URL: `https://doi.org/10.1051/epjconf/202328303003`.

[69] A. Coleman et al. “Ultra high energy cosmic rays The intersection of the Cosmic and Energy Frontiers”. In: *Astroparticle Physics* 149 (2023), p. 102819. ISSN: 0927-6505. DOI: `https://doi.org/10.1016/j.astropartphys.2023.102819`. URL: `https://www.sciencedirect.com/science/article/pii/S0927650523000051`.

[70] R. U. Abbasi et al. “An extremely energetic cosmic ray observed by a surface detector array”. In: *Science* 382.6673 (2023), pp. 903–907. DOI: `10.1126/science.abo5095`. eprint: `https://www.science.org/doi/pdf/10.1126/science.abo5095`. URL: `https://www.science.org/doi/abs/10.1126/science.abo5095`.

[71] Kuznetsov, Mikhail and Tinyakov, Peter. “UHECR anisotropy and extragalactic magnetic fields with the Telescope Array”. In: *EPJ Web Conf.* 283 (2023), p. 03004. DOI: `10.1051/epjconf/202328303004`. URL: `https://doi.org/10.1051/epjconf/202328303004`.

[72] T. Abu-Zayyad et al. “The surface detector array of the Telescope Array experiment”. In: *Nuclear Instruments and Methods in Physics Research Section A: Accelerators, Spectrometers, Detectors and Associated Equipment* 689 (2012), pp. 87–97. ISSN: 0168-9002. DOI: `https://doi.org/10.1016/j.nima.2012.05.079`. URL: `https://www.sciencedirect.com/science/article/pii/S0168900212005931`.

[73] H. Tokuno et al. “New air fluorescence detectors employed in the Telescope Array experiment”. In: *Nuclear Instruments and Methods in Physics Research Section A: Accelerators, Spectrometers, Detectors and Associated Equipment* 676 (2012), pp. 54–65. ISSN: 0168-9002. DOI: `https://doi.org/10.1016/j.nima.2012.02.044`. URL: `https://www.sciencedirect.com/science/article/pii/S0168900212002422`.

[74] Monica Gene Allen. “Ultra high energy cosmic ray energy spectrum and composition using hybrid analysis with telescope array”. PhD thesis. University of Utah, 2012. URL: `https://collections.lib.utah.edu/details?id=195782&facet_school_or_college_t=%22College+of+Science%22&facet_department_t=%22Physics+%26+Astronomy%22&facet_publication_type_t=%22dissertation%22&rows=100&facet_setname_s=ir_etd`.

[75] R.U. Abbasi et al. “The energy spectrum of cosmic rays above $10^{17.2}$ eV measured by the fluorescence detectors of the Telescope Array experiment in seven years”. In: *Astroparticle Physics* 80 (2016), pp. 131–140. ISSN: 0927-6505. DOI: `https://doi.org/10.1016/j.astropartphys.2016.04.002`. URL: `https://www.sciencedirect.com/science/article/pii/S0927650516300445`.

[76] T. Fujii et al. “An Event Reconstruction Method for the Telescope Array Fluorescence Detectors”. In: *International Symposium on the Recent Progress of Ultra-High Energy Cosmic Ray Observation*. Ed. by Hiroyuki Sagawa et al. Vol. 1367. American Institute of Physics Conference Series. Sept. 2011, pp. 149–152. DOI: `10.1063/1.3628732`.

[77] T. K. Gaisser and A. M. Hillas. "Reliability of the Method of Constant Intensity Cuts for Reconstructing the Average Development of Vertical Showers". In: *International Cosmic Ray Conference*. Vol. 8. International Cosmic Ray Conference. Jan. 1977, p. 353.

[78] D. Heck et al. *CORSIKA: a Monte Carlo code to simulate extensive air showers.* 1998.

[79] T. Abu-Zayyad et al. "Energy spectrum of ultra-high energy cosmic rays observed with the Telescope Array using a hybrid technique". In: *Astroparticle Physics* 61 (2015), pp. 93–101. ISSN: 0927-6505. DOI: `https://doi.org/10.1016/j.astropartphys.2014.05.002`. URL: `https://www.sciencedirect.com/science/article/pii/S0927650514000668`.

[80] T. Abu-Zayyad et al. "THE COSMIC-RAY ENERGY SPECTRUM OBSERVED WITH THE SURFACE DETECTOR OF THE TELESCOPE ARRAY EXPERIMENT". In: *The Astrophysical Journal Letters* 768.1 (2013), p. L1. DOI: `10.1088/2041-8205/768/1/L1`. URL: `https://dx.doi.org/10.1088/2041-8205/768/1/L1`.

[81] Matt Potts and Charles C. H. Jui. "Monocular Energy Spectrum using the TAx4 Fluorescence Detector". In: *Proceedings of 37th International Cosmic Ray Conference — PoS(ICRC2021)* (2021). URL: `https://api.semanticscholar.org/CorpusID:237718639`.

[82] Yuki Kusumori. "Monocular and Hybrid Analysis for TA×4 Fluorescence Detectors". In: *PoS* ICRC2023 (2023), p. 331. DOI: `10.22323/1.444.0331`.

[83] Greg David Furlich. "Observation of the GZK suppression with the telescope array fluorescence telescopes and deployment of the telescope array expansion". PhD thesis. University of Utah, 2020.

[84] *The Japanese website of the TAx4 experiment*. URL: `https://www.icrr.u-tokyo.ac.jp/~hsagawa/TAx4/index.html`.

[85] Rasha Abbasi et al. "The status of the TALE surface detector array and TALE infill project". In: *PoS* ICRC2021 (2021), p. 255. DOI: `10.22323/1.395.0255`.

[86] The Telescope Array Collaboration. "Surface detectors of the TAx4 experiment". In: *Nuclear Instruments and Methods in Physics Research Section A: Accelerators, Spectrometers, Detectors and Associated Equipment* 1019 (2021), p. 165726. ISSN: 0168-9002. DOI: `https://doi.org/10.1016/j.nima.2021.165726`. URL: `https://www.sciencedirect.com/science/article/pii/S0168900221007117`.

[87] Yada Kohei. "The Evaluation of the Performance of Particle Surface Detectors to Ob- serve the Highest Energy Cosmic Rays for the Telescope Array Extension". MA thesis. The University of Tokyo, 2020.

[88] Eiji Kido. "Updates of the surface detector array of the TAx4 experiment". In: *PoS* ICRC2023 (2023), p. 239. DOI: `10.22323/1.444.0239`.

[89] Toshiyuki Nonaka et al. "Long distance network link for TAx4 expansion". In: *PoS* ICRC2019 (2019), p. 372. DOI: `10.22323/1.358.0372`.

[90] Dmitri Ivanov. "Energy Spectrum Measured by the Telescope Array". In: *PoS* ICRC2019 (2019), p. 298. DOI: `10.22323/1.358.0298`.

[91] Kim, Jihyun et al. "Energy Spectrum Measured by the Telescope Array Surface Detectors". In: *EPJ Web Conf.* 283 (2023), p. 02005. DOI: `10.1051/epjconf/202328302005`. URL: `https://doi.org/10.1051/epjconf/202328302005`.

[92] T. Abu-Zayyad et al. “CORSIKA Simulation of the Telescope Array Surface Detector”. In: (Mar. 2014). arXiv: `1403.0644 [astro-ph.IM]`.

[93] Alfredo Ferrari et al. “FLUKA: A multi-particle transport code (Program version 2005)”. In: (Oct. 2005). DOI: `10.2172/877507`.

[94] W R Nelson, H Hirayama, and D W.O. Rogers. “EGS4 code system”. In: (Dec. 1985). URL: `https://www.osti.gov/biblio/6137659`.

[95] M. Kobal. “A thinning method using weight limitation for air-shower simulations”. In: *Astroparticle Physics* 15.3 (2001), pp. 259–273. ISSN: 0927-6505. DOI: `https://doi.org/10.1016/S0927-6505(00)00158-4`. URL: `https://www.sciencedirect.com/science/article/pii/S0927650500001584`.

[96] B. T. Stokes et al. “Dethinning Extensive Air Shower Simulations”. In: *Astropart. Phys.* 35 (2012), pp. 759–766. DOI: `10.1016/j.astropartphys.2012.03.004`. arXiv: `1104.3182 [astro-ph.IM]`.

[97] Dmitri Ivanov et al. “Energy spectrum measured by the telescope array surface detector”. In: *Ph. D. thesis. Rutgers U.* (2012).

[98] J. Allison et al. “Geant4 developments and applications”. In: *IEEE Transactions on Nuclear Science* 53.1 (2006), pp. 270–278. DOI: `10.1109/TNS.2006.869826`.

[99] Takashi Miyata. “Performance Evaluation of Telescope Array Surface Particle Detector”. MA thesis. Tokyo Institute of Science, 2007.

[100] John Linsley and Livio Scarsi. “Arrival Times of Air Shower Particles at Large Distances from the Axis”. In: *Phys. Rev.* 128 (5 1962), pp. 2384–2392. DOI: `10.1103/PhysRev.128.2384`. URL: `https://link.aps.org/doi/10.1103/PhysRev.128.2384`.

[101] T. Teshima et al. “Properties of 10^9-10^{10} GeV extensive air showers at core distances between 100 and 3000 m”. In: *Journal of Physics G Nuclear Physics* 12.10 (Oct. 1986), pp. 1097–1113. DOI: `10.1088/0305-4616/12/10/017`.

[102] S. Yoshida et al. “Lateral distribution of charged particles in giant air showers above 1 EeV observed by AGASA”. In: *Journal of Physics G: Nuclear and Particle Physics* 20.4 (1994), p. 651.

[103] D. Ivanov B. T. Stokes and G. B. Thomson. “A Comparison between Hadronic Interaction Models and Observations by the Telescope Array”. Presentation at ICRC2013, 33rd ICRC p742. 2013.

[104] R. U. Abbasi et al. “Study of muons from ultrahigh energy cosmic ray air showers measured with the Telescope Array experiment”. In: *Phys. Rev. D* 98 (2 2018), p. 022002. DOI: `10.1103/PhysRevD.98.022002`. URL: `https://link.aps.org/doi/10.1103/PhysRevD.98.022002`.

[105] R. S. Fletcher et al. “sibyll: An event generator for simulation of high energy cosmic ray cascades”. In: *Phys. Rev. D* 50 (9 1994), pp. 5710–5731. DOI: `10.1103/PhysRevD.50.5710`. URL: `https://link.aps.org/doi/10.1103/PhysRevD.50.5710`.

[106] Klaus Werner, Fu-Ming Liu, and Tanguy Pierog. “Parton ladder splitting and the rapidity dependence of transverse momentum spectra in deuteron-gold collisions at the BNL Relativistic Heavy Ion Collider”. In: *Phys. Rev. C* 74 (4 2006), p. 044902. DOI: `10.1103/PhysRevC.74.044902`. URL: `https://link.aps.org/doi/10.1103/PhysRevC.74.044902`.

[107] Steve Baker and Robert D. Cousins. “Clarification of the Use of Chi Square and Likelihood Functions in Fits to Histograms”. In: *Nucl. Instrum. Meth.* 221 (1984), pp. 437–442. DOI: `10.1016/0167-5087(84)90016-4`.

[108] Nariaki Sugiura. “Further analysis of the data by Akaike’s information criterion and the finite corrections”. In: *Communications in Statistics - Theory and Methods* 7.1 (1978), pp. 13–26. DOI: `10.1080/03610927808827599`. eprint: `https://doi.org/10.1080/03610927808827599`. URL: `https://doi.org/10.1080/03610927808827599`.

[109] Paul Sommers. “Cosmic ray anisotropy analysis with a full-sky observatory”. In: *Astroparticle Physics* 14.4 (2001), pp. 271–286. ISSN: 0927-6505. DOI: `https://doi.org/10.1016/S0927-6505(00)00130-4`. URL: `https://www.sciencedirect.com/science/article/pii/S0927650500001304`.

[110] T. P. Li and Y. Q. Ma. “Analysis methods for results in gamma-ray astronomy.” In: *apj* 272 (Sept. 1983), pp. 317–324. DOI: `10.1086/161295`.

[111] Noémie Globus, Anatoli Fedynitch, and Roger D. Blandford. “Treasure Maps for Detections of Extreme Energy Cosmic Rays”. In: *The Astrophysical Journal* 945.1 (2023), p. 12. DOI: `10.3847/1538-4357/acaf5f`. URL: `https://dx.doi.org/10.3847/1538-4357/acaf5f`.

[112] Planck Collaboration. “Planck intermediate results. XLII. Large-scale Galactic magnetic fields”. In: *Astronomy and Astrophysics* 596 (May 2016). DOI: `10.1051/0004-6361/201528033`.